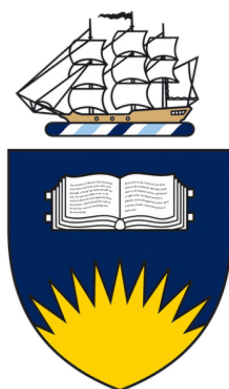


Aqueous Dispersion of Carbon Nanotubes
for Electronic Type-Selective Reactions
with Aryl Diazonium Salts



by

Adam J. Blanch

A thesis submitted in fulfilment of the requirements for the degree of
Doctor of Philosophy

School of Chemical and Physical Sciences
Flinders University

November 2011

CONTENTS

| | |
|--|------------|
| Summary | v |
| Declaration | vii |
| Acknowledgements | ix |
| Publications Arising From This Work | xi |
| Chapter 1 | |
| Introduction | 1 |
| 1.1 The Structure and Properties of Carbon Nanotubes..... | 2 |
| 1.2 Methods of Synthesis | 17 |
| 1.3 Purification..... | 21 |
| 1.4 Dispersion of Carbon Nanotubes | 23 |
| 1.5 Methods of Separation and Sorting..... | 26 |
| 1.6 Motivation and Research Aims..... | 31 |
| Chapter 2 | |
| Experimental & Analytical Techniques | 33 |
| 2.1 Dispersant and Nanotube Materials | 33 |
| 2.2 Preparation of Dispersed CNT Solutions..... | 35 |
| 2.3 Ultraviolet-Visible-Near Infrared (UV-Vis-NIR) Spectroscopy | 41 |
| 2.4 Raman Spectroscopy..... | 52 |
| 2.5 Atomic Force Microscopy (AFM) | 60 |
| 2.6 Other Techniques | 63 |
| Chapter 3 | |
| Comparison of Different Dispersing Materials | 71 |
| 3.1 Performance of Individual Dispersants..... | 71 |
| 3.2 Co-Surfactant Solutions | 84 |
| 3.3 Dispersion Stability in SDS and SDBS..... | 87 |
| 3.4 Optimised Dispersant Concentrations..... | 91 |
| Chapter 4 | |
| Influence of Centrifugation Parameters on Dispersion Properties | 101 |
| 4.1 Effects of Centrifugation Speed, Duration and Temperature..... | 101 |
| 4.2 Centrifugation as a Purification Technique..... | 118 |
| 4.3 Length Fractionation via Centrifugation..... | 125 |

Chapter 5

| | |
|--|------------|
| Influence of Sonication Parameters on Dispersion Properties | 129 |
| 5.1 Factors Affecting the Dispersion Process | 129 |
| 5.2 Duration of Ultrasound Exposure | 133 |
| 5.3 Effects of Nanotube Scission Due to Ultrasound Exposure | 137 |
| 5.4 Containing Vessel Geometry and Tip Placement | 145 |
| 5.5 Applied Ultrasonic Power | 146 |

Chapter 6

| | |
|--|------------|
| Decomposition of Aryl Diazonium Salts In Aqueous Dispersant Solutions | 155 |
| 6.1 Dediazonation Pathways and Reaction Mechanisms with CNTs | 155 |
| 6.2 Dediazonation in Dispersant Solutions | 158 |
| 6.3 Effect of Dispersant Concentration | 165 |
| 6.4 Dediazonation in the Presence of CNTs | 171 |

Chapter 7

| | |
|---|------------|
| Reactions of CNTs With Diazonium Salts in Dispersant Solutions | 173 |
| 7.1 UV-Vis-NIR and Raman Analysis of CNT Dispersions | 173 |
| 7.2 Methods of Measuring Selectivity | 176 |
| 7.3 Reactions in Different Dispersants | 179 |
| 7.4 Effect of pH in SDS, SDBS and Pluronic Dispersions | 188 |
| 7.5 Influence of Reaction Temperature, Diazonium Concentration and Dispersant Concentration | 197 |
| 7.6 Stepwise Additions for Improved Selectivity | 199 |

Chapter 8

| | |
|--|------------|
| Conclusions and Future Directions | 205 |
|--|------------|

Appendix A

| | |
|--|------------|
| Calibration Of Sonicator Power By Calorimetry | 211 |
|--|------------|

Appendix B

| | |
|---|------------|
| Deconvolution of Absorbance Spectra For Species Assignment | 219 |
|---|------------|

Appendix C

| | |
|--|------------|
| Supplementary Data For Sonication Studies | 229 |
|--|------------|

Appendix D

| | |
|---|------------|
| Kinetic Data For Diazonium Reactions | 233 |
|---|------------|

| | |
|---------------------------|------------|
| Bibliography | 241 |
|---------------------------|------------|

SUMMARY

In this work solutions of carbon nanotubes in water were obtained in a variety of different dispersants using a combination of ultrasonication and centrifugation. Suspensions containing nanotube samples possessing different diameter distributions were characterised using optical absorbance spectroscopy to compare the effectiveness of each dispersant. Larger diameter nanotubes were well-suspended by all dispersants while those of smaller diameter were best stabilised by smaller ionic surfactants as the bulkier polymeric variants were unable to conform to their higher degree of curvature. Differences in the stability provided by each dispersant and relative hydrophobic interaction strengths between the dispersing molecule and the nanotube sidewall were investigated, where ionic surfactants sodium dodecylbenzene sulfonate and sodium deoxycholate were found to be superior performers.

Altering the surfactant concentration was found to be more appropriate than tuning the surfactant to nanotube mass ratio to obtain optimally dispersed concentrations of nanotubes. The optimal surfactant concentration was determined for a number of different dispersants through analysis with both optical absorbance and Raman spectroscopy. At high dispersant concentration the nanotubes were found to be flocculated by attractive depletion interactions induced by the greater number of surfactant micelles in the solution volume. It was determined by atomic force microscopy that longer nanotubes are depleted first, leaving aggregates of short nanotubes in the solution.

Dispersions of nanotubes in sodium dodecylbenzene sulfonate were used to examine the sonication and centrifugation parameter space. The dispersion properties of concentration, mean length and degree of aggregation were probed by optical absorbance, Raman spectroscopy and atomic force microscopy to determine the relationship between these attributes and instrumental variables. It was found that both centrifugation and sonication have a significant influence on the mean length of the nanotube population, where the applied duration of both processes provides a large degree of control over this property, while the centrifugation step ultimately determines the average bundle size. The applied centrifugation force was found to affect the metallic impurity content in a more influential manner than either mean length or bundle size. The effect of sonication duration on the mean length of the nanotube population was examined in detail, while the relationship between the Raman D:G ratio

and the average nanotube length was determined for two different laser excitation energies. Increasing the sonication intensity was observed to induce surfactant foaming if the energy input was above a critical density. The input sonication energy density was determined to be a critical factor in controlling the dispersion properties for both tip and bath type ultrasonic instruments.

The decay mechanisms for aryl diazonium salts in aqueous solution were discussed and related to the possible mechanisms of nanotube functionalisation. Dediazoniation kinetics for the nitro- and bromo-benzenediazonium tetrafluoroborate salts in aqueous solutions containing a variety of dispersants were investigated and found to be uncorrelated with the reaction rates between the diazonium species and carbon nanotubes. The selectivity of the diazonium reaction towards metallic nanotubes was evaluated in a variety of dispersants and polyethylene-oxide containing variants were identified as superior performers, with Pluronic F-127 providing the greatest selectivity. Transfer of electron density between the dispersant and nanotube was observed to greatly affect the reaction selectivity. It was found that partial withdrawal of electron density by sodium dodecyl sulfate leads to increased functionalisation of semiconducting species relative to metallic nanotubes and produces similar effects to aggregation in the optical spectra of dispersions with this surfactant. Conversely, Pluronic F-127 strengthens the electron density of the nanotubes which enhances optical spectra and leads to improved selectivity in the diazonium reaction.

Conditions for which selectivity was improved were identified for the electric arc nanotube and Pluronic F-127 dispersant system. Reactions were performed in a number of dispersant-nanotube systems to the near exclusion of semiconducting species, indicating the potential for improved separation schemes with certain dispersant-nanotube type combinations.

DECLARATION

I certify that this thesis does not incorporate without acknowledgment any material previously submitted for a degree or diploma in any university; and that to the best of my knowledge and belief it does not contain any material previously published or written by another person except where due reference is made in the text.

Adam J. Blanch

November 2011

ACKNOWLEDGEMENTS

Firstly, I should acknowledge the Federal Government for providing me with an Australian Postgraduate Award which allowed me to undertake this research. I must thank my advisors Jamie Quinton and Claire Lenehan for their support and guidance during my candidature. I am also very grateful to Milena Ginic-Markovic for allowing me to use the Sonics VCX probe ultrasonicator without limitation and to Melissa Brown in the School of Biology for allowing me access to their ultracentrifuge facilities. These instruments were of tremendous value to this project and without your generosity none of this research would have been possible.

I am indebted to many people who lent me their knowledge regarding various aspects of this work, including Chris Gibson, Joe Shapter, Amanda Ellis, Mike Perkins, Anders Barlow, Leonora Velleman, Lauren Clements, Mark Bissett and Cameron Shearer, among many others who provided their help whenever I asked of it; for this I thank you. I also extend my gratitude to Kristina Constantopoulos for synthesising the carboxy-diazonium salt and providing me with helpful information along the way. In addition, I must acknowledge the work of the staff in both the Mechanical Workshop and Physical Sciences Store who provide their assistance whenever it is needed, which is always greatly appreciated.

To my colleagues I have not already mentioned (and also to those that I have), in particular those from the Smart Surface Structures group, thank you for your friendship over the years. The research experience is certainly more enjoyable when it is a shared one. I am also lucky to have the friends outside of university that I do, who have often tried to understand what, exactly, I have been doing with my time. Here is your answer. You may not ever read this, but thank you for being there - and do not underestimate the value of your friendship.

Finally, a huge thanks goes to my family, and to Jen, for your love, encouragement and support without which I definitely would not have made it this far.

PUBLICATIONS ARISING FROM THIS WORK

Peer Reviewed Journal Articles

Blanch, A. J.; Lenehan, C. E.; Quinton, J. S., Dispersant Effects in the Selective Reaction of Aryl Diazonium Salts with Single-Walled Carbon Nanotubes in Aqueous Solution. *J. Phys. Chem. C*, **2012**, *116* (2), 1709-1723

Blanch, A. J.; Lenehan, C. E.; Quinton, J. S., Parametric Analysis of Sonication and Centrifugation Variables for Dispersion of Single Walled Carbon Nanotubes in Aqueous Solutions of Sodium Dodecylbenzene Sulfonate. *Carbon* **2011**, *49* (15), 5213-5228

Blanch, A. J.; Lenehan, C. E.; Quinton, J. S., Optimizing Surfactant Concentrations for Dispersion of Single-Walled Carbon Nanotubes in Aqueous Solution. *J. Phys. Chem. B* **2010**, *114* (30), 9805-9811.

Peer Reviewed Conference Proceedings

Blanch, A.J., Lenehan, C.E., & Quinton, J.S., Optimising Surfactant Aided Dispersions of Carbon Nanotubes in Aqueous Solution, *Nanoscience and Nanotechnology (ICONN)*, 2010 International Conference on, pp.132-135, 22-26 Feb. **2010**

Chapter 1

INTRODUCTION

Carbon nanotubes (CNTs) possess a variety of desirable physical, chemical and optoelectronic properties that stem from their quasi-one dimensional structure. CNT based materials have been implemented in a multitude of applications spanning a diverse range of fields,¹ including use in electronics, catalysis, drug delivery and as mechanical components, however they have not yet achieved their full potential. A lack of uniformity in the properties of as-synthesised CNTs is one of the primary reasons why relatively few commercial applications for these carbon nanostructures currently exist.² Limitations imposed by a lack of adequate processing methods for raw nanotube materials also continue to hamper progress towards functional devices containing CNTs. Consequently, research towards the production and manipulation of bulk samples of individually dispersed CNTs that possess uniform properties is a goal towards which continuous progress has been made but is yet to be realised. The dispersion of nanotubes in liquid as individuals allows for manipulation of CNT materials at a level not possible with as-produced powders, while separation of the different types of CNT from one-another would allow for vast improvement in the performance of electronic devices and open further pathways for the utilisation of carbon nanotube-based materials.

1.1 The Structure and Properties of Carbon Nanotubes

Credit for the discovery of carbon nanotubes (CNTs) has been the topic of some debate,³ with many authors attributing it to Iijima in 1991⁴ although similar carbon fibres had been reported previously.⁵⁻⁸ In any case, Iijima's work brought CNTs to the forefront of scientific interest, and they have since been the focus of intensive research owing to their unique properties. Carbon nanotubes are, as their name suggests, elongated cylinders of graphitic carbon with nanoscopic dimensions. CNTs possess a hexagonal lattice arranged concentrically about a hollow central axis, while the ends are capped by hemispherical fullerene structures. In general terms there are two distinct types of carbon nanotube, both of which may be described using an analogy of a two dimensional, single layer sheet of graphite (graphene) rolled into cylindrical form. The aforementioned discovery of CNTs refers to initial observations of first of these types, being multi-walled carbon nanotubes (MWCNTs), which consist of two or more concentric cylindrical shells of graphene coaxially arranged around a central void. Ideally, there is a constant interlayer separation between the sheets of $\sim 3.4\text{\AA}$ according to the layer spacing of graphite, and MWCNTs can have diameters of several tens of nanometres depending on the number of shells they possess. The second type of nanotube involves only a single graphene cylinder, hence these are known as single-walled carbon nanotubes (SWCNTs). Since charge transfer can occur between layers in MWCNTs their electronic and optical properties are significantly different to those of the single-walled species which display novel phenomena defined by their one-dimensional nature, thus SWCNTs receive much more attention. In contrast to MWCNTs, the discovery of SWCNTs is unambiguously attributed to two papers published adjacently in *Nature* in 1993, one by Iijima and Ichihashi,⁹ the other by Bethune *et. al.*¹⁰ SWCNTs may have diameters as small as 0.3nm (albeit as the core of a MWCNT),¹¹ though typical free standing SWCNTs have a diameter in the range 0.7-2nm, and 0.7nm is expected to be the smallest diameter for such nanotubes to be chemically stable.¹²

As-produced MWCNTs and SWCNTs usually have lengths of several micrometers, although lengths upwards of 4cm have been reported.¹³ This large aspect ratio between the nanotube length and diameter is the reason CNTs are considered to have essentially one-dimensional structures and has a large influence on their intrinsic properties. SWCNTs may also behave as either metals or semiconductors depending on their

diameter and the helicity of the arrangement of hexagonal rings along the nanotube walls, thus the electronic properties of a particular nanotube may be derived from its atomic structure.

1.1.1 Geometric Structure

The properties of SWCNTs are dependent on their geometric structure, where the chirality and associated diameter of the specific nanotube will determine its electronic properties and chemical behaviour. In the consideration where a CNT may be represented by a single sheet of graphene seamlessly rolled into a hollow cylinder, the properties of the resultant nanotube are dependent on the ‘roll-up’ or chiral vector \mathbf{C}_h ,¹⁴ although it is important to note the use of ‘chiral’ here does not strictly refer to nanotubes that possess enantiomers.¹⁵ Following the notation of Dresselhaus *et al.*¹⁶ this chiral vector is written as

$$\mathbf{C}_h = n\mathbf{a}_1 + m\mathbf{a}_2 = (n, m), \quad (1.1)$$

where \mathbf{a}_1 and \mathbf{a}_2 are unit vectors of the hexagonal carbon lattice while n and m are integers. The graphene sheet is rolled such that the two crystallographically equivalent endpoints of the chiral vector are superimposed upon one another. In this formalism, many of the possible chiral vectors will produce equivalent nanotubes since the honeycomb lattice is highly symmetrical. However, there is a so called ‘irreducible wedge’ within which each point on the lattice defines a unique chiral vector, given by the limit $0 \leq m \leq n$. A small section of this wedge is shown in Figure 1.1, where points on the lattice are given (n, m) assignments according to the chiral vector, and each of these integer pairs represents a possible nanotube structure. These structures are generally classified by three subsets, $(n, 0)$, (n, n) and (n, m) , $m \neq n, 0$. Nanotubes having chiral vectors $(n, 0)$ are known as ‘zigzag’ nanotubes, and the zigzag axis represents one boundary of the irreducible wedge. The chiral angle, θ , is measured between \mathbf{C}_h and this zigzag axis ($\theta = 0^\circ$). Nanotubes for which $n = m$, denoted (n, n) , are known as ‘armchair’ nanotubes, where the armchair axis ($\theta = 30^\circ$) is the other boundary of the wedge, thus $0 \leq \theta \leq 30$. Zigzag nanotubes theoretically have two types of behaviour; when $n/3$ is an integer a zero-gap semiconductor (quasi-metallic nanotube) is expected, otherwise a semiconducting nanotube with a finite band gap results, whereas armchair nanotubes are always expected to be metallic. The remaining

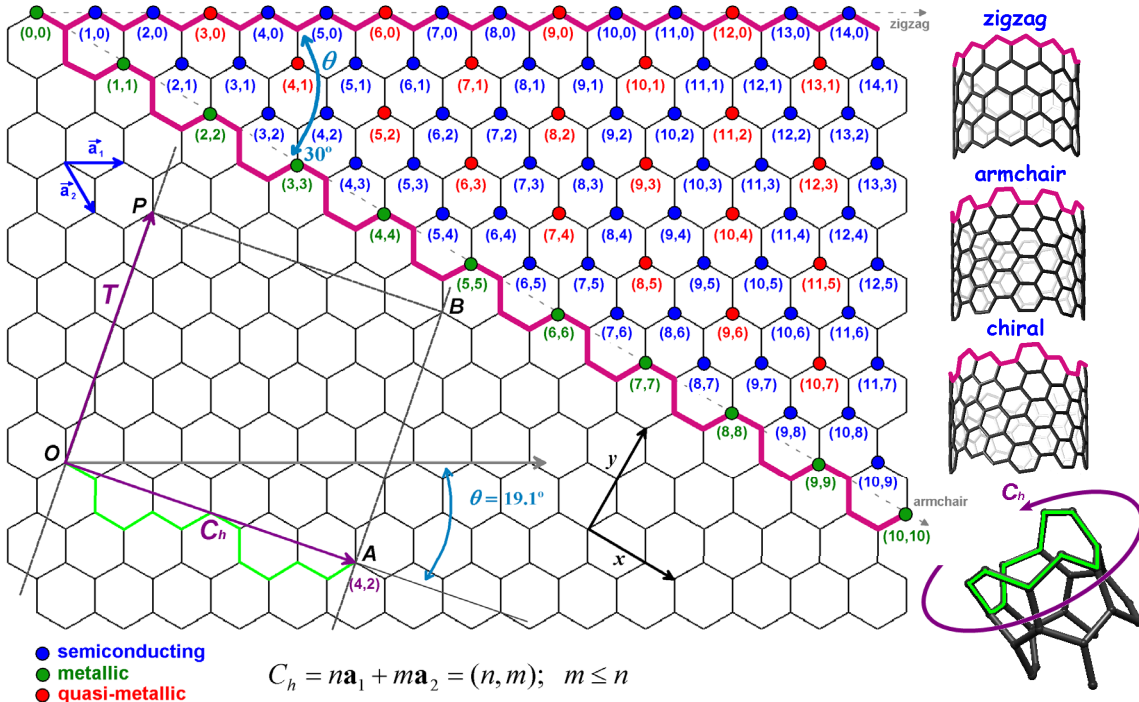


Figure 1.1: The first section of the ‘irreducible wedge’ of the graphite lattice, where \mathbf{a}_1 and \mathbf{a}_2 are the basis vectors defining the unit cell and C_h is the chiral vector defining a particular nanotube. The wedge is bounded by the zigzag and armchair axes given by $0 \leq \theta \leq 30$. Vectors $(n, 0)$ denote ‘zigzag’ nanotubes (top right), (n, n) denote ‘armchair’ nanotubes (middle right) and (n, m) where $m \neq n, 0$, define ‘chiral’ nanotube vectors (lower right). An example of a chiral vector C_h is shown for a (4,2) chiral nanotube (bottom right), where the vectors OA and PB define C_h and the translational vector (parallel to the nanotube axis) T , respectively. The rectangle $OABP$ defines the unit cell for this particular nanotube.

integer pairs (n, m) define ‘chiral’ nanotubes, with those having the property $|n - m| = 3q$ where q is a (non-zero) integer being quasi-metallic, having a very small band gap, while others are semiconducting. For chiral nanotubes, both right-handed ($\theta > 0^\circ$) and left-handed ($\theta < 0^\circ$) stereoisomers are possible due to the inequivalent helical operations of rolling the sheet in a direction either above or below the graphene plane,¹⁷ although for achiral zigzag and armchair nanotubes this is a reflection plane and the mirror image nanotubes are identical.¹⁸ However, the handedness of a CNT is not expected to significantly affect its properties.¹⁹

The length of a carbon-carbon bond (a_{C-C}) in sp^2 bonded graphite is 1.42\AA (0.142nm), and therefore the hexagonal unit cell can be used to find the lengths of the unit vectors,¹⁶ such that

$$a = |\mathbf{a}_1| = |\mathbf{a}_2| = (a_{C-C})\sqrt{3} = 0.246\text{nm}. \quad (1.2)$$

As the carbon-carbon bond length in nanotubes is slightly larger than that of graphite or

graphene due to curvature of the honeycomb lattice, the value of (a_{c-c}) is commonly taken as 0.144nm, and therefore $a = 0.249\text{nm}$.²⁰ The length L of the chiral vector \mathbf{C}_h (the circumference of the nanotube) is given by the relation

$$L = |\mathbf{C}_h| = a\sqrt{n^2 + nm + m^2}, \quad (1.3)$$

and it then follows that the diameter of the nanotube, d_t , is given by

$$d_t = \frac{L}{\pi} = \frac{a\sqrt{n^2 + nm + m^2}}{\pi}. \quad (1.4)$$

Finally, the chiral angle θ between the chiral vector and the zigzag axis is defined by the expressions¹⁶

$$\theta = \sin^{-1} \frac{m\sqrt{3}}{2\sqrt{n^2 + nm + m^2}}, \theta = \cos^{-1} \frac{2n+m}{2\sqrt{n^2 + nm + m^2}} \text{ and } \theta = \tan^{-1} \frac{m\sqrt{3}}{2n+m}. \quad (1.5)$$

It is evident from these equations that the pair of integers (n, m) that define the structure of a nanotube uniquely determine d_t and θ . However, it should also be noted

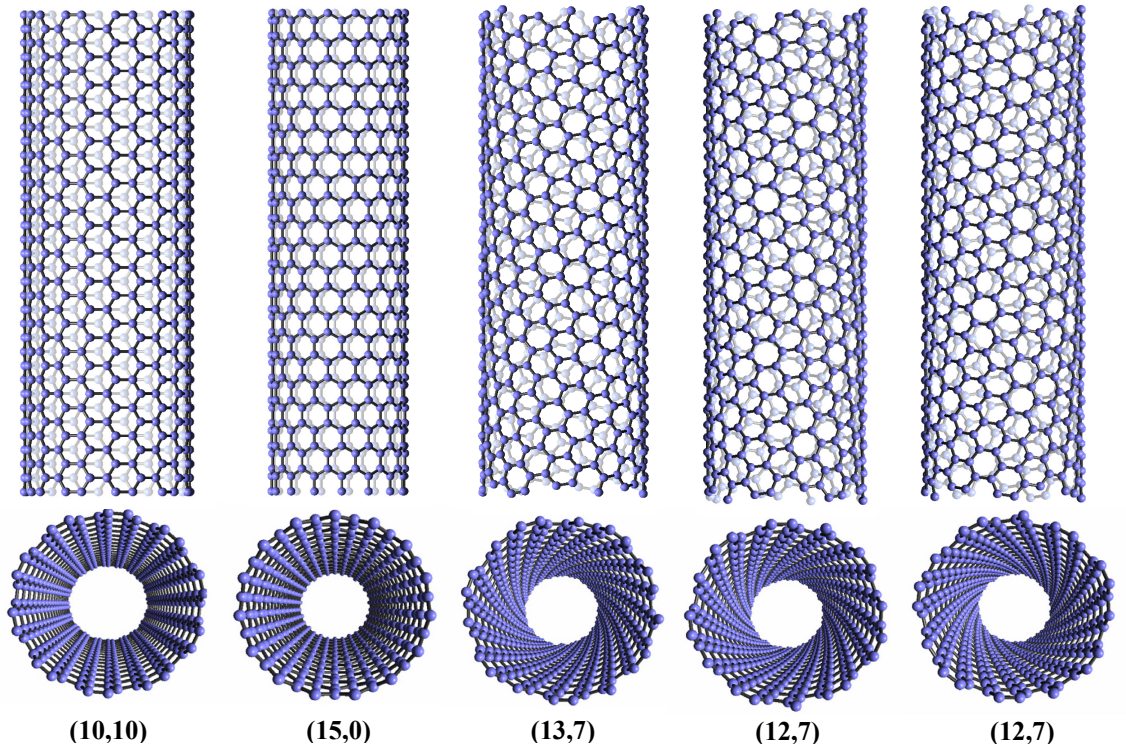


Figure 1.2: Different types of nanotubes displayed with viewpoints oriented both orthogonal to (top) and directly along (bottom) the tube axis. Theoretically, the (10,10) armchair tube is expected to be fully metallic, while the zigzag (15,0) and ‘chiral’ (13,7) nanotubes are quasi-metallic. The (12,7) nanotube is a finite band-gap semiconductor, shown here with its left and right-handed chiral enantiomers. While the (12,7) and (13,7) appear very similar to the eye, subtle structural differences dictate that the two tubes will behave very differently. Images were produced with the assistance of ‘Nanotube Modeler’ software (JCrystalSoft, v1.3.6).

that it is possible to have nanotubes of the same (or very similar) diameter that have a different chiral structure and hence exhibit different electronic properties, such as the (12,7) and (13,7) nanotube species shown in Figure 1.2.

The unit cell of the nanotube with respect to the graphene lattice is bounded by both C_h and the translational vector (or SWCNT unit cell vector) \mathbf{T} which points in the direction of the nanotube axis. \mathbf{T} can be expressed in terms of the graphene unit cell vectors as

$$\mathbf{T} = (t_1 \mathbf{a}_1, t_2 \mathbf{a}_2) = (t_1, t_2), \quad (1.6)$$

where t_1 and t_2 are integers.²⁰ Using the orthogonal condition $C_h \cdot \mathbf{T} = 0$ it follows that

$$t_1 = \frac{2m+n}{d_R} \quad \text{and} \quad t_2 = -\frac{2n+m}{d_R}, \quad (1.7)$$

where d_R is the greatest common divisor of $(2m+n)$ and $(2n+m)$ for a (n,m) nanotube, which allows the length of the nanotube unit cell vector to be written as

$$|\mathbf{T}| = a\sqrt{t_1^2 + t_1 t_2 + t_2^2} = \frac{L\sqrt{3}}{d_R}. \quad (1.8)$$

The area of the nanotube unit cell ($OABP$ in Figure 1.1 for a (4,2) CNT) can then be defined in terms of the number of hexagons (or graphene unit cells) it encloses, denoted N , which is given by

$$N = \frac{|C_h \times \mathbf{T}|}{|\mathbf{a}_1 \times \mathbf{a}_2|} = \frac{2L}{a^2 d_R} = \frac{2(n^2 + nm + m^2)}{d_R}. \quad (1.9)$$

Since each hexagon in the graphene lattice contains two carbon atoms as discussed in the following section, each nanotube unit cell contains $2N$ carbon atoms. $N = 2n$ for both zigzag and armchair nanotubes.

1.1.2 Electronic Structure

The basic electronic structure of SWCNTs can be derived from that of graphene if hybridisation effects due to finite curvature of the nanotubes are ignored.²¹ Figure 1.3 shows the two-dimensional lattice for graphene in both real and reciprocal space, where the corresponding unit vectors are

$$\mathbf{a}_1 = \left(\frac{a\sqrt{3}}{2}, \frac{a}{2}\right), \quad \mathbf{a}_2 = \left(\frac{a\sqrt{3}}{2}, -\frac{a}{2}\right) \quad \text{and} \quad \mathbf{b}_1 = \left(\frac{2\pi}{a\sqrt{3}}, \frac{2\pi}{a}\right), \quad \mathbf{b}_2 = \left(\frac{2\pi}{a\sqrt{3}}, -\frac{2\pi}{a}\right) \quad (1.10)$$

respectively. The unit cell in real space contains two carbon atoms A and B which are located at inequivalent sites on the hexagonal lattice for which all other lattice points

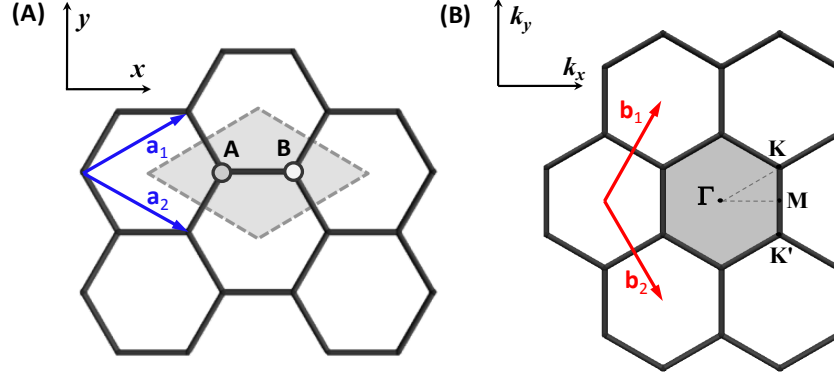


Figure 1.3: The hexagonal graphene lattice in real space (A) and reciprocal space (B). The shaded areas in (A) and (B) represent the unit cell and first Brillouin Zone respectively.

can be obtained by lattice transformations along unit vectors \mathbf{a}_1 and \mathbf{a}_2 . Thus, interactions between atomic orbitals for these two atoms may form the basis for construction of the electronic band structure of graphene. Here, a tight binding model that considers only the nearest neighbour interactions between π orbitals around A and B is adopted. The dispersion relation for graphene is then derived from diagonalisation of the 2x2 Bloch Hamiltonian for the diatomic unit cell containing two π electrons, which yields the solution

$$E_{g2D}^{\pm}(\mathbf{k}) = \frac{\epsilon_{2p} \pm \gamma_0 w(\mathbf{k})}{1 \mp s w(\mathbf{k})}, \quad w(\mathbf{k}) = \sqrt{1 + 4 \cos\left(\frac{k_x a \sqrt{3}}{2}\right) \cos\left(\frac{k_y a}{2}\right) + 4 \cos^2\left(\frac{k_y a}{2}\right)} \quad (1.11)$$

where ϵ_{2p} is the site energy of the 2p atomic orbital, γ_0 is the nearest neighbour carbon-carbon interaction energy between π orbitals ($\gamma_0 > 0$), s is the tight binding overlap integral associated with the asymmetry between the valence and conduction bands and $\mathbf{k} = (k_x, k_y)$ represents the two-dimensional wavevector components along the x and y directions in the Brillouin zone of graphene.^{20,22} This expression provides the energy dispersion for the bonding π orbitals (+) and antibonding π^* orbitals (-) of graphene as shown in Figure 1.4A.²³

The first Brillouin zone is hexagonal and possesses six vertices, known as K-points. Again, two of these are inequivalent, labelled K and K', while remaining points can be mapped by translation through \mathbf{b}_1 and \mathbf{b}_2 . The planar graphitic structure of carbon is a quasi-metal, or zero-gap semiconductor, whose valence (π) and conduction (π^*) bands contact at these six K points at the corners of the Brillouin zone, each of which lie at the Fermi energy (Fermi points).²⁴ Along directions in k -space that pass through these six Fermi points, i.e. in the Γ -K direction (where Γ is the position of greatest energy

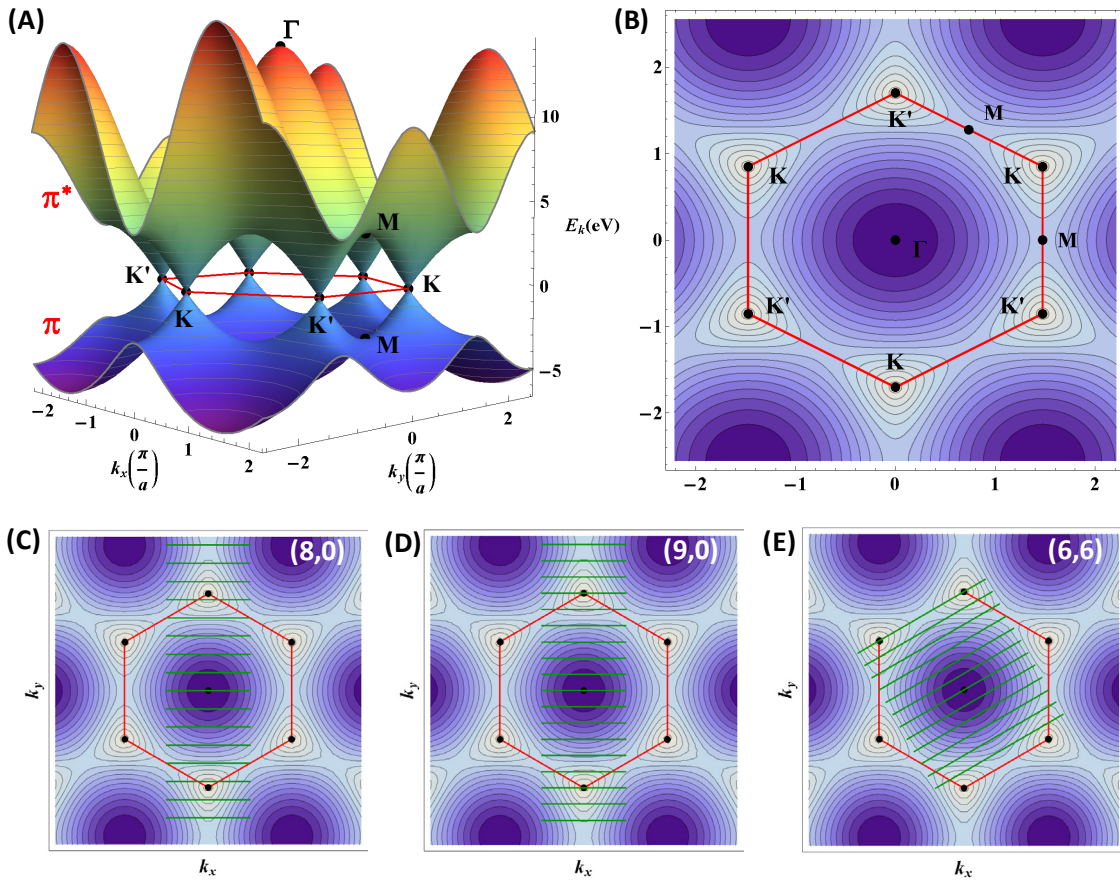


Figure 1.4: (A) Three-dimensional representation of the energy dispersion of graphene calculated using $\epsilon_{2p} = 0\text{eV}$, $\gamma_0 = 2.9\text{eV}$ and $s = 0.13$ over 1.5 Brillouin zones. A 2D projection of the π orbitals is shown in (B). Red hexagons define the first Brillouin zone of graphene while green lines indicate allowed wavevectors \mathbf{k} for the nanotubes. These are shown for the (8,0) and (9,0) zigzag nanotubes in (C) and (D) and for the (6,6) armchair nanotube in (E). The (9,0) and (6,6) nanotubes are expected to possess metallic electronic characteristics as their allowed 1D wavevectors pass through K points, while the (8,0) nanotube is a semiconductor. Images were produced using ‘Mathematica’ software (Wolfram Research, Inc., v8.0.1.0) with code adapted from the Wolfram Demonstration Project.²³

difference between π and π^* bands) and in five other directions differing by 60° , the electrons can move freely between the valence and conduction bands and hence the graphene behaves as a metal. In real space, these six unique directions correspond to free electron motion along the six possible orientations of the ‘zigzag’ direction of the graphene lattice.²⁵ However, in all other directions in k -space, such as the Γ -M direction (where M is the position of a ‘saddle point’, i.e. the energy difference between bands is essentially flat), the electrons encounter a semiconductor like band gap.

If this electronic structure is further applied to the case of a SWCNT, periodic boundary conditions are imposed upon the electron wave function by the confinement of the electrons around the tube circumference. The wavevector, \mathbf{k} , is therefore quantised in

the direction of \mathbf{C}_h according to the condition $\mathbf{k} \cdot \mathbf{C}_h = 2\pi q$, where q is an integer.^{21,24-27}

In geometric terms, the first nanotube Brillouin zone can be defined by the basis vectors

$$\mathbf{K}_1 = \frac{1}{N}(-t_2 \mathbf{b}_1 + t_1 \mathbf{b}_2) = \frac{[(2n+m)\mathbf{b}_1 + (2m+n)\mathbf{b}_2]}{Nd_R} \text{ and } \mathbf{K}_2 = \frac{1}{N}(m\mathbf{b}_1 - n\mathbf{b}_2). \quad (1.12)$$

Due to the one dimensional nature of the nanotube, only the vector \mathbf{K}_2 varies as a reciprocal lattice vector along the nanotube axis direction while \mathbf{K}_1 defines the spacing of quantisation in the circumferential direction. The periodic boundary condition provides N discrete allowed values of \mathbf{k} in the direction of \mathbf{K}_1 separated by $|\mathbf{K}_1|$, essentially slicing the graphene band structure along lines having a defined length $|\mathbf{K}_2| = 2\pi/|\mathbf{T}|$. Given a nanotube of finite length L_t , the allowed values of \mathbf{k} would then also be quantised along the axis of the nanotube in intervals of $2\pi/L_t$.²⁰

Substitution of the allowed values of \mathbf{k} into the energy dispersion relation for graphene provides the energy dispersion for a nanotube, where each band of graphene is sectioned into a number of 1D sub-bands labelled by q .²⁴ Only states parallel to the corresponding tube axis with a spacing of $\Delta\mathbf{k} = |\mathbf{K}_1| = 2\pi/L = 2/d_t$ are allowed, as shown in Figures 1.4C-E.²¹ If any of these allowed wavevectors pass through a K point then the tube will be metallic, otherwise it is semiconducting, which is the basis for the expectation that nanotubes will be metallic if $(n-m)/3$ is an integer.

More explicitly, for a nanotube of infinite length the band structure can be expressed in terms of the basis vectors \mathbf{K}_1 and \mathbf{K}_2 as¹⁹

$$E_\mu(\mathbf{k}) = E_{g2D}(\mathbf{k}) \left(k \frac{\mathbf{K}_2}{|\mathbf{K}_2|} + \mu \mathbf{K}_1 \right), \quad \mu = 1, 2, \dots, N \text{ and } -\frac{\pi}{|\mathbf{T}|} < k < \frac{\pi}{|\mathbf{T}|}. \quad (1.13)$$

The irreducible number of bands is given by the number of graphene unit cells inside the SWCNT unit cell N , and each is indexed by μ . Note that in Figure 1.4 an equivalent offset index $\mu = (-N/2 + 1), \dots, 0, \dots, N/2$ was used to plot each band. The energy dispersion is then comprised of $2N$ sub-bands for each nanotube, being N valence and N conduction bands. As examples the allowed wavevectors of the (8,0), (9,0) and (6,6) nanotubes are shown in Figures 1.4C-E, while their corresponding one-dimensional band structures (cross-sections of that of graphene) are plotted in Figure 1.5. The (9,0) nanotube has $N = 2n = 18$ allowed wavevectors corresponding to 18π and $18 \pi^*$ bands, however some of these are degenerate and therefore only 10 such pairs are different and distinguishable in Figure 1.5.

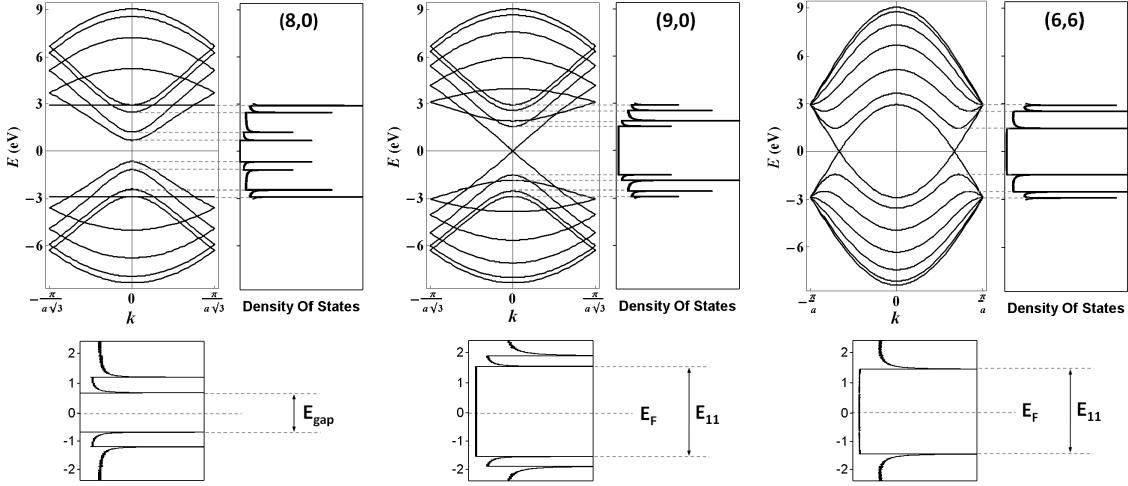


Figure 1.5: Approximate one-dimensional band structures for the (8,0), (9,0) and (6,6) nanotubes and the corresponding density of states (DOS) for each case. Plots of the DOS are reproduced from the data of Shigeo Maruyama.³² Expanded DOS are shown below each dispersion, where an energy gap exists for the (8,0) nanotube making it a semiconductor. The conduction and valence bands touch for the (9,0) and overlap for the (6,6) nanotubes, therefore they are classified as metallic. Energy dispersions were produced using ‘Mathematica’ software (Wolfram Research, Inc., v8.0.1.0) with code adapted from the Wolfram Demonstration Project.²³

Two special cases for the nanotube energy dispersion exist. For armchair nanotubes, C_h is oriented along the x -axis while T is in the y -axis direction. The quantisation of K_1 is then applied along k_x , such that

$$k_x = |\mathbf{K}_1|q = \frac{2\pi q}{L} = \frac{2\pi q}{na\sqrt{3}}, \quad q = 1, \dots, 2n \quad \text{with } |\mathbf{T}| = a \quad (1.14)$$

If this is substituted into the energy dispersion for graphene the phase factor becomes

$$w_q^{\text{arm}}(k_y) = \sqrt{1 + 4\cos\left(\frac{\pi q}{n}\right)\cos\left(\frac{k_y a}{2}\right) + 4\cos^2\left(\frac{k_y a}{2}\right)}, \quad -\frac{\pi}{a} < k_y < \frac{\pi}{a}. \quad (1.15)$$

For the zigzag nanotube case, where C_h and T are directed along the y - and x -axes respectively, the quantisation is then applied along k_y with the result

$$k_y = |\mathbf{K}_1|q = \frac{2\pi q}{L} = \frac{2\pi q}{na}, \quad q = 1, \dots, 2n \quad \text{with } |\mathbf{T}| = a\sqrt{3} \quad (1.16)$$

with the corresponding phase factor becoming

$$w_q^{\text{zig}}(k_x) = \sqrt{1 + 4\cos\left(\frac{k_x a\sqrt{3}}{2}\right)\cos\left(\frac{\pi q}{n}\right) + 4\cos^2\left(\frac{\pi q}{n}\right)}, \quad -\frac{\pi}{a\sqrt{3}} < k_x < \frac{\pi}{a\sqrt{3}}. \quad (1.17)$$

These expressions can be used to calculate one-dimensional energy dispersion diagrams for certain nanotubes such as those shown in Figure 1.5.

The prior calculations are based on graphene which possesses a planar lattice structure, neglecting the curvature of the nanotube. Curvature in nanotubes of small diameter leads to strong hybridisation of the σ/π bonding and σ^*/π^* antibonding orbitals which shifts the Fermi point away from the K point of the Brillouin zone.²⁸ For the case of zigzag nanotubes where the conduction and valence bands touch at the Fermi level (i.e. ‘metallic’ nanotubes), the Fermi point moves along the circumferential direction \mathbf{K}_1 such that the allowed wavevector \mathbf{k} no longer passes through the Fermi point.²⁹ This introduces a small bandgap on the order of tens of meV into the electronic band structure, although for most experimentally observed nanotubes (where $d_t > 0.6\text{nm}$) the thermal energy at room temperature is sufficient to excite electrons from the valence to the conduction band.³⁰ Hence, these nanotubes can effectively be considered metallic at room temperature. For armchair nanotubes, the Fermi point shifts along the nanotube axis (i.e. in the direction of \mathbf{K}_2) and therefore some allowed wavevectors will always intersect it.²¹ It is for this reason that zigzag nanotubes for which the metallic condition is met are considered to be quasi-metallic, while armchair nanotubes are considered to be truly metallic.

The density of states (DOS) can be obtained from the one-dimensional band structures of each nanotube using an integral of the form²²

$$D(E) = \frac{2}{N} \sum_{\mu=1}^N \int \left(\left| \frac{dE_{\mu}(k)}{dk} \right| \right)^{-1} \delta(E_{\mu}(k) - E) dE. \quad (1.18)$$

This expression relates to summing the number of electrons that exist at every energy level within each of the allowed bands. This is accomplished by dividing the k axis and the energy axis of the nanotube energy dispersion into a large number of small segments. By counting the number of k points in each energy interval, the number of states allowed at each energy value is calculated.²⁴ The density of states becomes large when the energy dispersion relation becomes flat as a function of k , resulting in spikes in the DOS which correspond to extrema in the energy dispersion relations. These are known as van Hove singularities (VHS) and characteristically manifest as peaks in one-dimensional systems.^{24,31} Figure 1.5 shows the corresponding DOS for band structures of the (8,0), (9,0) and (6,6) nanotube species which each possess these VHS at different energies.³² For each \mathbf{K}_1 vector there is an energy minimum between the valence and conduction energy sub-bands, giving rise to the energy differences $E_{ii}^{S,M}$ between symmetric VHS in the i th sub-bands of both semiconducting and metallic nanotubes.²²

The first VHS in semiconducting nanotubes arises from the band closest to the K point while for metallic nanotubes the closest band always intersects this point. This leads to the non-zero DOS at the Fermi level for metallic nanotubes, but also results in the condition that the energy difference between the first VHS for metallic nanotubes is approximately three times larger than for semiconducting species of similar diameter, or $E_{11}^M \cong 3E_{11}^S$.^{24,33} The first energy gaps may be approximated as $E_{11}^S = 2\gamma_0 a_{c-c}/d_t$ and $E_{11}^M = 6\gamma_0 a_{c-c}/d_t$ for semiconducting and metallic nanotubes respectively.^{22,24,34} Higher order VHS energy gaps can be estimated from the spacing of the singularities to occur at $E_{22}^S = 2E_{11}^S$, $E_{33}^S = 4E_{11}^S$, $E_{44}^S = 5E_{11}^S$... for semiconducting nanotubes and $E_{22}^M = 2E_{11}^M$ for metallic CNTs,²² although since these estimates ignore curvature effects and assume a linear dispersion of the π and π^* bands of graphene they are highly approximate.³⁴ Refinements to the tight binding model to include curvature of the graphitic structure have provided more accurate estimates,³⁵ however the general behaviour is well described by the simple model presented here.

1.1.3 Optical Properties

The optical properties of SWCNTs may be understood in terms of the single particle or band picture model in which electronic excitations arise from transitions between van Hove singularities in the DOS as discussed in Section 1.1.2. The dominant transitions for excitation connect bands with the same index whereas the transverse transitions are suppressed.¹⁹ In this consideration the electronic and optical bandgaps are equivalent, where each transition between the valence band v_i and conduction band c_i may be labelled as in the previous section by $E_{ii}^{S,M}$, where S and M denote excitations for semiconducting and metallic nanotubes respectively. According to this model the interband transitions produce free electron-hole pairs when excited by photons of an energy corresponding to E_{ii} . Since this transition energy is only dependent on the diameter of the nanotube, the relationship between d_t and E_{ii} can therefore be used to identify nanotube species using their optical transitions according to the so-called Kataura plot,³⁶ presented in Figure 1.6. Visibly separated bands corresponding to the different transition orders ii are evident, with S_{11} at the lowest energy followed by S_{22} , M_{11} and S_{33} etc. in order of increasing energy. Smaller diameter nanotubes possess larger bandgaps as per the inverse relationship between E_{ii} and d_t .

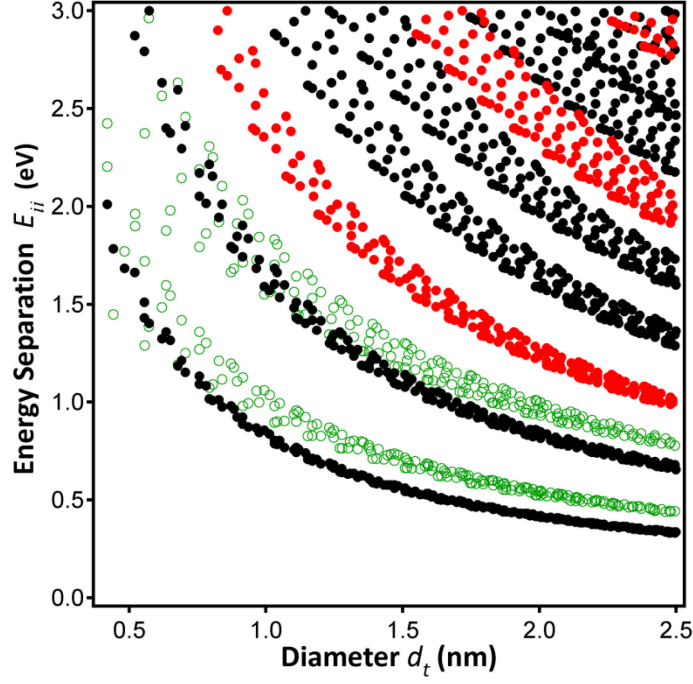


Figure 1.6: Kataura plot for the relationship between E_{ii} and d_t calculated using a simple tight binding model with $\gamma_0 = 2.9\text{eV}$ and $a_{c-c} = 0.144\text{nm}$ (reproduced from the data of S. Maruyama).³² Black points represent semiconducting nanotube transitions (E_{ii}^S) while red belong to metallic CNTs (E_{ii}^M). Green circles are the empirically derived fits for the first two semiconducting transitions E_{11}^S and E_{22}^S from the photoluminescence results of Weisman and Bachilo.³⁹

Photoluminescence may be observed for semiconducting nanotubes when excitation of the E_{22}^S transition (or a higher order) is coupled with emission from E_{11}^S .^{37,38} As each nanotube structure (n, m) will have a distinct excitation-emission combination, this technique provides an excellent method of probing the nanotube species present in a sample. However, metallic nanotubes do not fluoresce and must be detected through absorption. The results of Weisman and Bachilo³⁹ provided an empirical fit to experimental photoluminescence data to produce a Kataura plot for the first two transitions of semiconducting nanotubes as shown in Figure 1.6. The observed transitions show clear deviation from the energies expected from the tight binding band-to-band model, where E_{11}^S is often underestimated by up to 25% relative to the empirical values. Within the band model the ratio of the second and first interband transitions E_{22}/E_{11} is expected to be less than two for small diameter nanotubes due to curvature effects, but should approach two in the large diameter limit.²² The experimentally obtained ratio approaches a value closer to 1.75,⁴⁰ which is referred to as the ‘ratio problem’. These dissimilarities imply that Coulombic electron-electron and electron-hole interactions that are ignored by the tight-binding model strongly influence

the underlying physics of the optical transitions.³¹

There is now strong experimental evidence⁴¹ that the one-dimensional nature of a nanotube gives rise to strong Coulomb interactions between electrons and holes such that they become electrostatically bound in electron-hole pairs, or excitons, which were earlier predicted to occur in CNTs.⁴² The exciton binding energy in CNT systems was estimated to be large relative to the energy gap of $\sim 1\text{eV}$ ⁴³⁻⁴⁵ and has been found to be on the order of $0.3\text{-}0.5\text{eV}$.^{41,46,47} Optical absorption to excitonic energy states is usually only achieved at low temperatures, however the magnitude of the exciton binding energy in CNTs allows excitonic effects to be observed at room temperature.⁴⁸ Additionally, although screening of the attractive Coulomb interaction between the electron and hole by free conduction electrons is expected to prevent the formation of excitons in metals, the effectiveness of screening is significantly reduced in one-dimensional systems and excitons are readily observed in metallic CNTs.⁴⁹

The electron-electron Coulomb repulsion increases the magnitude of E_{ii} from its band model value while the binding energy of the exciton reduces it.^{42,50} Both the electrical bandgap E_{el} and the optical gap E_{opt} thus depend on the single-particle bandgap E_{ii} such that $E_{el} \approx E_{ii} + E_{ee}$ and $E_{opt} \approx E_{ii} + E_{ee} - E_{eh}$, where E_{ee} and E_{eh} are the electron-electron and electron-hole interaction energies, respectively. Experimental studies indicate that $E_{ee} > E_{eh}$, hence these many body interactions increase the optical bandgap E_{opt} above its simple band picture value E_{ii} , which explains the deviations between experimental observations and the simplest case of the tight binding model described previously.⁵¹ Extended tight binding models have been applied to include Coulombic interactions and are now able to predict experimentally observed behaviour, including the E_{22}/E_{11} ratio and the $2n + m$ family branching that occurs for nanotubes of small diameter.⁵⁰ As a result, the optical absorptions of CNTs are still generally referred to using an E_{ii} indexing scheme derived from the band-to-band model.

Photo-excited excitons in CNTs have been shown to have a correlation length of approximately $2\text{-}2.5\text{nm}$,^{41,52} which is larger than the nanotube diameter, hence the local dielectric environment may have a substantial effect on the optical properties of CNTs. The mobility of the long-lived exciton states has been shown to be around $\sim 90\text{nm}$ and is independent of the CNT structure.⁵³ Recent studies have indicated that the exciton ranges can be much larger than this, with measured and calculated values from 190-

370nm.^{54,55} However, more abundant short-lived exciton states have been shown to have a diffusion length less than 10nm,⁵² implying this is the length scale over which the majority of optical absorption bleaching (loss of intensity) occurs due to defects in the nanotube structure or alteration of the sidewall surface.

1.1.4 Chemical Reactivity

In discussing the reactivity of nanotubes it is useful to consider the chemistry of fullerenes, which are spherical aromatic structures, and the carbon pyramidalization angle (θ_p). The pyramidalization angle may be defined as $\theta_p = \theta_{\sigma\pi} - 90$, where $\theta_{\sigma\pi}$ is the common angle made by the π -orbital axis vector and the three σ bonds, and is related to strain (curvature) in the carbon lattice.⁵⁶ In the two dimensional graphene sheet carbon atoms are arranged in a hexagonal network where the tetravalent atoms have an sp^2 -hybridised (trigonal) geometry. Carbon atoms in the trigonal bonding system prefer a planar structure, as in graphite, corresponding to a pyramidalization angle of 0° , whereas in the tetrahedral arrangement (i.e. an sp^3 -hybridised carbon atom) $\theta_p = 19.47^\circ$ (Figure 1.7).⁵⁷

In the case of fullerenes, the spherical arrangement of carbon atoms imparts a large amount of strain on the hexagonal lattice and as a result the pyramidalization angle is always greater than $\sim 9.7^\circ$.⁵⁸ A consequence of this curvature induced strain is that fullerenes are inherently reactive and undergo addition reactions quite readily. In the fullerene C_{60} (Figure 1.8A), the pyramidalization angle of the carbon atoms is 11.6° , which is better approximated by the tetrahedral arrangement. Strain in the carbon

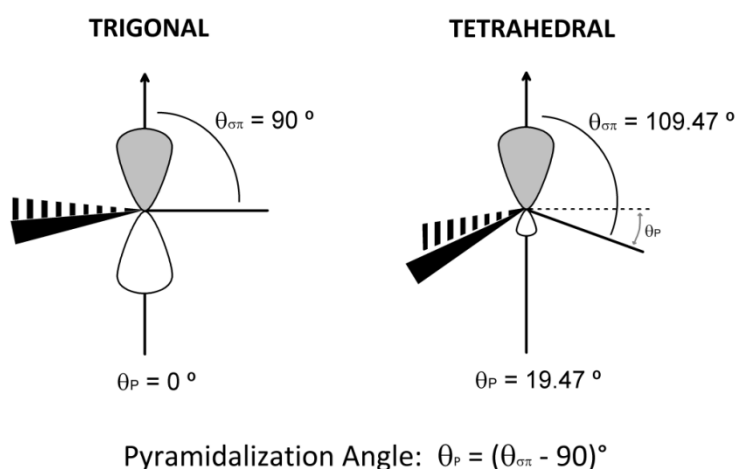


Figure 1.7: Diagrams showing the pyramidalization angle for carbon in the trigonal planar and tetrahedral geometries.

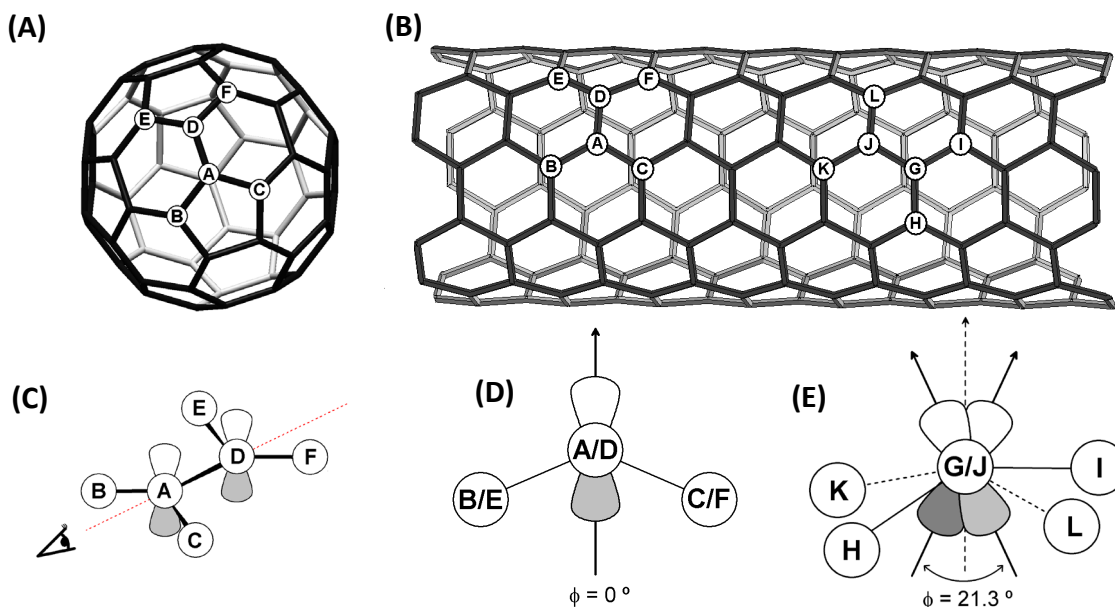


Figure 1.8: Pyramidalization and π -orbital misalignment in the fullerene C₆₀ (A) and a (5,5) armchair nanotube (B). The viewing angle along the bonds A-D and G-J in (A) and (B) is shown in (C), with the bond between the atoms designated A and D possessing no π -orbital misalignment (D), and the bond between the atoms G and J having a misalignment of 21.3° between π -orbitals (E).

framework is relieved by the conversion of any trivalent atom to a tetravalent atom, thus addition reactions are favoured. Since fullerenes are essentially continuous aromatic sheets, without this curvature they would be no more reactive than an ideal graphite layer.⁵⁶ Similarly, the reactivity of nanotubes is derived from their curvature, though nanotubes are only curved in one dimension (along the sidewall) while fullerenes are curved in two dimensions. Thus, for a fixed radius of curvature the conjugated carbon lattice will be more distorted for a fullerene than for the corresponding nanotube. Consequently, as nanotubes are often capped by hemispherical fullerene structures, there is always an increased reactivity at the end caps irrespective of the nanotube diameter. However, when the nanotubes are open-ended, the reactivity is enhanced at these ends due to dangling bonds. Figure 1.8B shows an open (5,5) armchair SWCNT, which is usually capped by a C₆₀ fullerene hemisphere. At the end caps of the nanotube $\theta_p = 11.6^\circ$, while along the sidewall $\theta_p = 5.97^\circ$, hence the end caps are more reactive. Even though both fullerenes and nanotubes are curved, conjugated carbon systems, their sidewall addition chemistries differ. The chemical reactivity in strained carbon systems arises primarily from two factors as the curvature induced strain in non-planar conjugated organic molecules has two principal sources; either pyramidalization of the

conjugated carbon atoms, as is most prevalent in fullerenes, or π -orbital misalignment between adjacent carbon atoms.⁵⁷

The pyramidalization angle in fullerenes is useful toward classifying their reactivity as there is very little π -orbital misalignment in these spherical structures. Indeed, in the case of C_{60} there is a zero misalignment between the π -orbitals, and this is also the case for pairs of atoms aligned parallel to the circumference (or orthogonal to the nanotube axis) of the (5,5) nanotube (Figure 1.8D). However, there are also bonds running at an angle to the circumference where the curvature of the sidewall invokes a misalignment of the π -orbitals of some angle (ϕ), and in the case of the (5,5) nanotube $\phi = 21.3^\circ$ (Figure 1.8E). In contrast to fullerenes, this π -orbital misalignment is believed to be the principal source of strain in carbon nanotubes, though both the pyramidalization angle and π -orbital misalignment should be considered. Both of these parameters are dependent on the radius of curvature in the conjugated lattice, thus for nanotubes both will depend on diameter and will scale inversely in proportion to it. For this reason, nanotubes with smaller diameters will exhibit a higher reactivity owing to the greater extent of π -orbital misalignment and the larger pyramidalization angles associated with their sidewalls.

1.2 Methods of Synthesis

Current methods for the bulk synthesis of SWCNTs rely on three main techniques as depicted in Figure 1.9; arc-discharge,^{59,60} laser ablation^{61,62} and chemical vapour deposition (CVD).⁶³⁻⁶⁶ The CNTs produced by each method have significant variations in their purity, quality and diameter distribution that critically depend on experimental variables involved with each process. An extensive amount of research has been conducted on improving these qualities, and although considerable progress has been made in this regard most commercially available CNT material is still highly heterogeneous and contains a significant amount of impurities.

1.2.1 Electric Arc Discharge

The most common and perhaps simplest method for CNT fabrication is that of electric arc-discharge, which was originally developed for the production of fullerenes.⁶⁷

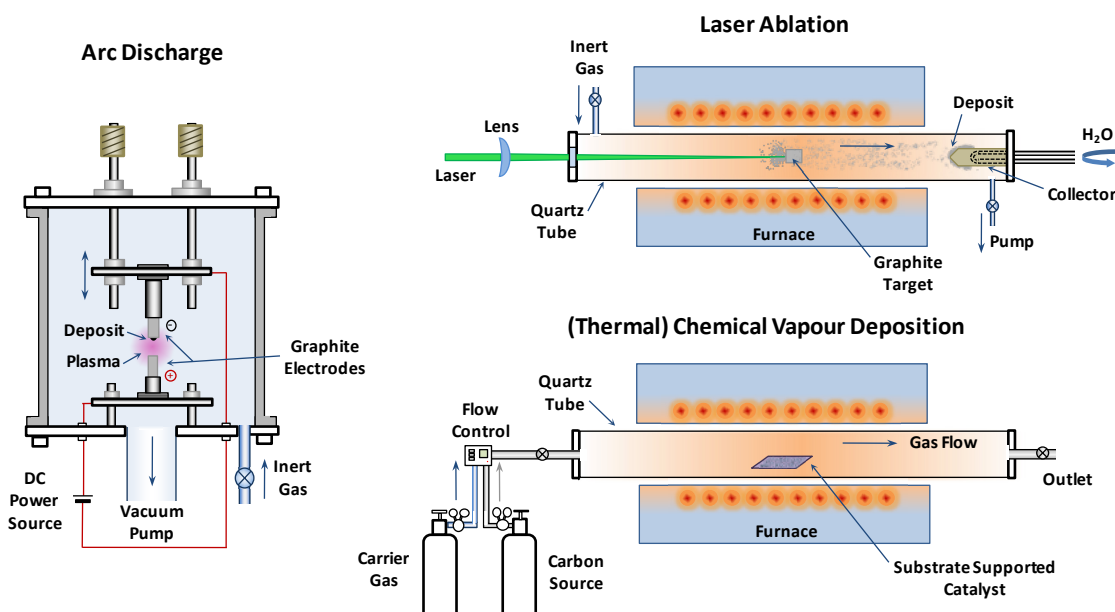


Figure 1.9 Schematic representations of the main techniques for bulk synthesis of CNTs.

Indeed, initial reports of CNTs were made concerning material prepared using this technique.^{4,9,10} Here, an arc discharge is generated between two graphite electrodes under an inert atmosphere at controlled pressure.⁵⁹ The high temperature produced during the process allows for sublimation of carbon at the anode which can result in the formation of nanotubes under the right conditions. Generally, temperatures of around 2000-4000K are achieved meaning nanotubes with a reasonably high degree of crystallinity are obtained.⁶⁸ For pure graphite electrodes MWCNTs are produced although a significant amount of impurities such as amorphous carbon, fullerenes and graphitic nanoparticles are also formed. Adding a metallic catalyst to the anode, usually a transition metal such as Fe, Co, Ni, Y, Mo or an alloy of these, allows the synthesis of SWCNTs through this method. However, MWCNTs and other forms of carbonaceous material are still produced in conjunction with the SWCNTs, and the yield of each type of carbon structure is dependent on experimental conditions such as the nature of the metal catalyst and its concentration, the type of gas and its associated pressure, the applied current and the geometry of the electrodes.^{67,68} Variation within these parameters can significantly alter the proportions of carbonaceous structures in the deposited product, which usually has a large proportion of non-nanotube material and a high weight percentage of metallic catalyst residue. Additionally, the diameter distribution of the SWCNT ensemble produced via this technique is also influenced by these experimental parameters, where the size and nature of the metallic catalyst is

expected to be the dominant variable.

1.2.2 Laser Ablation

The laser ablation technique is similar to the arc-discharge process in that it involves the heating of a graphite target embedded with a transition metal catalyst under an inert atmosphere.⁶¹ In this instance, the target is mounted in a quartz tube inside a high temperature furnace which operates at around 1500K. A focussed laser (which can be operating in either pulsed or continuous mode) vaporises the target while gas is bled into the chamber. The gas flow directs vaporised species to a water-cooled copper collector at the end of the reactor where they condense.⁶⁸ Again, experimental variables such as the nature of the metal catalyst and inert gas type may be changed in order to optimise the CNT yield, this time including the power and wavelength of the laser. The nanotubes produced by this method are cleaner than those obtained by arc-discharge, forming without layers of amorphous carbon coating their sidewalls as is often the case for arc CNTs, though non-nanotube carbonaceous material is still present.⁶⁷ Yields of greater than 70% SWCNTs are possible, forming mostly in tightly bound ropes and bundles.⁶² With the same type of metal catalyst the laser ablation technique provides CNTs of a similar diameter distribution to those synthesised by arc discharge, indicating similar growth mechanics. Although the yield and quality are slightly better with laser ablation, operation of a high intensity laser increases the cost of synthesis.

1.2.3 Chemical Vapour Deposition (CVD)

CVD synthesis of CNTs involves the decomposition of a volatile (usually gaseous) carbon source over an active metal catalyst which serves as a nucleation site for the initiation of nanotube growth.⁶⁷⁻⁶⁹ The first such synthesis was demonstrated in 1993 for MWCNTs^{64,66} followed shortly by SWCNTs in 1996,⁶⁵ and an expansive amount of research has since been performed on various CVD based methods. CVD is the most versatile route for the production of CNTs as it offers a considerable degree of control over the growth conditions, with a large number of possible precursor gases, reaction temperatures, types of catalyst and substrate materials having been examined. Decomposition of the source gas can be achieved either through heating (thermal CVD) or through use of plasma in a process referred to as plasma-enhanced CVD (PE-CVD).

In both cases the nanotube structures obtained depend heavily on the type of catalyst and the size of the metal nanoparticles,^{65,70} while other experimental factors also have a significant influence.^{68,69} Utilising certain parameters has allowed the synthesis of both MWCNTs and SWCNTs with a limited level of control over their morphology and structure, defining properties such as diameter distribution and number of walls. CVD methods may also produce CNTs in a variety of architectures, from nanotube soot in the bulk phase to aligned CNT forests and well-separated individuals supported on flat substrates or suspended across trenches and terraces.^{71,72} However, nanotubes produced by CVD have a higher defect density compared with those from arc discharge and laser ablation owing to lower synthesis temperatures, while they also contain amorphous and polyhedral carbon impurities.⁷³

One CVD method that has been shown to produce CNTs on an industrial scale is the high pressure disproportionation of CO (HiPCO) process, which utilises a continuous-flow gas phase in a high temperature reactor with CO as the carbon feedstock and $\text{Fe}(\text{CO})_5$ as the catalyst precursor.⁷⁴ Here, the organometallic catalyst species decomposes at high temperature forming metal clusters on which nanotubes nucleate and grow, where the SWCNT yield and diameter distribution may be tuned by changing variables such as the reaction temperature and CO pressure. The HiPCO process generally produces nanotubes smaller than those obtained by arc discharge or laser ablation, having diameters of around 0.7-1.1nm, while the distribution of (n, m) species is also wider.⁷⁵

Another CVD technique of note is the catalytic decomposition of CO on bimetallic Co–Mo catalysts (CoMoCAT)⁷⁶ method of production which is capable of producing SWCNTs in high yields and with significantly reduced diameter distributions. It has been shown that CoMoCAT synthesis is capable of producing nanotube ensembles highly enriched in certain chiralities.⁷⁷ Other CVD methods have also been reported to produce CNTs with limited selectivity, such as the specific growth of semiconducting CNTs^{78,79} and synthesis of CNTs with reduced diameter populations,⁸⁰ while the impurity content can be reduced by including water in the gas feedstock.⁸¹

With continued progress in control over CVD growth conditions, including the size and structure of catalyst nanoparticles, it is conceivable that eventually pure nanotubes of specific (n, m) type will be able to be selectively grown in an architecture according to the desired application. However, until this goal is ultimately realised, the purification

and post synthesis sorting of mixed-diameter CNT material containing carbonaceous and metallic impurities remains necessary.

1.3 Purification

As-produced SWCNT material can contain upwards of 30% (by weight) metallic catalyst particles that are necessary for the growth of single-walled nanotubes. Other carbonaceous species, such as MWCNTs, amorphous carbon, fullerenes, graphitic particles and nanocones or nanohorns may also be present depending on the method of synthesis and related conditions.^{73,82} The prevalence of impurities in as-produced electric arc CNTs is apparent in the electron microscopy images shown in Figure 1.10. Both amorphous and ordered carbonaceous impurities are visible, while metal catalyst particles are abundant in the raw material.

Oxidative treatments are commonly employed in purification schemes due to their relative simplicity and efficiency in removing both metallic particles and non-nanotube carbonaceous material. While metal catalysts and amorphous carbon may be removed by relatively mild procedures, graphitic and polyhedral carbon components have similar oxidation temperatures to the nanotubes themselves, thus elimination of these impurities is coupled with substantial damage to or destruction of the CNTs.⁷³ Also, metal catalyst particles are often encapsulated by a carbon shell, varying from disordered to graphitic in nature, which acts as a barrier to oxidation and makes their removal more challenging.⁸³

Liquid phase techniques usually involve acid treatment in HNO₃, HCl, H₂SO₄ or mixed acids although refluxing with a strong oxidising agent, for instance KMnO₄ or H₂O₂, is also effective.^{82,84,85} These chemical-based purification methods are able to remove the majority of amorphous and polyhedral carbon material and metal catalyst particles, however harsh oxidative processing can considerably damage CNT structures or consume them completely.^{84,86,87} Gas phase processes involving oxidation of samples under various atmospheres such as air, O₂ and H₂O have also been demonstrated to be capable of opening CNT end-caps and reducing the metallic and amorphous carbon content.⁷³ Many commonly employed purification methodologies rely on a combination of acid treatment and thermal oxidation to remove as many impurities as possible.^{86,88-90} However, oxidative methods are known to cause damage to the nanotube sidewalls and can result in nanotubes with a high degree of carboxyl addends. While this may

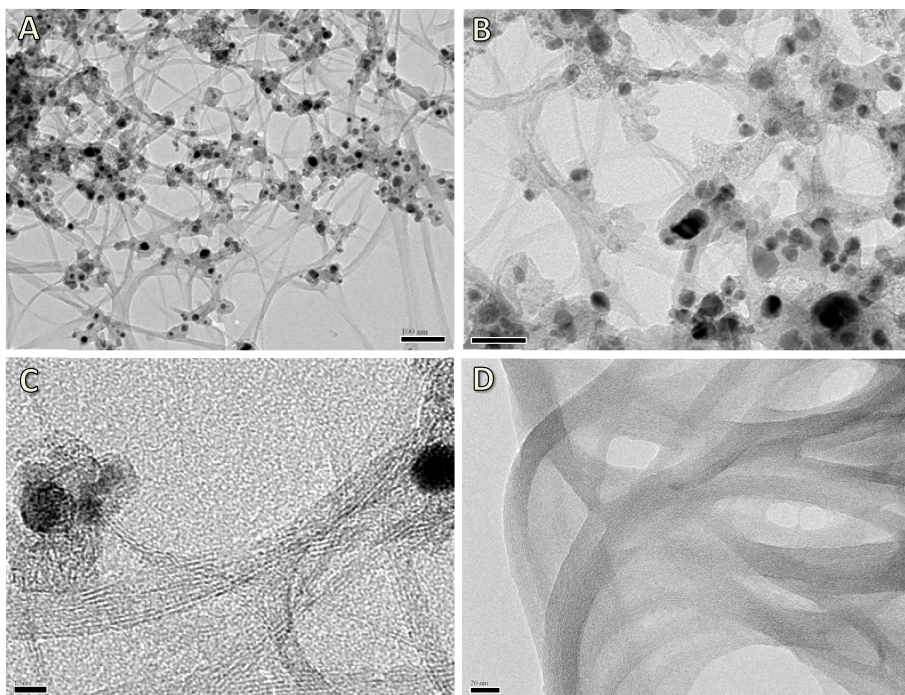


Figure 1.10: Transmission electron microscopy images of as-produced electric arc CNT soot recorded at different magnifications showing metallic (high contrast) and carbonaceous (low contrast) components; scale bars are 100nm (A), 50nm (B) and 10nm (C). An image of the same CNT material purified through centrifugation is shown in (D), with a scale bar of 20nm. The size of the CNT bundles is increased after purification and filtering.

facilitate further chemical functionalisation or assist with dispersion of nanotubes in solution,⁹¹ functionalisation of the nanotube sidewall is not always desirable. For this reason other physically based purification methods have been investigated, for example it has been demonstrated that metal catalyst particles may be removed by magnetic filtration,^{92,93} though this a relatively slow process and is incapable of removing carbonaceous impurities.

Purification of CNTs using centrifugation has become a popular approach owing to the advantage of simultaneous removal of nanotube bundles.³⁸ Initially demonstrated for CNTs suspended in an aqueous solution of sodium dodecyl sulphate (SDS)⁹⁴ and later in the organic solvent dichlorobenzene,⁹⁵ this method is favoured as a non-oxidising alternative to chemically based procedures. In general, it is expected that metallic particles and larger amorphous and graphitic carbon material can be removed in the sediment while well-dispersed nanotubes are retained in the supernatant.⁹⁶⁻⁹⁸ Such purification is usually accomplished by a process depicted in Figure 1.11, where sonication of the nanotube soot in a surfactant dispersion is followed by centrifugation at speeds around ten to thirty thousand times the force of gravity (g), where

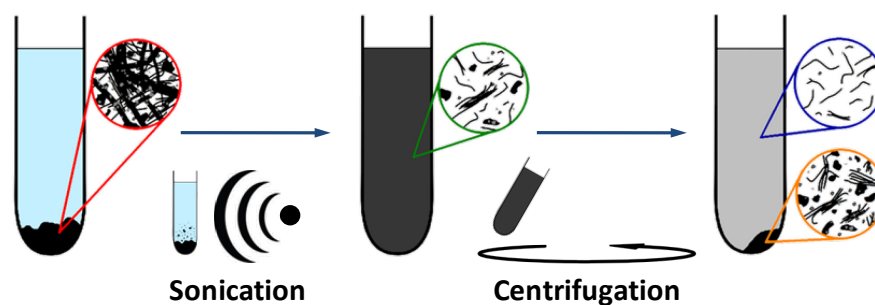


Figure 1.11: Centrifugation based purification of CNT soot. As-produced material is dispersed in solution through sonication with the aid of a dispersant. Centrifugation causes sedimentation of heavier particles, including metal catalysts and large CNT bundles.

$g = 9.8\text{m}\cdot\text{s}^{-2}$. As with other purification methods, specific protocols vary among the literature with regards to applied centrifugation forces and duration, while the dispersion methodology is also highly diversified. Additionally, if oxidative purification is implemented prior to centrifugation this affects the resultant suspension, where air-oxidized SWCNTs may be preferentially suspended over carbonaceous impurities.⁹⁹ Treatment with nitric acid to afford carboxylated CNTs can also alter the dispersability of amorphous carbon particles, leaving them highly suspended,¹⁰⁰ although CNTs are still recoverable.¹⁰¹

Successful enrichment of the nanotube fraction in a sample is partly why centrifugation has become the basis for a number of CNT sorting methods as will be discussed in Section 1.5.3; however both centrifugal separation and purification rely on the ability to disperse hydrophobic, intractable CNTs in solution as individuals which is not a trivial exercise.

1.4 Dispersion of Carbon Nanotubes

CNTs are notorious for ‘bundling’, where the large intermolecular van der Waals attraction of the nanotubes causes them to agglomerate into mats, ropes or bundles when fabricated,⁶² presenting a significant barrier for the vast majority of possible applications. Bundles have been shown to be larger after purification processes are applied than in the original as-produced material (see Figure 1.10),¹⁰² while the cohesive forces binding the nanotubes together have been estimated to be approximately 500eV per micrometer of intertube contact which is a substantial amount of energy.^{38,103} For this reason, CNTs are inherently insoluble in both water and organic solvents, with

dispersion methods almost universally relying on ultrasonic processing to exfoliate the nanotube material.¹⁰⁴

Although some organic solvents have shown the ability to disperse CNTs well,¹⁰⁴⁻¹⁰⁶ the stability of these suspensions is generally poor, with nanotubes re-aggregating into ropes and bundles relatively rapidly.¹⁰⁷ Additionally, individuals are usually obtained only at low concentrations.¹⁰⁸ Recent results have shown promising new solvents that provide better dispersion¹⁰⁹ while the use of dispersive agents may also improve stability,^{110,111} however CNTs dispersed in organic media have a limited application range. Consequently, the dispersion of nanotubes in water has been studied more extensively.

Aqueous dispersion requires modification of the hydrophobic CNT surface, and methodologies toward this end may be grouped into either chemical (covalent) or physical (non-covalent) approaches.¹¹² Surface functionalisation of CNTs has been shown to be effective for dispersion in both aqueous and organic media,¹¹³ though the intrinsic electronic and mechanical properties of the nanotubes are adversely affected.¹¹⁴ Dispersion via non-covalent methods has the advantage of preserving the conjugated π system of the nanotubes and hence their electrical properties, and CNTs have been successfully dispersed in water with the aid of a vast number of different dispersive agents such as surfactants,¹¹⁵⁻¹²³ polymers,¹²⁴⁻¹²⁸ pyrenes,¹²⁹ perylenes¹³⁰ and single-stranded DNA,¹³¹ among others.¹³²⁻¹³⁴ The mechanism for dispersion is expected to be primarily due to hydrophilic and hydrophobic interactions, where attraction between the CNT surface and the dispersant's hydrophobic segment facilitates adsorption while the hydrophilic group associates with water.¹¹⁴ Effective dispersants often contain aromatic components that adsorb through π - π stacking interactions with the conjugated nanotube sidewall. Dispersions involving ionic surfactants are believed to be stabilised by electrostatic repulsion between the hydrophilic head groups, while for non-ionic surfactants and polymers, steric hindrance prevents nanotube agglomeration.^{112,126,135}

Sonication of CNTs in solution is able to split larger bundles while the dispersant prevents the individual nanotubes from re-bundling. It has been suggested, at least in the case of ionic alkyl amphiphiles such as SDS, that the mechanism follows an 'unzipping' action, where sonication causes the ends of the bundles to fray, allowing surfactant molecules to attach at the exposed ends thus forcing further splitting.¹³⁶ This

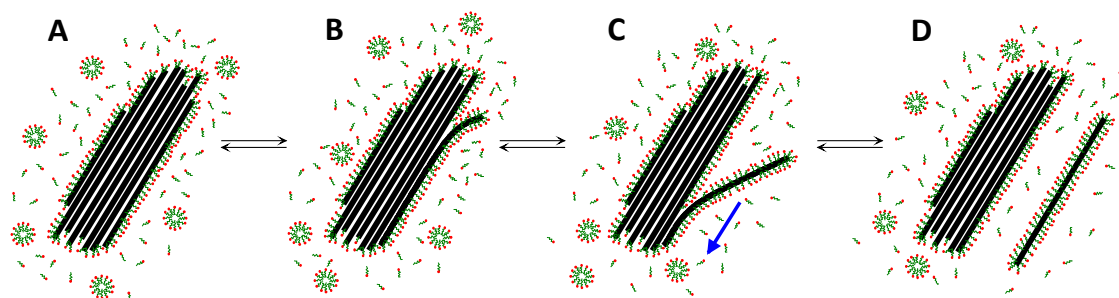


Figure 1.12: Proposed mechanism of surfactant assisted exfoliation of nanotube bundles into individual micelle-suspended tubes for an ionic alkyl amphiphile. The solution containing nanotube bundles (A) is exposed to ultrasonic irradiation, causing the bundle ends to fray (B). The splitting allows additional surfactant molecules to adsorb to the newly exposed inner surfaces, and this propagates along the length of the tube (C). The ‘unzipping’ process continues, ultimately resulting in the release of an isolated surfactant coated nanotube (D).

process propagates along the length of the nanotube until it is eventually separated from the bundle as shown in Figure 1.12. However, a dynamic equilibrium is expected to exist between free individuals and bundles in the solution, i.e. the unbundling process is reversible, which implies that there will always be a small concentration of bundles present in the solution.¹³⁶ Care must also be taken in ultrasonic processing as it has been shown to mechanically cut nanotubes,¹³⁷⁻¹⁴⁰ while at high energy inputs the nanotubes may be significantly damaged.¹⁴¹ Sonication may also act to degrade the solvent or dispersant, for instance under ultrasonic irradiation a polymer is formed by the solvent dichlorobenzene,¹⁴² while radicals produced by ultrasonic cavitation of water in the presence of surfactants may act to chemically dope the CNTs.¹⁴³ In any event, ultrasonication has been proven as an efficient and effective means of debundling CNTs in solution and is likely to continue to be used for this purpose. Evaluation of sonication processing parameters and their influence on the dispersions obtained is critical to implementation of CNTs in further applications. Additionally, methods for the separation and sorting of nanotubes possessing different properties are facilitated by the individualisation of the nanotubes in solution, thus the degree of dispersion is very important. While it is also possible to perform separations of semiconducting and metallic bundled materials, the enrichment factor is likely to be smaller due to aggregation of the two nanotube types.

1.5 Methods of Separation and Sorting

CNT material produced by current fabrication methods is generally polydisperse in nanotube diameter with a distribution dependent on the conditions of formation within each synthesis technique. The ratio of semiconducting to metallic CNTs also varies, as does the length of the nanotubes. Separation of CNTs by electronic type and chirality has become a highly active area of research, with a variety of physical and chemical methods being devised for this purpose.^{2,18,26,144-150} Length separation has also been investigated, though to a lesser extent.¹⁵¹

1.5.1 Selective Destruction

It has been reported previously that metallic nanotubes in a bundle may be selectively broken down by electrical current-induced oxidation.¹⁵² In a similar vein, metallic CNTs in a bundle or film may be destroyed by electrochemical etching in an electrolyte solution.¹⁵³ Etching using gaseous sources is also able to remove metallic nanotubes with limited selectivity, which has been performed using hydrogen¹⁵⁴ and methane¹⁵⁵ plasma treatments, though smaller diameter nanotubes are also destroyed. Exposure of CNTs to fluorine gas (although not fluorine plasma) followed by heat treatment has shown that metallic nanotubes of small diameter are preferentially etched while semiconducting nanotubes are retained.¹⁵⁶ Additionally, solution phase destruction of metallic SWCNTs has been demonstrated using nitronium ions.¹⁵⁷ On the other hand, slight preferential removal of semiconducting nanotubes may potentially be accomplished via hydrogen peroxide oxidation.¹⁵⁸

Irradiation of mixed electronic type CNT samples by microwaves has also been reported to reduce the metallic nanotube content,¹⁵⁹ with microwave based elimination of metallic CNTs also being achieved in mixed acid dispersions.¹⁶⁰ Similarly, illumination of CNTs deposited on a substrate using a white light source can reduce the conductivity of the film through a light-mediated oxidation that is more prevalent for small diameter metallic CNTs.¹⁶¹

The above techniques mainly rely on differences in chemical reactivity between semiconducting and metallic nanotubes where the greater availability of electrons in metallic CNTs allows them to be chemically targeted, however smaller diameter semiconducting CNTs are also commonly consumed by these techniques. Additionally, such methods for selective destruction or removal of CNTs are primarily directed

towards the depletion of metallic species for the creation of transistor devices. As it is desirable to recover metallic nanotubes as well, many non-destructive techniques for sorting nanotubes according to their electronic type have also been examined.

1.5.2 Electrophoretic and Chromatographic Approaches

Field flow fractionation (a technique where a force field is applied perpendicular to a flowing suspension to effect particle separation according to differing mobilities) was one of the first methods used to separate nanotubes according to their length, with some success.¹⁶² By using this technique with a dielectrophoretic field component limited separation of CNTs by electronic type can be obtained,¹⁶³ while a non-electric field based cross-flow filtration method has also been shown to sort nanotubes by length to a certain degree.¹⁶⁴ Likewise, separation using capillary electrophoresis has been demonstrated to separate CNTs into discrete fractions mainly according to their length,^{165,166} while gel phase electrophoresis is able to separate nanotubes according to both length and diameter to some extent.¹⁶⁷ Alternatively, alternating current dielectrophoresis has been used to exploit the difference in dielectric constants between metallic and semiconducting nanotubes to achieve separation by electronic type, where metallic nanotubes may be deposited on a substrate leaving the solution phase enriched in semiconducting CNTs.¹⁶⁸⁻¹⁷² Unfortunately, the dielectrophoretic force rapidly reduces with distance above the electrodes such that the majority of the nanotubes in the solution do not experience a significantly strong interaction, thus presenting a problem of scalability.¹⁴⁵ However, continuous extraction of metallic CNTs has been reported using dielectrophoresis in a microfluidic channel which could provide a solution to this issue.¹⁷³

Size exclusion chromatography (SEC) has been one of the more successful methods for sorting nanotubes according to their length and was first demonstrated using a gravity fed column with porous glass as the stationary phase,¹⁷⁴ with gel based filtrations also being reported.¹⁷⁵ SEC has been performed using a high performance liquid chromatography system, though again separation was by length only.¹⁷⁶ Heller *et al.* established that a combination of gel electrophoresis and gravity flow SEC could separate nanotubes by both length and diameter, where these two processes used in conjunction were able to produce nanotube fractions with narrow length distributions and partially controlled diameter populations.¹³⁷ By using three SEC chromatographic columns of different pore size fractionation by length can be achieved with higher

resolution (<10% variation,¹⁷⁷ which is better than the 30-80% variations reported where only a single column was used^{137,174,176}).

Ion-exchange chromatography (IEC) may be used to separate CNTs dispersed with single-stranded DNA into distinct diameter fractions, though this separation depends more on the periodic self-assembly of specific oligonucleotide sequences along the nanotube structure.^{131,178,179} Specifically designed sequences can provide a high degree of recognition for individual species, where well resolved separation of a selection of semiconducting chiralities has been demonstrated.¹⁸⁰ Metallic CNTs have less structurally selective interaction with DNA due to their similar electronic character between species, although armchair chiralities can be wrapped preferentially.¹⁸¹

1.5.3 Selective Adsorption

Bulk separation of nanotubes has been demonstrated to a limited extent through selective adsorption of octadecylamine to semiconducting CNTs dispersed in tetrahydrofuran.^{182,183} Here, metallic SWCNTs are precipitated upon evaporation of the solvent, resulting in a solution enriched in semiconducting species. Contrastingly, it has been suggested that octylamine and propylamine molecules adsorb more strongly to metallic nanotubes when dispersed in tetrahydrofuran,¹⁸⁴⁻¹⁸⁶ which allows enrichment of metallic CNTs in the solution via centrifugation. The difference between these two methods may be related to the level of oxidation of the starting material,¹⁸⁶ suggesting any purification methods applied to the CNTs beforehand may greatly affect the separation efficiency obtained.

It has been reported that addition of salts to surfactant stabilised dispersions of CNTs can offer some control over the SWCNT aggregation state, where destabilisation is species-sensitive depending on the concentration and ionic strength of the salt.¹⁸⁷ Similarly, it has been shown that addition of bromine ions selectively destabilises metallic CNTs in dispersions of Triton X-100, facilitating enrichment of semiconducting CNTs in the solution.¹⁸⁸

One of the more successful methods of nanotube separation that has gained significant momentum is based on the centrifugal fractionation of well-dispersed CNTs in a medium denser than water, known as density gradient ultracentrifugation (DGU).¹⁸⁹ Pioneered by Arnold *et al.*, this technique was originally demonstrated using single-stranded DNA,¹⁹⁰ but has been improved through the use of specific co-surfactant mixtures.¹⁹¹ Separation in this instance relies on the competitive, diameter dependent

adsorption of surfactants to the nanotube sidewall.¹⁹² Typically SDS and a bile salt molecule are utilised, usually sodium cholate or deoxycholate, although certain copolymers are also capable of achieving separation.¹⁹³ The surfactant packing arrangement alters the nanotube densities such that certain diameters will reach equilibrium at different positions within the gradient, allowing for separation by chirality.¹⁹⁴ The gradient medium iodixanol is typically employed¹⁹⁴⁻¹⁹⁹ though sucrose has also been used,²⁰⁰ and while a step-wise gradient is currently standard practice, uniform gradients may offer similar separation abilities thus reducing the complexity of the process.²⁰¹ An alternative DGU separation has also been demonstrated with fluorocarbon polymers in an organic solvent and gradient system.²⁰²

Density gradients have been applied to separate nanotubes according to bundle size²⁰³ and length²⁰⁴⁻²⁰⁶ as well as chiral handedness.^{199,207} Recent results have shown that both hollow and water filled nanotubes can coexist within a sample depending on the intensity of the dispersion protocol and that these species appear at different density bands within the gradient, which is a complication.^{208,209} Nonetheless, DGU has emerged as an effective method of separating CNTs and is currently a leading technique. However, although the level of purity attainable through DGU is now very high,²¹⁰ small volumes are collected for each density fraction such that a large amount of processing produces a relatively low quantity of separated material.

The interaction of SDS suspended CNTs with agarose gels has also been demonstrated as a successful means of separating CNTs by electronic type, where semiconducting nanotubes adhere to the gel phase and metallic CNTs are recovered in the solution.²¹¹ This method has a reasonably high degree of selectivity and poses the potential for scalable sorting of nanotubes using multiple gel-containing columns.²¹² This technique also offers diameter selectivity through gel chromatography when incorporating the same SDS-bile salt interaction used in DGU.²¹³ The suggestion has been made that both the DGU and agarose gel methods that rely on the use of SDS may be enabled by preferential suspension of metallic CNTs as individuals by this surfactant while semiconducting nanotubes are found in bundles.²¹⁴ However, recent results indicate that aggregation state effects do not have a pronounced effect on agarose gel based separations, and it is the orientation of the SDS molecules on the CNT surface that facilitates the segregation of electronic types.²¹⁵

Various other organic molecules have been designed to separate CNTs and have performed with various degrees of success, including aromatic polymers,¹²⁵ derivatives

of pentacene,^{216,217} coronene tetracarboxylic acid,²¹⁸ condensed benzenoid molecules,²¹⁹ docosyloxymethyl pyrene,²²⁰ flavin mononucleotide²²¹ and polymeric porphyrin-peptide composites.²²²

1.5.4 Selective Functionalisation

Selective covalent sidewall additions generally rely on differences in the electronic DOS between nanotubes, where metallic nanotubes have a finite electron density at the Fermi level while semiconducting nanotubes have a distinct band gap. Due to this difference in the availability of electrons, any addition reaction in which the nanotube is the electron donor will favour preferential functionalisation of metallic nanotubes over semiconducting species. For instance, the interaction of osmium tetroxide (OsO_4) with CNTs in toluene and under UV irradiation provides selective functionalisation of metallic nanotubes, where OsO_4 is reduced to OsO_2 nanoparticles on the nanotube surface.²²³ Functionalisation of small diameter metallic nanotubes with triethylsilane is also possible through spontaneous formation of a covalent carbon-silicon bond.²²⁴ Conversely, selective functionalisation of semiconducting CNTs has been shown to occur with electron rich molecules such as azomethine ylides.²²⁵

Perhaps the most studied example of selective covalent functionalisation is the preferential reaction of water soluble diazonium reagents with metallic SWCNTs.²²⁶ Typically, para-substituted benzenediazonium tetrafluoroborate salts are added to solutions of surfactant suspended CNTs to afford covalently bound aryl groups on the nanotube sidewall.²²⁶⁻²²⁹ While this functionalisation disrupts the lattice structure of metallic nanotubes and hence degrades their optoelectronic properties, it has been shown that thermal pyrolysis of the functionalised nanotubes at approximately 300°C in an inert atmosphere effectively cleaves the aryl moieties from the sidewalls, restoring the electronic structure and associated properties of the nanotubes to a large extent. Aryl groups may also be removed by thermal annealing under vacuum²³⁰ or by irradiation with an ultraviolet laser.²³¹ However, this effect can be exploited, where creation of semiconducting thin films and field-effect transistors is enabled by selective elimination of conductive pathways in metallic CNTs through perturbation of their structure.²³²⁻²³⁵ The dielectric mobility of the nanotubes is also altered by such functionalisation, which has been used to improve separations using dielectrophoresis²³⁶ as well as free solution electrophoresis.^{237,238} Alternatively, a chromatographic approach to separate nanotubes

using this selective functionalisation has employed aryl diazonium salts possessing functional groups of different polarity appended preferentially onto the CNTs of different electronic type. Gravity filtration through silica gel was then applied to separate the nanotubes based on the respective polarity of the addends, with thermal treatment to recover CNTs in enriched fractions of both electronic types.²²⁷ While this method was only mildly successful, the selectivity of functionalisation is dependent on many experimental factors, one of the most influential of which is the constituent functional group of the diazonium salt.²³⁹ A number of functional groups have been investigated, including Cl,^{226,240} Br,^{235,241} OH,^{237,238,242-244} NO₂,²³⁹ COOH,²⁴⁵ COOCH₃ and OCH₃,²⁴⁶ as well as both unmodified^{247,248} and fluorinated²⁴⁹ alkyl chains. On the contrary, the effect of the dispersing medium has not been examined to any great extent, with most reactions being performed in SDS despite evidence of surfactant influence on the reaction.²⁴⁵

1.6 Motivation and Research Aims

Many of the separation methods discussed have shown promising results, while others are far from ideal. Those that are successful are still hindered by many shortfalls, such as low separation yields, complex or multiple step processes, the use of reagents that are expensive to synthesise or the ability to process only relatively small volumes of material. Although separation through diazonium salt functionalisation has not achieved levels of fractionation comparable to that obtained by the DGU or agarose gel methods, sorting through chemical functionalisation has much greater potential for scalability. If the selectivity of the diazonium based technique could be improved, the low cost and ease of this method could make it a competitor for commercial electronic type separation. Such improvement would allow for enhanced enrichment of yields in separation schemes as well as greater preferential elimination of conductive pathways in devices based on CNT films.

In order to utilise the selective functionalisation method the nanotubes must first be dispersed in solution, preferably as individuals. Since the diazonium reaction depends on the electronic properties of the CNT, it is imperative that the perturbation of the nanotube structure be minimised in the dispersion process. Consequently, investigations were initially targeted towards optimising the dispersion of unmodified CNTs in aqueous solution. Subsequent studies were concerned with the interactions between

diazonium salts and nanotubes within different dispersant systems and focussed towards determining favourable conditions for selective functionalisation.

Primarily, this work was directed towards the following goals; (1) identifying superior dispersants for CNTs in water and the concentrations at which they are effective, (2) examining dispersion protocols to minimise sidewall damage and maximise the degree of individualisation, and (3) to analyse the reactions of diazonium salts with the dispersed nanotubes in order to determine conditions for maximum selectivity.

Chapter 2

EXPERIMENTAL & ANALYTICAL TECHNIQUES

This thesis is concerned primarily with the dispersion of carbon nanotubes in water using sonication and centrifugation. Several techniques commonly employed in the analysis of such dispersions, namely ultraviolet-visible-near infrared absorption spectroscopy, Raman spectroscopy and atomic force microscopy, were used extensively to examine these solutions. In order to provide a detailed account of specific methods used in the acquisition of analytical values, exemplar experimental results will be introduced and their subsequent processing described as part of this chapter.

2.1 Dispersant and Nanotube Materials

The structures of the dispersants used in this work are shown in Figure 2.1, including sodium dodecyl sulfate (SDS, Sigma-Aldrich, min. 99.0%), sodium dodecylbenzene sulfonate (SDBS, Aldrich, technical grade), sodium deoxycholate (DOC, Sigma-Aldrich, 97%), sodium cholate (SC, Sigma, $\geq 99\%$), Pluronic F-127 (PF-127, Sigma, typical $M_w \approx 12,600$), Brij S-100 (previous trade name Brij 700, Aldrich, average $M_w \approx 4,670$), Tween 60 (Fluka, typical $M_w \approx 1,312$), didodecylammonium bromide (DDAB, Aldrich, 98%) and cetyltrimethylammonium bromide (CTAB, Ajax Chemicals, approx.

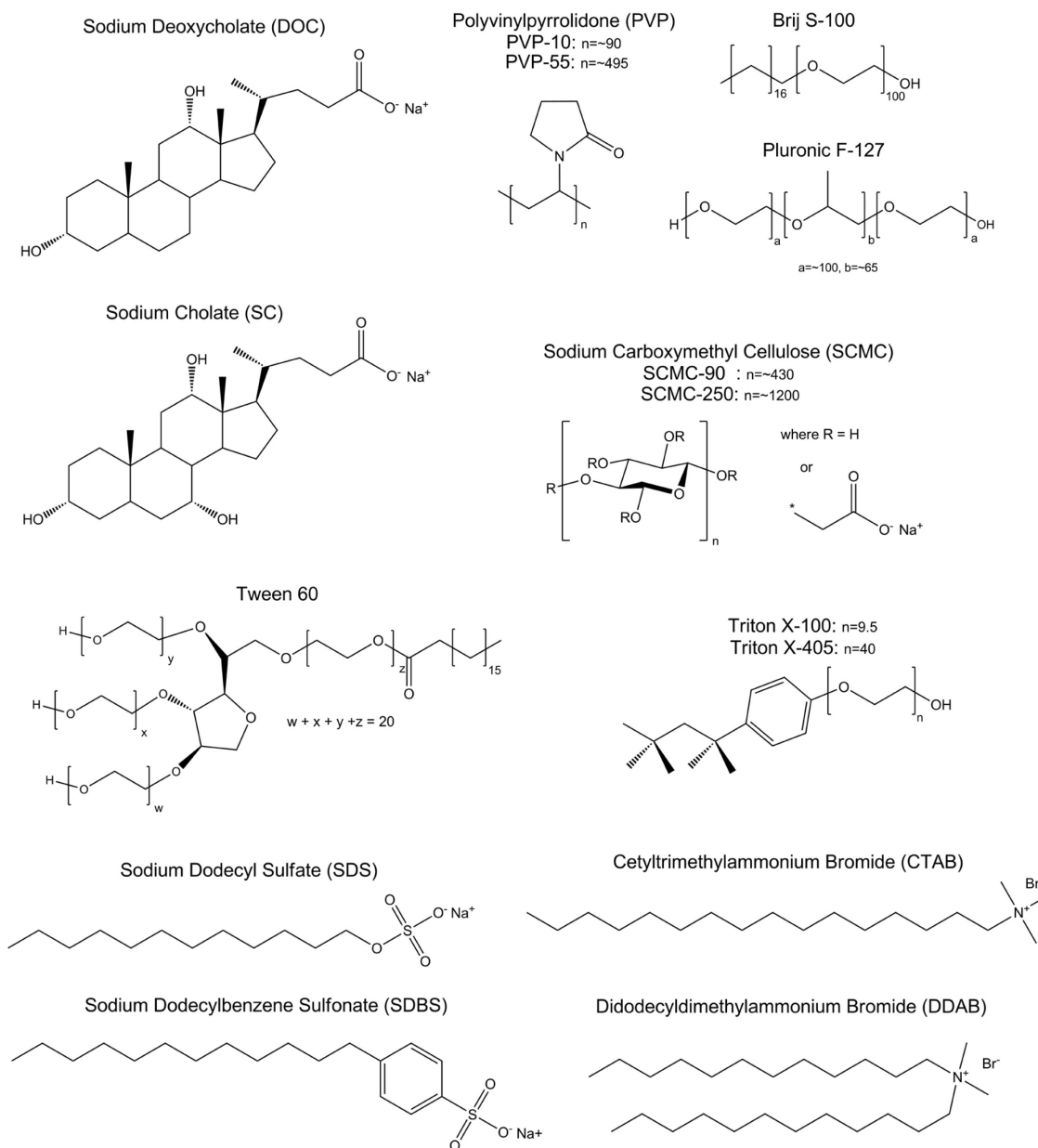


Figure 2.1: Structures of the dispersants used in this work.

95%, also known as hexadecyltrimethylammonium bromide). Dispersants of the same structure having different lengths were also examined. These were polyvinylpyrrolidone (PVP) polymers of molecular weights $\sim 55,000$ (PVP-55, Sigma-Aldrich) and $\sim 10,000$ (PVP-10, Sigma-Aldrich) along with sodium carboxymethylcellulose (SCMC) polymers of molecular weights $\sim 90,000$ (SCMC-90, Aldrich) and $\sim 250,000$ (SCMC-250, Aldrich) as well as Triton X-100 (TX-100, Sigma-Aldrich, average $M_w \approx 624.8$) and Triton X-405 (TX-405, 70% in H_2O , Sigma-Aldrich, $M_w \approx 1968.4$). All dispersants were purchased from Sigma-Aldrich (Sydney, Australia), except for CTAB which was acquired from Ajax Chemicals (Sydney, Australia), and used as received. These

surfactants were chosen to represent a varied selection of ionic (both cationic and anionic), non-ionic and polymeric surfactants for comparative purposes. All of these dispersants have been previously demonstrated as having the capability to disperse CNT material,^{116,121} with the exception of DDAB which was chosen as an additional cationic surfactant.

As-produced carbon nanotube soot was purchased from Carbon Solutions Inc. (Riverside, California, USA; Lots AP-251(3g) and AP-387(3g)). These nanotubes are produced by electric arc discharge using Ni and Y as the transition metal catalyst species, with the manufacturer quoting a residual metal content of around 30% by weight as determined by thermogravimetric analysis in air. Alternatively, as produced HiPCO CNT material possessing a different diameter distribution was obtained from Carbon Nanotechnologies Inc. (Houston, Texas, USA; now merged with Unidym; Lot R0554). This material is expected to contain less than 35% by weight residual Fe content. Both electric-arc and HiPCO nanotube material was dispersed in as-received form, without purification.

2.2 Preparation of Dispersed CNT Solutions

2.2.1 Ultrasonication

Theory

Dispersion of nanotubes in solution was facilitated by ultrasonic agitation, applied either directly to the solution with an ultrasonic probe or indirectly through use of a sonication bath. In both types of sonicator device a piezoelectric transducer transforms an electrical voltage oscillating at an ultrasonic frequency into a longitudinal mechanical vibration, which in turn generates compression waves in the liquid medium. This sinusoidal pressure leads to an effect known as acoustic cavitation, where microscopic voids or bubbles containing either permanent gas or vapour are formed by the motion of the fluid.²⁵⁰ Cavitation may be divided into two categories, stable and transient, where both types of bubble formation can generate forces capable of exfoliating nanotubes from a bundle. Stable cavitation occurs when a microbubble oscillates, often non-linearly, around a resonant equilibrium size. Stable cavities may continue oscillating for many cycles of the acoustic pressure and generally occur in low-

intensity fields,²⁵¹ however the motion of the microbubble may be sufficient to generate shear forces capable of debundling CNT aggregates. Transient cavitation typically occurs at higher intensities and in this instance the microbubbles are characterised by short lifetimes, usually only existing for around one acoustic cycle. The bubble expands rapidly during the rarefaction phase of the cycle, inflating to at least double its initial size and often much larger. This is followed by violent bubble collapse during the compression phase due to the inertia of the surrounding fluid, where disintegration into smaller bubbles may occur.²⁵⁰ The compression forces during transient bubble collapse generate high local temperatures and pressures, up to 5000K and 1000bar respectively,^{252,253} while high shear forces and radial shock waves arise in the liquid in the vicinity of the imploding cavity.²⁵¹ These conditions are capable of producing free radicals and degrading molecules present in the solution as well as disrupting larger aggregates of material such as CNT bundles. The prevalence of cavitation events and the radii of the produced microbubbles may be increased by raising the ultrasound intensity; however both are reduced at higher frequencies.²⁵⁰ Consequently, probe tip ultrasonicators (which typically operate at lower frequencies and higher intensities than ultrasonic baths) provide much more acoustic cavitation and thus a greater input power to the solution.²⁵²

Instrumentation

Two different instruments (as depicted in Figure 2.2) were used in this study; an Elmasonic S30H ultrasonic bath (Elma, Singen, Germany) operating at 37kHz, and a Sonics Vibra-Cell VCX 750W probe sonicator (Sonics, Newtown, Connecticut, USA) operating at 20kHz. Probe sonication was conducted with solid tapered microtips of either 5 or 6.5mm in tip diameter, with the smaller diameter tip generally used to process lower volumes at higher intensity. These microtips were constructed from the titanium alloy Ti-6Al-4V, which has a chemical composition of approximately 90% titanium, 6% aluminium and 4% vanadium, while it may contain up to 0.3% iron and 0.2% oxygen.²⁵⁴ The VCX 750W probe sonicator offers the ability to change the input power through altering the oscillation amplitude up to a maximum of 40% for a tapered microtip, with 20% being the minimum setting available. The instrument is designed to provide a constant amplitude of oscillation such that for any resistance to the movement of the probe a corresponding increase in power is delivered by the power supply, ensuring that the excursion at the probe tip remains constant. The energy delivered to

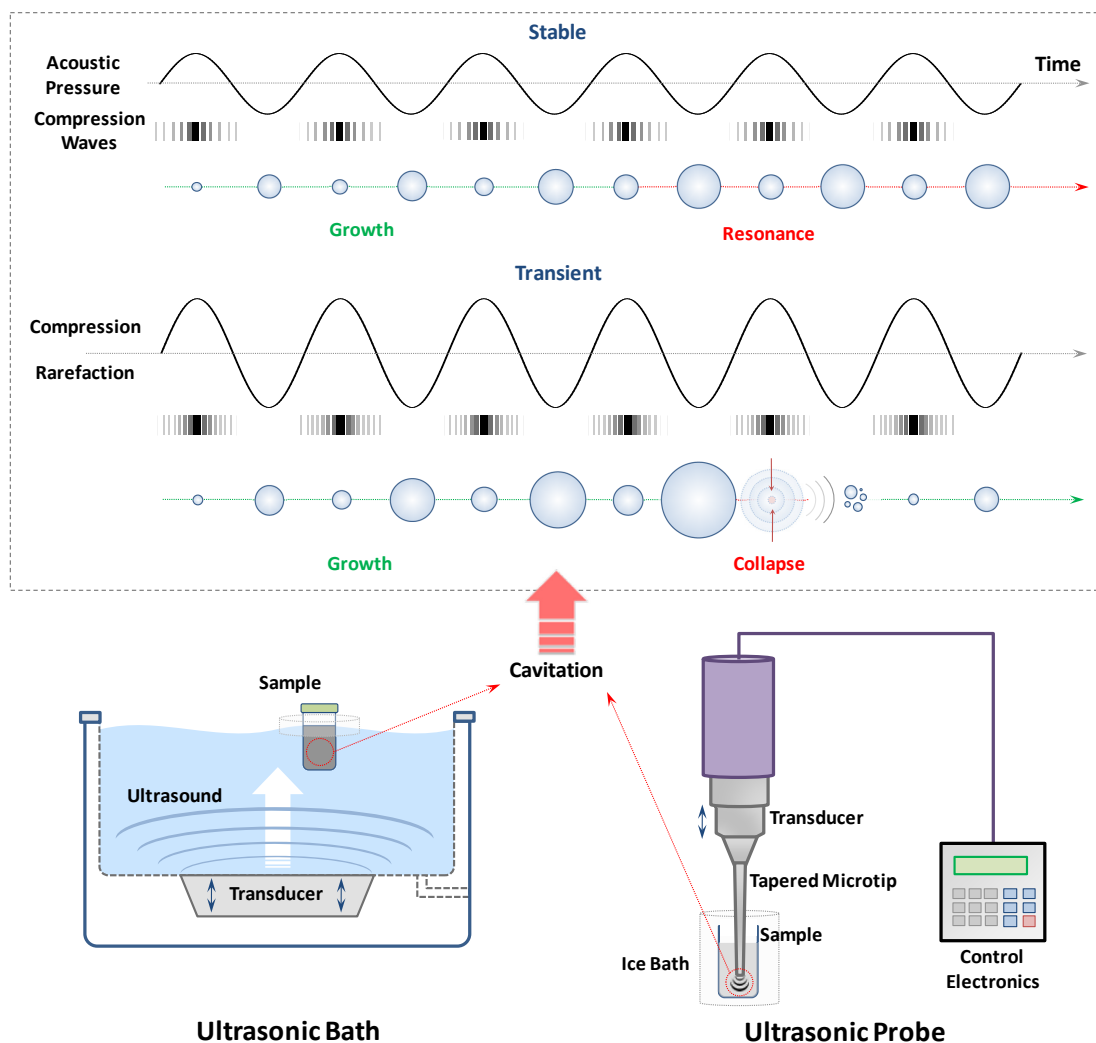


Figure 2.2: Schematic representations of the bath and probe ultrasonicators used in this work (bottom), with depiction of acoustic cavitation in liquid media under ultrasonic irradiation of the same frequency but differing intensities (top). Lower intensity promotes stable cavitation, where pre-existing microbubbles oscillate and grow in size until a resonant diameter is reached. At higher intensity cavitation becomes more transient, where microbubbles grow rapidly for a small number of cycles before the compression half-cycle forcibly induces its collapse, producing localised shear forces, shock waves and heat.

the probe is monitored internally by the system and is reported in joules at the end of the run.

Upon ultrasonic irradiation of a solution a temperature increase occurs due to acoustic cavitation. The increase in temperature with prolonged sonication can reduce cavitation and potentially decouple the probe,²⁵² hence solutions were cooled with ice water during sonication. This also helps reduce any thermal damage to the CNTs that may occur during the dispersion process. However, the temperature increase imparted to a known

volume of water enables calorimetric calibration of the input power, which can then be compared to the amplitude set on the instrument (and the recorded energy delivered to the probe) to determine the relative power output for each amplitude setting. This was performed for the Sonics VCX 750W and the results are presented in Appendix A. All power values reported herein for the tip sonicator are instrument recorded energy values adjusted to the calibration curve obtained using the pristine 6.5mm tip.

Experimental Details

Aqueous solutions containing 0.1-9% surfactant by mass (wt%) were prepared, with a typical concentration of 1wt%. As-produced CNT material was added to the dispersant solutions at concentrations ranging from 0.25 to 0.75mg·mL⁻¹, where 0.5mg·mL⁻¹ was the standard value. A volume of 10 or 25mL was often used to accommodate the capacity of the different centrifuge tubes, however the solution volume was also varied. In a typical experiment dispersion of the CNT material was accomplished through continuous sonication for fixed time periods with water cooling. The sonication duration was varied greatly, with typical values being 60 minutes for the bath-based instrument and 10-20 minutes for the tip sonicator.

In the bath sonicator case the bath water was completely replaced every 30minutes. Alternatively, ice was added directly to the bath, though in small amounts to avoid disrupting the transmission of ultrasound waves. The sample was floated in a foam holder cut to the size of the vial and positioned in the approximate centre of the bath, as this was the position of maximum ultrasound intensity. When solutions in a series were prepared via bath sonication each sample was sonicated consecutively in the same location within the bath, as the energy density provided by the instrument was found to be highly variable with position (see Appendix A).

For probe sonication, solutions were held in open-top vials placed inside a beaker which was packed with ice. This has the advantage of holding the sample in position in addition to providing cooling. Paper-towel padding was further utilised to prevent movement of the vial during processing. The ice bath was replaced every 10-20 minutes for extended sonication periods using the pause function on the probe sonicator. Standard preparations involved 10mL of solution in glass vials of internal diameter ~25mm for the 5mm microtip, while 25-50mL samples in 39mm diameter polypropylene vessels were used for the larger 6.5mm tip. Although the sonication intensity was varied, samples were typically sonicated at a tip amplitude of 20%.

2.2.2 Ultracentrifugation

Theory

In centrifugation the direction of the accelerating force causes denser components in the solution to migrate away from the rotational axis of the centrifuge. Under intense forces this material will settle at the furthest point of revolution, separating into a precipitate, allowing collection of lower density components in the supernatant liquid. All stated experimental accelerating forces herein are given as the average relative centrifugal forces experienced by the solution at the mean rotational radius of the fixed angle rotors ($r = r_{\text{avg}}$), where the relative centrifugal force (RCF) is calculated according to the formula

$$\text{RCF} = \frac{\text{acceleration}}{\text{gravity}} = \frac{\omega^2 r}{g}. \quad (2.1)$$

Since the angular velocity $\omega = 2\pi(\text{RPM})/60$, this equation can alternatively be expressed as $\text{RCF} = 1.12 \times 10^{-6} \text{RPM}^2 r$, with r in millimetres.

The settling velocity of a particle in the solution is dependent on many factors including the particle morphology, the viscosity of the liquid and the applied accelerating force, while any density difference between the particle and the liquid medium can be important (as with DGU). Bundles of undispersed CNTs, larger carbonaceous material and metallic particles are able to be sedimented from CNT solutions by centrifugation under various conditions due to the differences in buoyant density between these materials and individually dispersed CNTs. However, the accelerating forces needed are higher than those attained by standard centrifuges and thus required the use of a preparative ultracentrifuge.

Instrumentation

Two different instruments were utilised, a Beckman L8-70 ultracentrifuge and subsequently an Optima L-100XP ultracentrifuge (Beckman-Coulter, Sydney, Australia) which replaced the former apparatus. Both instruments were capable of operating with the same titanium fixed angle rotors under vacuum at high speed. The L-100XP was used for most experiments, where specifications for this instrument state speed control to within ± 10 revolutions per minute (rpm) of the set speed. Re-usable polycarbonate bottle assemblies with screw caps (Beckman-Coulter, Gladesville, New

South Wales, Australia) were used as the centrifuge tubes as these were cost-effective and sufficiently resistant to all of the dispersants examined.

The Optima ultracentrifuge is thermoelectrically refrigerated and allows a rotor temperature to be set for the cycle. The chamber temperature is measured by a thermocouple when the pressure is above 100mTorr, however the instrument requires a vacuum to operate at high speed (the rotor will not surpass 3000rpm until the pressure drops below 750mTorr). When the centrifuge is in operation the pressure in the drum eventually drops below 100mTorr, at which point the rotor temperature is measured directly by an infrared sensor.

Experimental Details

Solutions were centrifuged as soon as possible after sonication in an attempt to avoid re-aggregation of the dispersed nanotubes, as the exfoliation process is reversible on termination of ultrasound exposure.²⁵⁵ Pairs of centrifuge tubes were filled with liquid to their maximum capacity and balanced by weight to within 1mg before loading into opposite rotor slots to prevent rotor imbalance.

Initial experiments were conducted with 10mL volumes of solution in 10.4mL capacity tubes as a standard procedure. These were spun in a Type 50 Ti rotor which has a maximum rated speed of 50000rpm and holds up to 12 samples. For larger volumes of solution the Type 70 Ti rotor was utilised, which has a rated speed of 70000rpm and may hold a maximum of 8 samples. In this instance 26.3mL capacity polycarbonate bottle assemblies possessing aluminium screw caps were employed. Both of these rotors are featured in Figure 2.3 along with a cross-section view of the tube slots showing corresponding radial dimensions.

Typical centrifugation conditions involved accelerating forces around $120 \times 10^3 g$ for 1 hour. At completion of the centrifuge run, the upper ~70-85% of the supernatant solution was collected via pipette, taking care to avoid collecting residue from the sediment or from the outward wall of the tube. This precipitated material is visible in the inset of Figure 2.3 for a 10mL CNT solution spun in the 50 Ti rotor at 43000rpm (approximately $122 \times 10^3 g$). When comparing samples between the two different rotors, the rotation speed was adjusted to provide the same RCF. However, there is a difference in the clearing factor (k-factor) between the rotors, which depends on r_{\min} , r_{\max} and the maximum rotor speed, hence the Type 50 Ti provides a slightly greater sedimentation efficiency at equal RCF over the same run time.



Figure 2.3: Rotors used for ultracentrifugation of CNT solutions of different volume and their radii of rotation; Type 70 Ti (top) employed for 25mL volumes and Type 50 Ti (bottom) used for 10mL volumes. Inset: Centrifuge tube with CNT dispersion both prior to centrifugation (black liquid) and after spinning at 43000rpm for 1hr in the 50 Ti rotor showing sedimentation at the tube base and along the wall.

For centrifugation temperature studies the rotor and samples were pre-cooled (or heated) to the desired value under vacuum, i.e. with direct temperature measurement, before beginning the run. In all other studies a set-point temperature of 5 or 10°C was used and the rotor was spun starting from room temperature. For centrifugation times less than 1 hour, the rotor temperature reaches a value in the range 10-14°C with an average ~12°C upon completion of the cycle, while for times greater than 1 hour the set temperature is met by the end of the run.

2.3 Ultraviolet-Visible-Near Infrared (UV-Vis-NIR) Spectroscopy

2.3.1 Theory

The absorption of light from the ultraviolet-visible (UV-Vis) region of the electromagnetic spectrum is often used to examine electronic transitions from the ground to excited states of organic molecules as they are mostly resonant with photons

of energies around 1-6eV in magnitude, although certain transitions also extend into the near infrared (NIR) region. A schematic for a basic UV-Vis spectrophotometer is depicted in Figure 2.4. In a typical instrument light generated by a lamp is split by a monochromator before being passed through the sample where the subsequent intensity is measured by a detector. The absorbance (A) of a liquid sample at a particular wavelength λ is determined from the ratio of the incident light intensity (I_0) to that transmitted by the sample (I) by the relation $A = \log_{10}(I_0/I)$. The absorbance of a sample may then be related to the concentration of the absorbing species through the Beer-Lambert law, $A = \epsilon c l$, where A is absorbance, ϵ is the extinction coefficient, c is the analyte concentration and l is the path length of the holding cell.²⁵⁶

2.3.2 Instrumentation

Two different spectrophotometers were used in this work, either a Cary 50 UV-Vis or Cary 5G UV-Vis-NIR instrument (Varian, Melbourne, Australia) depending on the wavelength range required. The Cary 50 operates from 190-1100nm and utilises a xenon flash lamp source across this entire range. However, the optical transitions for CNTs also occur in the NIR region, hence their observation required use of the Cary 5G. This instrument has a deuterium arc lamp for operation from 175-350nm and a tungsten filament lamp for the 350-3300nm range, while two independent detectors are also used for different wavelength regions with a changeover at 800nm.

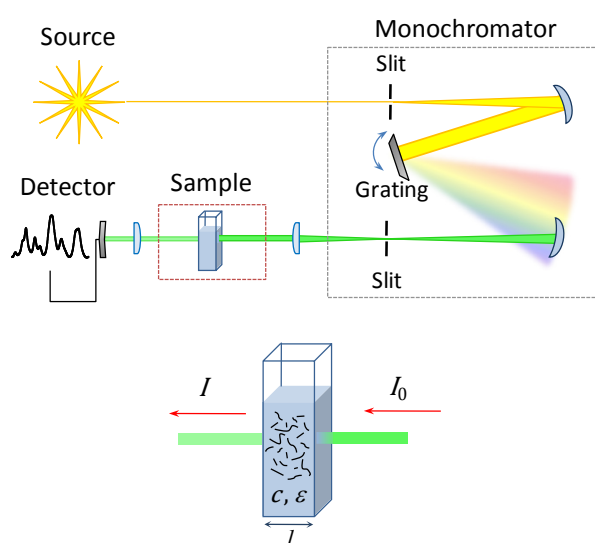


Figure 2.4: A simple depiction of a UV-Vis spectrophotometer with a Czerny-Turner monochromator, as found in the Cary 50 instrument.

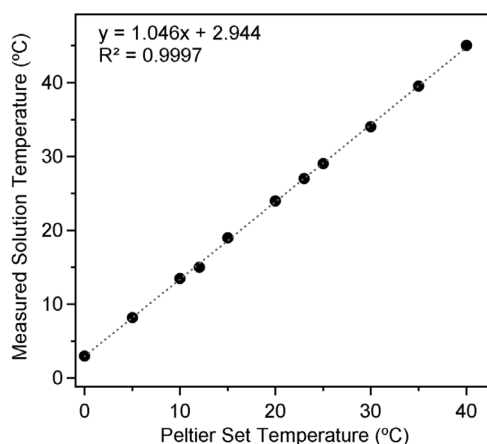


Figure 2.5: Calibration of the measured sample temperature against the set value on the Peltier cell holder.

A method was adapted to collect spectra from solutions that could be heated or cooled to a set temperature using a Peltier regulated cell holder mounted inside the Cary 5G instrument. In order to perform these temperature studies in the Cary 5G the Peltier cable was passed under the edge of the removable front panel of the sample chamber. The heat exchange mechanism of the Peltier consists of flowing water through the cell mount while it is in the spectrometer chamber, thus an inlet and outlet tube are required to be passed from the cell mount to an external reservoir and the spectrometer lid cannot be fully closed. As a consequence, the roller switch that is tripped by closing the sliding lid must be taped down to allow a scan to be taken. The coolant water was initially circulated by a peristaltic pump in early experiments, but this was later exchanged for a small pond pump which allowed for a higher flow rate. Although the Peltier control ramps the temperature slowly to the set value, several minutes were allowed for thermal equilibration between the cuvette, solution and cell mount before scanning a sample. A setting of 23°C was found to produce a thermometer measured temperature of 27°C inside the sample solution, while this offset was found to vary slightly over the range of temperatures studied for the diazonium reactions as shown in the Peltier temperature calibration curve in Figure 2.5.

2.3.3 Experimental Details

In general, 3mL volumes of the solutions were placed in 10mm path length quartz cuvettes (Banksia Scientific, Bulimba, Queensland, Australia; ES Quartz glass, transmission range ~190-2500nm) while reference spectra of dispersant solutions

without CNTs were taken for baseline subtraction. Typical scanning parameters for both instruments were 600nm/min at a data spacing of 1nm, which corresponds to an integration time of 0.1s.

Reactions with Diazonium Salts

For each reaction a fresh diazonium solution was prepared by dissolving a predetermined amount of the salt through agitation and brief bath sonication (<30s). Sonication is a very effective method for dissolution of the salts, and exposure of a diazonium solution to ultrasound for durations less than 1 min was found to negligibly affect its absorbance spectrum at both low and high concentrations. In general, 3mL of CNT solution was placed in a cuvette and a small volume of diazonium salt dispersed in water was added directly via pipette to obtain the desired diazonium concentration. Typically a concentration of 2mM was used, which involved dissolving 22.0mg of carboxy-, 22.1mg of nitro-, or 25.2mg of bromo-benzenediazonium tetrafluoroborate in 1.5mL water and adding 0.1mL of this diazonium solution to the 3mL aliquot of CNT dispersion.

Reactions of diazonium salts with the CNTs were monitored by kinetic UV-Vis-NIR scans on the Cary 5G. Since a spectrum from 200-1400nm takes approximately 2.5min to be recorded, scans were performed at 3min intervals for the first hour, although this interval was reduced to 10min for the second hour and further to 20 minutes up to 20 hours, as the reaction slows considerably over time. After the first 20 hour period scans were then performed hourly if the reaction was still proceeding.

For instances where rapidly occurring reactions were monitored over time, the scan rate could be increased to 1818nm/min (0.033s integration) or the scan range could be reduced to 570-1310nm to allow scans to be completed over shorter intervals (~1min).

As mentioned previously, the instrument was modified to hold a Peltier regulated cell to keep samples at fixed temperature for kinetic analysis, and reactions were performed in quartz cells at 27°C as a standard procedure. Specific experiments are described in further detail in the relevant sections. For information on the diazonium salts themselves, refer to Section 6.2.1 of Chapter 6.

2.3.4 Absorbance Spectra of H₂O and D₂O

Absorbance spectra recorded of the chamber (i.e. air), an empty quartz cell, water and heavy water (deuterium oxide, D₂O) are shown in Figure 2.6. The quartz cell provides minimal absorbance over the examined wavelength range, however the baseline is slightly above that of the fluid samples due to reflections between the cell walls.²⁵⁷ Wetting of the interfaces leads to slight refraction of the incident light, reducing interference losses and thus lowers the baseline. The absorbance spectra of both H₂O and D₂O over the region 400-2000nm contain peaks arising due to excitation of overtone and combination transitions of their fundamental molecular vibration frequencies. For the water molecule these fundamental vibrations are usually designated ν_1 (symmetrical stretching of the O-H bonds), ν_2 (scissor-like bending of the molecule) and ν_3 (asymmetrical O-H stretching) as shown in Figure 2.6. The fundamental modes for liquid H₂O have frequencies of around 3280cm⁻¹ (3050nm), 1645cm⁻¹ (6080nm) and 3490cm⁻¹ (2865nm) for ν_1 , ν_2 and ν_3 respectively, while for D₂O they are shifted to

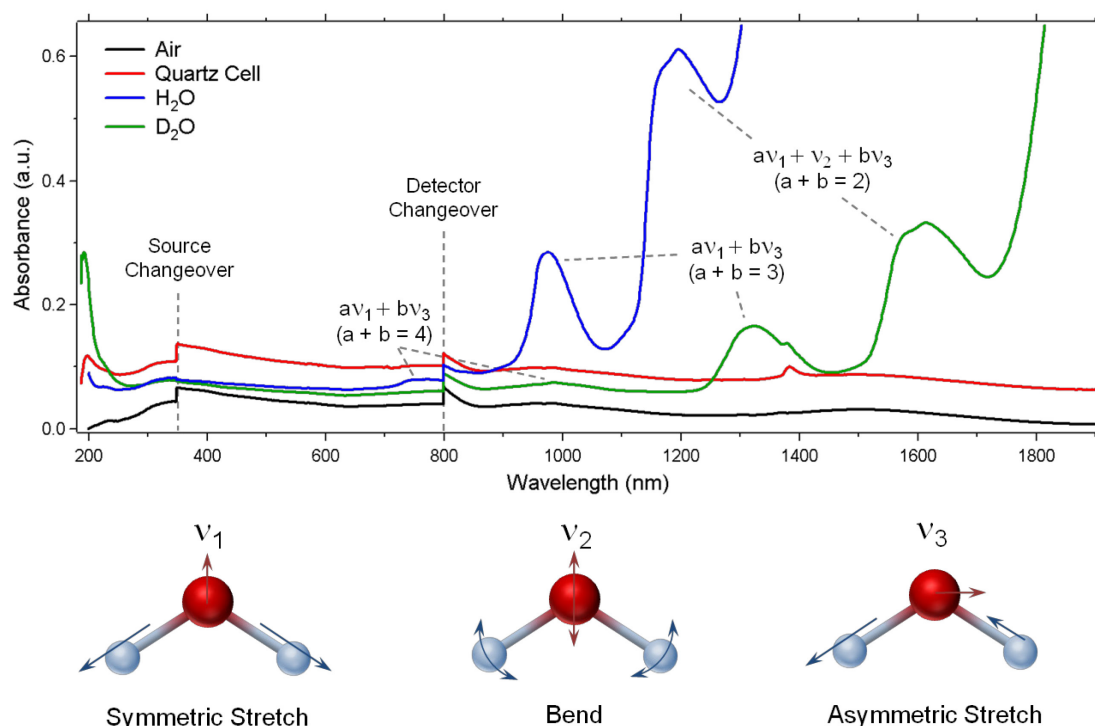


Figure 2.6: UV-Vis-NIR absorbance spectra for the chamber, a quartz cuvette, water and deuterium oxide over the range for which CNT peaks are expected. The absorbance peaks of H₂O and D₂O in this region are combinations of the fundamental vibrational modes of their molecules, which are depicted in the lower part of the figure.

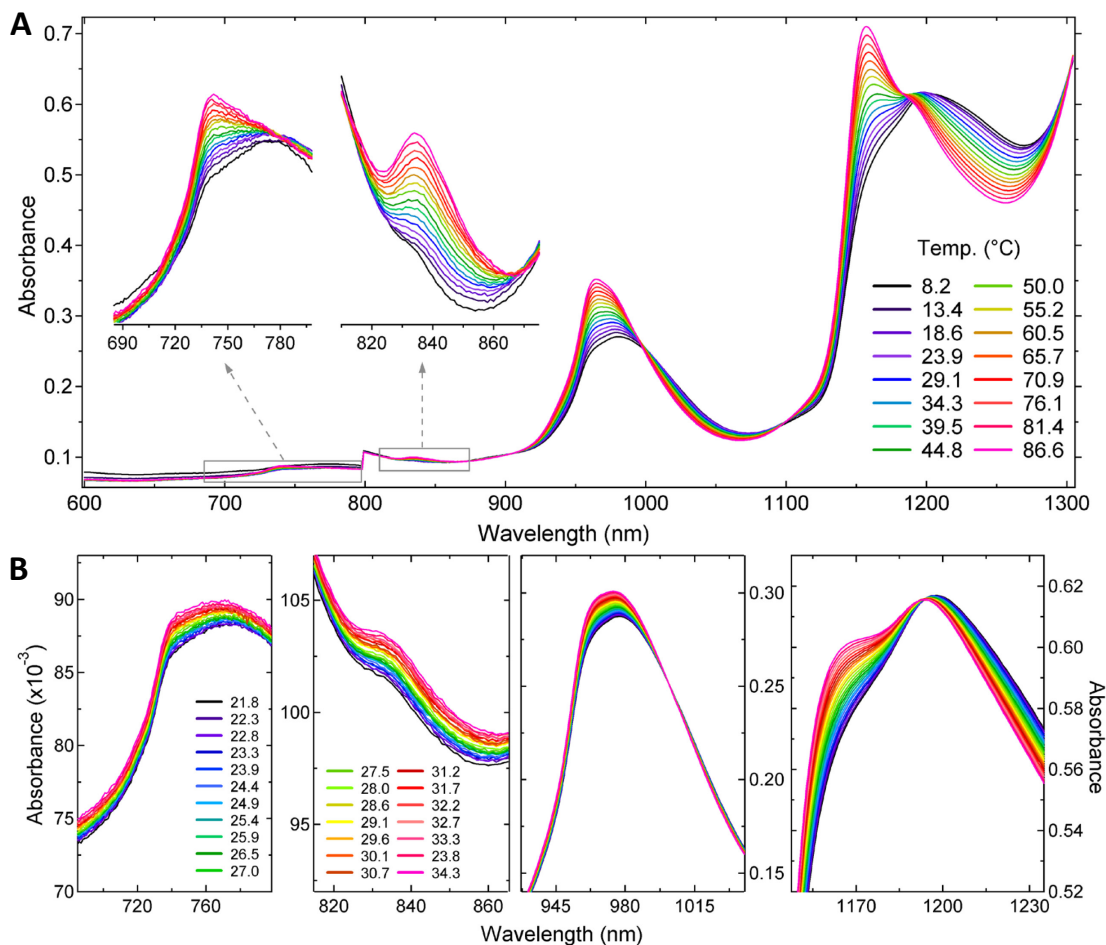


Figure 2.7: UV-Vis-NIR absorbance spectra for a 1% SDBS aqueous solution recorded at different temperatures (A). At 8.2 and 13.4°C condensation forms on the cell wall, slightly increasing absorbance across the entire region; thus these spectra are vertically shifted to accommodate the trend. Absorbance spectra of pure H₂O are shown for 0.5°C increments over the set temperature range 18-30°C in (B). All labelled temperatures are calibrated values.

lower frequencies (longer wavelengths).²⁵⁸ Observable absorbance bands for water within the examined wavelength range were assigned to certain possible combinations of these modes,^{257,258} occurring at approximately 740nm ($av_1 + bv_3$; $a + b = 4$), 835nm ($av_1 + v_2 + bv_3$; $a + b = 3$), 970nm ($av_1 + bv_3$; $a + b = 3$), and 1200nm ($av_1 + v_2 + bv_3$; $a + b = 2$), where a and b are integers with $a, b \geq 0$. These peaks were found to be sensitive to changes in temperature, particularly the peak at around 1200nm. The extent of this variation was quantified to identify a possible source of error within absorbance spectra of nanotube dispersions recorded with baseline subtraction, as these water peaks occur at positions that coincide with those of certain nanotube species (see the following section).

A water solution (also containing 1% SDBS, which does not absorb over the 700-1400nm range) was placed into the temperature regulated cell holder mounted in the Cary 5G and the cuvette was capped with a Teflon lid. Spectra were recorded at a number of set temperatures in steps of 5°C and are shown in Figure 2.7A. Note that all temperature values in this figure are given as calibrated values, which differ from the value that was set on the control electronics. Figure 2.7B shows the subtle differences in the spectra of pure water over smaller incremental temperature changes, which better reflect the temperature variation that may occur between the sample and reference solution. The peaks due to absorption of water shift to higher energy and become sharper with rising temperature. The current leading model for liquid water suggests that it is composed of a mixture of two different structures, known as ice-Ih (the common hexagonal structure associated with solid water) and ice-II (a rhombohedral structure).²⁵⁹ At low temperatures the more strongly bound ice-Ih structure dominates, however as the temperature is increased the equilibrium gradually shifts towards the ice-II species. As the hydrogen bond strength is reduced in the ice-II structure, the strength of the O-H bonds is correspondingly increased which results in the absorbance shifting to higher energy.²⁶⁰ The extent of the spectral shift is negligible in the 740, 835 and 970nm peaks over a temperature difference of around 5°C, however the peak at 1200nm shows some relatively significant changes. The temperature difference between the sample and its reference spectrum is not expected to be greater than approximately 2°C (due to temperature differences between laboratories), so the region from 1150-1240nm is the only segment of the spectrum that is likely to be affected. In some instances a small absorbance drop or increase could occur in this region due to temperature differences between the baseline and sample spectra, which would introduce errors into the analysis. This did not occur often, though the problem (if observed) could be rectified by simply re-scanning the reference spectrum after allowing the solutions to acquire equilibrium with the spectrometer room temperature.

2.3.5 Absorbance Spectra of Carbon Nanotubes

UV-Vis-NIR absorbance spectroscopy is a common technique for characterizing CNT dispersions and has the capacity to probe all species of nanotube simultaneously. A UV-Vis-NIR spectrum collected from the supernatant of a centrifuged solution of arc CNTs dispersed by 1% SDBS in D₂O is shown in Figure 2.8C. CNTs exhibit characteristic

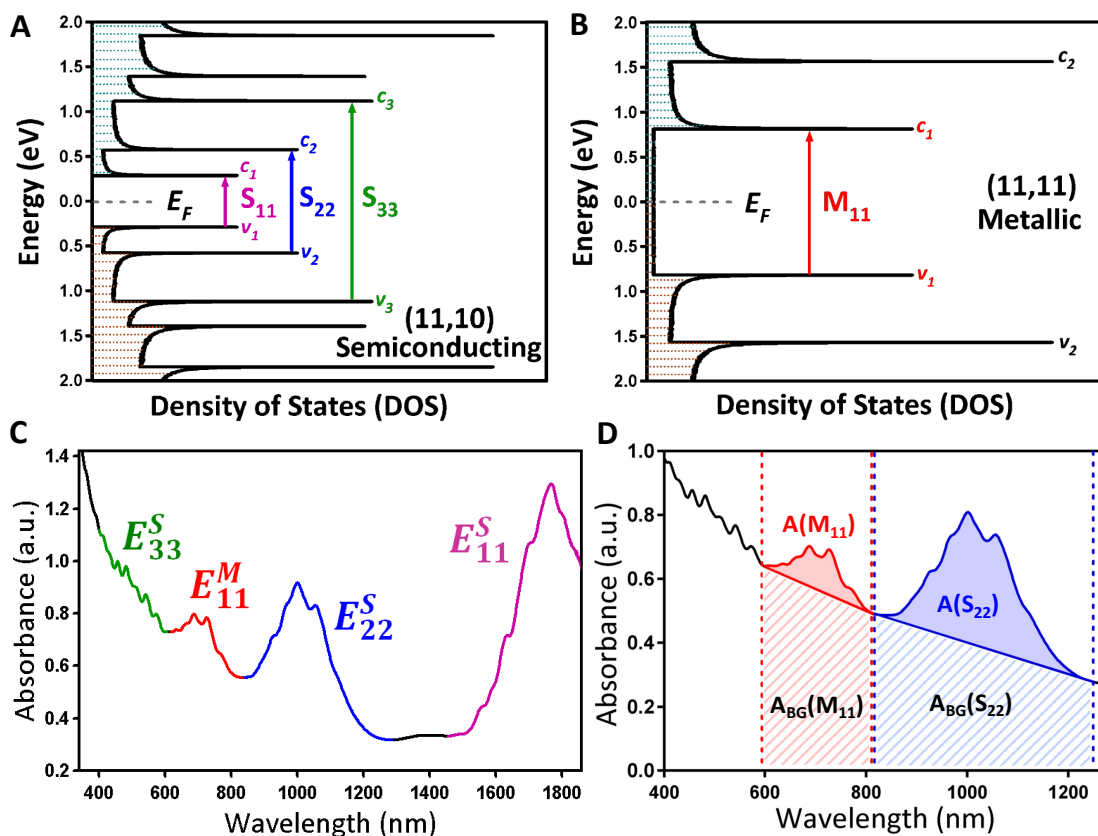


Figure 2.8: Theoretical DOS for semiconducting (11,10) (A) and metallic (11,11) (B) CNTs from the simple tight binding model showing the electronic transitions between van Hove singularities that may contribute to optical absorbance bands in the UV-Vis-NIR spectrum (C) of electric arc CNTs (dispersed in D₂O with the aid of 1wt% SDBS). The areal absorbance regions used for relative concentration and resonance ratio calculation are shown in (D).

absorbance peaks in their UV-Vis-NIR spectra, the origins of which are discussed in Section 1.1, and these peaks are identical in both D₂O and H₂O. Each individual species of nanotube possesses excitation transitions that occur at energies associated with its particular diameter, while these peaks are convoluted for a solution containing a mixed population of nanotubes and occur in bands as observed in Figure 2.8C. Since the observed excitonic transitions essentially coincide with electronic transitions predicted by the simple band model, the van Hove singularity based indexing scheme remains valid, thus the peaks are grouped according to their corresponding single particle transitions $E_{ii}^{S,M}$. The origins of these transitions according to the single-particle approach are displayed in Figures 2.8A and B for a semiconducting (11,10) and metallic (11,11) nanotube respectively. These particular species possess diameters and energy gaps of the appropriate order to be associated with the arc nanotube spectrum and are

potentially present in the dispersion. Since deconvolution of optical absorbance spectra allows for estimated assignments of nanotube species within an ensemble, this was performed for CNTs produced by both the arc discharge and HiPCO methods and is provided in Appendix B. The (11,10) nanotube was identified as being present in the arc CNT sample through its E_{22}^S absorption at $\sim 1.28\text{eV}$, while the presence of the metallic (11,11) species could not be verified due to a lack of available reference data (although it is likely to be a component species).

The nanotube absorption peaks are superimposed on top of broad absorptions due to plasmon resonances in the free electron cloud of the π electrons which occur in the conjugated structure of carbonaceous materials. These modes are centered in the ultraviolet region and include the π -plasmon (which is associated with the collective excitations of π electrons), appearing around 310-155nm (4.0-8.0eV), and the $\pi + \sigma$ plasmon (associated with all electrons) at approximately 125-40nm (10-30eV).²⁶¹ The π -plasmon is the most important of these modes as it is a major component in the baseline of the nanotube interband transition region. The π -plasmon may be split into two modes both parallel and perpendicular to the CNT axis, occurring close to 4.5 and 5.2eV respectively.^{262,263} The positions of these two peaks have been demonstrated to be dependent on the nanotube diameter²⁶¹ and aggregation state.²⁶⁴ Additionally, the peak at $\sim 4.5\text{eV}$ has been shown to depend on the dielectric environment, suggesting it may have a physical origin other than plasmon excitation.²⁶⁵ This absorption possibly arises from π - π^* interband transitions near the M point of the hexagonal Brillouin zone of graphene.²⁶⁶ The plasmon modes are best described by Lorentzian curves, hence their background contribution may be subtracted from the absorbance spectrum using a fitting procedure. One such study has used a single Lorentzian peak to approximate the plasmon absorbance and to simultaneously remove contributions from amorphous and particulate carbons,⁸⁹ as small carbonaceous particles are suggested to exhibit similar peaks in the UV region.^{96,267} Unfortunately, the maxima of the plasmon peaks lie below the surfactant absorbance edge of SDBS which precludes their characterisation within solutions of this dispersant.

When CNTs are dispersed in water the E_{11}^S (S_{11}) band is completely masked by solvent absorption from H_2O , while it is only slightly truncated by that of D_2O . Since all but a select few samples were dispersed in water, analysis of the absorbance spectra focuses on the semiconducting E_{22}^S (S_{22}) and metallic E_{11}^M (M_{11}) peak groups. For well-dispersed

nanotube solutions these peaks are more intense compared to the background, while peaks from distinct species become more resolved as a larger fraction of individual nanotubes is obtained. A broadening of the peaks is observed for more bundled suspensions and is accompanied by a red-shift in their positions.^{38,96,203} Additionally, as the exciton energies in nanotubes depend heavily on the strength of the Coulomb interaction, the precise energies of the optical transitions are influenced by the extent of dielectric screening in various solvents or with different adsorbed molecules.^{268,269} When the nanotube is encased by a dielectric medium, either a solvent or adsorbed molecule, the Coulombic interaction is weakened and the exciton energies are red-shifted. The mutual dielectric screening of nanotubes in a bundle is expected to be responsible for the red-shifts observed in aggregated CNTs,²⁷⁰ while a similar red-shift is also observed for the π -plasmon energy.²⁶⁴ It is therefore extremely important to take into account the local environment of the nanotubes when analysing optical absorption spectra of CNTs.

The peak areas of the S_{22} and M_{11} peak groups (centered at $\sim 1000\text{nm}$ and $\sim 689\text{nm}$ for SDBS dispersions, respectively) were used as measures of the relative amount of nanotubes dispersed. Although the Beer-Lambert law could be used to approximate CNT concentrations, measurement of the maximal absorbance intensity was avoided as it was observed to lead to exaggerated relative concentrations with the surfactants of larger molecular weight. This is expected to be due to an increase in the solution viscosity, leading to a greater amount of the non-nanotube carbonaceous material remaining in the supernatant for a fixed set of centrifugation parameters. Areal peak absorbance values were used to negate this effect and were obtained after subtraction of a linear background as shown in Figure 2.8D. This linear subtraction removes absorption due to the carbon π -plasmon, residual carbon particulates and other components that contribute to the background.^{89,271} Both S_{22} and M_{11} peaks were analysed, however since the CNT raw product contains approximately 2/3 semiconducting and 1/3 metallic nanotubes, results focus on the more intense semiconducting S_{22} peak as it has a greater signal. The M_{11} areal absorbance trends were also studied and were generally found to be equivalent to those of the S_{22} band (see Appendix C).

The values $A(S_{22})/A_{BG}(S_{22})$ and $A(M_{11})/A_{BG}(M_{11})$ depicted in Figure 2.8D (referred to as the $S_{22}:\text{BG}$ and $M_{11}:\text{BG}$ ‘resonance ratios’, respectively) are the areal ratios of the

nanotube peaks to the non-resonant background. The S_{22} resonance ratio value was used as an indicator of the aggregation state and composition of the solution, as it has been used previously as a relative measure of both dispersion state^{116,272} and purity^{98,271,273-275} in CNT solutions. As the background absorbance is expected to arise mainly from non-nanotube carbonaceous material, a larger such ratio may indicate a more ‘pure’ suspension in which the concentration of CNTs is enriched relative to that of the impurities.²⁷⁵ An increase in this value may also suggest a less aggregated sample, as the intensity of the nanotube peaks is expected to increase as the nanotubes become more disperse.²⁷²

Chemical functionalisation can have a strong impact on the strength of the transitions in the absorption spectrum.²⁷⁶ Covalent functionalisation of the nanotube sidewalls disrupts the periodicity of the lattice via the conversion of sp^2 -hybridised trivalent carbon atoms to sp^3 -hybridised tetravalent carbons upon the addition of moieties to the sidewall. These defect sites destabilise the band structure, resulting in the loss of available electronic transitions.²⁷⁷ It is therefore possible to monitor chemical reactions through the UV-Vis-NIR absorption spectrum, although both non-covalent (charge transfer) interactions and covalent attachment often produce similar effects.²⁴⁰ With non-covalent interactions the strength of the nanotube absorbance peaks may be altered as charge transfer or redox interactions between the adsorbate and the nanotube surface can occur.²⁷⁸ Such interactions may also have the effect of depleting the valence electrons or saturating the conduction band, which leads to the quenching of optical transitions.

Analysis of Spectra

Analysis of absorbance spectra, including peak background subtractions and area integration, was performed with IGOR Pro software (version 4.04, Wavemetrics, Inc., Portland, Oregon, USA). Macro functions were written to fit linear baselines between the endpoints of the M_{11} (600-816nm) and S_{22} (820-1250nm) regions and subtract the corresponding background signal from the spectral segment. The functions also return values for the integrated area above and below this baseline for the defined region which are used to calculate the resonance ratio. Peak positions were calculated using the inbuilt FindPeak algorithm which determines the location of the maximum from the smoothed first and second derivatives of a curve. As the data spacing is 1nm for the absorbance spectra, analysing the derivatives allows interpolation of peak positions at

intervals of less than 1nm. However, there is some error involved in this process, thus a peak shift of at least $\pm 0.5\text{nm}$ should be observed for the result to be significant.

2.4 Raman Spectroscopy

2.4.1 Theory

Raman Spectroscopy is an analytical technique based on the Raman effect, which is concerned with the inelastic scattering of photons.²⁷⁹ When light is incident on a material most photons undergo elastic scattering, or Rayleigh scattering, where there is no energy exchange between the photon and the sample and hence the scattered light remains at the same energy as the incident radiation. However, a small number of photons (approximately 1 in 10^7) may exchange energy with the material such that the energy of the scattered light is shifted slightly with respect to the incident photon energy.^{279,280} This exchange interaction may occur with a rotational, vibrational or electronic transition of the sample system, though for the most part signals observed in Raman spectroscopy are the result of scattering through coupling with a vibrational state or phonon.

Raman scattering occurs when the incident radiation excites the sample system from its ground state or a low lying energy level to an intermediate state at a virtual energy level, where subsequent relaxation through emission of a photon may return it to a different energy state than its original one (see Figure 2.9).²⁸⁰ If the final state of the sample system is more energetic than the initial state, i.e. energy is absorbed by the material, then the re-emitted (scattered) photon is of lower energy than the incident light and hence its frequency is downshifted. This is referred to as a Stokes shift. Conversely, if the final state is of lower energy than the initial state then the scattered photon possesses greater energy and frequency than the incident radiation, which is known as an anti-Stokes shift.²⁷⁹ Inelastic Stokes and anti-Stokes scattering interactions with vibrational levels in a sample will therefore produce peaks on either side of the elastic Rayleigh peak in a Raman spectrum. Additionally, since the shifts are defined by the vibrational energy levels of a particular system and are not dependent on the scattering process, the dispersion will be symmetric about the Rayleigh line. Stokes scattering is generally much more intense than anti-Stokes as the ground state of a system is usually more

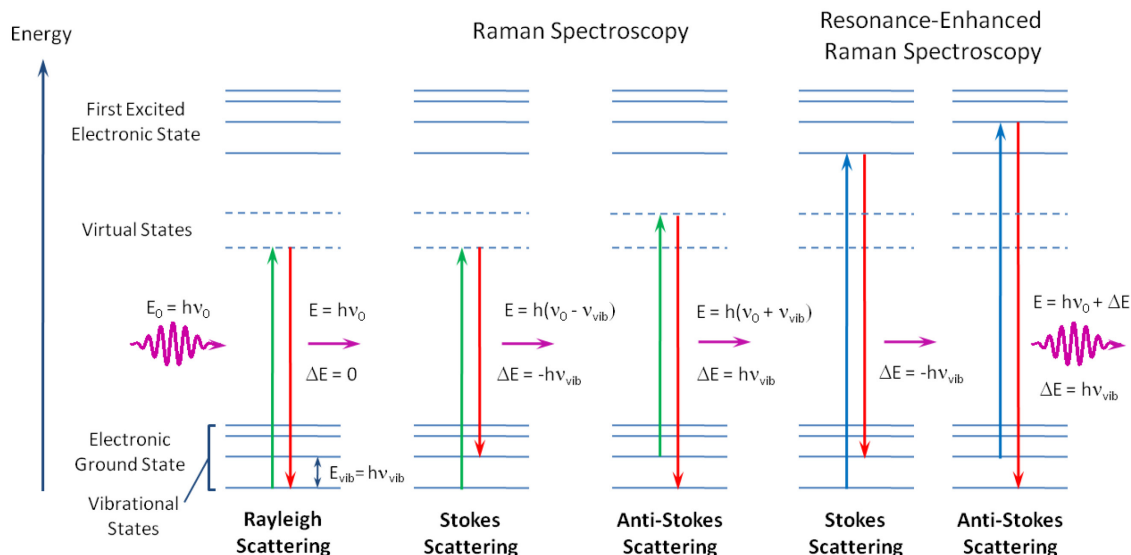


Figure 2.9: Scattering processes in Raman spectroscopy.

populated than the higher energy excited states, while both are extremely weak compared to the Rayleigh process.²⁸⁰ However, if the energy of the incident radiation matches a real energy state of the system, a resonance-enhanced Raman effect is observed where the intensity of the Raman spectrum may increase approximately one-thousand fold compared to the non-resonant case.¹⁹ This enhancement effectively overwhelms the signal that may be generated from other non-resonant Raman scattering transitions in a many-component system, thus for CNTs where multiple species may be present only those that are resonant with the incident light produce a dominant spectrum. The change in energy due to scattering interactions is usually reported in terms of the frequency shift (in wavenumbers) with respect to the incident photons, referred to as Raman shift.

2.4.2 Instrumentation

Raman spectra of CNT dispersions and films were recorded on a WITec α -300 confocal Raman spectrometer (WITec, Ulm, Germany) utilizing a 2.33eV (532nm, frequency doubled from 1064nm) Nd:YAG laser or 1.58eV (785nm) diode laser coupled to a Nikon 40x objective with a numerical aperture of 0.6. A schematic of this instrument is shown in Figure 2.10. Each laser requires a separate spectrometer/detector attachment and fibre coupling unit, the interchange of which is not trivial. Two gratings (possessing different line spacings) are housed within each spectrometer setup, one capable of

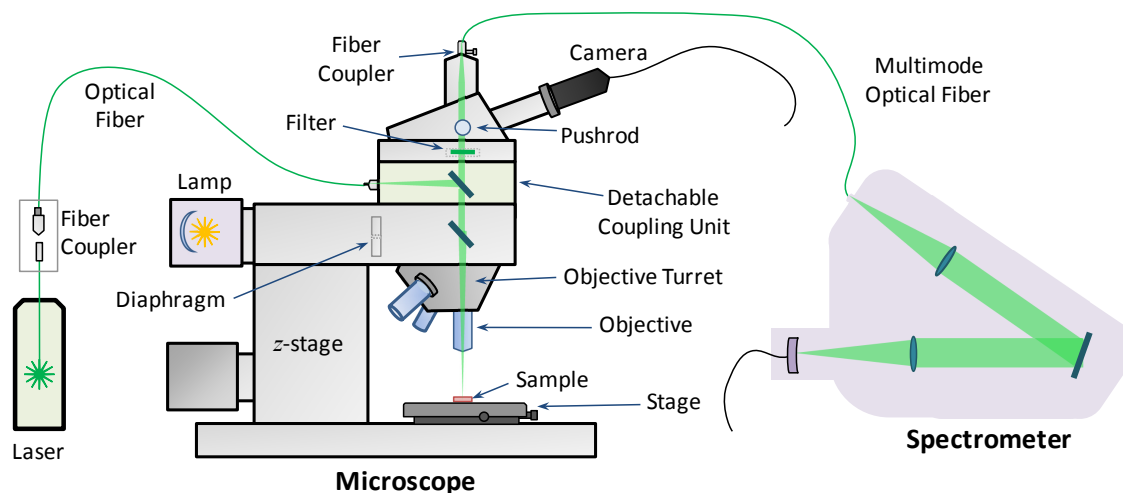


Figure 2.10: Schematic of the Witec α -300 confocal Raman spectrometer.

recording a broad-range spectrum and another allowing higher resolution scans for regions of fixed width. For both lasers a grating with 600lines/mm provides the broad scan, while grating densities of 1200 and 1800lines/mm afford higher resolution scans for the 1.58eV and 2.33eV setups respectively. Selecting the higher grating density enables more accurate determination of peak positions and spectral widths, however this is accompanied by a significant decrease in the Raman signal as the same number of scattered photons are split into a larger number of detection bins.

2.4.3 Experimental Details

For solution phase spectra 0.2mL aliquots of the samples were placed into makeshift sample holders fashioned from plastic vial lids and placed under the objective. The focal plane of the laser was generally aligned from 20-100 μ m below the solution surface depending on the length of the integration time. Integration times of 1-30 seconds were used while multiple (4 to 20) accumulations were taken for each spectrum. Lower focal depths were applied in the case of longer integration times as slow evaporation of the solution could eventually lower the air-water interface below the focal plane, resulting in a loss of Raman signal. Though aqueous dispersions of CNTs have a greater capacity to dispense the heat generated by interaction with the laser beam and may therefore be examined at higher laser powers than nanotube films, the rate of evaporation is increased under photon irradiation. For this reason the laser power was always adjusted at the beginning of an experiment such that maximum signal was obtained at \sim 20 μ m

below the solution surface, but was not further increased once the maximum signal was obtained. The laser power was not precisely controlled between experiments due to the inaccuracy of the controlling system (power is set by a manual wind-up knob), however spectra of samples in any given series were recorded at the same laser power.

For spectra recorded from solid state samples much lower power was used to prevent combustion of the CNT films. 10 second accumulations were recorded for at least 10 unique locations within the film as the spectra of solid materials can vary significantly with position.²⁸¹ The focus was optimised for the G-band intensity at each position before collection of the data.

2.4.4 Baseline Raman Spectra of Water and SDBS

Figure 2.11 shows the Raman spectra of water along with that of a 0.5% SDBS aqueous solution collected at an excitation energy of 2.33eV. The Raman spectrum of water over the studied region possesses a single major feature associated with the fundamental O-H stretching modes which produce a broad peak from 3000-3700cm⁻¹,²⁸² while a smaller peak due to the O-H bending mode is also observed at 1645cm⁻¹. At low wavenumber a translational mode of water produces a peak at around 160cm⁻¹,²⁸³ the tail of which is cut off by the Rayleigh filter. Broad low-energy peaks due to librations (rocking motions in which the molecule repeatedly rotates slightly back and forth) occur at frequencies around 430, 650 and 795cm⁻¹,²⁸³ though the precise energies of these modes vary among reported literature.²⁸⁴ The libration modes L₁, L₂ and L₃ are jointly responsible for the increase in Raman signal at low wavenumber, while the broad peak centred at approximately 2120cm⁻¹ is a combination mode of the O-H bend and these oscillations. The sharp peaks at approximately 480 and 2435cm⁻¹ arise from photons emitted by the fluorescent lights illuminating the laboratory, being present in spectra recorded without a sample and with the laser shuttered but absent when the lights are turned off (Figure 2.11C). As these peaks are not located in positions associated with those of CNTs it was not considered necessary to collect all Raman spectra in the dark. The Raman spectrum of SDBS includes all peaks present in that of water along with many additional vibrational peaks in the region 900-1500cm⁻¹ which are expected to be related to C-C, C-H, S=O and S-O⁻ bonds present in the aliphatic chain and sulfonate headgroup of the surfactant, while the small peak at 1605cm⁻¹ superimposed on the ν_2 band is expected to be related to the aromatic ring of SDBS.²⁸⁰ The peaks due to SDBS

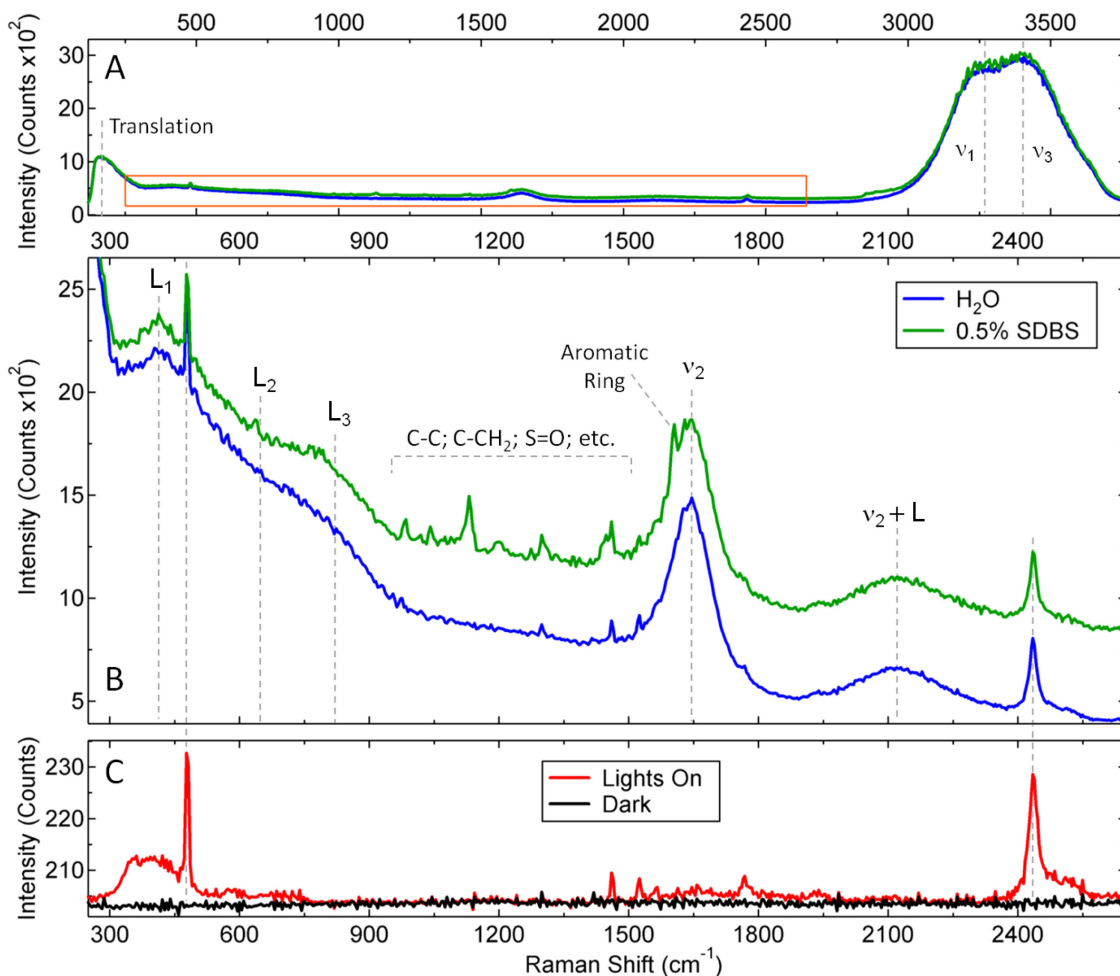


Figure 2.11: Unmodified Raman spectra for (A) 30x10s accumulations of water (blue) and 0.5% SDBS in aqueous solution (green), and (B) 15x60s accumulations of the same samples showing lower energy librations and vibrational modes of water. 30x10s spectra recorded without laser illumination and no sample present are shown in (C), where fluorescent lights produce a Raman signal (red). All spectra were collected at an excitation energy of 2.33eV.

are generally insignificant on the scale of the CNT spectrum (see Figure 2.12 and the following section), however peaks associated with water appear in regions corresponding to the radial breathing mode and G-band and consequently must be accounted for. The presence of SDBS also raises the background signal compared to that of water, possibly due to a weak fluorescence signal produced by the surfactant. Therefore, to compare Raman intensities between spectra from nanotube samples a baseline spectrum was manually subtracted using Fityk²⁸⁵ software (freeware; version 0.8.0 or 0.9.7) by selecting points along the background signal, as shown in Figure 2.12 for an SDBS-based CNT dispersion. This baseline removal allows nanotube peak intensity trends to be compared within a sample series, however contributions from

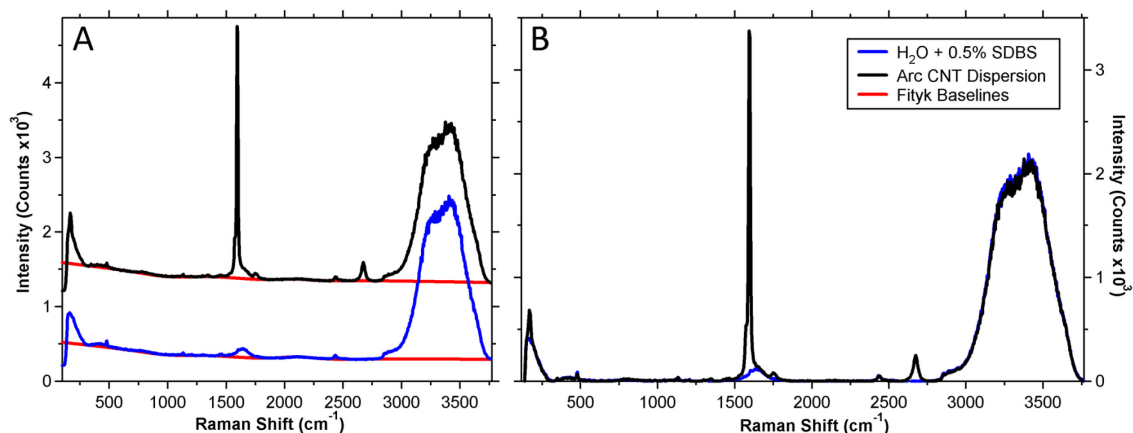


Figure 2.12: Subtraction of baselines from the spectrum of 0.5% SDBS and arc CNTs dispersed in this surfactant (A) and the overlain background subtracted spectra (B). In panel (A) the CNT spectrum and its associated baseline are offset vertically by 1×10^3 counts.

water peaks at ~ 160 and $\sim 1645 \text{ cm}^{-1}$ remain embedded in the Raman spectra of the CNTs. For the majority of analyses these were not removed for trend evaluation as the contributions from water are expected to be close to equal across solutions within each sample series.

2.4.5 Raman Spectrum of Carbon Nanotubes

Raman spectra of arc nanotubes dispersed in 0.5% SDBS are shown in Figure 2.13 for both excitation energies, displaying peaks that are characteristic of CNTs as well as the intense Rayleigh peak due to elastic scattering. An edge filter is employed to reduce the intensity of the radiation that has not undergone any Raman shift which results in the sharp decrease in the intensity at low wavenumbers (around 130 cm^{-1}). The Rayleigh peak position was shifted to zero as a calibration offset, as it generally deviated by 4 to 8 cm^{-1} from this expected value. The offset was determined using the half-width of the peak base rather than the maxima as Rayleigh scattering often saturates the detector, despite being filtered. The magnitude of the offset was found to vary with the different spectrometer and grating combinations, though it was usually consistent for any spectra recorded with the same grating within a particular session. Hence, for spectra recorded with the high resolution grating that did not encompass the Rayleigh peak, the offset value from a region recorded in the same session (in which the Rayleigh peak was visible) was applied. This method was also checked for a silicon calibration sample and found to be valid.

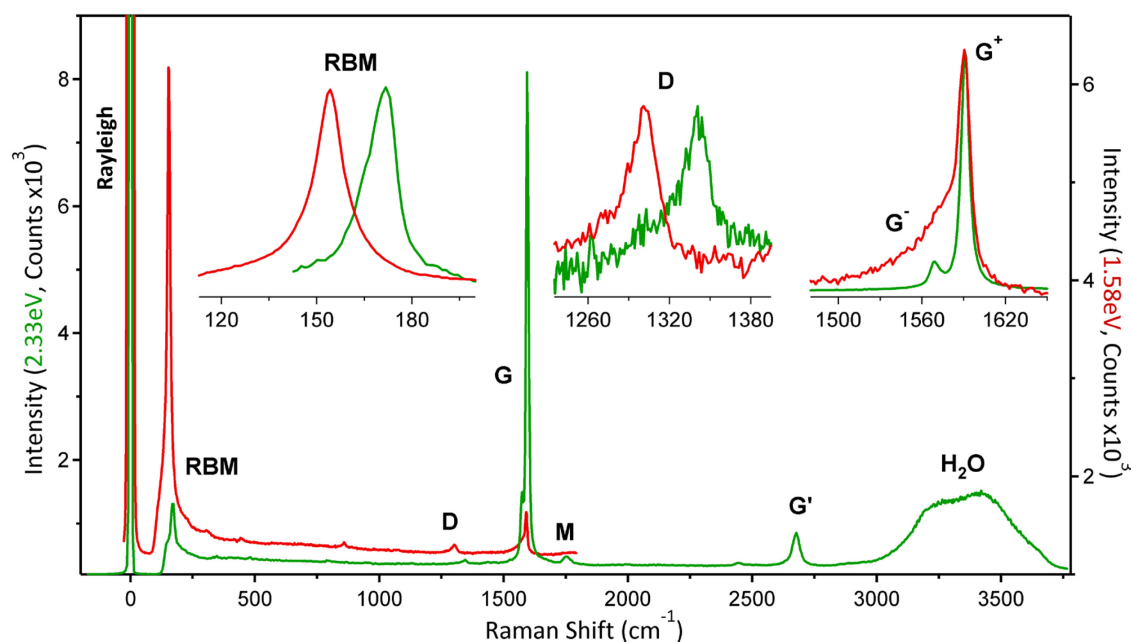


Figure 2.13: Raman spectra of arc nanotubes dispersed by 0.5wt% SDBS in water, recorded at excitation energies of 2.33eV (green) and 1.58eV (red) with a 600line/mm grating. Enlargements of the RBM, D and G regions of the spectra are shown as insets, with the 1.58eV RBM recorded at 1200lines/mm and all 2.33eV enlargements recorded using the 1800line/mm grating. The Rayleigh scattering peak was shifted to 0cm^{-1} as a calibration offset for each spectrum.

Peaks typically observed in the Raman spectra of CNTs are labelled in Figure 2.13. The radial breathing mode (RBM) arises from expansion and contraction of the nanotube about its central axis and is directly related to the nanotube diameter via the relation $\omega = A/d + B$, where ω is the frequency of the RBM, d is the nanotube diameter, A is a constant of proportionality and B is a constant related to the surrounding environment.^{19,37,286-288} The values of these constants vary considerably within literature as the values of both A and B are substantially influenced by the environmental state of the sample.²⁸⁹ Additionally, only a sub-population of nanotube species will be resonant with a particular laser energy, and these constants can depend on the nature of the dominant species, be they metallic or semiconducting. Using the values of A and B reported by Cheng *et al.*,²⁹⁰ specific diameters of CNTs used in this work may be estimated from RBM peak maxima. Approximate diameters $d \approx 1.43\text{nm}$ and $d \approx 1.59\text{nm}$ were determined from RBM frequencies $\omega = 172\text{cm}^{-1}$ and $\omega = 154\text{cm}^{-1}$ at 2.33eV and 1.58eV respectively.

The disorder induced mode D, a dispersive mode occurring around 1340cm^{-1} for 2.33eV and 1300cm^{-1} for 1.58eV excitation, is due to a second order scattering process and is

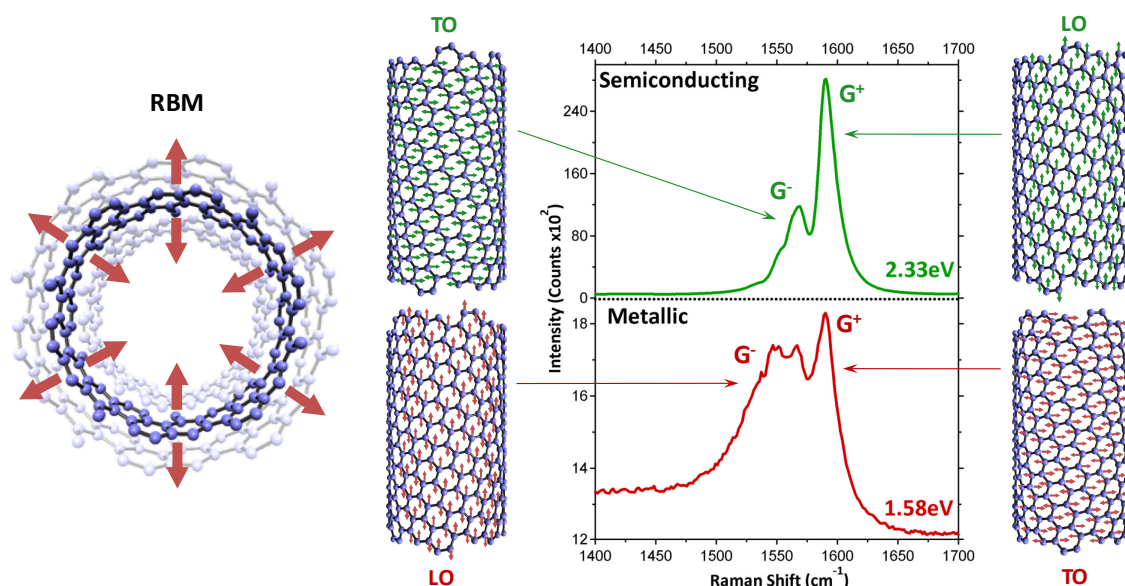


Figure 2.14: Left: Diagram depicting the expansion and contraction vibration responsible for the radial breathing mode. Right: Phonons related to the G-band in CNTs. The split G-band components G⁺ and G⁻ arise from LO and TO modes in semiconducting nanotubes, respectively. For the G-band of metallic nanotubes the corresponding phonons are reversed. Raman spectra were recorded from a CNT film formed via vacuum filtration of an SDBS-based dispersion.

enhanced by the presence of defects in the nanotube structure.^{19,281} The G-band at 2.33eV may be split into the G⁺ ($\sim 1590\text{cm}^{-1}$) and G⁻ ($\sim 1570\text{cm}^{-1}$) modes arising from in-plane vibrations along the nanotube axis (longitudinal optical, or LO) and around the circumference of the nanotube (transverse optical, or TO), respectively.²⁹¹ The assignment of vibrational modes in the G-band for metallic nanotubes is suggested to be reversed compared to the semiconducting case, with the G⁺ peak attributed to the circumferential TO mode and the G⁻ peak arising from the axial LO phonon as depicted in Figure 2.14.^{291,292} The G⁺ mode is analogous to the in-plane scattering mode from graphite and is a first order peak, hence it is independent of the presence of defects. Consequently, the intensity ratio between the D and G⁺ peaks, I_D/I_{G^+} (I_D/I_G) or D:G, is often used to monitor the defect density and chemical modification of CNTs.²⁸¹ Since the D band is also enhanced by the presence of amorphous carbon this ratio reflects the purity of the CNT sample to some extent.^{271,274}

The G⁻ mode is sensitive to nanotube diameter, while its line-shape may also indicate whether the CNTs present are metallic or semiconducting in nature. In this case, semiconducting nanotubes are probed at 2.33eV, while metallic nanotubes are resonant at 1.58eV as observed by the broadening of the G⁻ band from a Lorentzian to a Breit-Wigner-Fano (BWF) line shape.¹⁹ This BWF shape is proposed to arise from a

resonance between surface plasmons and the TO phonon in metallic CNTs.²⁹² However, recent results have shown that the BWF feature of the G⁻ band does not occur in armchair nanotubes, thus its presence indicates resonance with transitions of quasi-metallic nanotubes with non-zero energy gaps in their band structure.^{181,293} The position, width and intensity of the BWF feature in the G⁻ peak for such metallic nanotubes has been shown to be dependent on both bundle size and chemical functionalisation, as well as charge transfer and doping.²⁹⁴⁻²⁹⁶

Additional peaks in the Raman spectrum include the M band, which is an overtone of an out-of-plane mode from graphite ($\sim 1750\text{cm}^{-1}$), and the G' band which is a second harmonic of the D band (thus sometimes designated 2D), but is less sensitive to defects, occurring at approximately $\sim 2670\text{cm}^{-1}$.¹⁹

2.5 Atomic Force Microscopy (AFM)

2.5.1 Theory and Instrumentation

In atomic force microscopy (AFM) forces acting between a probe and a sample are used to examine the topography of a surface. The probe consists of a cantilever with a sharp tip at one end, having a radius of curvature on the order of nanometres.²⁹⁷ When the probe and surface are brought into close proximity interactions between the tip apex and the sample cause deflection of the cantilever, thus precise measurement of the cantilever position can produce a surface image. This displacement is usually measured using a laser reflected off the rear surface of the cantilever into a split photodiode. In static (contact) mode AFM, the probe tip is brought into contact with the surface and rastered across it, hence the topography of the surface may be measured directly through displacement of the cantilever.²⁹⁸ However, in this mode of operation the tip may scratch soft surfaces or shift loosely adsorbed particles, thus dynamic (non-contact) modes of AFM are often employed in cases where this is likely to occur. In non-contact mode the cantilever-tip assembly is vibrated by a sinusoidal drive signal sent to a piezoelectric transducer on which it is mounted. The drive frequency is tuned to a value slightly offset from the fundamental resonance frequency of the cantilever such that the oscillation amplitude is close to maximised and is typically around 10nm.²⁹⁹ The tip is then brought within close range of the surface such that tip-sample interactions act to

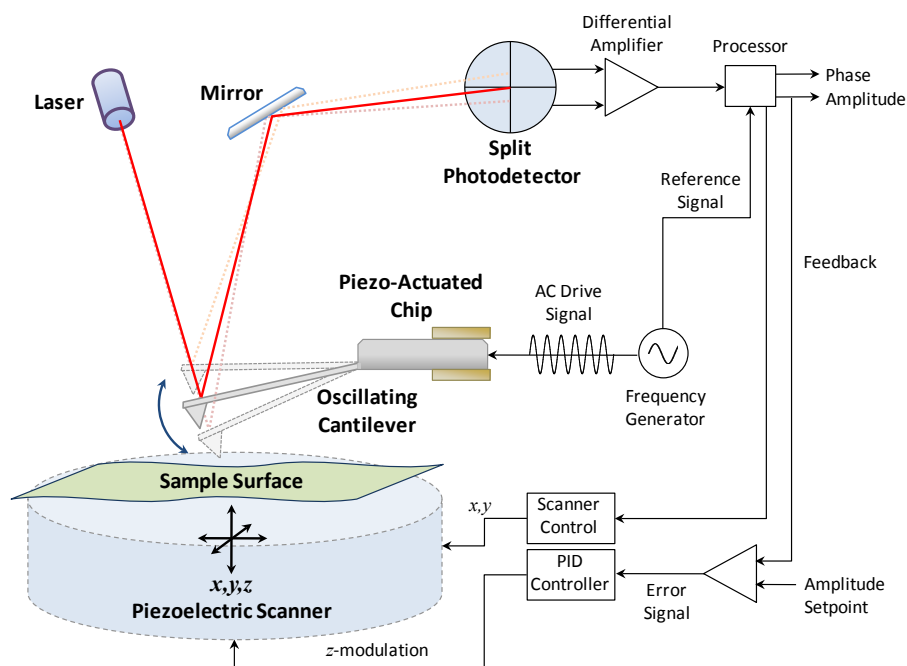


Figure 2.15: Schematic of an atomic force microscope operating in tapping mode. Surface topography is mapped through the change in oscillation amplitude of a cantilever due to interaction with the surface, which is measured by the displacement of a laser beam reflected off the back of the cantilever. A piezoelectric scanner rasters the sample in the x,y plane while a feedback loop controls the z height in order to maintain a constant oscillation amplitude.

shift the frequency and amplitude of oscillation, which is used in a feedback loop as an error signal with respect to the input drive signal. The tip-sample interaction distance (z -scanner height) is modulated to compensate for this error signal in order to maintain constant amplitude (or frequency), thus the sample topography is mapped by the differential z -scanner signal.³⁰⁰ Under ambient conditions a water meniscus bridge may form between the tip and the surface which can interfere with the measurement of non-contact interaction forces.²⁹⁸ The use of a dynamic mode in which the oscillation amplitude is relatively large, known as tapping mode, can prevent this layer from forming.

As with non-contact mode AFM, in tapping mode (or intermittent contact mode) the cantilever is oscillated close to its resonant frequency. In this case the vertical oscillation of the cantilever is on the order of 20-100nm, and once the tip and surface are engaged the tip contacts the surface periodically.²⁹⁸ The amplitude of vibration of the oscillating cantilever decreases due to this cyclic repulsive contact between tip and surface. Again, through feedback control the z -scanner position is adjusted to maintain constant oscillation amplitude as the probe is scanned across the sample, generating a

height image. As the amplitude and phase of the cantilever signal also change with respect to the drive signal, topographic images based on these parameters may also be generated. A simple diagram of an AFM instrument operating in tapping mode is depicted in Figure 2.15.

2.5.2 Experimental Details

To examine the morphology of nanotube dispersions by AFM it was first necessary to transfer the CNTs from solution to a surface. Several methods were tested, including drop casting, immersion and spin coating. Spin casting onto silicon wafers was found to be the most effective technique and was performed as outlined in Section 2.6.1. Topographic height and amplitude images of the wafers were collected with a multi-mode head and Nanoscope IV controller (Digital Instruments, Veeco, Santa Barbara, California, USA) operating in tapping mode. The instrument was updated to a Nanoscope V controller operating with version 8 of the control software during this work. Both E (maximum $10 \times 10 \mu\text{m}$ x,y scan area) and J (maximum $125 \times 125 \mu\text{m}$) scanners were employed to record images of 512×512 pixels over an area either $8 \times 8 \mu\text{m}$ or $5 \times 5 \mu\text{m}$ in dimension. Scan rates of 0.5-1Hz were used, with the maximum scan speed being $16 \mu\text{m} \cdot \text{s}^{-1}$ for any acquired image. Generally the integral and proportional gains were set to 0.2 and 0.4 respectively for the Nanoscope IV controller, while these were increased to 1 and 5 for the Nanoscope V controller. Si tips (NSC15, Mikromasch, San Jose, California, USA) possessing typical tip radii of approximately 10nm and resonant frequencies around 320kHz were employed under ambient conditions, where an offset of 5% from the peak resonant frequency was applied to the drive signal. An example image of nanotubes on a silicon substrate recorded with the scanner z -height, oscillation amplitude and phase channels is shown in Figure 2.16. The height image was analysed for length and diameter measurements in all cases, however the phase and amplitude images could be used to optimise the drive voltage within the feedback loop.

All height images were levelled by x,y -plane fit (3rd order) and flattening (0th order) algorithms before length or diameter measurements were taken. CNT lengths were measured manually in ImageJ³⁰¹ (version 1.42) using segmented line traces, while NanoScope Analysis software (version 1.20, Veeco Instruments Inc.) was used to determine the associated diameters via the section tool. Diameter values were extracted through the parameter R_{max} which returns the difference in height between the highest

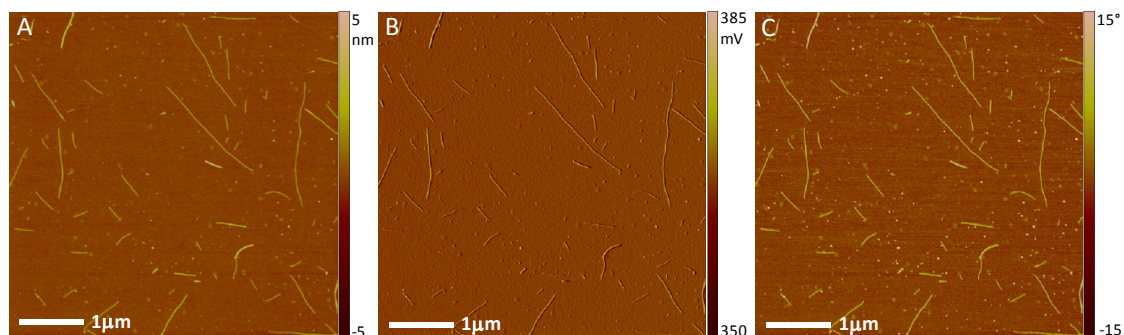


Figure 2.16: A $5 \times 5 \mu\text{m}$ AFM image of single-walled nanotubes deposited on a silicon wafer collected for height (A), amplitude (B) and phase (C) channels simultaneously. The image is 512×512 pixels and was recorded at a scan speed of 0.6 Hz ($6 \mu\text{m} \cdot \text{s}^{-1}$) using the Nanoscope V controller.

and lowest points within the marked region of the cross-section. $8 \times 8 \mu\text{m}$ images were typically used for length measurements, while diameters were determined from $5 \times 5 \mu\text{m}$ images to reduce the error in height measurement.³⁰² For simultaneous length and diameter analysis $8 \times 8 \mu\text{m}$ images were used.

2.6 Other Techniques

2.6.1 Spin Coating

Theory

Spin coating is a procedure used to deposit uniform coatings of materials on flat substrates in the form of a thin film. The basic process involves a solution being placed onto the substrate which is then rotated on the order of thousands of revolutions per minute, where the influence of the centrifugal force causes the fluid to spread out evenly over the surface. Under continuous rotation excess fluid is spun off the edges of the substrate causing a uniform reduction in the layer thickness,³⁰³ while simultaneous thinning of the film occurs through evaporation of the solvent.

The spin coating process can be divided into four separate stages, as shown in Figure 2.17: (1) deposition of the solution onto the substrate, (2) acceleration of the substrate up to its nominal rotation speed, (3) rotation at constant speed where thinning of the liquid layer is dominated by fluid viscous forces, and (4) rotation at constant speed where the thinning is dominating by solvent evaporation. The last two stages generally overlap, especially if the solvent is highly volatile.³⁰⁴

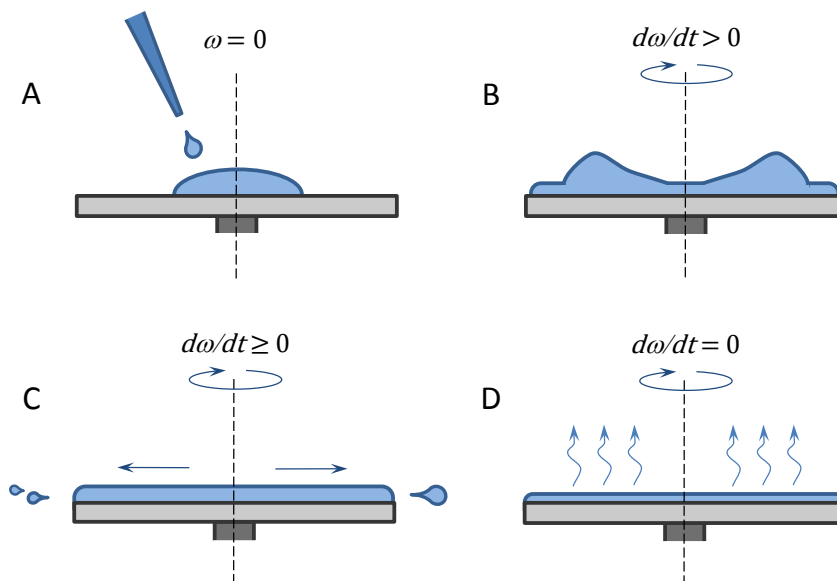


Figure 2.17: The spin coating process; (A) deposition, (B) acceleration, (C) steady rotation dominated by viscous forces, and (D) steady rotation dominated by solvent evaporation.

While spin coating has been primarily used for deposition of polymer or photoresist layers, the technique has also been demonstrated to provide films of well dispersed particulate material from colloidal suspensions. Transparent and conducting films of CNTs may be produced through spin coating of surfactant stabilised suspensions.³⁰⁵ At low concentrations, the individual nanotubes are not interconnected which allows measurement of their lengths through AFM.^{306,307}

Experimental Details

To prepare nanotube coated surfaces, Si wafers (phosphorous(n)-doped, (111), resistivity $10\text{-}20\Omega\text{cm}^{-1}$) were cut into small segments approximately 1.5 by 1.5cm in size. These flat surfaces were washed thoroughly with water, acetone and ethanol then dried by a stream of nitrogen. $25\mu\text{L}$ aliquots of the CNT dispersions were deposited onto the wafers before spinning at 1000rpm using a WS-400-6NPP-LITE spin coater (Laurell Technologies, North Wales, Pennsylvania, USA) for 30 seconds. This step was followed by consecutive operation at 2000rpm for an additional 30 seconds to remove excess fluid before allowing the samples to dry. The surfaces were subsequently rinsed with a copious amount of water to remove the residual surfactant layer and blown dry with N_2 before imaging with AFM.

2.6.2 Transmission Electron Microscopy (TEM)

Theory

Electron microscopy uses the interactions of a focussed electron beam with a sample to produce an image. The resolving power of electron microscopes is facilitated by the wavelengths of the electrons used for imaging, which are substantially smaller than those of visible light.³⁰⁸ This allows sample features to be distinguished well below the limit of conventional optical microscopes, however the experiments must be conducted under vacuum. In transmission electron microscopy (TEM) the electron beam is commonly produced through thermionic emission from a tungsten filament or lanthanum hexaborate source and subsequently accelerated by an anode (typically by a potential greater than 100keV) down the optical axis.³⁰⁹ The incident beam is focused by an electromagnetic condenser lens (or multiple lenses) onto the sample, where it is partly transmitted or scattered by the sample depending on its composition. This interaction produces an image within the intensity profile of the electron beam. The image is magnified by an objective lens and further by a series of intermediate and projector lenses before the beam strikes a fluorescent shield, facilitating visual observation of the sample.³⁰⁰ This shield may be removed to expose the beam to a camera that records the image. A schematic diagram of a TEM instrument is shown in Figure 2.18.

Experimental Details

TEM images of CNT films were collected in order to evaluate the relative metal content of nanotube samples. The films were prepared by vacuum filtration of CNT dispersions over 0.22 μ m polytetrafluoroethylene (PTFE) membranes (Millipore, Sydney, Australia) using acetone to flocculate the nanotubes, followed by excessive washing with H₂O to remove residual surfactant. Without acetone flocculation, shorter CNTs may be carried into or through the filter membrane by the surfactant.¹⁶⁴ The films were then dried in an oven at 80°C for several hours. Segments of the films were placed in ethanol solution and briefly bath sonicated to break them apart. Exfoliated film fragments were transferred to lacy-carbon coated copper grids via droplet addition of the ethanol solution. Images were collected on a Philips CM 200 microscope operating with an accelerating voltage of 200keV. These experiments were performed at Adelaide

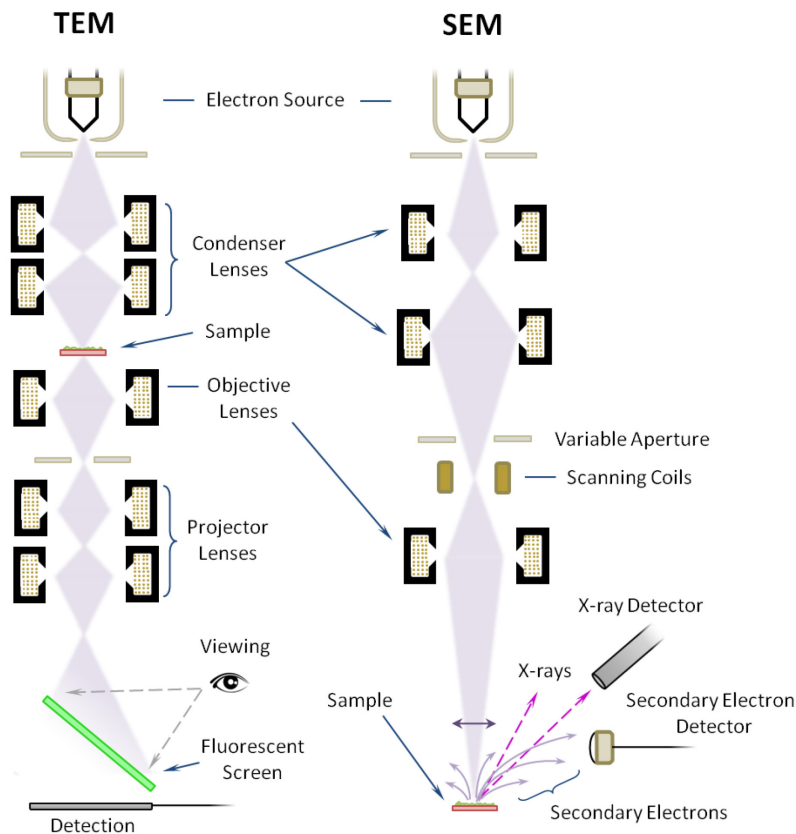


Figure 2.18: Schematic representations of both transmission (left) and scanning (right) electron microscopes.

Microscopy, located within The University of Adelaide (Medical School North, basement level, Frome Rd. Adelaide SA 5005).

2.6.3 Scanning Electron Microscopy (SEM)

Theory

Similar to TEM, in an SEM instrument (Figure 2.18) an electron beam is also generated from a heated filament or a field emission tip. The electrons are accelerated by an electric potential on the order of 500eV to 30keV and are directed down a column towards the sample stage, confined to the optical axis by condenser lenses.³⁰⁸ The electron beam is tightly focused to a spot by an objective lens while scanning coils raster it across the sample surface. Electrons from the incident beam may pass part of their energy to bound electrons within the sample upon collision with the surface. The electrons to which this energy is imparted are able to escape the sample surface and are known as secondary electrons, being ejected from the sample with a certain kinetic

energy obtained from the collision process. The secondary electron yield may be recorded as a function of the primary electron beam position, producing an image of the sample. The low energy (around 20eV) possessed by the secondary electrons allows only those close to the sample surface to reach the detector, thus the technique is surface sensitive.³⁰⁹

Experimental Details

Segments of CNT films prepared in the same manner as those for TEM were attached to aluminium stubs using conductive carbon tape. Images of the films were collected at Adelaide Microscopy using a Philips XL30 SEM with a field emission source at an accelerating voltage of 10kV.

2.6.4 Energy Dispersive X-Ray Spectroscopy (EDX)

Theory

The production of secondary electrons that occurs in SEM (and in TEM) is also accompanied by the generation of X-rays. When an electron in the sample is ejected through collision and energy transfer with an electron in the primary beam, a bound electron in a higher energy level of the atom it escaped from may relax to fill the now unoccupied energy level as shown in Figure 2.19. This transition results in the evolution

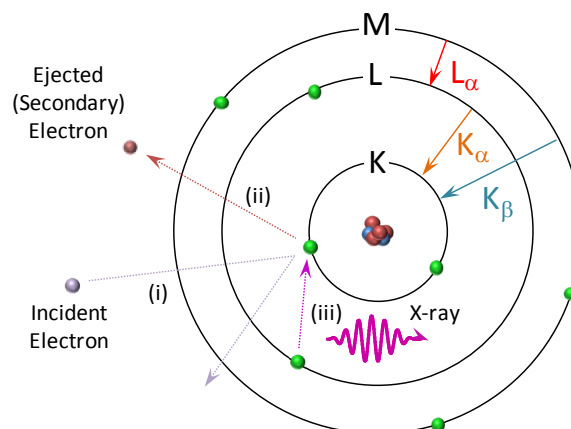


Figure 2.19: Production of secondary electrons and X-rays from interaction with the incident electron beam; incoming electrons (i) collide with inner-shell electrons and eject them from the atom (ii). An electron from a higher energy level then decays to the empty lower state through emission of an X-ray (iii) possessing an energy characteristic of the band separation. In this example the X-ray corresponds to a K_{α} transition.

of an X-ray possessing an energy equal to that of the spacing between the bands of the atom from which it was emitted, and these energies are unique for atoms of each element.³⁰⁸ Consequently, analysis of the X-rays produced by electron irradiation of a sample is able to provide information about its elemental composition and is known as energy-dispersive X-ray spectroscopy (EDX). X-rays produced by electronic transitions between the M and L electronic levels are labelled as L_{α} , while those from the L and M shells to the K level are designated as K_{α} and K_{β} respectively.³⁰⁸

Experimental Details

The metal content remaining in the centrifuged nanotube dispersions was assessed by EDX of CNT films produced via vacuum filtration as per TEM and SEM studies. In this case film fragments were baked onto Al stubs at $\sim 80^{\circ}\text{C}$ for around 20 minutes after wetting with H_2O to facilitate adhesion. Both carbon and copper-based double-sided conductive tapes were avoided as they were found to produce an X-ray signal which would interfere with EDX analysis, while the adhesive could potentially leach into the sample. EDX was performed on a FEI Quanta 450 system (FEI, Brisbane, Australia) using an accelerating voltage of 20keV and a large spot size (5) rastered over an area approximately $500\mu\text{m}$ wide. At least two such areas were scanned for each sample and the average spectrum was used for analysis.

2.6.5 Thermogravimetric Analysis (TGA)

Thermogravimetric analysis (TGA) is a technique that measures the change in weight of a sample as a function of temperature. Oxidation of different components of the sample occurs at different temperatures, which may allow the composition of the sample to be elucidated. In terms of nanotube samples the residual ash content, or percentage of the sample that did not undergo combustion over the examined temperature range, is a measure of the metallic catalyst content within a sample.^{90,310} A derivative of the weight loss curve allows the approximate temperatures of greatest change to be determined, hence the nature of the carbonaceous impurities may be inferred from these values. TGA of as-produced CNT soot was performed on an AutoTGA 2950 HR V6.1A instrument (TA Instruments, New Castle, Delaware, USA). Samples were placed into Pt pans and heated to 900°C at 5°C per minute under an air atmosphere provided at a flow rate of $50\text{mL}\cdot\text{min}^{-1}$.

2.6.6 pH Measurement

pH may be measured using the potential difference that develops between solutions containing different hydrogen ion concentrations. A combination glass electrode consisting of a probe electrode (usually silver chloride wire inside a doped-glass bulb that contains embedded ions) and an internal reference electrode (which provides a baseline voltage), both contained in internal ionic solutions, can be utilised for such measurements. When the bulb is immersed in the analyte solution, ion exchange creates a potential difference of around 60mV per pH unit across the glass membrane, allowing hydrogen ion activity to be measured.

All pH values were recorded using a Meterlab PHM210 pH meter (Radiometer Analytical, Lyon, France). A two-point calibration using IUPAC standard solutions of pH 7.000 and 4.005 was performed prior to sample measurements. The glass bulb was fully immersed in each solution to be analysed and care was taken to not contact the vial walls with the electrode, while readings were taken only after the pH value had remained stable for several minutes.

Chapter 3

COMPARISON OF DIFFERENT DISPERSING MATERIALS

3.1 Performance of Individual Dispersants

3.1.1 Adsorption Mechanisms

Dispersion of nanotubes in water by amphiphiles is facilitated via hydrophobic interactions between the nanotube surface and the dispersing molecule. Ionic surfactants are expected to stabilise suspensions of nanotubes through electrostatic repulsion between their charged head groups, and both cationic and anionic surfactants have been demonstrated to adequately disperse CNTs (with neither showing superiority).¹¹² For non-ionic dispersants, steric repulsion between the large hydrophilic groups of these molecules can provide stability to the suspension and act as a barrier for nanotube aggregation.¹²¹ A recent theoretical study by Xu *et al.* reports that in the ionic surfactant SDS the sodium counter-ion essentially balances the electrostatic forces,³¹¹ thus even in ionic surfactants the dominant stabilisation mechanism may be steric in nature.

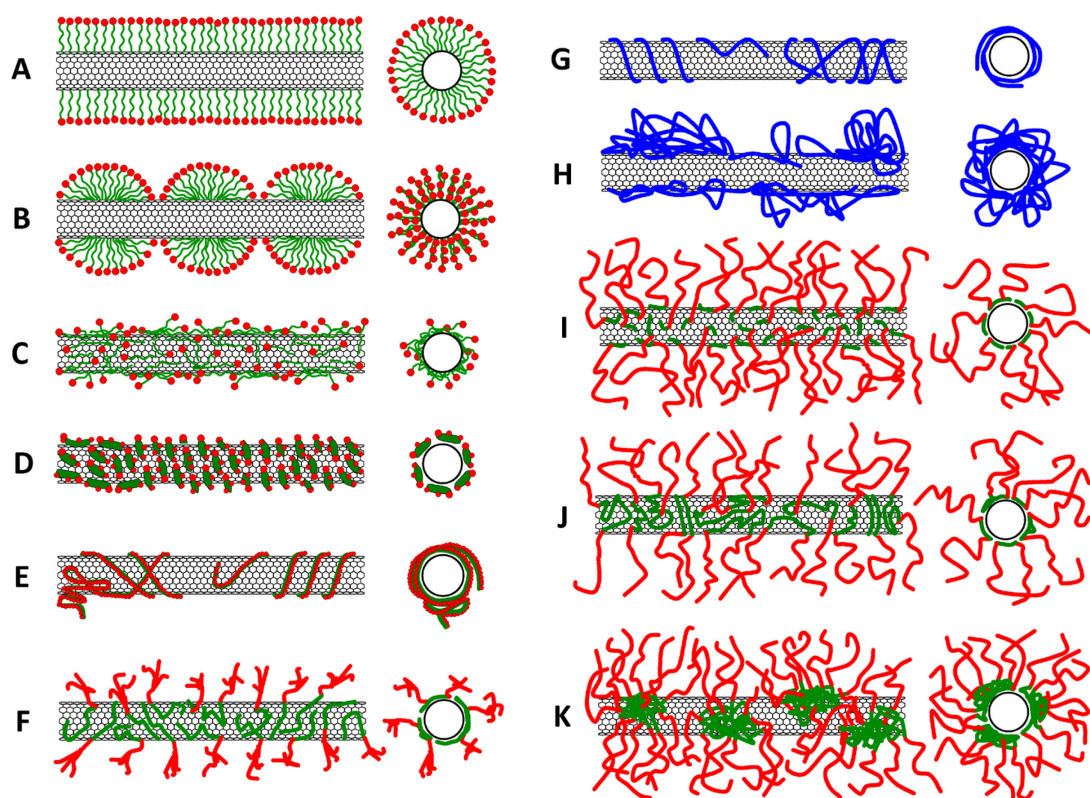


Figure 3.1: Representations of the possible adsorption conformations for each of the different types of dispersant used in this study (based on various literature reports). Green components designate hydrophobic segments of the molecules while red depicts hydrophilic portions; blue is used for SCMC where no clear segregation of these groups is apparent. For ionic, alkyl surfactants (SDS, SDBS, CTAB) structures include (A) encapsulation in a cylindrical micelle, (B) adsorption of hemi-micelles and (C) random adsorption. Steroid based bile salts (SC, DOC) are expected to adsorb as in (D). Polymeric dispersants PVP (E) and SCMC (G) are likely to wrap the nanotube, although in either case adsorption of coils to the sidewall (H) is also possible. Tween 60 is also represented in (F), along with Triton X surfactants and Brij S-100 in (I), while potential conformations of the block-copolymer PF-127 include sporadic decoration (J) and adsorption of polymer micelles (K). Diagrams are schematic only; they do not reflect accurate packing densities and are not to scale.

The assembly of short chained amphiphilic surfactants around a CNT has been proposed to occur through encapsulation in a cylindrical micelle,^{38,312} adsorption of hemi-micelles^{122,313,314} or random adsorption,³¹⁵ though recent simulations suggest that all of these conformations are possible and are dependent on both the surfactant concentration^{316,317} and nanotube diameter.³¹¹ The formation of micelles is not necessarily a prerequisite for CNT dispersion and many surfactants function as dispersants below their critical micelle concentration (CMC),³¹⁸ however their performance is greatly improved at concentrations above the CMC.³¹⁹ Long-chained

polymers (including DNA) are known to wrap around a CNT helically,^{124,125,131,320} though a non-wrapping polymer conformation is also possible,¹³⁵ while block copolymers are more likely to decorate the CNT along its sidewall.^{126,321} Based on the aforementioned literature, the most likely of these potential adsorption mechanisms are depicted in Figure 3.1 for each of the dispersants used in this work.

It has also been found experimentally that the dispersion efficiencies of some surfactants are sensitive to the diameter of the nanotubes.^{322,323} A large number of previous dispersion studies in the literature focus on HiPCO CNTs^{117-119,121,122} or the similarly produced CoMoCAT nanotubes,^{116,272} with those produced by the electric arc and laser-vaporisation methods studied to a lesser extent.^{120,122} As HiPCO ($d \sim 1.0 \pm 0.3 \text{ nm}$)³²⁴ CNTs tend to have smaller diameters compared to electric arc nanotubes ($d \sim 1.4 \pm 0.2 \text{ nm}$),¹²⁰ differences in the effectiveness of each dispersive agent between nanotube types should be expected. Indeed, it has previously been shown that both SC and SDS preferentially stabilise nanotubes of smaller diameter.^{322,325}

3.1.2 UV-Vis-NIR Spectroscopy of Baseline Solutions

Absorbance spectra of aqueous solutions containing 1% of each dispersant were scanned for baseline subtraction. These spectra are plotted in Figure 3.2, showing the transmission ranges for each different material. The spectral cut-offs for the dispersants are located below 350nm in most cases. SDBS and Triton X, which contain benzene rings in their structures, absorb strongly in the ultraviolet region. SDS shows no absorption over the studied range, having a baseline spectrum equivalent to that of water, while the dispersants Brij S-100, Pluronic F-127, SC and DOC also have relatively broad transmission ranges. Overall, significant absorbance by the dispersants themselves does not occur over the wavelength range for which the major nanotube absorbance peaks are expected to occur. However, for the surfactants CTAB, DDAB and Tween 60 the baseline intensity is noticeably raised, particularly in the case of CTAB. Solutions containing CTAB were observed to form large crystalline aggregates during processing. The formation of this phase occurred both in the absence and presence of the CNTs and may therefore hinder the suspending ability of this surfactant, however these aggregates were found to be completely removed upon centrifugation and did not reform in nanotube-containing dispersions. The aggregates were also readily

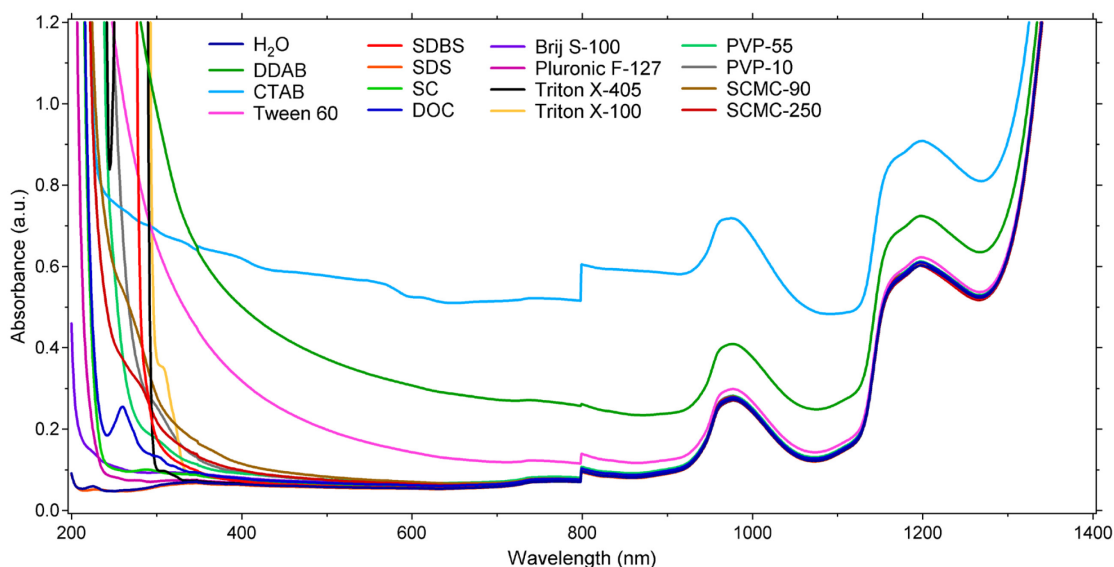


Figure 3.2: UV-Vis-NIR absorbance spectra for 1% dispersant solutions in water.

dissolved upon gentle heating, though an exact transition temperature was not determined.

In contrast to CTAB, where the crystallites formed were observed to be large and to sediment from the solution under gravity, DDAB and Tween 60 solutions turned turbid over time. This turbidity is believed to be due to surfactant coagulation, which increases scattering in UV-Vis-NIR spectra and therefore increases the baseline absorbance. This effect is more prominent below about 600nm for both of these dispersants, while DDAB forms a greater fraction of aggregates relative to Tween 60. Unlike in CTAB, coagulation of the surfactant also occurred in CNT dispersions of DDAB and Tween 60 over time, leading to destabilisation of the colloids.

The presence of scattering particulates in the CTAB, DDAB and Tween 60 reference solutions prevented accurate baseline subtraction since centrifugation effectively removes these aggregates from the nanotube dispersions, thus the measured sample absorbance is considerably reduced comparative to its real value. Consequently, pure H₂O was used as a baseline for these three surfactants, although in the case of DDAB and Tween this leads to an increase in the sample absorbance below 600nm due to the presence of surfactant aggregates in the nanotube solution. Water could be used as a baseline for each of the dispersants studied without significantly affecting the absorbance spectrum above ~400nm, and water-only baseline subtraction was applied for the stability studies in Section 3.1.4.

3.1.3 UV-Vis-NIR Spectroscopy of Nanotube Dispersions

UV-Vis-NIR spectra can provide a simple and rapid measure of the relative dispersion state of CNT solutions through analysis of the characteristic nanotube absorbance peaks.^{116,272} Both electric-arc and HiPCO produced CNTs were dispersed at a concentration of $0.5\text{mg}\cdot\text{mL}^{-1}$ in solutions containing 1% by mass (i.e., mass surfactant per total mass, 1wt%) of each surfactant or polymer. Dispersions were prepared in 10mL of H₂O via 10 minutes of tip sonication (5mm tip, 20% amplitude) followed by ultracentrifugation at $122\times 10^3\text{g}$ for 1 hour. A surfactant concentration of 1% was used as this is the most common approach reported in literature, likely since this was established as the optimal concentration for both SDS³²⁶ and Triton X-100.³²⁷ A direct comparison between the UV-Vis-NIR absorbance spectra of HiPCO and arc type nanotubes in each dispersant is made in Figure 3.3. These spectra were collected with 1% dispersant solution for baseline correction with the exception of CTAB, DDAB and Tween 60 for which the spectrum of water only was subtracted. The concentration of nanotubes remaining in the supernatant after centrifugation was greater in most cases for HiPCO CNTs. This probably arises from two factors; a) the lower purity of the raw arc nanotubes, having less CNT per weight of the starting material, and b) the larger diameter arc nanotube/surfactant assemblies are expected to be heavier, leading to a faster sedimentation rate and hence less material remains after centrifugation under the same conditions.

It is clearly evident from the magnitude and observed resolution of the CNT peaks in the absorbance spectra that the yield and quality of the dispersion achieved by the different surfactants can vary markedly. Most dispersants were capable of stabilising a reasonable concentration of arc nanotubes in the collected supernatant, though many showed a reduced performance with HiPCO nanotubes. As can be seen in Figures 3.3A and B the smaller anionic surfactants SDBS, DOC and SC produce the most resolved spectra for both sets of nanotubes, thus indicating a greater fraction of individual nanotubes in their dispersions. For SDBS, the presence of a phenyl group in the surfactant is suggested to provide superior dispersive ability due to π - π stacking interactions,^{122,272} despite being at the hydrophilic end of the molecule. The phenyl group may play a role in the initial separation of an individual nanotube from a bundle, adsorbing laterally in the narrow space between adjacent nanotubes where the surfactant cannot adsorb perpendicular to the nanotube surface.¹³⁶

The absence of a hydroxyl group in DOC results in better dispersion of CNTs than with SC, which has been noted previously,^{116,120} though the difference is slight in these results. The hydroxyl group likely hinders the association of the SC molecule to the CNT sidewall through hydrophobic attraction in some way (despite being on the hydrophilic face of the molecule), thus its removal provides DOC with improved dispersive ability. While SDS performed reasonably well for the HiPCO nanotubes, fine

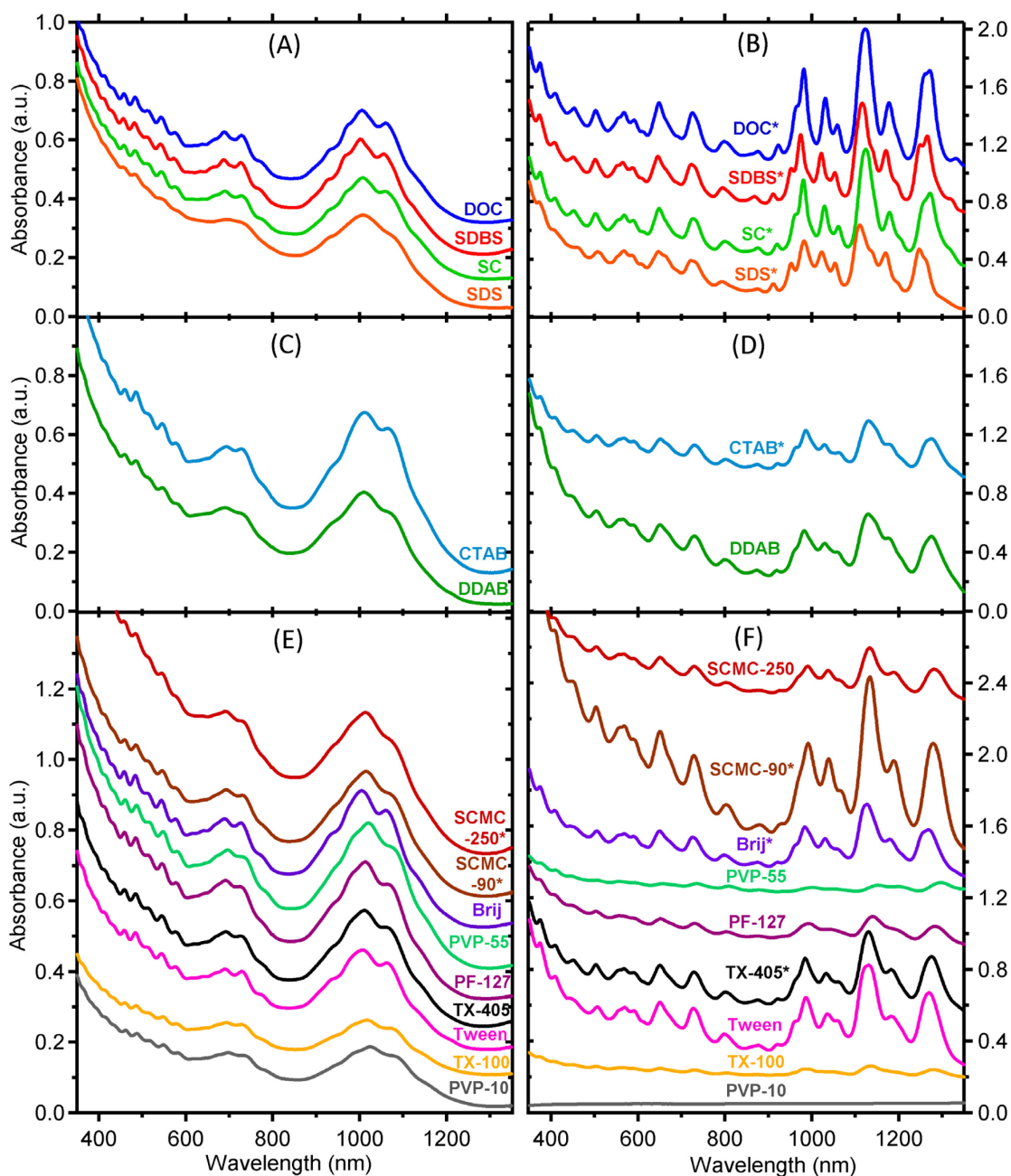


Figure 3.3: UV-Vis-NIR absorbance spectra for arc (left) and HiPCO (right) type CNTs dispersed in water by sonication-ultracentrifugation using 1% solutions of various anionic (A, B), cationic (C, D) and nonionic (E, F) surfactants and polymers. Asterisks indicate spectra after a 1:2 dilution by dispersant solution. Spectra are vertically offset for clarity.

structure for arc CNTs suspended in SDS was only observed immediately after centrifugation (see Section 3.3.1). This structure disappeared within 24 hours of standing, thus in SDS re-aggregation of the nanotubes seems to begin directly after sonication ceases²⁵⁵ and is quite rapid compared to the other surfactants. Furthermore, it has previously been suggested that SDS preferentially dissolves impurities over CNTs,¹²⁰ hence SDS is not the ideal dispersant for arc nanotubes.

As can be seen in Figures 3.3C and D the cationic surfactants CTAB and DDAB are not as effective as DOC or SDBS. While CTAB resulted in the largest absorbance peak area of all the dispersants, the individual absorptions for both arc and HiPCO nanotubes were not as well resolved as those for DOC or SDBS, suggesting a lower fraction of individual tubes. Based on the intensity of the spectra DDAB provides slightly fewer dispersed CNTs than CTAB for arc nanotubes and approximately 1/3 the amount for HiPCO nanotubes, thus CTAB is clearly the superior dispersant of the two.

Of the non-ionic dispersants (Figures 3.3E and F), the block co-polymer Pluronic F-127 and longer linear polymers PVP-10 and PVP-55 appear to perform far better for arc CNTs than for HiPCO nanotubes, perhaps due to tighter ‘wrapping’ or adsorption conformations being required for smaller diameter tubes. No CNTs were retained in the supernatant for PVP-10, making it the least effective surfactant for HiPCO nanotubes of the selection studied, however the longer PVP-55 appears to disperse at least a small amount of HiPCO nanotubes. As larger diameter nanotubes have smaller band-gaps and therefore exhibit peaks at longer wavelengths, the HiPCO S₁₁ peak at ~1300nm being more intense than the peak at ~1150nm in PVP-55 supports the suggestion that CNTs of larger diameter are more easily dispersed in this polymer.

In contrast, Triton X-100 appeared to be a relatively poor dispersant for both sets of CNTs (though especially ineffective for HiPCO tubes), while Triton X-405 dispersed both types reasonably well. This result, along with that of the two PVP polymers, supports the assertion that longer chain lengths are more effective for non-ionic surfactants due to increased steric repulsion, irrespective of nanotube diameter.¹²¹ However, the length of the dispersant chains significantly affects solution viscosity, where long chains generally create highly viscous solutions. This hinders sonication based dispersion³²⁸ as well as significantly increasing the concentration of material remaining after centrifugation. Therefore it is possible that the increased nanotube concentration in dispersants with longer chains is a result of decreased sedimentation during centrifugation rather than improved dispersion of the nanotubes. This effect

would probably be more pronounced in PVP than Triton X due to the size difference between the molecules, hence the improved dispersion with Triton X is most likely due to enhanced steric stabilisation as previously reported.

In the case of SCMC, the shorter chain SCMC-90 provided better dispersion than SCMC-250. This is in contrast to a previous report which showed greater efficiency of SCMC-250 compared to SCMC-90,¹¹⁶ although the sonication protocol employed therein was more intense and 12 times as long as the one used here, thus a significant amount of polymer scission may have occurred.²⁵³ As SCMC-90 is considerably longer than all the other surfactants examined and SCMC-250 is more than double that length again, the viscosity of 1% SCMC solutions is substantially increased compared to the other dispersants. Consequently, the amount of material (including large bundles and impurities) left in the supernatant of SCMC dispersions was much greater, with an approximate 3-fold increase in the CNT concentration for arc nanotubes. A similar increase was observed for HiPCO CNTs in SCMC-90, although SCMC-250 showed relatively poor dispersion of the smaller diameter nanotubes. This is likely due to the limited effect of sonication on dispersion within the highly viscous solution, and it is noted that HiPCO nanotubes were extremely difficult to submerge in the SCMC-250 solution in the first instance, while arc nanotubes were far easier to immerse in both cellulose polymer variants. Neither of the SCMC dispersions showed particularly well resolved fine-structure for either type of nanotubes, although SCMC-90 is the clear superior of the two under the experimental conditions used in this study.

Brij S-100 dispersed both types of nanotubes relatively well, although the resolution of the CNT peaks is slightly better for arc nanotubes with this surfactant. Again, the large molecule may be restricted in binding to a nanotube with a higher degree of curvature. Similarly, Tween 60 disperses arc CNTs to a greater degree, though the difference in the retained CNT concentration between nanotube types is much more pronounced in this case. This accounts for the discrepancy observed in previous examinations of the Tween surfactant series which have reported relatively good dispersion where arc nanotubes were used¹²⁰ and poor dispersion where HiPCO nanotubes were suspended in similar Tween surfactants of low molecular weight.¹²¹

It is probable that the overall enhanced ability of smaller surfactant molecules to disperse the CNTs is related to the de-bundling mechanism, postulated to occur through ‘unzipping’ of the CNT bundle during ultrasonic agitation as discussed in Section 1.4.¹³⁶ Bulkier surfactant/polymer molecules would undoubtedly find it more difficult to

enter the gaps between adjacent tubes and exfoliate the CNTs. Conversely, longer chains might enable improved mobility and wrapping of surfaces with greater curvature, while also affording enhanced steric stabilisation; thus a trade-off between the initial exfoliation stage and the ability to sustain nanotube separation probably exists. As smaller surfactants would also adsorb with a higher packing density on the nanotube surface, they may also provide a better steric barrier to re-aggregation.

3.1.4 Dispersion Stability

The stability of each dispersion was investigated by re-measuring the absorbance spectrum after 3 months of incubation. The spectra were normalised to the S_{22} peak maxima (~1000-1020nm) for electric arc nanotubes and to the S_{11} peak maxima (~1110-1150nm) for HiPCO CNTs, while the absorbance was also equalised at 850nm for arc and 900nm for HiPCO nanotubes. The results are displayed in Figures 3.4 and 3.5 for arc and HiPCO nanotubes respectively. For the most part, only slight shifts are observed in the spectral features that are present, suggesting that the majority of the dispersions are quite stable. However, it is known that absorbance spectra are not especially sensitive to re-bundling of CNTs,³²⁹ therefore at least some aggregation of the nanotubes is expected over this time scale. Indeed, there is some subtle shifting of the peaks in most of the dispersants, even where their spectra appear to overlap. Spectral shifts over the 3 month period were measured by determining the position of the peak maxima for the M_{11} and S_{22} bands in arc nanotubes as well as positions of the M_{11} band and three separate S_{11} peak maxima for HiPCO CNTs using the FindPeak function in Igor Pro, and these values are tabulated in Table 3.1.

The initial positions of these peaks are different among the examined surfactants, which may partially be due to varied levels of nanotube agglomeration between the different dispersants, where more blue-shifted energies represent more dispersed solutions.^{96,330} However, the various dispersants will also provide different levels of dielectric screening and thus the transition energies for the individualised tubes will depend on the nature of the adsorbed molecules.³³¹ Also, the presence of water can cause a red-shifting of these peak energies due to an increase in the micropolarity at the nanotube surface.^{322,332} Therefore a more blue-shifted peak may simply represent a weaker dielectric screening effect or greater exclusion of water from the interface by a

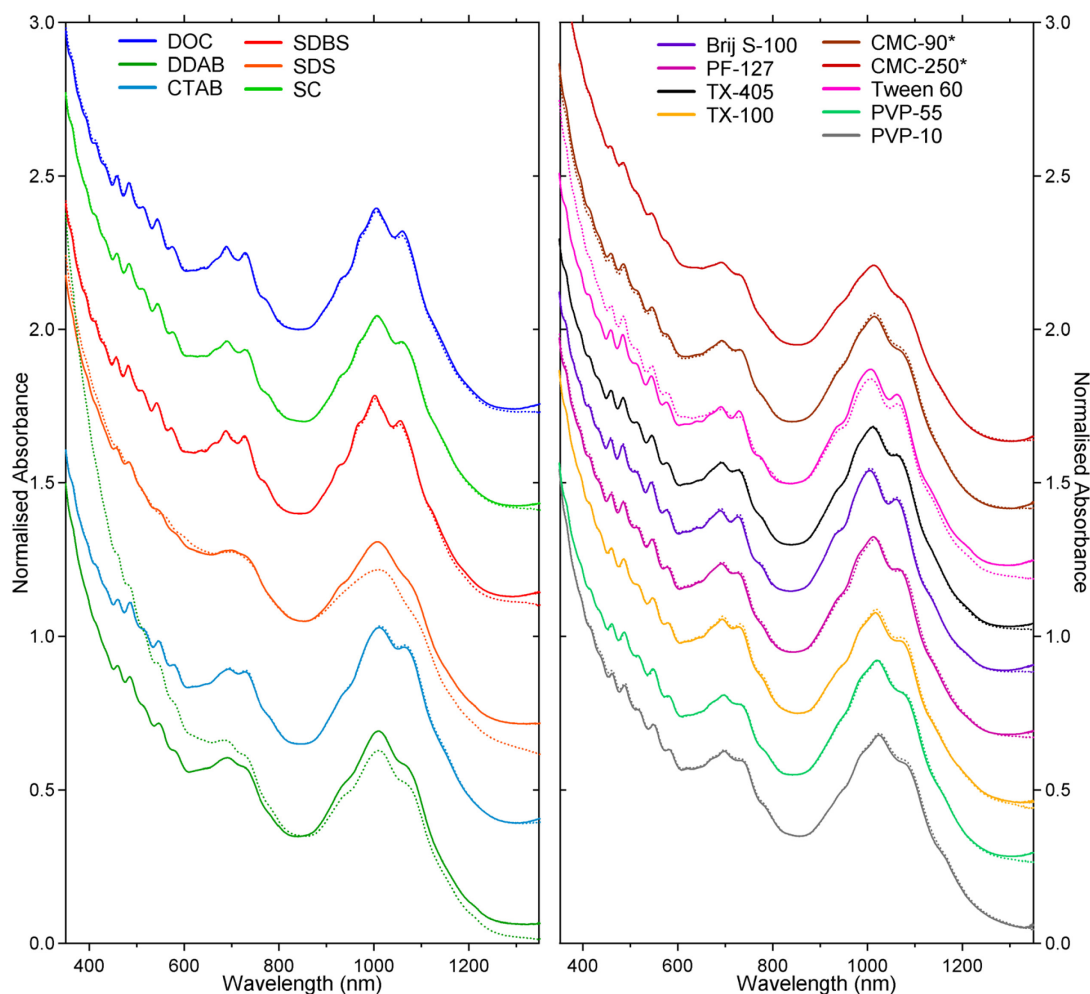


Figure 3.4: UV-Vis-NIR absorbance spectra for arc CNTs dispersed in ionic (left) and non-ionic (right) surfactants and polymers immediately after preparation (solid lines) and after 3 months of incubation (dotted lines). All spectra were recorded with water baselines and normalised to the S_{22} peak maximum at ~ 1010 nm. Asterisks indicate spectra collected after 1:2 dilution by dispersant solution. Spectra are vertically offset for clarity.

particular dispersant, rather than improved nanotube individualisation; however within each of the surfactant systems a red-shift is indicative of nanotube aggregation.

In most instances the observed peak shifts are positive (red-shifted), although in some cases the values are negative (blue-shifted). This occurs because the measured peak maxima belong to bands comprised of a number of absorbance peaks from individual nanotube species; thus if these species experience differing degrees of aggregation, even though the de-convoluted peaks are red-shifted by bundling, the overall absorbance peak may appear to blue-shift. Consequently, to compare amongst the different dispersants (without peak-fitting the spectrum in each case) the absolute value of the shift was averaged over every measured band within both types of CNTs.

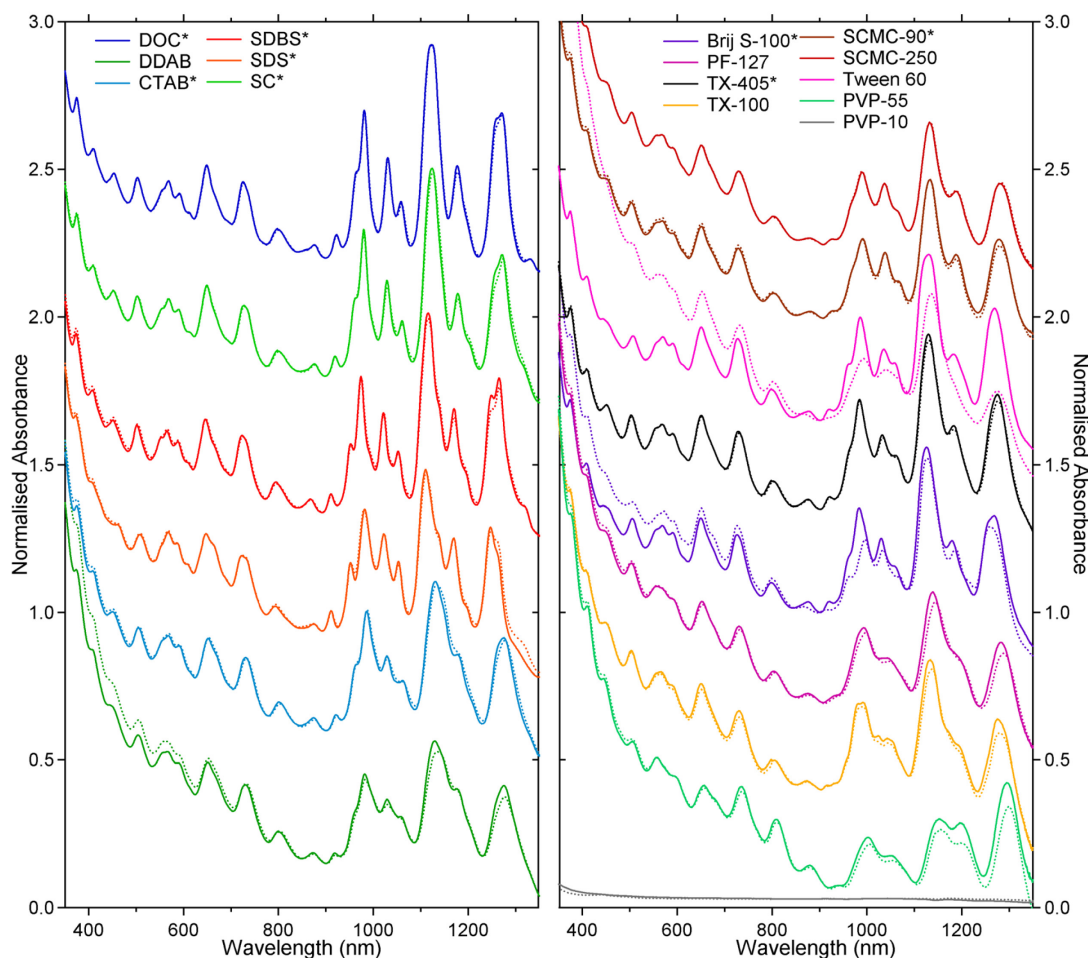


Figure 3.5: UV-Vis-NIR absorbance spectra for HiPCO CNTs dispersed in ionic (left) and non-ionic (right) surfactants and polymers immediately after preparation (solid lines) and after 3 months of incubation (dotted lines). All spectra were recorded with water baselines and normalised to the S_{11} peak maximum at $\sim 1120\text{nm}$ (except that of PVP-10 for which no nanotube peaks were observed). Asterisks indicate spectra collected after 1:2 dilution by dispersant solution. Spectra are vertically offset for clarity.

Significant loss of absorbance intensity and spectral shifts are observed in the DDAB, Brij S-100 and Tween 60 HiPCO dispersions while similar behaviour occurs in SDS, DDAB and Tween-60 for arc nanotubes, implying a substantial amount of re-bundling of the CNTs for these surfactants. Notably, for the surfactants Tween 60 and DDAB the absorbance signal is increased towards shorter wavelengths due to the formation of surfactant aggregates. This desorption and coagulation of surfactant molecules destabilises the suspension, although the CNT peaks are still clearly visible indicating that the nanotubes remain dispersed to some degree. Interestingly, the increase in absorbance was less intense for DDAB in the HiPCO CNT dispersion compared to the arc nanotubes and vice versa for Tween 60, suggesting that surfactant adsorption on the CNT may be slightly more stable than surfactant self-agglomeration in these cases.

Brij S-100 dispersions of HiPCO nanotubes were found to be quite unstable over time despite initially appearing to be one of the better performing non-ionic dispersants, although dispersion of arc CNTs in Brij were far more stable. Some loss of intensity is observed for dispersions of HiPCO nanotubes in Pluronic F-127, Triton X-100 and PVP-55, however this was anticipated as these dispersants initially produced poor quality suspensions of HiPCO nanotubes. All three appear to be much more stable over time for arc nanotubes; despite exhibiting large spectral shifts relative to SDBS and DOC the peak intensity and spectral shape were essentially preserved. Other dispersants showed only minor spectral changes for both types of nanotubes, with the least amount

| Arc Nanotubes | | | | | | | | | |
|----------------|---------------------|---------------------|-------------------------------|----------|-------|-------------------------------|----------|-------|--------|
| Dispersant | A(S ₂₂) | S ₂₂ :BG | M ₁₁ Position (nm) | | | S ₂₂ Position (nm) | | | |
| | | | Original | 3 Months | Shift | Original | 3 Months | Shift | |
| | | | DOC | 52.3 | 0.429 | 688.4 | 689.9 | 1.5 | 1005.6 |
| SDBS | 52.0 | 0.412 | 687.5 | 688.9 | 1.4 | 1002.0 | 1002.8 | 0.8 | |
| SCMC-90 | 48.1 | 0.379 | 692.8 | 692.9 | 0.1 | 1014.6 | 1016.1 | 1.5 | |
| Triton X-405 | 46.0 | 0.425 | 691.9 | 692.1 | 0.3 | 1011.5 | 1012.3 | 0.8 | |
| SC | 45.7 | 0.362 | 689.8 | 689.6 | -0.2 | 1007.4 | 1007.5 | 0.1 | |
| SCMC-250 | 49.5 | 0.275 | 691.7 | 691.2 | -0.5 | 1013.5 | 1014.0 | 0.5 | |
| CTAB | 77.8 | 0.420 | 693.9 | 694.8 | 0.9 | 1011.5 | 1013.7 | 2.2 | |
| PVP-55 | 58.3 | 0.412 | 696.1 | 697.2 | 1.1 | 1020.1 | 1023.1 | 3.0 | |
| DDAB | 50.5 | 0.371 | 691.0 | 688.0 | -3.0 | 1009.4 | 1010.5 | 1.1 | |
| Pluronic F-127 | 52.4 | 0.406 | 691.5 | 693.9 | 2.4 | 1012.6 | 1016.6 | 4.0 | |
| Brij S-100 | 53.0 | 0.426 | 689.4 | 690.2 | 0.8 | 1005.2 | 1005.9 | 0.7 | |
| SDS | 37.6 | 0.278 | 700.0 | 704.0 | 4.0 | 1007.3 | 1011.0 | 3.7 | |
| Tween 60 | 38.9 | 0.410 | 690.7 | 692.3 | 1.6 | 1006.7 | 1006.0 | -0.7 | |
| Triton X-100 | 20.4 | 0.338 | 693.4 | 694.8 | 1.4 | 1017.0 | 1018.6 | 1.6 | |
| PVP-10 | 22.9 | 0.351 | 697.7 | 696.8 | -0.9 | 1024.1 | 1024.7 | 0.6 | |

| HiPCO Nanotubes | | | | | | | | | | | | | Average Shift (nm) |
|-----------------|-------------------------------|----------|-------|-------------------------------|----------|-------|-------------------------------|----------|-------|-------------------------------|----------|-------|----------------------------|
| Dispersant | S ₁₁ Position (nm) | | | S ₁₁ Position (nm) | | | S ₁₁ Position (nm) | | | M ₁₁ Position (nm) | | | |
| | Original | 3 Months | Shift | |
| DOC | 981.3 | 981.6 | 0.3 | 1122.7 | 1122.5 | -0.2 | 1271.0 | 1271.6 | 0.6 | 502.4 | 502.6 | 0.2 | 0.49 |
| SDBS | 974.1 | 974.6 | 0.5 | 1115.6 | 1115.7 | 0.1 | 1265.3 | 1265.6 | 0.3 | 501.3 | 502.4 | 1.1 | 0.69 |
| SCMC-90 | 991.3 | 990.6 | -0.7 | 1133.4 | 1132.6 | -0.8 | 1279.0 | 1280.2 | 1.2 | 503.4 | 503.5 | 0.1 | 0.73 |
| Triton X-405 | 984.6 | 985.0 | 0.4 | 1129.9 | 1130.9 | 1.0 | 1275.4 | 1276.6 | 1.2 | 502.8 | 503.9 | 1.1 | 0.79 |
| SC | 980.2 | 979.9 | -0.3 | 1124.1 | 1126.0 | 1.9 | 1271.7 | 1273.8 | 2.1 | 502.1 | 502.6 | 0.5 | 0.86 |
| SCMC-250 | 990.0 | 989.7 | -0.3 | 1132.8 | 1133.2 | 0.4 | 1280.7 | 1283.1 | 2.4 | 503.6 | 503.8 | 0.2 | 0.72 |
| CTAB | 986.1 | 987.0 | 0.9 | 1130.9 | 1133.8 | 2.9 | 1275.3 | 1277.5 | 2.2 | 504.5 | 505.9 | 1.4 | 1.75 |
| PVP-55 | 1002.2 | 1006.5 | 4.3 | 1153.3 | 1155.5 | 2.2 | 1294.9 | 1298.9 | 4.0 | 505.2 | 504.4 | -0.8 | 2.57 |
| DDAB | 982.1 | 983.3 | 1.2 | 1129.9 | 1135.3 | 5.4 | 1275.1 | 1277.1 | 2.0 | 503.7 | 504.8 | 1.1 | 2.31 |
| Pluronic F-127 | 993.4 | 996.9 | 3.5 | 1139.1 | 1144.2 | 5.1 | 1282.5 | 1287.5 | 5.0 | 503.2 | 503.9 | 0.7 | 3.45 |
| Brij S-100 | 983.8 | 996.0 | 12.2 | 1126.0 | 1127.2 | 1.2 | 1268.2 | 1259.5 | -8.7 | 505.1 | 505.4 | 0.3 | 3.98 |
| SDS | 982.0 | 980.8 | -1.2 | 1110.3 | 1111.7 | 1.4 | 1247.0 | 1248.2 | 1.2 | 507.2 | 507.5 | 0.3 | 1.97 |
| Tween 60 | 986.3 | 993.3 | 7.0 | 1130.6 | 1135.7 | 5.1 | 1269.1 | 1274.6 | 5.5 | 506.6 | 507.0 | 0.4 | 3.39 |
| Triton X-100 | 991.7 | 991.8 | 0.1 | 1133.4 | 1137.9 | 4.5 | 1275.5 | 1279.0 | 3.5 | 502.8 | 503.2 | 0.4 | 1.92 |
| PVP-10 | - | - | - | - | - | - | - | - | - | - | - | - | 0.76 |

Table 3.1: Spectral shifts in arc (top) and HiPCO (bottom) nanotubes observed over 3 months in different dispersants. Areal absorbance values and S₂₂:BG resonance ratios are provided for arc CNTs, while average (absolute) shifts are summed for each dispersant over both types of nanotube.

of variance observed in DOC, SDBS, SCMC and Triton X-405 over this time scale.

3.1.5 Summary of Dispersant Comparison

It is difficult to compare surfactants quantitatively as measures of nanotube concentration (S_{22} Area), the degree of individualisation (fine structure), stability (spectral shift) and purity (S_{22} :BG ratio) should all be considered simultaneously. In an attempt to rank the dispersants used here an empirical value derived from the improvised relation $A(S_{22}) \times [S_{22}:BG]/|Avg. Shift|$ was used as a comparative indicator. This value has no physical meaning and was devised to incorporate the three measured properties into a single value for which a larger number corresponds to improved dispersion. The dispersants are plotted in Figure 3.6 in the resultant order corresponding to this value, displaying data for the three measured parameters used in its determination. Although there are clearly superior surfactants for dispersion of CNTs, such as DOC and SDBS, all of the dispersants were capable of dispersing at least some nanotube material. These results emphasise the importance of the diameter distribution within the nanotube population, which is a critical factor. Most surfactants were far more suited to dispersion of arc nanotubes, while the smaller diameter HiPCO CNTs were more difficult to suspend. Small, ionic surfactants are evidently better suited to the task, though ultimately the choice of surfactant will depend on the nature of the nanotube sample to be dispersed and its intended application.

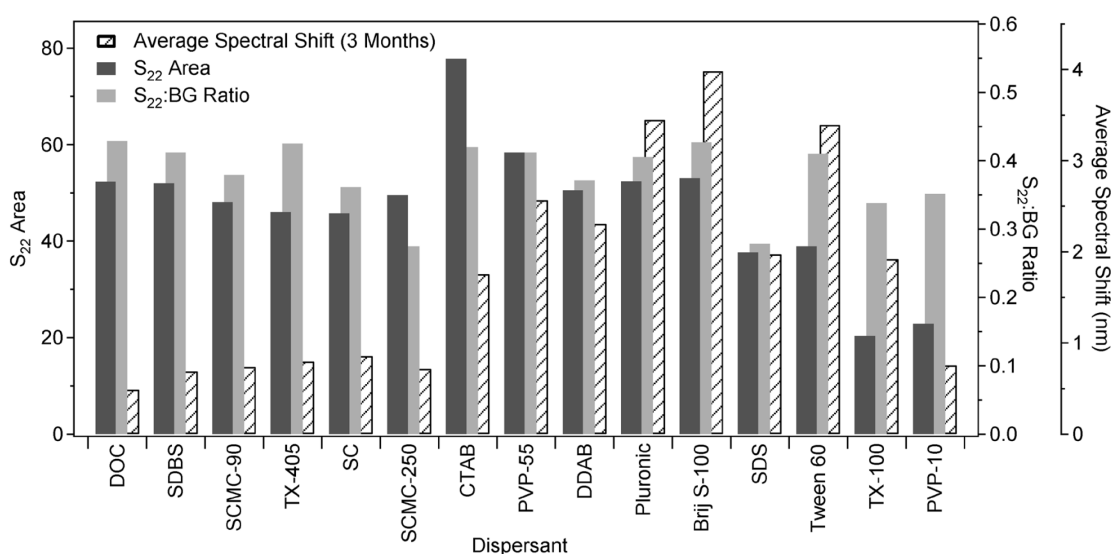


Figure 3.6: Comparison of dispersant performance (using spectral shifts combined for both arc and HiPCO CNTs), ranked in decreasing order of effectiveness from left-to-right.

3.2 Co-Surfactant Solutions

A fundamental question that arises from the above studies is whether the strength of the hydrophobic adsorption to the CNT sidewall or the physical dimensions of the dispersant molecule is the more dominant factor behind the observed variation in dispersion effectiveness. In an attempt to investigate this, mixtures of surfactants were employed using DOC and SDBS as these were identified as exceptional dispersants and are seemingly comparable for both types of nanotubes. Dispersions of arc and HiPCO nanotubes in co-surfactant mixtures of the two materials were prepared (1% total surfactant concentration, $0.5\text{mg}\cdot\text{mL}^{-1}$ CNTs, 10mL, 10min sonication with 5mm tip at 20% amplitude, $122\times 10^3\text{g}$ for 1hr) and their absorbance spectra are shown in Figure 3.7. The UV-Vis-NIR spectra of co-surfactant dispersions exhibit strong nanotube absorbance peaks of similar intensity to those of the neat surfactants while also possessing equivalent fine structure, hence CNT dispersion is clearly achieved to a similar extent in the combined system. In Figure 3.7B the positions of the individual absorption peaks within the S_{22} band of arc nanotubes are observed to be red-shifted by approximately 4nm for DOC dispersions when compared to SDBS. The dispersions consisting of 3:1 and 1:1 ratios of DOC:SDBS share identical peak positions to those observed in the DOC spectrum, while for the 1:3 dispersion the red-shift is only $\sim 2\text{nm}$, i.e. a peak position halfway between those of the two individual spectra. A similar result is observed with HiPCO nanotubes (Figure 3.7C) where the 1:1 co-surfactant mixture produces a spectrum that is essentially identical to that of DOC alone. Since the absorbance spectrum is influenced by the local environment surrounding the CNT³³³ this implies that DOC is preferentially adsorbed onto the CNT sidewall. It is unknown whether this takes place to the exclusion of SDBS or if mixed phase adsorption occurs, though the latter would likely produce spectra with more median peak positions such as in the 1:3 DOC:SDBS arc CNT dispersion. Therefore it appears that DOC has greater affinity for binding to the CNTs relative to SDBS, probably due to stronger hydrophobic interactions with the linked cyclic rings in DOC compared to the single alkyl chain of SDBS. The area of interaction with a DOC molecule would be larger due to the size of its hydrophobic face, implying that the smaller SDBS molecules are displaced. Therefore it seems that the hydrophobic interactions are indeed the major driving force behind dispersion, and other systems were subsequently examined to determine relative interaction strengths.

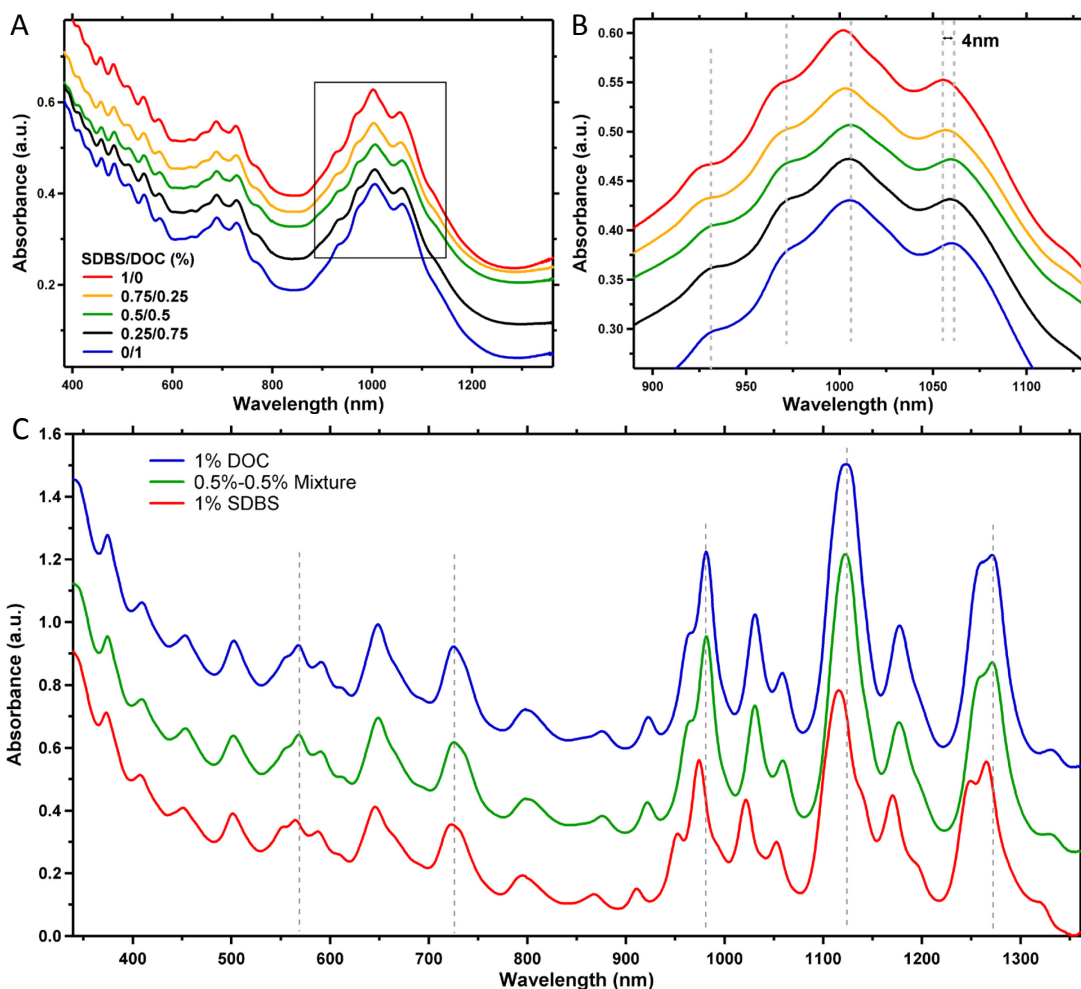


Figure 3.7: Absorption spectra for dispersions of CNTs in co-surfactant mixtures of SDBS and DOC. Spectra for arc nanotubes dispersed by different ratio mixtures are shown in (A), with an enlargement of the S_{22} region (B), while those for HiPCO nanotubes are given in (C). Spectra are offset vertically by multiples of ± 0.25 (HiPCO) and ± 0.05 (arc) for clarity.

Dispersions of HiPCO CNTs in 1:1 co-surfactant mixtures of DOC or SDBS with Brij S-100, PVP-55, TX-405 and SDS were prepared (1% total surfactant concentration, $0.5\text{mg}\cdot\text{mL}^{-1}$ CNTs, 10mL, 10min sonication with 5mm tip at 20% amplitude, $122\times 10^3\text{g}$ for 1hr) and the UV-Vis-NIR spectra recorded from these solutions are shown in Figure 3.8. In mixtures of the non-ionic dispersants with SDBS the peak positions are red-shifted from those of SDBS alone towards those of the other surfactants. Their spectral shapes also possess a form that appears to arise from a combination of those of the two individual components, though they bear more resemblance to that of SDBS in each case. Visual inspection of the spectra suggests that the variations imparted by the presence of the non-ionic dispersants are greatest for Brij S-100 and weakest for PVP-55, while Triton X-405 induces an intermediate effect. Although the spectral differences

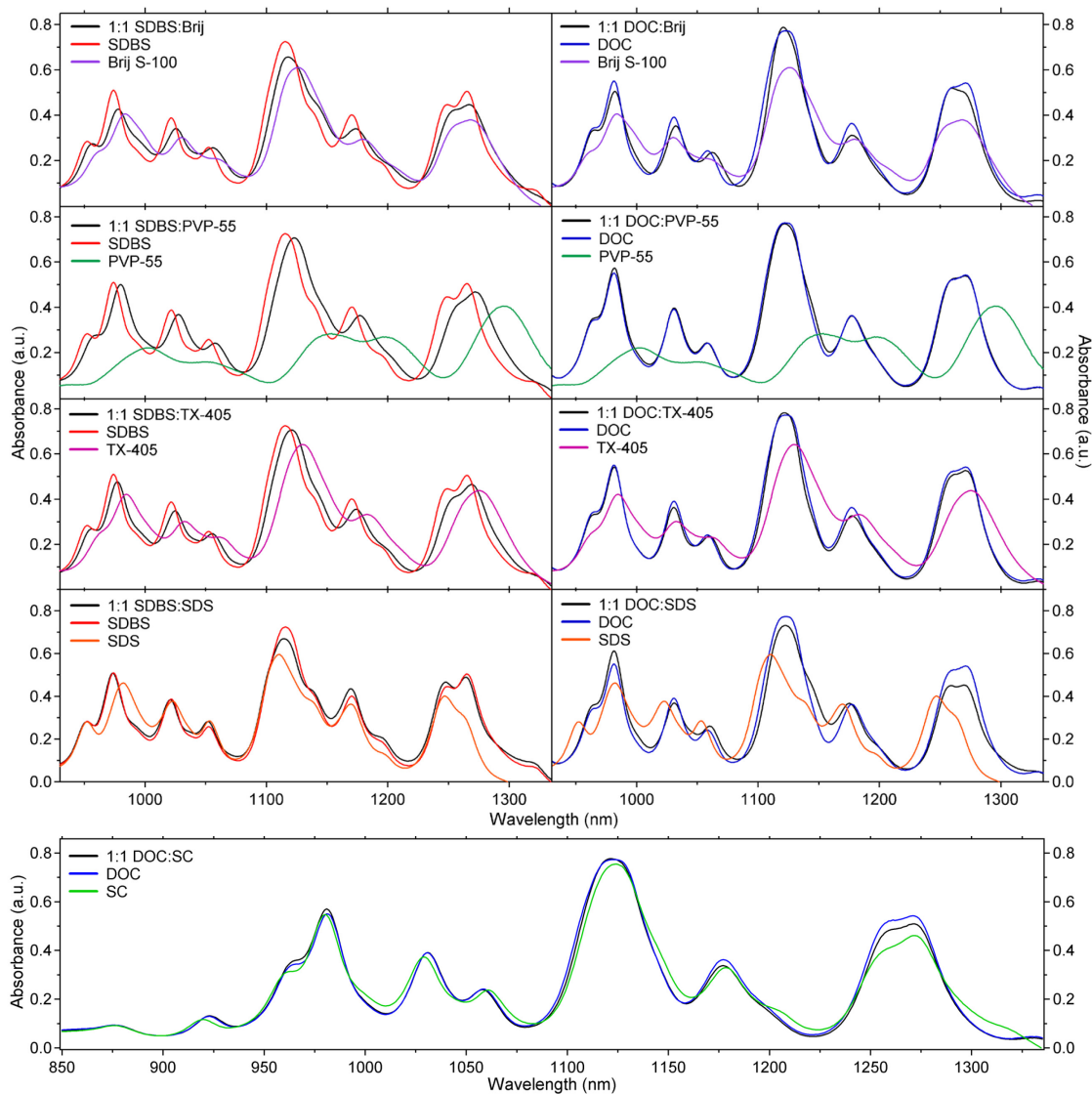


Figure 3.8: Absorption spectra for dispersions of HiPCO CNTs in 1:1 co-surfactant mixtures (1% total concentration) of Brij S-100, PVP-55, TX-405 and SDS with either SDBS (left) or DOC (right). An expanded view of a 1:1 mixture of DOC and SC is shown in the lowest panel. Spectra of neat surfactants (from Figure 3.5) are shown in the same frames for comparison. All spectra were normalised to the peak at $\sim 1130\text{nm}$ and equalised to a value of 0.05 at 900nm .

engendered by these three dispersants in DOC dispersions are much weaker than with SDBS, again suggesting SDBS is more easily displaced from the nanotube surface, the strength of the introduced changes follows the same trend. Also, similar to dispersions of Brij alone, mixtures containing this surfactant were considerably unstable over time, whereas other co-surfactant mixtures all possessed relatively stable spectra over a 6 month period. This implies that Brij has a stronger influence within the co-surfactant mixtures than either Triton X or PVP.

In the presence of SDS, both SDBS and DOC produce an optical absorbance spectrum that bears semblance to their individual solutions over that of SDS, suggesting that both of these surfactants impede the adsorption of SDS onto the nanotube surface. Also, between the bile salt molecules DOC and SC it is again apparent that DOC is preferentially adsorbed to the nanotube, although both cholate salt dispersions produce a very similar absorbance spectrum.

By making the assumption that the smaller anionic dispersants SC and SDS possess greater affinity for binding to the CNT surface than their non-ionic counterparts (which may be reasonable considering the results of Figure 3.5), it can be inferred from these results that the strength of the hydrophobic interactions between the studied dispersing molecules and HiPCO CNTs follows the trend $\text{DOC} > \text{SC} > \text{SDBS} > \text{SDS} > \text{Brij S-100} > \text{TX-405} > \text{PVP-55}$. However, this is a tentative assessment as more dispersant combinations would need to be studied in further detail to confirm this apparent order.

3.3 Dispersion Stability in SDS and SDBS

3.3.1 Stability of SDS Dispersions

SDS is one of the most commonly used dispersants in the literature³³⁴ and was applied in the first description of electronic-type selective reactions between HiPCO nanotubes and diazonium salts.²²⁶ It has also been the surfactant of choice in subsequent studies.^{240,243} However, dispersions of arc CNTs with SDS were found here to be highly unstable, with re-aggregation occurring rapidly after preparation of the dispersion. Figure 3.9 shows the absorption spectrum of arc CNTs dispersed in SDS (1%, $0.5\text{mg}\cdot\text{mL}^{-1}$ CNTs, 10mL, 15min sonication with 5mm tip at 20% amplitude, centrifuged at $122\times 10^3\text{g}$ for 30 min) collected immediately after centrifugation alongside spectra of the same solution recorded over a 72 hour timeframe. Clear loss of fine structure and red-shifting of the peaks occurs during settling of the dispersion, indicating significant nanotube aggregation. The shifting of absorbance peaks is most pronounced for the semiconducting nanotube peaks, suggesting they may be more sensitive to aggregation.

The S_{22} areal absorbance and $S_{22}:\text{BG}$ values were measured from these spectra along with additional scans and are plotted in Figure 3.10 as a function of time. Both

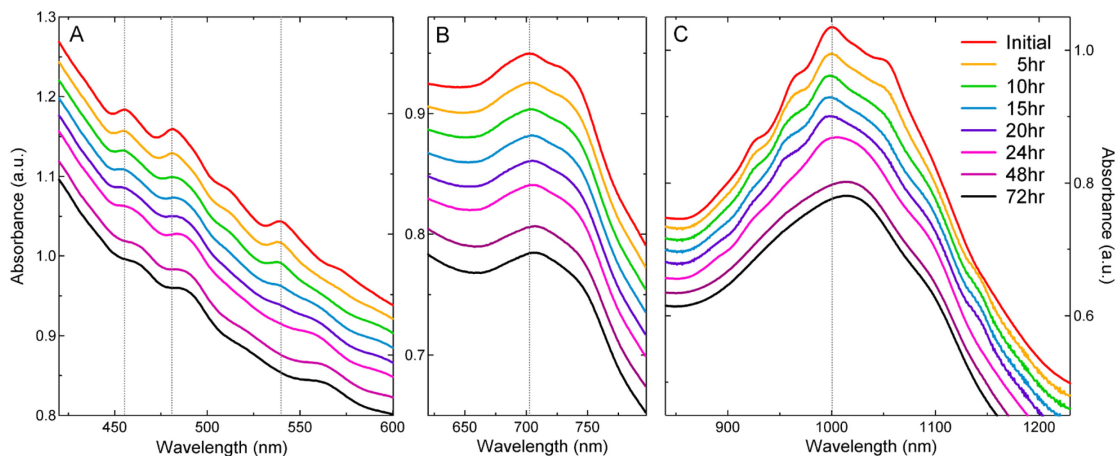


Figure 3.9: UV-Vis-NIR spectra of arc CNTs in 1% SDS monitored over time for the S_{33} (A), M_{11} (B) and S_{22} (C) regions. Spectra are offset by multiples of 0.02 for clarity.

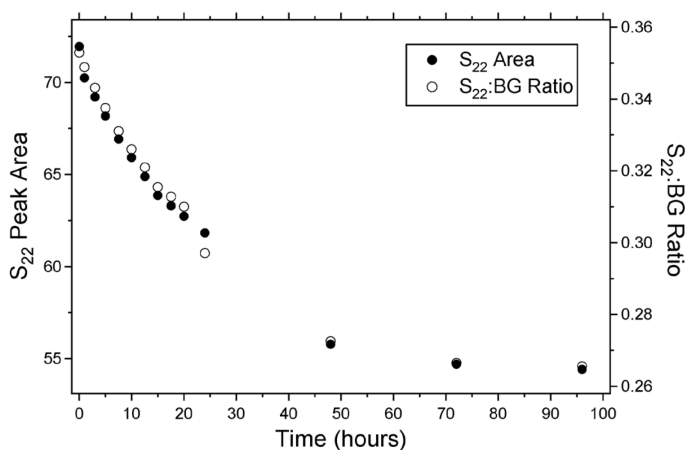


Figure 3.10: S_{22} areal absorbance and S_{22} :BG values for arc CNTs in 1% SDS monitored over time.

parameters are sensitive to the bundling state of the nanotubes, hence the majority of re-aggregation appears to occur during the first 48 hours after preparation. Little further change to the spectrum occurs over several months following this initial decay.

AFM images were recorded from an SDS dispersion (1%, $0.5\text{mg}\cdot\text{mL}^{-1}$ CNTs, 10mL, 10min sonication with 5mm tip at 20% amplitude, centrifuged at $122\times 10^3\text{g}$ for 1hr) spun coat onto a Si wafer immediately after preparation, as well as after 24 and 72 hours of standing (Figure 3.11). The CNTs are initially dispersed to a reasonable degree, though most nanotubes are present in long bundles of 3-6nm in height. Given an average diameter of approximately 1.5nm is expected for these CNTs, this is consistent with bundles containing at least several nanotubes. A large number of shorter objects are also present, with heights pertaining to individual nanotubes. After standing for a

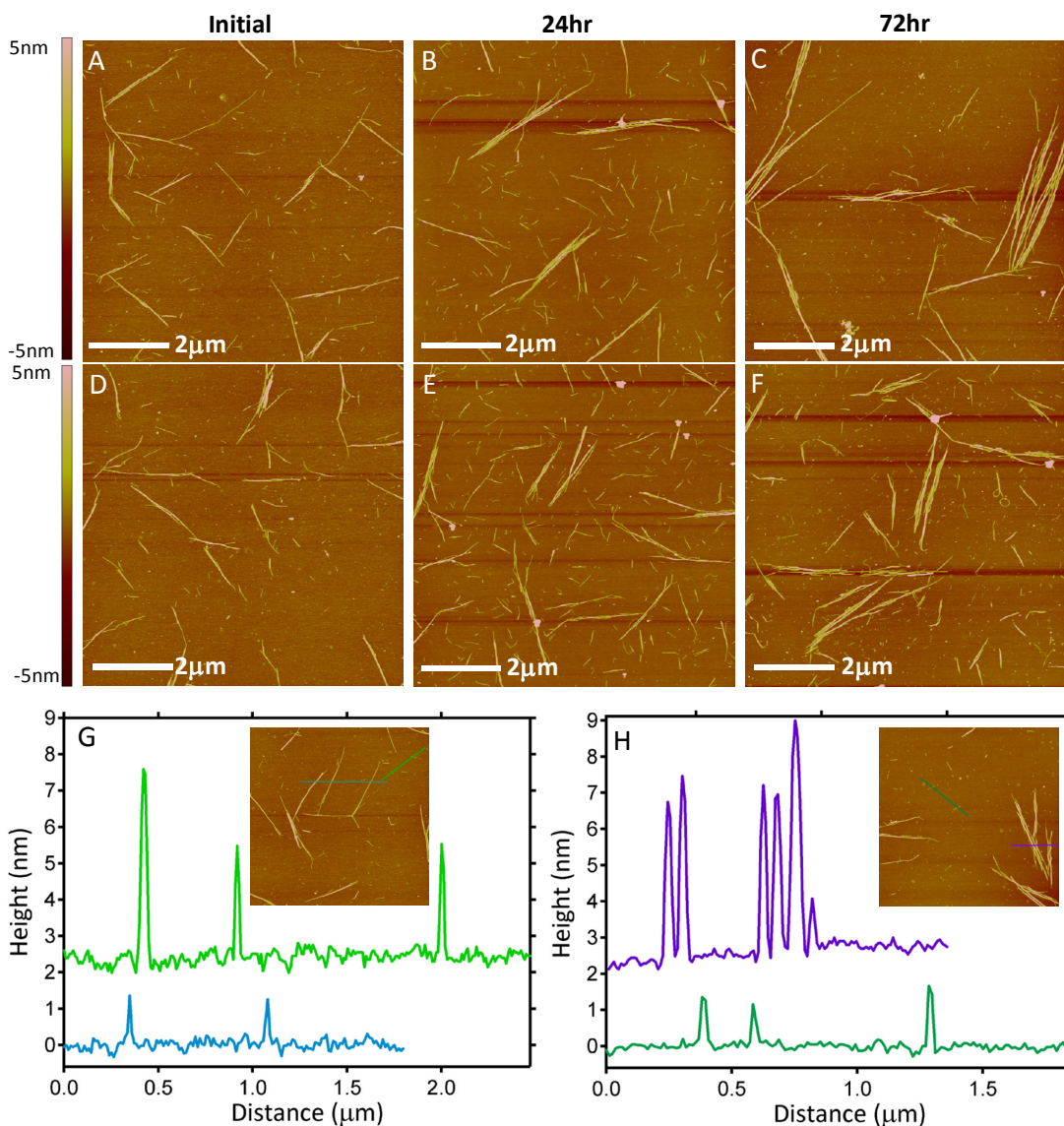


Figure 3.11: 8x8 μ m AFM height images for arc CNTs spun from a 1% SDS dispersion onto Si wafers. Samples were prepared immediately after centrifugation (A and D), after standing for 24hrs (B and E) and after 72hrs (C and F). Cross-sections (coloured lines) of additional 5x5 μ m AFM images (inset) for the initial (G) and 72hr (H) dispersions are also shown, with the upper section vertically offset by 2.5nm in each case.

period of 24 hours, slightly larger bundles begin to become more commonplace, while even larger aggregates are found after 72 hours. In some cases the CNTs in these large aggregates lie parallel but are seemingly still separated in structures that resemble those observed via cryo-TEM.³³⁵ However, even though the absorbance spectrum has decayed significantly, some shorter nanotubes remain dispersed as individuals after 72 hours.

3.3.2 Stability of SDBS Dispersions

Absorbance spectra of arc CNTs dispersed in SDBS (0.5%, $0.5\text{mg}\cdot\text{mL}^{-1}$ CNTs, 120min sonication with 6.5mm tip at 20% amplitude, centrifuged at $122\times 10^3\text{g}$ for 1hr) are shown in Figure 3.12 for the initial solution, the same dispersion after 7 months of incubation and again after 9 months of standing with 2 minutes of additional tip sonication. In contrast to SDS, dispersions of arc CNTs in SDBS exhibit minimal change in spectral fine structure, even after many months of storage. Only subtle loss of resolution is observed due to broadening of the individual nanotube absorbance peaks within the M_{11} and S_{22} bands.

AFM images of the same SDBS dispersion spun coat onto Si wafers were recorded for the initial solution immediately after preparation as well as after 6 months of standing. After 9 months the dispersion was regenerated by sonication for 2 minutes and further analysed by AFM. These results are displayed in Figure 3.13. In the original supernatant the CNTs are quite well dispersed, exhibiting a significantly greater number of objects that could be individual nanotubes compared to SDS. After 6 months most nanotubes are found to exist in relatively large bundles of similar width to those appearing in SDS after 72 hours. However, this aggregation does not appear to have the same level of influence on the absorbance spectrum as observed in SDS. It is possible that aggregates in SDBS may still be partially separated by adsorbed surfactant while in solution, thus facilitating absorption profiles close to those of individualised nanotubes. However, although the SDS dispersion does display a high percentage of bundles in the initial

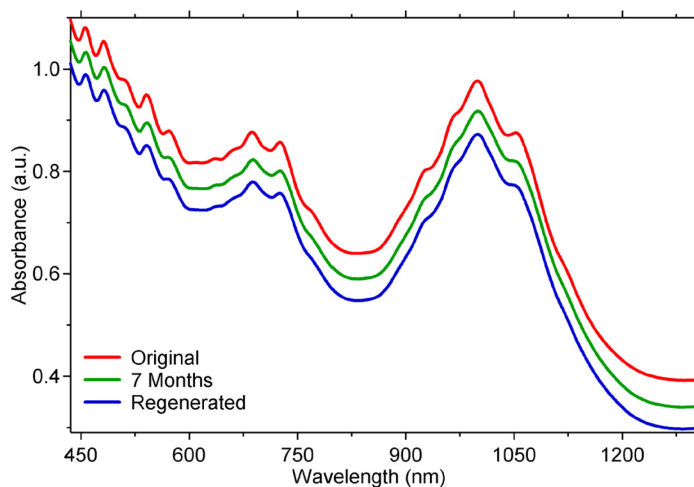


Figure 3.12: UV-Vis-NIR absorbance spectra of arc CNTs in 0.5% SDBS after initial preparation, after 7 months of incubation and regenerated via 2 minutes of tip sonication after 9 months standing. Spectra are offset vertically by ± 0.02 .

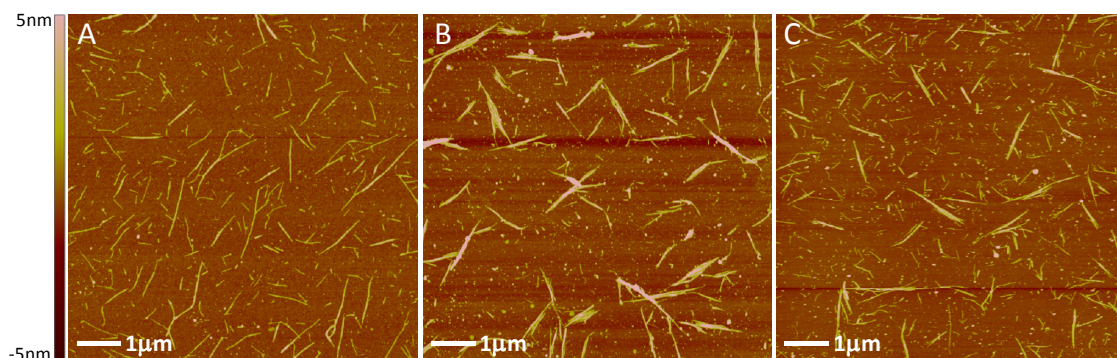


Figure 3.13: 8x8 μ m AFM height images for arc CNTs dispersed in 0.5% SDBS immediately after preparation (A), after 6 months of incubation (B) and regenerated via 2 minutes of tip sonication after standing for 9 months (C).

solution and these become progressively larger over the 72 hour period for which the spectral decay is observed, the extent of absorbance intensity loss does not seem to correlate with the level of aggregation observed. This implies that an additional mechanism of spectral decay is also in effect in SDS solutions, a possibility that is explored experimentally and discussed in greater depth in Chapter 7.

The aggregated SDBS dispersion could be regenerated to some extent through additional sonication, as shown in Figure 3.13C for the SDBS solution after 9 months of standing followed by 2 minutes of processing at 20% amplitude with the 5mm tip. While this does not completely return the nanotubes to their original level of separation, the size and prevalence of the bundles are significantly reduced. This result suggests that dispersions exhibiting a reasonable degree of stability in their absorbance spectrum may be stored for a period of time and further utilised following a short sonication step, although it remains preferable to use freshly prepared solutions.

3.4 Optimised Dispersant Concentrations

3.4.1 SDBS and DOC: Dispersant Concentrations and Mass Ratios

Although it has been demonstrated that optimal concentrations exist for nanotube dispersion,^{326,327} few surfactants have been examined to such an extent.^{115,118} Optimal surfactant concentrations were therefore determined for a selection of surfactants that provided reasonable dispersion for arc CNTs. As SDBS and DOC were established to be the most efficient dispersants, displaying the greatest resolution of absorbance fine structure and good stability for both types of CNTs, these were analysed in detail. Two

differing approaches toward optimising nanotube dispersions have been discussed in the literature. One approach suggests that enhanced dispersion may be accomplished through selection of an appropriate surfactant concentration.^{118,327} Alternatively, improved dispersion might be obtained through tuning of the mass ratio between the dispersant and the nanotube material.^{122,123} In order to determine the best optimisation method for dispersing arc-type nanotubes, both of these parameters were examined simultaneously.

Three separate series of solutions with varied surfactant content were produced at initial CNT loadings of 0.25, 0.5 and 0.75mg·mL⁻¹ in both DOC and SDBS through 10 minutes of tip sonication (10mL, 5mm tip, 20% amplitude) and 1 hour of centrifugation at 122x10³g and their UV-Vis-NIR spectra were recorded. Figures 3.14A and B show the amount of CNTs remaining in the supernatant (measured via the S₂₂ areal absorbance) as a function of surfactant concentration for DOC and SDBS respectively. Figures 3.14C and D show the same data as a function of the surfactant to CNT mass ratio, using the weight of the raw CNT material (thus including all impurities). Some amount of scatter is present, particularly for the 0.25mg·mL⁻¹ CNT loading series at low DOC concentrations, which may be related either to the inhomogeneity of the raw

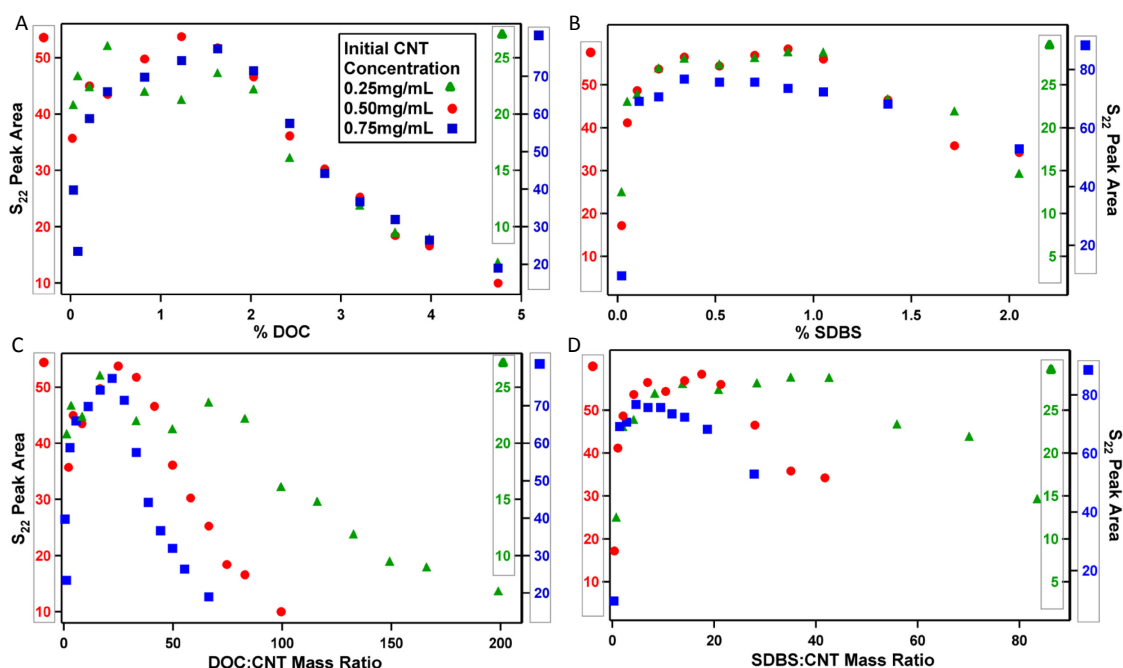


Figure 3.14: Relative amounts of arc CNTs remaining in the supernatant as a function of surfactant concentration for DOC (A) and SDBS (B) for three different initial CNT loadings, as measured by the S₂₂ areal absorbance. The same data are reproduced as a function of the ratio of surfactant to CNT material by mass for DOC (C) and for SDBS (D). Separate scales are used for each series for ease of comparison.

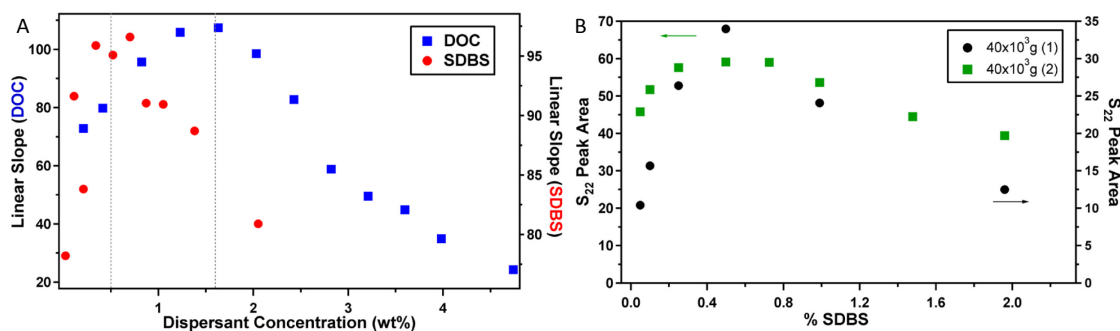


Figure 3.15: (A) Results of linear regression analysis of the peak areas obtained for the three series of different nanotube loading presented in Figure 3.14; and (B) S_{22} peak areas for two repeat series of $0.5\text{mg}\cdot\text{mL}^{-1}$ arc CNTs bath sonicated in SDBS solutions of varied concentration and centrifuged using lower accelerating force ($40\times 10^3\text{g}$).

material or to mass errors from measuring such a low weight of CNTs. The maximum amount of nanotubes remaining in the supernatant (or optimal dispersion effectiveness) is evidently far more correlated with the absolute surfactant concentration in both cases, rather than the ratio of surfactant to CNT material. Although only a small range of CNT concentrations have been examined, this is strong evidence in favour of the defined surfactant concentration approach to nanotube dispersion.

In order to extract the optimal concentrations for SDBS and DOC the peak area data in Figure 3.14 was plotted for each individual surfactant concentration as a function of the initial nanotube loading concentration. This provided 10-12 separate curves (each containing 3 data points) that were each fit with a linear regression. The resulting slopes for these fits were then plotted against the dispersant concentration as shown in Figure 3.15A, where the optimal concentrations are more clearly defined. The optimal values were determined to be $\sim 1.6\%$ for DOC and $\sim 0.5\%$ for SDBS (dotted lines in the figure). The S_{22} peak areas measured for two repeats of the $0.5\text{mg}\cdot\text{mL}^{-1}$ SDBS solution series dispersed using bath sonication (1 hour) and a lower centrifugation speed ($40\times 10^3\text{g}$) are given in Figure 3.15B. These samples were more weakly dispersed due to the lower energy input of the bath sonicator, therefore a lower centrifugation speed (approximately one-third the RCF used for tip-sonicated samples) was applied. Despite this, these series also exhibited a similar peak in the remaining nanotube concentration, occurring in approximately the same position as the tip-sonicated samples. These two series were prepared in exactly the same manner with the exception that the depth of the bath was varied by several millimetres, being lower in the series labelled (1). The altered depth of the bath likely reduced the energy transfer efficiency as it resulted in

poorly dispersed samples and thus lower values of $A(S_{22})$. However, the more weakly dispersed samples serve to highlight the peak in supernatant CNT concentration as the nanotubes were depleted to a greater extent during the centrifugation cycle in this series.

3.4.2 Determining Optimal Concentrations for Alternate Dispersants

A selection of non-ionic dispersants were also analysed in order to determine optimal concentrations for arc nanotube dispersion. The changes in relative CNT concentration for arc nanotubes dispersed in Brij S-100, Triton X-405, Pluronic F-127 and PVP-55 (10mL, 10min sonication with 5mm tip at 20% amplitude, centrifuged at $122 \times 10^3 g$ for 1hr) are displayed Figure 3.16. The initial CNT loading was $0.75 \text{ mg} \cdot \text{mL}^{-1}$ in each case. An optimal surfactant concentration may be derived from the S_{22} areal absorbance for each dispersant except for PVP-55, where the apparent CNT concentration increases with surfactant concentration up to 17% at which point the absorbance spectrum is saturated. Similarly, the $S_{22}:\text{BG}$ resonance ratio displays similar behaviour to the S_{22} peak trend in each case except for PVP-55 which exhibits a decreasing $S_{22}:\text{BG}$ ratio

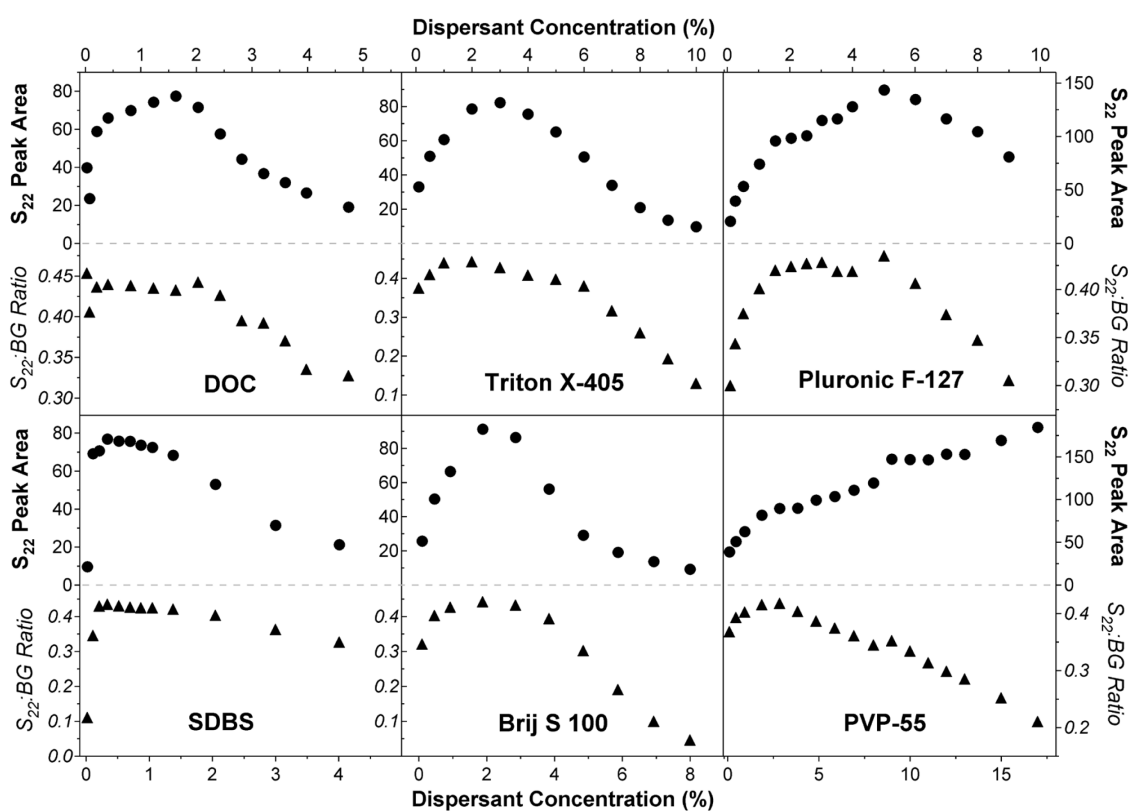


Figure 3.16: Relative arc CNT concentrations remaining in the supernatant as a function of surfactant concentration, measured via the S_{22} peak area of the absorbance spectra for six different dispersants. The $S_{22}:\text{BG}$ ratio is also shown in each case. Initial CNT mass loading was $0.75 \text{ mg} \cdot \text{mL}^{-1}$ for all samples.

above 3%, i.e. the background absorbance is increasing at a greater rate than that of the CNT peaks. Thus, it is likely that the cause of the increase in CNT concentration is not that more surfactant is available for dispersion, but rather it is due to the increase in solvent viscosity, resulting in more material (including large bundles and non-nanotube carbon particles) being retained in the supernatant for a fixed centrifugation speed and time. This effect was also noted (though to a lesser extent) for the other large dispersants Pluronic F-127, TX-405 and Brij S-100, manifesting as an increased overall concentration in the supernatant with increasing dispersant content, and is a primary reason for using S_{22} peak area instead of the measured absorbance intensity. It is likely more pronounced in the case of PVP-55 as it is a long-chained linear polymer possessing a molecular weight five times greater than the next largest surfactant analysed, which would increase the solvent viscosity at a faster rate. Therefore, the optimal dispersion concentration for PVP-55 is taken as the inflection in S_{22} peak area at 3%, corresponding to the maximum in the S_{22} :BG ratio. Note that the break between 8-9% PVP-55 (and 4-5% for Pluronic F-127) arose from two sample sets being centrifuged separately due to limited rotor slots, and a small amount of systematic deviation occurs between centrifugation runs. In summary of these results the optimal surfactant concentrations for arc CNT dispersion are approximately 1.6 (DOC), 0.5 (SDBS), 3 (Triton X-405), 2 (Brij S-100), 5 (Pluronic F-127) and 3% (PVP-55).

The value of 5% for Pluronic F-127 is similar to a previous result, where multi-walled CNTs were found to be less dispersed by this surfactant at around 5% weight per volume.³³⁶ For SDBS, varied optimal concentrations have been reported, including ~0.09%,³¹² 0.5%,³³⁷ ~0.74%¹²² (considering a ratio of 1:10 CNT to surfactant under the conditions used here) and above ~1.37%.³¹⁹ The values of 0.5 and 0.74% agree quite well with the results presented here, falling within the peak range of areal absorbance values between ~0.3 and 0.8%. In the determination of 0.09%, a significantly lower starting CNT concentration was used, which may account for the discrepancy, although the range examined did not exceed 0.45% and no peak was observed. The suggestion that nanotubes are individualised only at concentrations greater than 1.37% does not account for the reduced dispersion obtained at higher surfactant content observed here. More recently, the amount of CNTs remaining has been shown to fall away sharply after reaching around 1.5% SDBS for HiPCO nanotubes,¹¹⁸ with a similar trend. Dispersions of nanotubes in DOC have been reported to saturate at concentrations above 0.5% of this surfactant,³³⁸ however relatively few data points were presented and

concentrations above 2% were not investigated, thus no peak in dispersion efficiency was observed. Although dispersions have been obtained using a range of concentrations for the other surfactants, optimal values have not been previously reported in the surveyed literature.

Analysis of these same solutions using Raman spectroscopy was applied to provide additional data in support of the optical absorbance results. The intensities of the RBM and G bands after background subtraction were used as indicators of the relative amount of nanotubes dispersed in solution, and these peaks scaled equivalently across each sample series. The Raman spectrum of PVP-55 recorded at concentrations above approximately 1% of the polymer showed a broad fluorescent background which is consistent with sample degradation under the high intensity laser beam, therefore further analysis of this series was not performed. The RBM trends are presented in Figure 3.17, along with calculated D:G ratios. The D:G ratio is considered to be associated with the purity of the solution in some form as the D-band is related to defects in the CNT

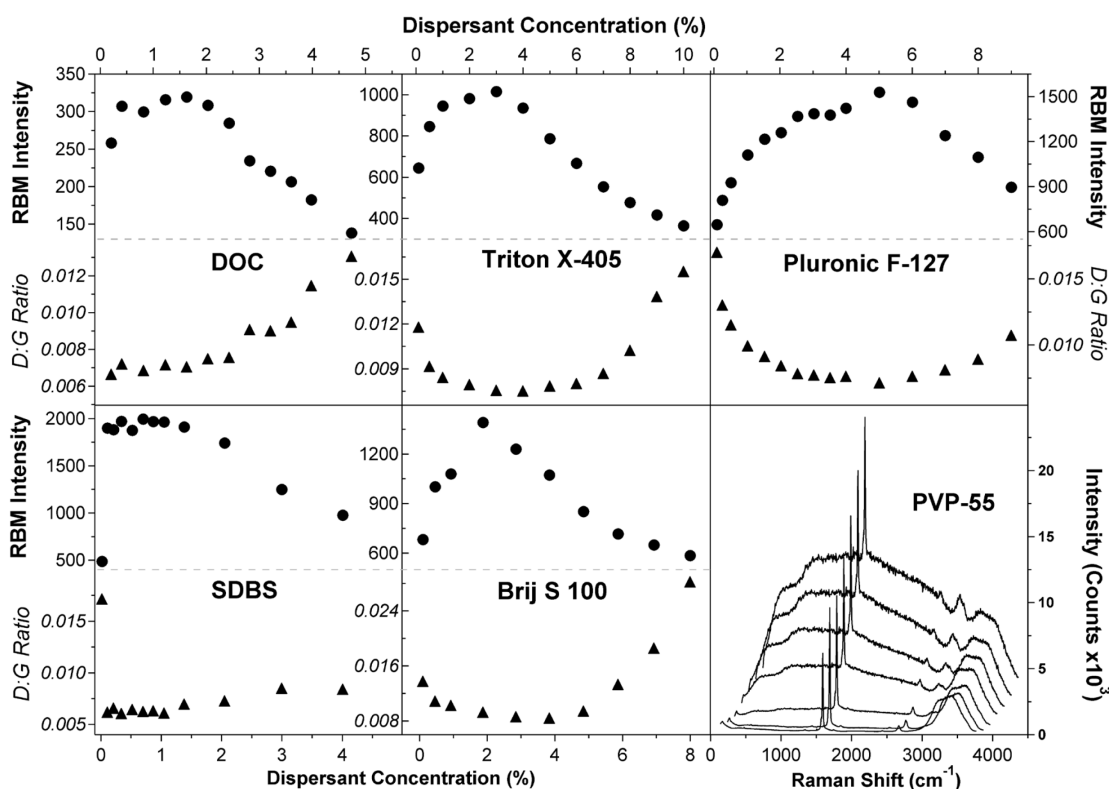


Figure 3.17: RBM intensity and D:G ratio trends (from spectra recorded at 2.33eV excitation) for arc nanotubes dispersed in a series of concentrations of each dispersant. For PVP-55, a broad fluorescence background that increased with concentration prevented accurate intensity determination. Raman spectra for aqueous PVP-55 solutions at 0.1, 0.9, 2.9, 5.9, 8, 12 and 17% are shown (bottom right), from lowest to highest intensity respectively, with a horizontal offset increasing by 100cm⁻¹ with each spectrum.

structure as well as the amorphous carbon content. However, the bundling state also influences the D:G ratio, with more disperse nanotubes producing a lower value.^{339,340} Since each sample was processed in the same manner, the defect density should not be significantly different between samples. The amount of impurities retained may differ slightly between each dispersant due to the viscosity of the solution etc., however the smaller surfactants (of low viscosity) exhibit the same D:G behaviour as the larger (higher viscosity) molecules. Consequently, the observed changes in D:G ratio are more likely to be dependent on the aggregation state of the nanotubes rather than impurity content, though these effects are convoluted. The RBM and D:G trends correlate reasonably well with the UV-Vis-NIR data, with maximum RBM intensities and minimised D:G ratios occurring at approximately the same positions as for the S₂₂ areal absorbance and S₂₂:BG ratio maxima, supporting the previously determined optimal concentrations for dispersion.

3.4.3 Attractive Depletion in SDBS Dispersions

The CNT concentration remaining in the supernatant is thought to decrease at higher surfactant concentrations due to attractive depletion interactions.^{94,326,327} Simulations using rods (CNTs) and spheres (surfactant micelles) have shown these effects to depend on the length of the rod,³⁴¹ with longer rods inducing greater depletion. Therefore, once the pressure exerted by the surfactant micelles is large enough to induce re-aggregation of the nanotubes, longer nanotubes are forced together preferentially to provide a larger reduction in the osmotic pressure. The hydrodynamic radius of the micelle will also have an influence on the extent of the depletion attraction, thus each surfactant will induce a depletion effect at a different micelle volume fraction dependent on the nature of the molecule involved. This explains the variation in the surfactant concentration at which the onset of depletion is evident for the different dispersants in Figure 3.16.

The depletion effect is not immediately apparent in the UV-Vis-NIR spectra of sonicated (uncentrifuged) dispersions, with the optical absorbance being similar for each concentration as shown in Figure 3.18. However, sedimentation is observed after several days of standing, with higher surfactant concentrations inducing a faster rate of flocculation. Figure 3.18B displays a photograph of the uncentrifuged solutions after approximately 4 months of incubation, where no visible flocculation has occurred for an SDBS concentration of 0.5%. A significant percentage of the CNTs have re-aggregated

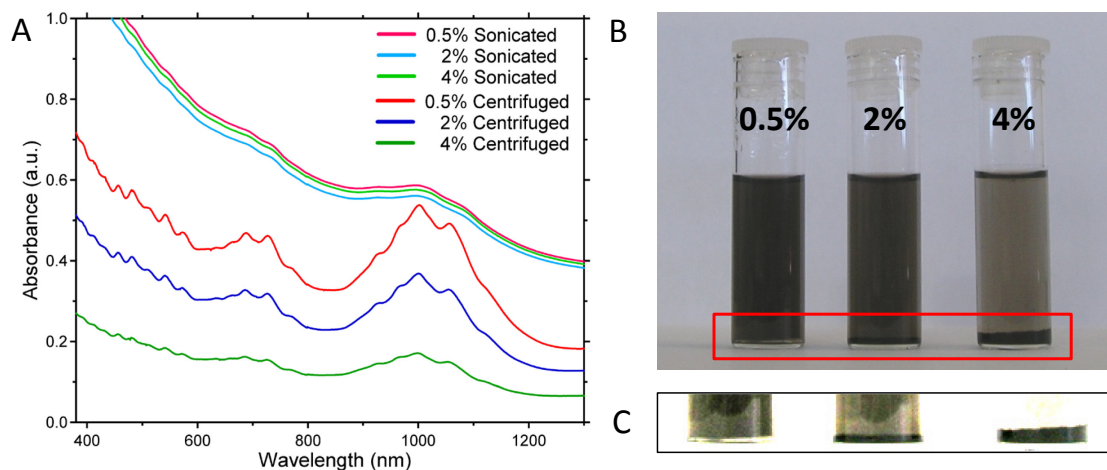


Figure 3.18: UV-Vis-NIR absorbance spectra of arc CNTs dispersed in 0.5%, 2%, and 4% SDBS before and after centrifugation (A). Spectra of sonicated samples are diluted 1:10 and scaled by 0.5 for comparison. An image of the diluted, uncentrifuged solutions after several months is shown (B) with an enhanced high contrast image of the highlighted segment (C). Visible sedimentation of CNTs is negligible for 0.5%, significant for 2%, and dominant for 4% SDBS.

for the 2% sample, while at 4% SDBS the majority of CNTs are no longer dispersed. Absorbance spectra of the remaining suspensions after flocculation showed substantially reduced intensity but essentially identical spectral shapes to the original uncentrifuged solutions.

Centrifugation greatly enhances the depletion effect, since once the nanotubes re-bundle the agglomerates sediment out under the enhanced gravitational forces. Figure 3.19 shows AFM images of CNTs on Si wafers cast from SDBS dispersions having surfactant concentrations of 0.5, 2 and 3%. The CNTs appear to be well dispersed in 0.5% SDBS, existing primarily in small bundles or as individual tubes. Increasing the SDBS concentration to 2% appears to result in a slight reduction in CNT concentration and a significant amount of re-bundling. While this re-bundling could potentially be an artefact of the spin coating and drying processes, mainly individual tubes are observed for lower SDBS concentrations over a large number of images, hence it is most likely to be a direct reflection of the dispersion state in solution. There seems to be a close association of bundles to one-another, forming elongated networks. Such network formation may be a result of preferential stabilisation of nanotube junctions, where the surfactant adsorbs to adjacent hydrophobic surfaces.³¹⁶ Much shorter bundles remain in the supernatant when the SDBS concentration is further increased to 3%, though the nanotubes still appear to be tightly grouped. This length reduction is analogous to that

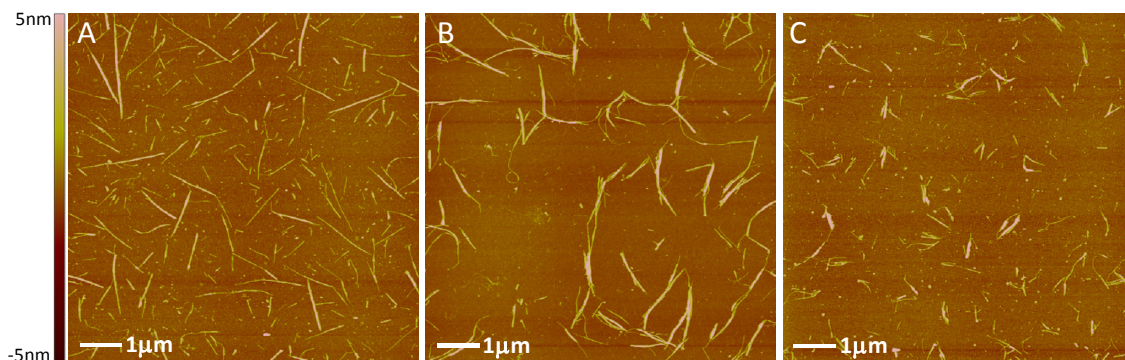


Figure 3.19: AFM height images ($8\times 8\mu\text{m}$) of arc CNTs spin coated onto Si wafers from dispersions of 0.5% (A), 2% (B), and 3% (C) SDBS.

previously observed in SDS⁹⁴ and may potentially be used as a simple method to separate out shorter nanotubes, although the low yield and aggregated state of the CNTs are significant disadvantages. Indeed, a recent study has utilised attractive depletion effects induced by adding polyethylene glycol to CNTs dispersed with DNA in order to fractionate nanotubes by length with promising results, suggesting that other nanoparticles may also be sorted by size in a similar manner.³⁴² An alternative explanation for the aggregation of CNTs at high surfactant loading is through the formation of micellar networks which could bridge aggregates and cause the larger CNT-dispersant complexes to sediment out during centrifugation.³⁴³ However, this mechanism does not offer an explanation for the observed length separation, hence depletion effects are the most likely cause of nanotube aggregation.

The AFM results confirm that the CNTs are well dispersed where the S_{22} absorbance area is maximised, and that increasing the surfactant concentration beyond the position of this maximum causes flocculation of the CNTs into long thin ‘ropes’ or loosely associated bundles. It has been suggested that increasing the initial mass ratio of CNT can inhibit this effect as more surfactant is required to disperse the CNT, thus reducing the micelle concentration and shifting the onset of depletion effects to higher surfactant concentrations,¹²⁶ however this effect was not observed to any appreciable degree for the different CNT concentrations used in this work.

As the average length of the nanotubes remaining in the supernatant is drastically reduced with increasing surfactant concentration, this further explains the behaviour of the Raman D:G ratios in Figure 3.17. Since the D:G ratio is increased by the presence of defects, and shorter nanotubes possess more nanotube ends per volume, a reduction in nanotube length produces larger values of the D:G ratio for the ensemble.³⁴⁴ Thus, at

low surfactant concentration the nanotubes are initially poorly dispersed and slightly aggregated, hence the D:G ratio is relatively large. With an increase in surfactant concentration, more exfoliated CNTs of moderate length may be retained in the supernatant, thus the ratio is reduced. This continues until the maximum concentration of nanotubes for that dispersant is reached, which corresponds to the minimum in the D:G ratio (and maximum RBM intensity). The onset of attractive depletion effects then drives the longer nanotubes out of solution, decreasing the average length of those that remain in the supernatant, thus the D:G ratio is gradually increased by shortening of the bundles. The effect of length reduction on this ratio is likely to be stronger than that of aggregation, as documented in the following chapters, though both effects would contribute to the increasing D:G value.

Chapter 4

INFLUENCE OF CENTRIFUGATION PARAMETERS ON DISPERSION PROPERTIES

4.1 Effects of Centrifugation Speed, Duration and Temperature

In order to analyse the effects of the centrifugation parameters of accelerating force, duration and rotor temperature on the properties of the resulting nanotube dispersion obtained in the supernatant, three series of samples containing $0.5\text{mg}\cdot\text{mL}^{-1}$ of as-produced arc CNTs in 0.5% SDBS solution were prepared via tip sonication and centrifuged under different conditions. Specifically, these series were: (1) 50mL solutions sonicated for 30 min at 22% amplitude with a 6.5mm microtip and centrifuged at $120\times 10^3\text{g}$ for times ranging from 20 minutes to 6 hours in the Type 70 Ti rotor; (2) 50mL solutions sonicated as per (1) with the applied accelerating force varied from 20×10^3 to $240\times 10^3\text{g}$ and centrifugation time kept constant at 1 hour (also in the Type 70 Ti rotor); (3) 10mL solutions dispersed via 10min sonication at 20% amplitude with a 5mm microtip and centrifuged at $122\times 10^3\text{g}$ for 1 hour in the Type 50 Ti rotor at different temperatures. For series (1) and (2) duplicates were prepared for a selection of

samples such that a sufficient volume was collected for production of CNT films through vacuum filtration. The supernatants of both replicates were combined into a single solution in these cases.

The nanotube-containing supernatant solutions from each series were analysed by UV-Vis-NIR spectroscopy, Raman spectroscopy and AFM. The results obtained from these techniques are combined in Figure 4.1 for ease of comparison, while details of the specific procedures used in the acquisition of this data are presented in the following sections along with a more thorough analysis for each technique.

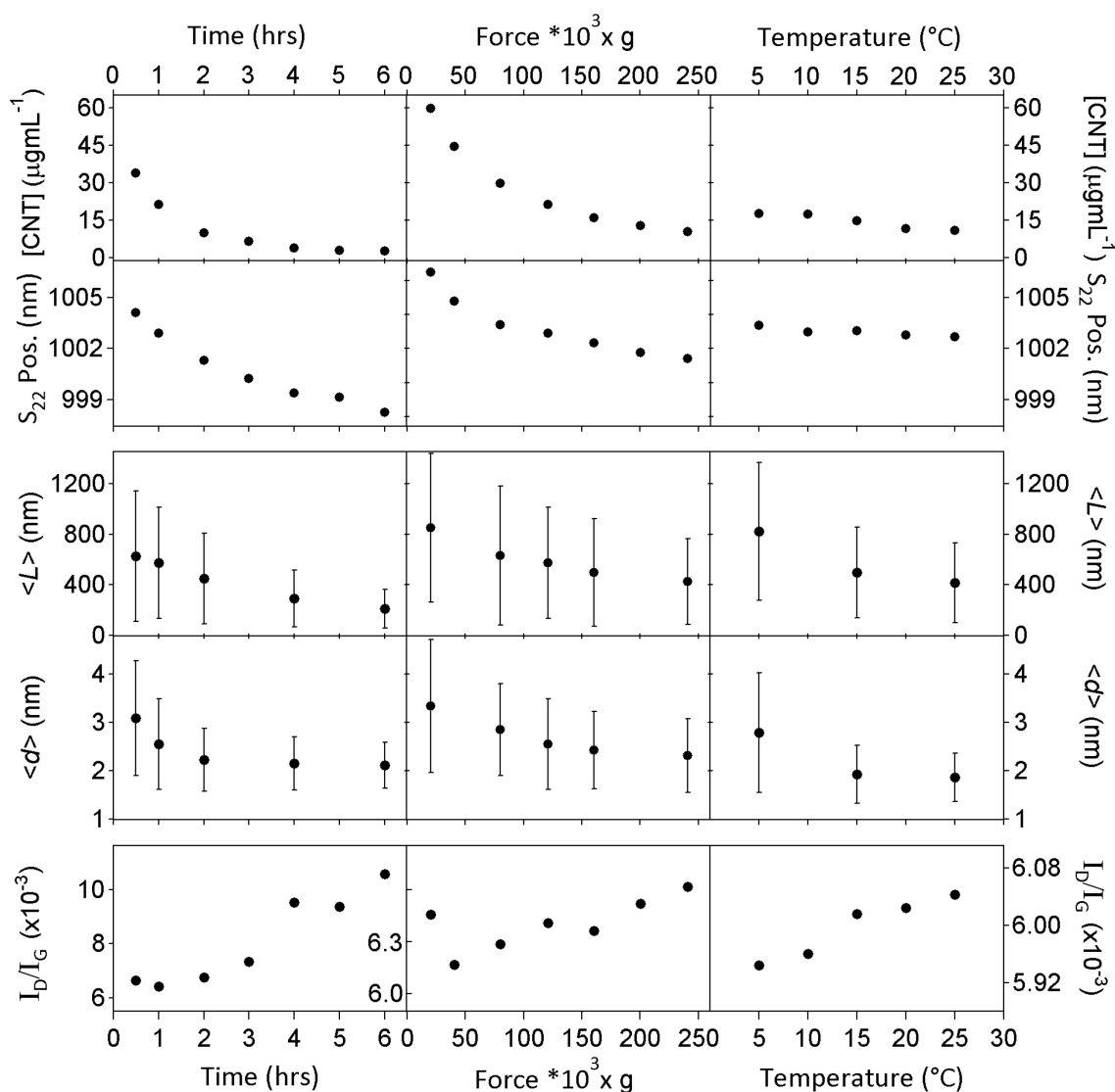


Figure 4.1: Results obtained for UV-Vis-NIR (top), AFM (centre) and Raman (bottom) analysis of CNTs dispersed in SDBS centrifuged under different conditions. Concentrations of nanotubes in the supernatant, $[CNT]$, were determined from absolute absorbance at three different wavelengths (see Section 4.1.1 for details) and averaged, while the S_{22} peak position was determined at the maxima of the band. For AFM data average values of length $\langle L \rangle$ and diameter $\langle d \rangle$ for the measured distributions are shown, with error bars denoting average deviation from the mean. Raman intensity ratios I_D/I_G were generated at an excitation energy of 2.33eV.

4.1.1 Measurement of the Extinction Coefficient

The concentration of CNTs remaining in the supernatant may be estimated through application of the Beer-Lambert law to optical absorption spectra. However, as the positions of the CNT peaks shift slightly with exfoliation or removal of CNT bundles from the suspension, the measured concentration may not be an accurate reflection of the true one if the reference extinction coefficient (ϵ) was calculated from a more (or less) disperse sample. An increase in the absorption coefficient at low nanotube concentrations has been reported, which may be related to this de-bundling effect.¹⁰⁸ Additionally, the extinction coefficient is different for metallic and semiconducting CNTs,¹⁸⁰ and likely between nanotube species, thus estimates of the CNT concentration may vary for a given sample subject to the chosen wavelength. Nonetheless, an attempt to quantify the concentration of nanotubes remaining in the supernatant was made by calculating the extinction coefficient from the sequential dilution of a solution of known concentration.

As-produced CNTs were first purified through dispersion in 0.5% SDBS by 30 minutes of tip sonication (6.5mm tip) at 22% amplitude before centrifugation at $\sim 20 \times 10^3 g$, with the supernatant collected and subsequently filtered through a 0.22 μm PTFE membrane. 0.55mg of this pre-purified CNT material was redispersed in 10mL 0.5% SDBS via sonication (5mm tip, 20min at 20% amplitude) and diluted sequentially to generate a calibration curve. The absorbance spectra recorded for this consecutively diluted sample are displayed in Figure 4.2A. Extinction coefficients were extracted by linear regression of plots of the absorbance at fixed wavelength as a function of the nanotube concentration, exemplified in Figure 4.2B for wavelengths of 689, 850 and 1000nm. The extinction coefficient varies significantly with wavelength as shown in Figure 4.2C. Calculated extinction coefficients are given in Table 4.1 and compared with previously reported values for various CNT samples at different wavelengths. In general, coefficients are in the vicinity of 29-35mL \cdot mg⁻¹ \cdot cm⁻¹ for wavelengths centered over the M₁₁ and S₂₂ peaks, but are significantly lower when measured on or near the 'background' absorbance level.

The nanotube absorbance spectrum of the re-dispersed CNTs is significantly red-shifted relative to that of the centrifuged samples (~ 13 nm shift for S₂₂, ~ 6 nm shift for M₁₁), thus the extinction coefficients calculated at wavelengths corresponding to the peak maxima will be reduced relative to those of the centrifuged samples, resulting in estimated

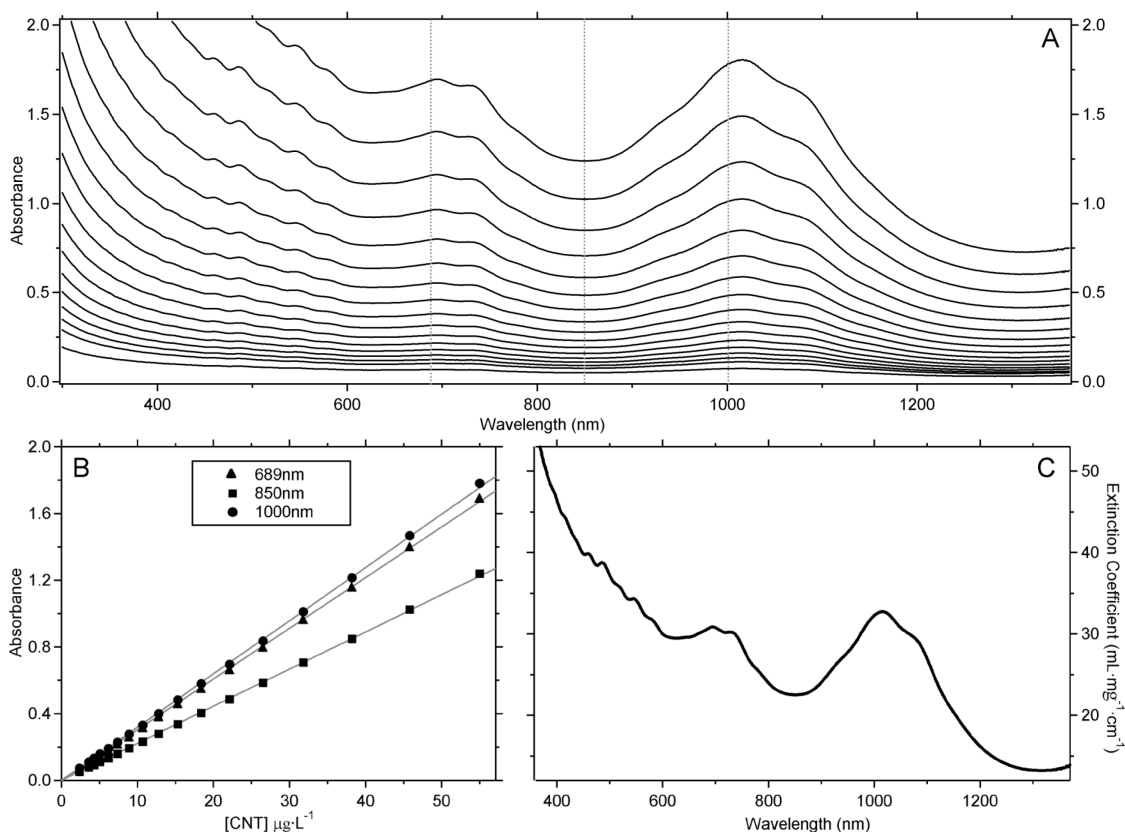


Figure 4.2: UV-Vis-NIR absorbance spectra for sequential dilution of a known concentration of arc CNTs in 0.5% SDBS (A), plots of absorbance vs. concentration for several wavelengths (B), and the calculated extinction coefficient as it varies with wavelength (C).

concentrations greater than their actual values. To partially compensate for this, as well as the previously mentioned ambiguities in estimates of CNT concentration, calculations were performed at three wavelengths; 689 (M_{11} , $\epsilon = 30.76$), 850 (background, $\epsilon = 22.51$) and 1000 nm (S_{22} , $\epsilon = 32.27\text{mL}\cdot\text{mg}^{-1}\cdot\text{cm}^{-1}$), with the average value taken as the approximate CNT concentration in solution (although the value calculated from the background at 850nm is likely the most accurate as the spectral shape in this region is the least affected by changes in aggregation state, and this concentration was always lower than for the other two wavelengths). The concentration of CNTs remaining in the supernatant after centrifugation was determined via this method for the samples centrifuged under different conditions, where the accelerating force, duration and rotor temperature were varied, and these values are presented in Figure 4.1 with corresponding discussion in the following section. The average deviation over the three wavelengths was approximately $\sim 1.6\mu\text{g}\cdot\text{mL}^{-1}$ for all samples analysed, which equates to a mean variance within a sample of $\pm 4.1\%$ of the estimated

concentration. This percentage variance between calculated concentrations from the three different wavelengths reached a maximum of $\pm 6.7\%$ of the mean value for any given sample.

| ϵ (mL·mg ⁻¹ ·cm ⁻¹) | | λ (nm) | CNT Type | Reference # |
|---|------------|-------------------|-------------|----------------|
| This Work | Literature | | | |
| 30.0 | 33.4 | 600 | Arc | 140 |
| 29.8 | 32.6 | 660 | HiPCO | 108 |
| 29.8 | 33.9 | 660 | HiPCO | 345 |
| 30.8 | 32.3 | 689 | Arc | 346 |
| 28.4 | 30.0 | 751 | Arc | 89 |
| 23.5 | 22.0 | 891 | CoMoCAT | 116 |
| 31.9 | 30.3 | 1035 | Arc | 346 |
| 30.8 | 35.0 | 1050 | Arc | 89 |

Table 4.1: Extinction coefficients for CNTs dispersed in SDBS calculated at various wavelengths.

To combat such errors in the determination of nanotube concentration from absolute absorbance, areal absorbance measurements of the M_{11} and S_{22} peaks may also be used as indicators of the relative amount of nanotubes dispersed in solution. This method is perhaps more accurate than use of the absolute absorbance as it includes contributions from each species within a band simultaneously, rather than calculating a concentration from a single wavelength. Errors that might be introduced due to different nanotube species possessing slightly varied extinction coefficients may also be reduced, while the areal method is less affected by the background absorbance which arises from many factors such as the amorphous carbon content, spectral congestion and aggregation effects.³⁴⁷ Despite this, a linear relationship generally exists between the calculated values of CNT concentration and the measured areal absorbance for each data set as shown in Figure 4.3. Therefore either method may provide an estimate of the CNT concentration, although the accuracy of both is affected by the original calibration curve and the nature of the solution from which it was derived. Further trends throughout this work will be described in terms of the S_{22} peak area as a relative measure of concentration, however peak area values may be converted to an estimate of concentration through the relations determined in Figure 4.3; $A(S_{22}) = 2.881 \cdot [\text{CNT}]$ and $A(M_{11}) = 0.510 \cdot [\text{CNT}]$. Note that for significantly high concentrations or poorly dispersed nanotubes these relationships would break down.

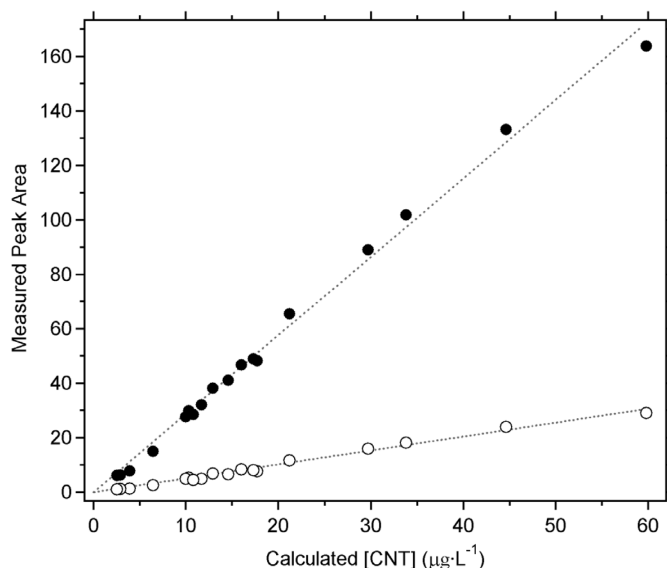


Figure 4.3: Relationship between measured S_{22} (solid circles) and M_{11} (open circles) areal absorbance values and the calculated concentration of nanotubes remaining in the supernatant as determined via the Beer-Lambert law.

4.1.2 Analysis by UV-Vis-NIR Spectroscopy

UV-Vis-NIR absorbance spectra for the solutions prepared under various centrifugation conditions are provided in Figure 4.4. The nanotube concentration in the supernatant is gradually depleted with increasing centrifugation force and time, asymptotically approaching a constant value (Figure 4.1). While a lower CNT concentration is also found with increasing rotor temperature, it is clear that this parameter has the least

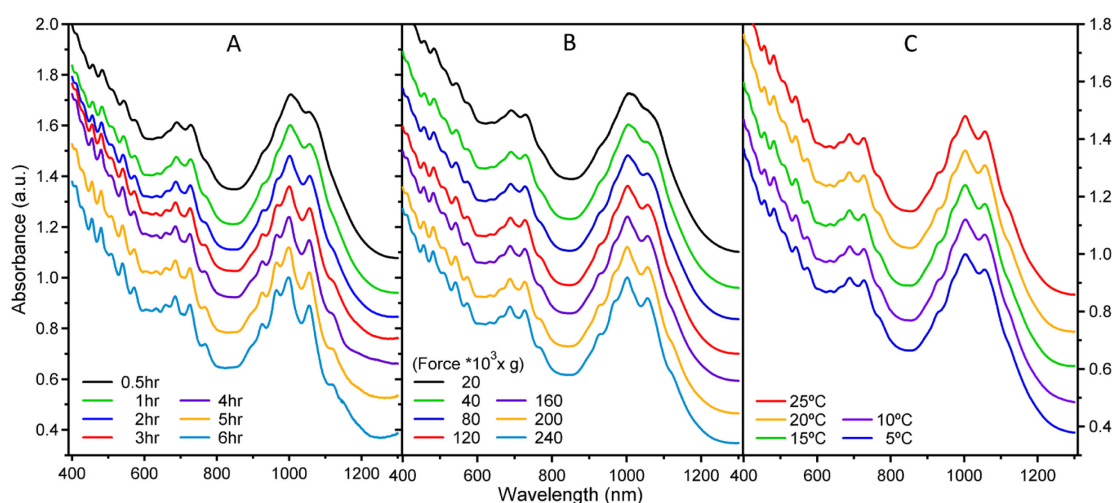


Figure 4.4: Optical absorbance spectra for supernatant solutions of as-produced CNTs dispersed in SDBS via tip sonication and centrifuged for different durations (A), under different accelerating forces (B) and at different rotor temperatures (C). Spectra are normalised to the S_{22} peak and offset by 0.12 for clarity.

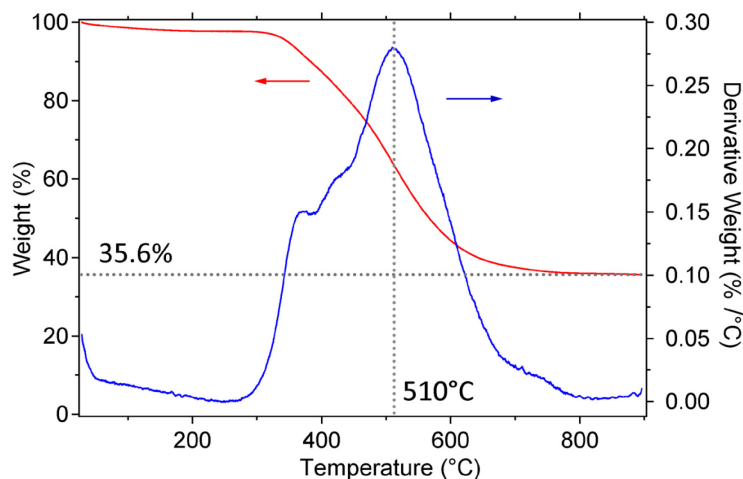


Figure 4.5: TGA analysis of raw arc CNT soot. Residual ash content was measured as approximately 35.6 weight percent, which is slightly higher than the expected 30% metal content reported by the manufacturer (also determined by TGA in air).

influence on the amount of CNTs retained in the supernatant. Concentrations from ~ 2.5 - $60 \mu\text{g}\cdot\text{mL}^{-1}$ were measured using the method described in the previous section, with approximately 12% of the original material retained at $20 \times 10^3 \text{g}$ for 1hr while a meagre 0.5% of the original mass remains after 6 hours at $120 \times 10^3 \text{g}$. Although metallic catalyst particles account for around 35% of the original mass according to TGA results (see Figure 4.5), and further contributions from amorphous and graphitic carbon particles are also involved, ultracentrifugation of these dispersions is a considerably low yield process.

For arc nanotubes, having relatively large diameters, absorptions from individual CNT species are closely spaced and are difficult to resolve.¹²⁰ In Figure 4.4 it is shown that absorption peaks from individual species within the S_{22} and M_{11} bands become more distinct with centrifugation at greater accelerating forces, higher temperatures and for longer times. This evolution of the fine structure within the absorption bands is linked with the removal of bundles from the solution with increasing force, time and temperature. While increasing the speed of rotation does promote faster removal of the nanotube aggregates, centrifuging for longer periods of time results in much better separation, with the progressive improvement in resolution being most pronounced for the time series. While greater accelerating forces are available this increases the strain in the rotor; the polycarbonate tubes used in this work were not rated above $265 \times 10^3 \text{g}$. Further removal of bundles would be achieved with more intense forces, though at a cost of lower yield as with increasing centrifugation time. Although minimal differences

in the spectra are observed with changing rotor temperature, altering it in combination with the applied force or duration could increase either the rate of separation (higher temperatures) or the amount of CNT retention (lower temperatures) as desired.

Removal of CNT aggregates leaves an increasingly greater percentage of individual nanotubes in the solution, which is coupled with the blue-shift of the absorbance peaks as shown in Figure 4.1 where the trends in CNT concentration and peak position are strongly correlated. This is a well-documented effect, however the use of peak position in UV-Vis-NIR spectra as a measure of dispersion state is not common practice, likely because the positions of peak maxima depend highly on the type of nanotubes being studied and the associated (n, m) species present. Peak positions and spectral profiles have recently been found to vary considerably between empty and water-filled CNTs,^{208,209} adding the possibility that the observed blue-shift could be partially due to the removal of filled CNTs during centrifugation while empty nanotubes remain. However, due to the relatively intense nature of ultrasound processing applied in this instance the vast majority of CNTs in these dispersions are expected to be open-ended and thus contain water.

The position of S_{22} peak maxima is found to vary up to 8nm among the dispersions presented here, from ~1006nm for the lowest accelerating force down to ~998nm when centrifuged for the greatest amount of time. This shift in absorbance peak position complicates estimates of nanotube diameter that are based on optical absorbance spectra, though the expected mean diameter may still be approximated from the observed energies. Using the relations provided by Saito *et al.*³⁴⁸ the average diameters of the CNTs in these suspensions are calculated as 1.37, 1.40 and 1.44nm from the S_{11} (1768nm), S_{22} (1000nm) and M_{11} (687nm) peak maxima respectively (from an SDBS dispersion in D_2O). However, deconvolution of the S_{22} absorbance bands of semiconducting nanotubes reveals these values to be an underestimate, likely due to the relatively high uncertainty in the derivation process for these particular relationships. According to (n, m) assignments made using the empirical Kataura plot produced by Weisman and Bachilo³⁹ (see Appendix B), CNTs with diameters from ~1.25-1.75nm are present in these samples with an average diameter around 1.5nm. A mean diameter of 1.53nm is calculated from the relation $d = 2\gamma_0 a_{c-c} / (E_{11}^S - 0.154)$ given by Li *et al.*,³⁴⁹ which is closer to the value found from direct species assignment (taking $\gamma_0 = 2.9\text{eV}$ and $a_{c-c} = 0.144\text{nm}$).

4.1.3 Analysis by Raman Spectroscopy

Raman D:G ratios for CNT dispersions prepared using different centrifugation parameters were presented earlier in Figure 4.1, and this ratio was found to increase with centrifugation force, time and temperature. As the relative purity of CNTs increases with the removal of carbonaceous and metallic impurities from the solution with centrifugation, one might expect that the Raman D:G ratio would be reduced with increasing force or duration as the relative concentration of nanotubes is increased. However, the removal of the large non-CNT carbon impurities and residual catalyst is mostly accomplished at relatively low centrifugation forces and short periods of time, as will be discussed in Section 4.2. Thus, as with the effect of attractive depletion on the D:G ratio at high surfactant concentrations (see Chapter 3, Section 3.4.3), it is the change in average length of the nanotube ensemble that causes an increase in the D:G value. AFM results, discussed in the following section, show that the centrifugation process serves to enrich the supernatant in short CNTs which have a greater measured defect density due to the increased number of tube ends per cumulative length of nanotube sidewall.^{344,350} This explains the corresponding increase in D:G ratio with increasing centrifugation force, duration and temperature as the dispersed CNT population is reduced in length.

Figure 4.6 shows the D:G ratios determined from Raman spectra of nanotube films that were generated from filtration of the time and force series supernatant solutions. The increasing trend with both force and duration is again apparent in these results; however the D:G values calculated from the solid state spectra are around double those measured in the solution phase. This is consistent with the notion that more bundled nanotube samples produce a larger D:G ratio. Accordingly, the reduction in bundle size with centrifugation time and force should result in a decreasing trend for the D:G ratio,

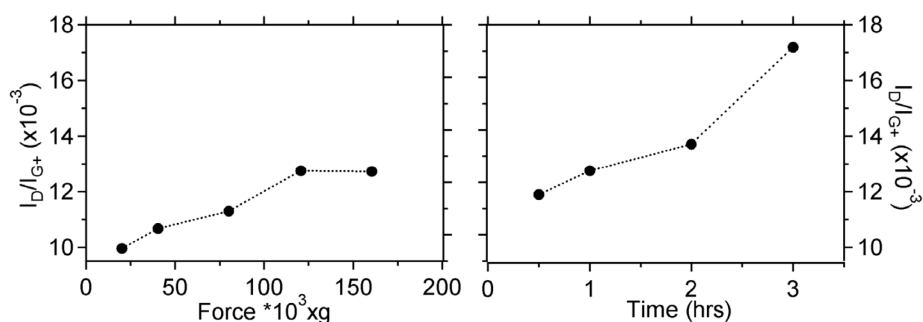


Figure 4.6: Raman D:G ratios determined from Raman spectra of CNT films for the centrifugation force (left) and duration (right) sample series at an excitation energy of 2.33eV.

however it is apparent that the effect of this relationship is overwhelmed by the increase in D:G that accompanies the simultaneous shortening of the bundles. Since the disorder mode is dominated by the defect density of the nanotubes and this quantity is predominantly influenced by the number of nanotube ends in the ensemble, it is not surprising that the CNT length is the primary factor governing the D:G ratio. This result implies that the D:G ratio may be employed toward estimating the mean length of a particular nanotube sample, as will be discussed in Chapter 5.

4.1.4 Analysis by Atomic Force Microscopy

AFM analysis was performed to determine the length and diameter distributions of each sample, as shown in Figure 4.7 for the temperature series and in Figure 4.8 for both the force and duration series. Average values for these distributions are plotted in Figure 4.1, however it is noted that the majority of the measured objects sit below the mean value. Although average diameter values are inflated by the presence of larger bundles, measurements from ‘individual’ CNTs are in the range 1.2-1.8nm, which is expected from optical absorbance data and is reflected by the histograms in Figures 4.7 and 4.8. Populations of dispersed nanotubes may be best described by a log-normal distribution in both length and diameter,^{307,328} where the distribution possesses a greater number of objects with shorter lengths and smaller diameters. This behaviour was observed for all samples, with the distributions positively skewed towards smaller dimensions. Though the log-normal fit may be loosely applied to each sample, it does not fully accommodate for the long tail observed at larger dimensions in some cases, particularly for samples that have been weakly centrifuged.

It is clear that both the average length $\langle L \rangle$ and average diameter $\langle d \rangle$ of the nanotubes (bundles) in the supernatant steadily decrease with increasing centrifugation force and duration. This is expected, as the settling velocity of cylindrical objects in a centrifugal field is influenced by both the diameter and length of the particle, due to their non-exact orientation in the direction of the accelerating force.³⁵¹ Therefore, the migration of the dispersed nanotubes during centrifugation is dependent on both these properties, with longer nanotubes and larger diameter bundles being sedimented earlier. The depletion of longer, thicker objects leads to the decrease in the average length and diameter of the distributions. Again, the duration of centrifugation is more influential than is the applied force over the examined range, while keeping the rotor temperature low results in the

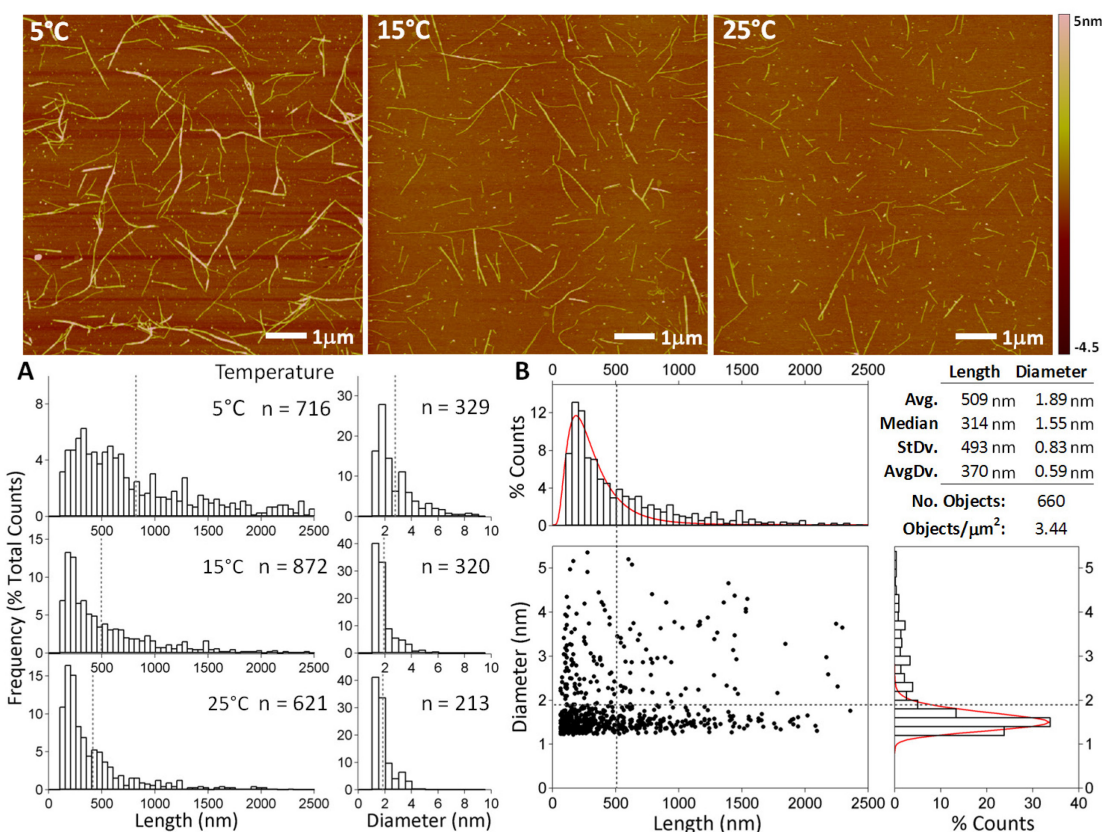


Figure 4.7: AFM analysis of dispersions of arc CNTs in 0.5% SDBS centrifuged with rotor temperatures of 5, 15 and 25°C. 8x8 μm height images are shown (top) for each sample, with the distributions for measured objects given in (A). The value n is the total population for each distribution. Lengths and diameters were determined from 8x8 and 5x5 μm images respectively. In (B) simultaneous length and diameter measurements were made from three 8x8 μm images for the sample centrifuged at 15°C, with statistics for this analysis provided in the table. Grey dashed lines indicate the average values for the distributions, while solid red lines in (B) are log-normal approximations of the data.

retention of slightly longer bundles in the supernatant. Figure 4.7 compares the dispersions prepared at different temperatures, showing that mostly individual nanotubes are present after centrifuging at 15-25°C, while a greater fraction of thicker bundles remain at 5°C. As CNTs dispersed in SDBS remain dissolved in water at 0.5% down to temperatures $\leq 1^\circ\text{C}$ without visible aggregation, and AFM images of a sample spun cast from a solution cooled to $\sim 1^\circ\text{C}$ onto a pre-cooled substrate were found to be essentially identical to those of its room temperature parent (Figure 4.9), this is simply assigned to the greater mobility of the nanotube objects at higher rotor temperature and not due to aggregation of the surfactant-CNT complexes upon cooling.

The mean diameter for arc CNTs was determined by optical absorbance to be approximately 1.5nm, thus from the AFM results presented in Figures 4.7 and 4.8 it is

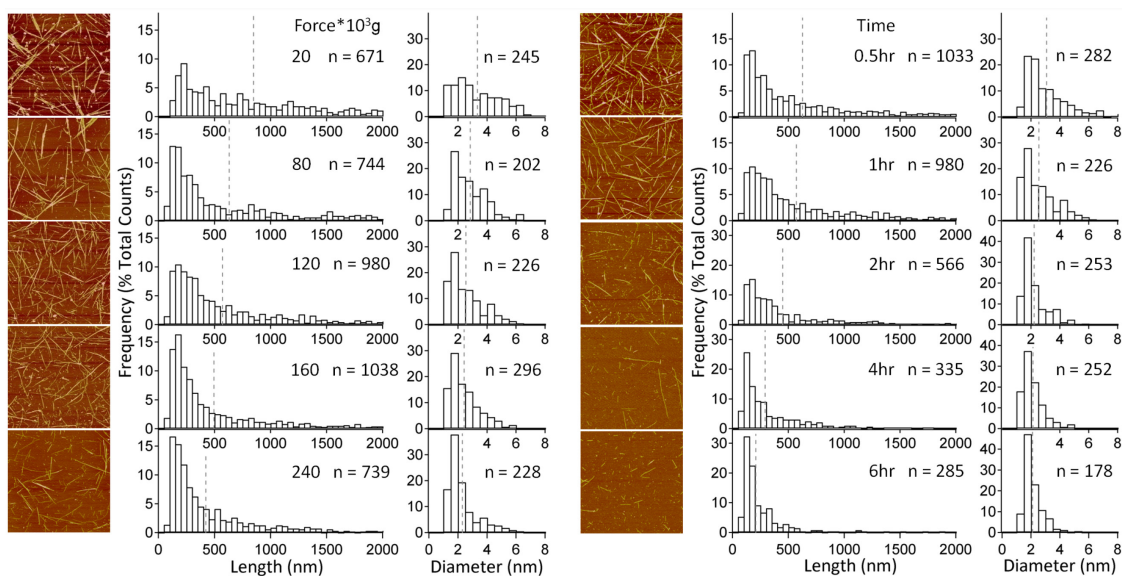


Figure 4.8: Analysis of nanotube bundle lengths and diameters for samples centrifuged with different accelerating forces and for various durations. Representative $5 \times 5 \mu\text{m}$ AFM height images are shown for each sample, where solutions were deposited on the Si surface using 4 deposition cycles. The number of objects analysed in each distribution is given by n , while grey dashed lines indicate average values for the data sets.

apparent that the sonication conditions employed were not sufficient to completely debundle the nanotubes. The smallest diameter within the arc nanotube distribution is slightly greater than 1.2nm , therefore in a close-packed arrangement involving 3 such nanotubes the expected bundle height would be on the order of $\sim 2.3\text{nm}$. Hence, any object with a diameter less than this value has the potential to be an individual object, or possibly a flat bundle containing nanotubes stacked adjacently in a ribbon formation. For the longest durations and highest accelerating forces the number of objects that could potentially be individual nanotubes (taken as any object with measured $d < 2\text{nm}$) is greater than 55%, with less than 10% being close-packed bundles of more than ~ 5 -6 nanotubes ($d > 3\text{nm}$). The amount of individuals present increases to values greater than 75% for the samples centrifuged at 15 and 25°C , which could be due either to a difference in dispersion power between the sonication parameters employed in each sample set (as will be discussed in Chapter 5), or possibly to the greater sedimentation efficiency of the Type 50 Ti Rotor. However, a previously reported study by Bonaccorso *et al.* states that while dispersion of CNTs in SDBS is quite good, individualisation is not.¹⁸⁹ Furthermore, it is also suggested that preferential stabilisation of small bundles may occur in SDBS based dispersions.³⁴³ It is important to consider that these results are primarily from experiments involving nanotubes produced by the

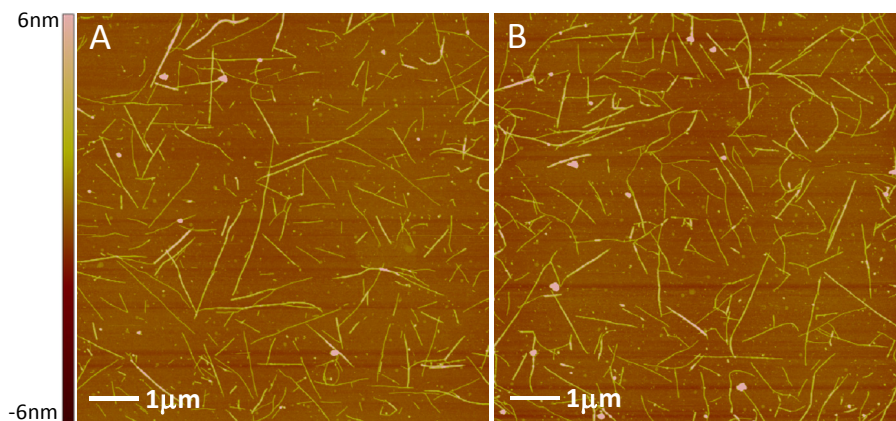


Figure 4.9: 8x8 μm AFM height images of arc CNTs spun coat from 0.5% SDBS solution at room temperature (A) and from a solution cooled to $\sim 1^\circ\text{C}$ deposited onto a pre-cooled Si substrate (B).

HiPCO³⁵² or CoMoCAT¹⁸⁹ methods which are of smaller diameter ($\sim 0.6\text{-}1.2\text{nm}$) to those used here, and the dispersion of CNTs by a specific surfactant is critically sensitive to their diameter as shown in Chapter 3. While some previous results have suggested no diameter dependence for SDBS based dispersions,^{322,325} this surfactant has also displayed a tendency to favour larger diameter nanotubes within the HiPCO distribution,^{189,323} which may imply greater individualisation for CNTs of larger diameter with SDBS. Another point of note is that use of a fixed angle rotor results in some sedimentation along the wall of the centrifuge tube rather than at the base, which could result in the recovery of larger bundles in the supernatant solution. It would be preferential to use a swinging bucket rotor to avoid collecting such residual aggregates.

4.1.5 Uncertainties in AFM Measurement

It is important to note that AFM measurements have a large degree of uncertainty associated with them. In the first instance, AFM only samples a very small sub-population of the dispersion, so a large number of images and objects must be analysed in order for the results to be statistically valid. There are also significant uncertainties inherent in length measurements from the lateral resolution of the instrument, typically on the order of 20-50nm,¹²² with further errors being introduced during determination of the length from the image where misalignment by a single pixel can introduce variations of $\pm 16\text{nm}$ for an 8x8 μm image with 512x512 pixels.

Height measurements can be affected by the condition of the AFM tip, the strength of the applied tapping force, and may also depend on the image resolution and scan

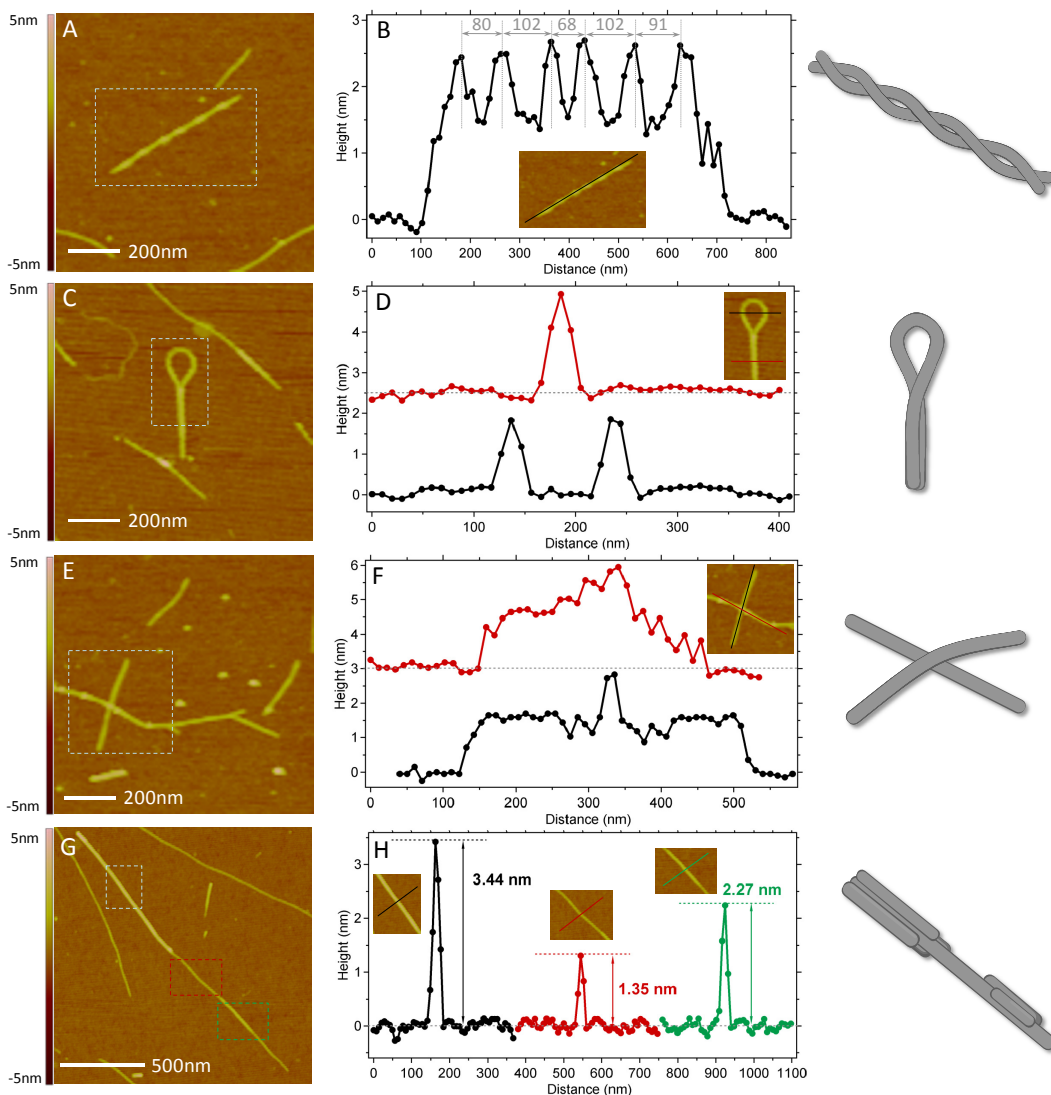


Figure 4.10: AFM height images showing different observed structures of CNTs; (A) spiral bundle, (C) hairpin formation, (E) overlaid individuals, and (G) a bundle of variable thickness. Cross-sections are shown in (B), (D), (F) and (H) for these phenomena, while schematic representations are also pictured (right).

speed.³⁰² Although the most likely configuration for a CNT bundle is the triangular close-packed arrangement,⁶² other conformations are possible for thin bundles. It is essentially impossible to distinguish between individual nanotubes and bundled CNTs that may lie parallel and adjacent to one another in a ‘ribbon’ or raft-like formation, thus estimates of the fraction of individual nanotubes may be exaggerated.³⁵³

Two adjacent nanotubes may twist helically around each other in a spiral bundle, as shown in Figure 4.10A and again in Figure 4.11, although these were not the most common bundle formation observed. The screw pitch of these twisted bundles was consistently measured to be between 60 and 110nm (~80nm on average), which is on

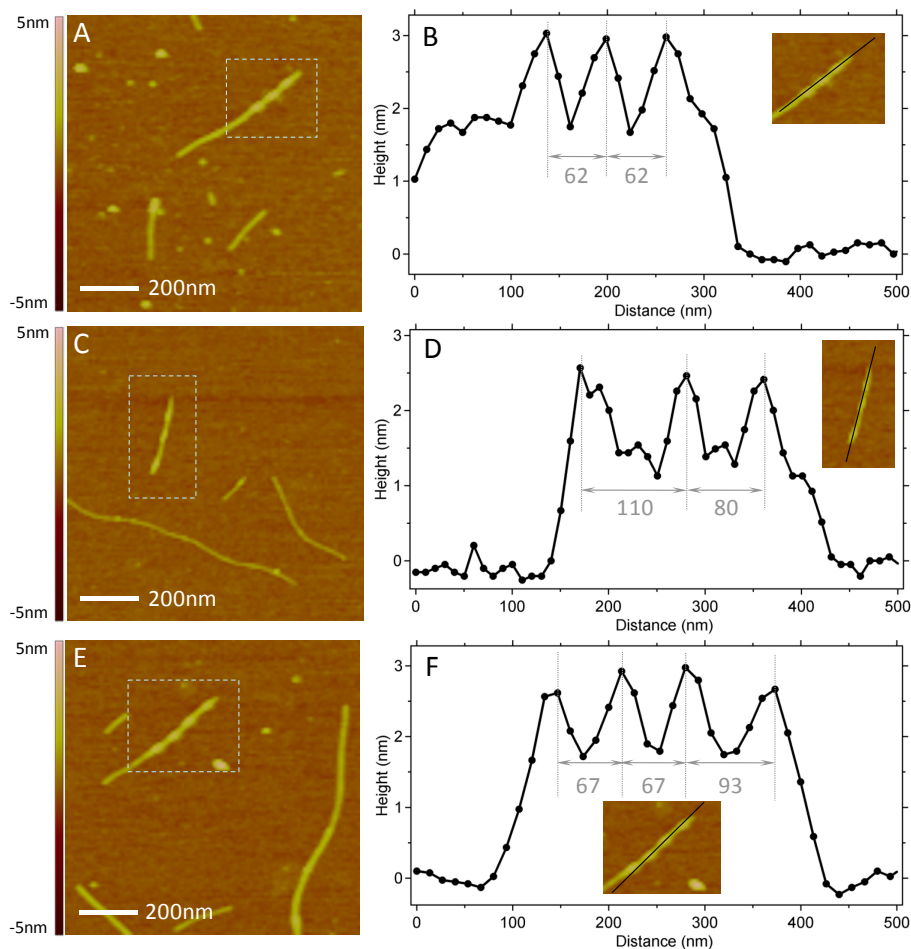


Figure 4.11: (A), (C) and (E) are AFM height images showing spiral bundles of CNTs. (B), (D) and (F) depict cross-sections where screw pitches of the helical bundles are measured from consecutive maxima

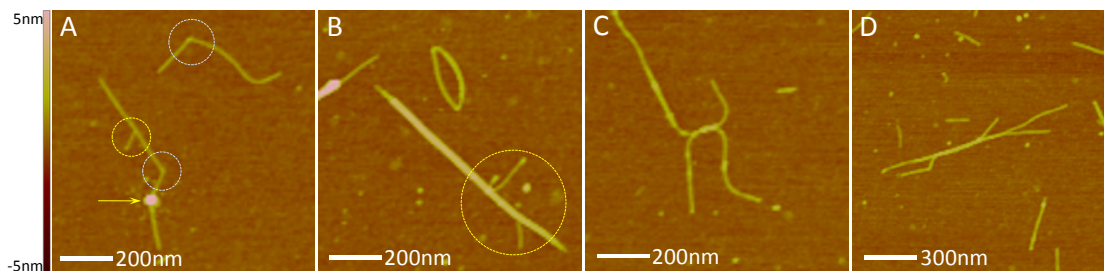


Figure 4.12: AFM height images showing kinks (A), ring folding (B), tangling (C) and bundle splitting (D). Bundle splitting is also evident in (A) and (B) as highlighted by the yellow circles, while the arrow in (A) points to a potential catalyst particle.

par with the smallest such value measured for free standing nanotube bundles.³⁵³ Nanotubes grown on the substrate were found to possess larger screw pitches (~ 200 nm) and were found to be more likely to form ribbon-like bundles. Therefore, the fact that bundles observed here possess screw pitches closer to those exhibited by free standing CNT bundles may indicate that the ribbon-like bundles observed by Wang *et al.* are formed preferentially by nanotubes grown on the silicon wafer and not necessarily by

solution-deposited CNTs. However, there is still a significant probability that spin-coated nanotubes assemble into flat, raft like bundles upon coming into contact with the substrate and are present within the AFM results presented here; although if such a bundle were to be deposited from solution it is likely that it would bend over itself, leading to raised sections within the bundle which would allow elucidation of its actual form.

Spiral bundles complicate measurements of diameter using cross-sections as height values may change along the bundle length. This is also true for single nanotubes that sometimes double back on themselves in a hairpin formation (Figure 4.10C), where an individual nanotube could potentially be measured as a bundle. Additionally, where individual nanotubes overlay each other (Figure 4.10E) the measured height is increased for the upper nanotube as it arches over its underlying counterpart. Bundles were also observed to change intrinsically in thickness along their length, with CNTs potentially terminating at intermediate positions within the bundle as in Figure 4.10G (though such a profile could also be produced by a twisted ribbon-like bundle). Partially exfoliated bundles were commonly observed with shorter segments often peeling off from the main strand (Figures 4.12B and D). Large bundles were generally measured as a single object, although where the exfoliated nanotube ends were clearly separated from the aggregate these were measured as separate nanotubes if the length approached 200nm, since these objects could produce optical spectra similar to completely individualised nanotubes based on exciton diffusion lengths.

The occurrence of distinct kinks and catalyst-particle mediated breaks (Figure 4.12A), rings with no visible endpoints (Figure 4.12B) and randomly tangled networks of CNTs (Figure 4.12C) also cause complications for measurements of nanotube length. For these reasons, algorithm-based height and length measurements that may be performed on AFM images were avoided in favour of manual determination of diameter and length which allowed a certain level of discretion in these measurements. However, care had to be taken not to bias the results, thus selection of bundle segments of intermediate thickness for cross-section measurement was attempted in all cases.

Height measurements were also found to be highly dependent on the reference points taken on the 'flat' surface, which may have a significant level of roughness associated with it. Cross-sections of the silicon substrate taken from a 5x5 μm height image are shown in Figure 4.13, where a maximum height variation of $\sim 0.5\text{-}0.6\text{nm}$ per μm is

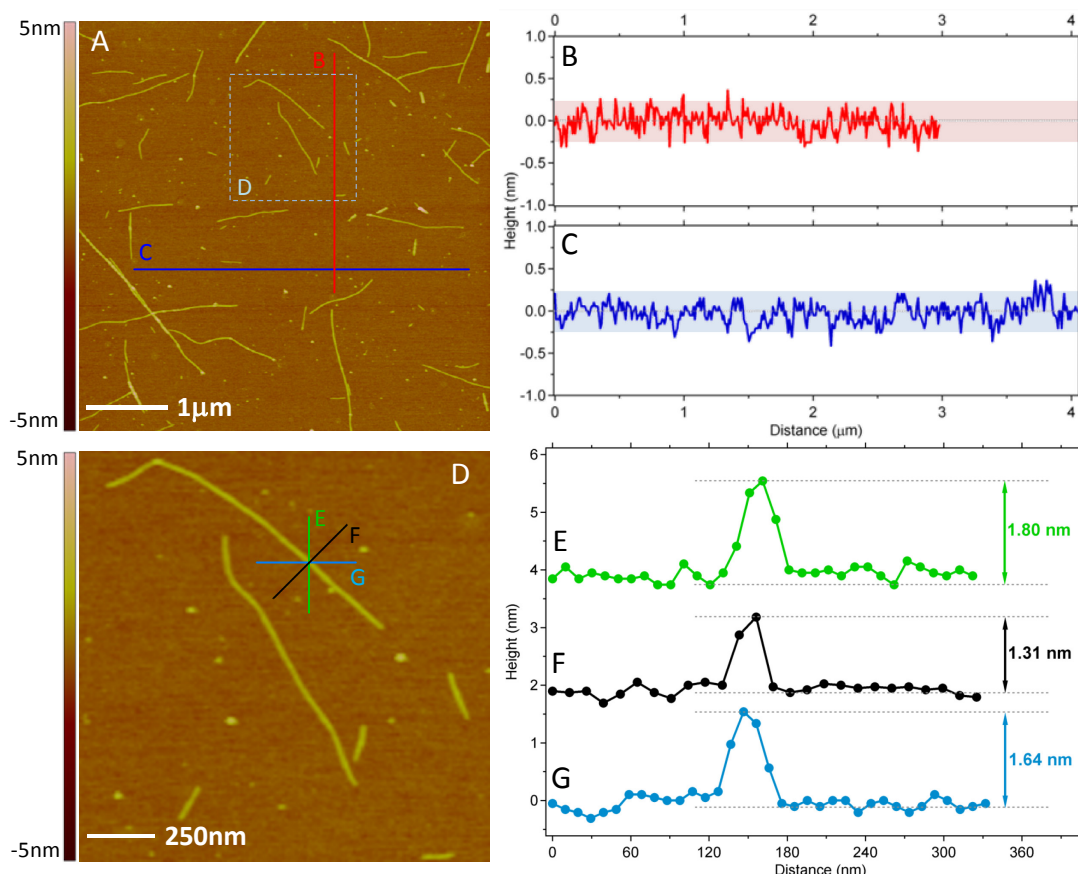


Figure 4.13: A $5 \times 5 \mu\text{m}$ AFM height image of arc CNTs spun coat from 0.5% SDBS solution (A), with sections taken along the silicon substrate perpendicular (B) and parallel (C) to the scan direction. Shaded bands in (B) and (C) are 0.5nm in width. An expanded region from A is shown in (D), where cross-sections taken perpendicular to the scan direction (E), across the nanotube axis (F) and along the scan direction (G) yield different height (diameter) values. Sections (E) and (F) are vertically offset by 4 and 2nm respectively.

observed. For these reasons, height (diameter) measurements may exhibit large deviations when recorded from multiple positions on the same individual object and also depend on the direction of the cross-section, as shown in Figure 4.13D. Consequently, variation can be considerably large within measurements of the same object, thus several sections were usually taken to determine an intermediate value for each particular bundle. Although comparisons may be made between samples based on relative changes in the average bundle diameter, considering the number of potential sources of error AFM may not be the best technique for accurately determining nanotube diameters for large sample populations. It is certainly not possible to assign (n, m) indices to any individual nanotubes from their AFM images, particularly if recorded over such a large length scale and with relatively fast scan rates.

Generally, diameters measured from individual nanotubes are expected to be lower than their actual values due to radial deformation of the tube structure on the surface through van der Waals forces, though this effect is predicted to be small for CNTs in the diameter range examined in this work (and is likely not detectable within error in any case).³⁵⁴ Measured values below the expected height were encountered, but this was probably due to surface roughness. Residual surfactant remaining on nanotube surfaces could also have increased measured diameter values, though additional washing or baking of the surfaces at $\sim 200^{\circ}\text{C}$ under vacuum did not alter the height distributions.

Finally, it is known that spin-coating of CNT solutions can lead to separation according to length and bundle size due to the centripetal forces applied during deposition, with longer nanotubes being more prevalent at greater radial distances.³⁰⁶ Deposition was performed at a relatively slow rotation speed with low acceleration to minimise this effect, with all images collected near the centre of the wafer for the analyses presented here. AFM images collected from near the substrate periphery did not appear to differ in length from those collected elsewhere on the sample under these deposition conditions.

4.2 Centrifugation as a Purification Technique

4.2.1 Analysis of CNT Films by SEM

SEM images of unmodified nanotube samples at various stages of the dispersion-centrifugation process are shown in Figure 4.14. Note that these samples were prepared separately to those analysed in Section 4.1, and were dispersed using bath sonication for 1 hour while centrifugation was performed using the Type 50 Ti rotor.

The as-produced arc nanotube soot is highly disperse, containing large clusters of non-nanotube material which appears to be the dominant component. Sonication in 0.5% SDBS solution and filtering through a $0.22\mu\text{m}$ membrane produces a more compact film, however the majority of the non-nanotube material is retained; i.e. the nanotube content is not noticeably improved simply by filtering the dispersions as the majority of impurities are larger than the pore size of the PTFE membrane used in this instance. A slight residue also appears to be present on the film surface and is observed to fuse under electron irradiation, which may suggest some remaining surfactant within the samples despite rinsing with both acetone and water, however the carbonaceous

material and nanotubes themselves might also be ablated by bombardment with high energy electrons in the absence of any such residue (melting of the centrifuged nanotube films also occurred for prolonged exposures at high magnification). Determining the presence of residual surfactant through EDX of the sonicated film is not rigorously conclusive since the as-produced material contains a substantial amount of sulfur, however EDX spectra of the films shown in Figure 4.14 did not show any signal from sodium which would be expected if the surfactant was retained in significant quantities.

The CNT films obtained after centrifugation are much smoother and more uniform, containing far less visible particulate matter. Dense networks of nanotube bundles are

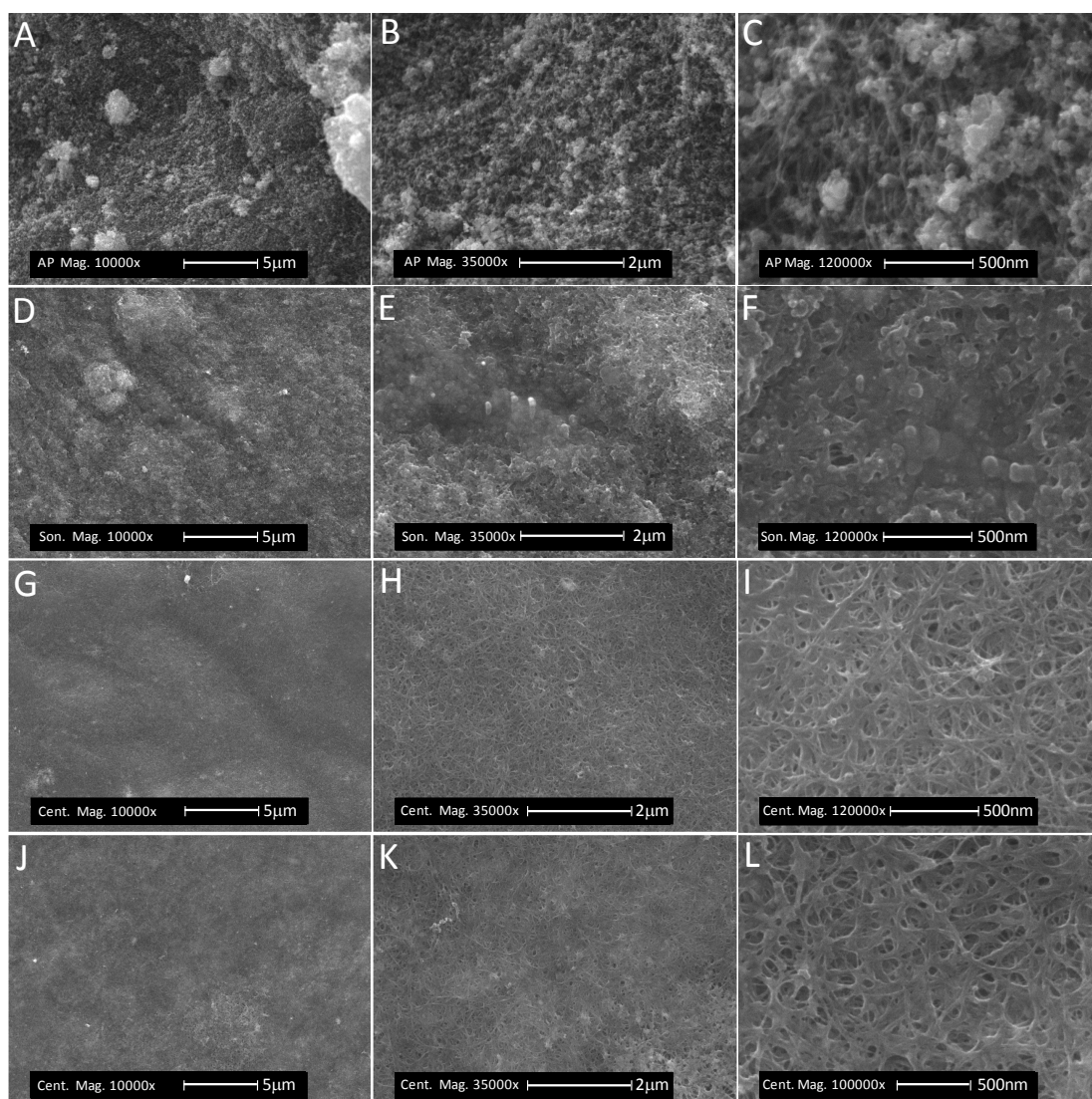


Figure 4.14: SEM images of as-produced arc nanotubes (A-C) as well as CNT films produced from sonicated SDBS dispersions prepared without centrifugation (D-F), after centrifugation at $40 \times 10^3 \text{g}$ (G-I) and after centrifugation at $122 \times 10^3 \text{g}$ (J-L). Images were recorded using secondary electron detection at an accelerating voltage of 10keV.

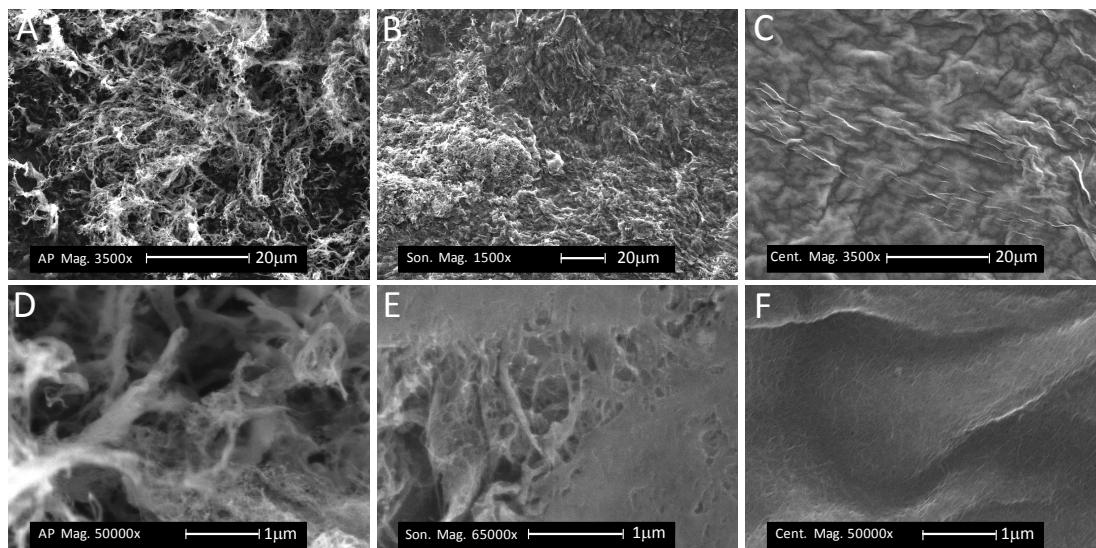


Figure 4.15: SEM images of as-produced HiPCO nanotubes (A and D) as well as films produced from SDBS dispersions before (B and E) and after centrifugation at $122 \times 10^3 \text{g}$ (C and F). Images were recorded using secondary electron detection at an accelerating voltage of 10keV.

revealed in the centrifuged samples at high magnification, while these films are virtually indistinguishable between the two applied accelerating forces of 40×10^3 and $122 \times 10^3 \text{g}$. This suggests that reasonable purification of nanotube material is possible using comparatively low centrifugation forces, however a more detailed analysis is required to determine the relative impurity content for samples centrifuged under different conditions. Similar to arc CNTs, considerable improvement in the uniformity of HiPCO nanotube films recovered from SDBS dispersions was observed between the as-produced material, a dispersion filtered before centrifugation and the filtered supernatant solutions (Figure 4.15), although the HiPCO raw product does not appear to contain as many non-nanotube impurities.

4.2.2 Analysis of CNT Films by TEM and EDX

Films of CNTs were also obtained from vacuum filtration of the supernatants of the centrifuged samples analysed in Section 4.1, with EDX analysis performed for both the time and force series. Spectra were collected using an electron beam energy of 20keV and a 60 second count time, while all spectra were normalised to the carbon K_{α} peak at approximately 0.28keV for comparison. An additional nanotube film was also prepared from a tip-sonicated dispersion without centrifugation, where this film was washed only with acetone. EDX spectra for this sample as well as that of the as-produced nanotube

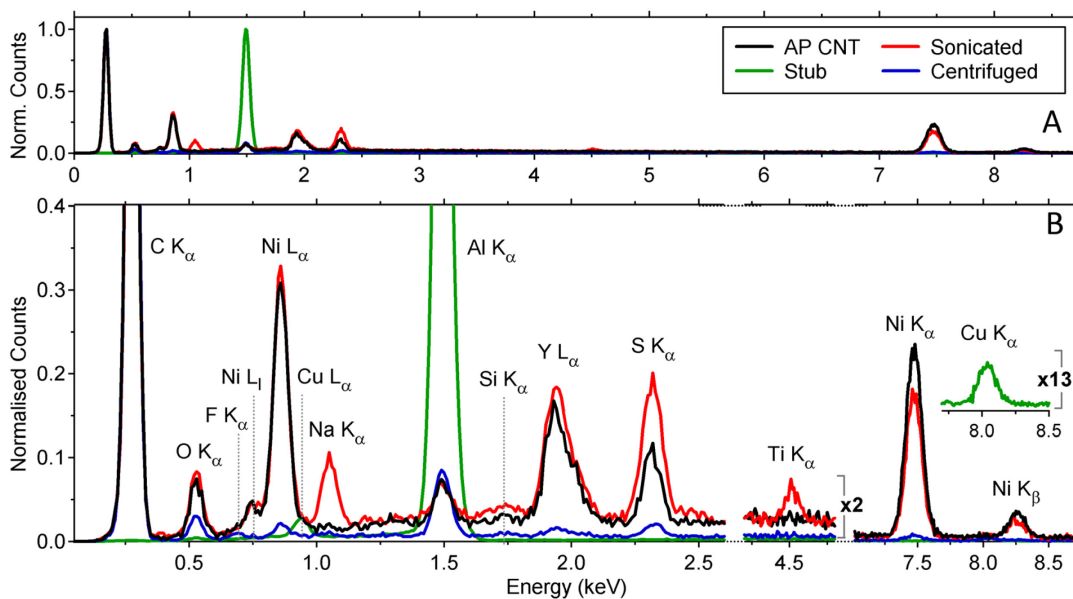


Figure 4.16: (A) EDX spectra for as-produced arc CNTs (black), an aluminium SEM stub (green), a CNT film produced from an SDBS dispersion without centrifugation or H₂O rinsing (red), and the film produced from the sample centrifuged at $40 \times 10^3 \text{g}$ for 1 hour (blue). Expanded energy regions with elemental peak assignments are shown in (B). All EDX spectra were normalised to the carbon K_α peak.

soot, a bare aluminium stub and the sample centrifuged at $40 \times 10^3 \text{g}$ for an hour are shown in Figure 4.16. The stub shows peaks from Al and Cu which are also visible in spectra of the nanotube samples. Neither of these metals are expected to be present in the CNT soot at any stage and therefore these peaks are assigned to the sample mount alone. The raw arc nanotube soot contains a large amount of both nickel and yttrium, the catalyst metals used to dope the graphite rods during the CNT synthesis process. As previously mentioned, a large amount of sulfur is also present in the as-produced nanotube material. This is also a residual product from the synthesis process, however the exact form in which it exists in the sample is proprietary manufacturer information. The sulfur signal appears to scale with those of the metallic catalysts Ni and Y hence it may be associated with the nanoparticles, perhaps as metal sulfides. The filtered dispersion that did not undergo centrifugation contains approximately the same level of metallic nanoparticles as does the raw material, again suggesting that filtering does not assist in purification. The sonicated film has a larger sulfur X-ray signal than the as-produced nanotubes, indicating that acetone is not a good solvent for SDBS and that the surfactant is retained in the film. This increase in the sulfur peak is accompanied by the appearance of a sodium peak of significant intensity, which suggests that in the absence

of the sodium peak (as for the majority of the films rinsed with water) most of the surfactant has been removed.

The sonicated but uncentrifuged film also contains a small amount of titanium embedded in it which is due to erosion of the sonicator microtip during cavitation, an effect which will be discussed further in Chapter 5. Ti particles are generally removed during the centrifugation step as evidenced by the lack of this peak in centrifuged samples. In a similar manner, a small silicon peak is also observed in some samples which may be due to cavitation-based corrosion of the silicate glass vial that contains the nanotube dispersion. However, such particles would also be expected to be removed through centrifugation, hence it is possible that the Si peak may indicate contamination of the samples by an unknown source. Contamination of the CNT film by the PTFE filter membrane was also evident for the 20×10^3 and 40×10^3 g samples which show a small fluorine peak.

EDX spectra for each of the samples from the force and duration series are shown in Figure 4.17. To determine the relative metal content remaining within each CNT film, the ratio of the carbon K_{α} peak to both the Ni K_{α} and Y L_{α} peaks was calculated and the resulting values are plotted in Figure 4.18. An increase in this ratio defines a reduction in the metal catalyst content of the sample, and the remaining catalyst content is observed to vary with centrifugation time and force. However, instead of the expected gradual decrease in relative nanoparticle concentration with increasing centrifugation intensity, an initial decrease followed by an increase in relative metal content is observed. This unexpected result warranted further study, thus TEM analysis was conducted on segments of these films for the time series as shown in Figure 4.19.

Both TEM and EDX analysis of the films confirm that a substantial portion of metal catalyst particles is removed from the starting material even after mild centrifugation, which has been demonstrated previously.⁹⁸ However, there is indeed a significant amount of metallic impurities remaining in samples that have been subjected to relatively intense centrifugation. As mentioned earlier, the as-produced material contains a large fraction of Ni and Y particles (approximately 35wt% in this case), most of which are much greater in diameter than the nanotubes themselves. These particles are routinely observed to be coated in a thick layer of carbon which would facilitate surfactant adsorption to their surface and thus allow them to remain well suspended in solution. The largest of these metallic particles and clusters are removed by

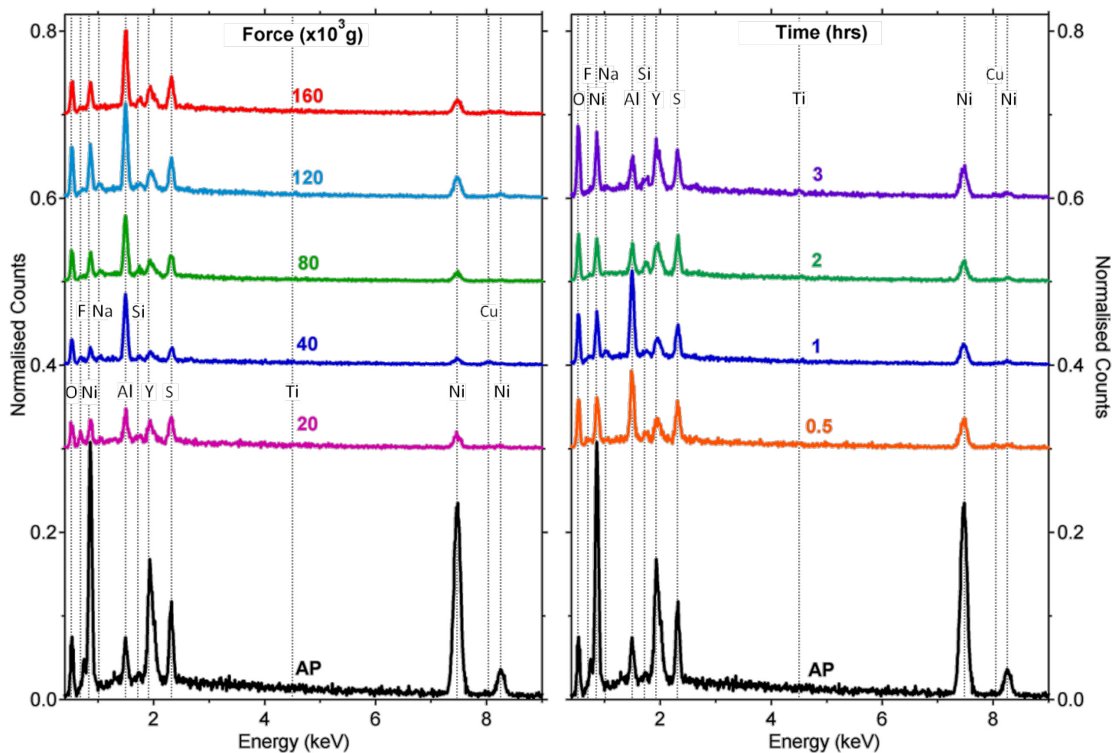


Figure 4.17: EDX spectra for CNT films produced from supernatant solutions of samples centrifuged under different conditions. The spectrum of as-produced (AP) arc CNT soot is also shown for comparison. All EDX spectra were normalised to the carbon K_{α} peak which is off-scale.

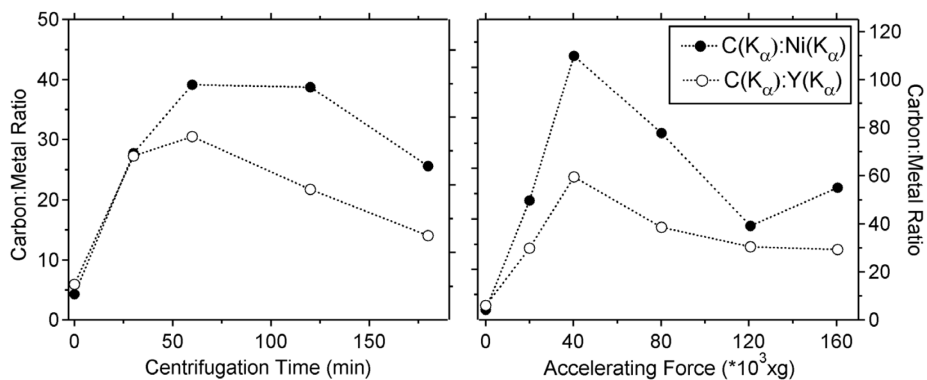


Figure 4.18: Ratios of the carbon K_{α} peak to the Ni K_{α} (filled circles) and Y L_{α} (open circles) peaks calculated from EDX spectra as a function of centrifugation parameters.

centrifugation with low applied forces or over short time scales, which results in the initial increase in the C:Ni and C:Y ratios observed in the EDX spectra, while smaller particles may remain buoyant. As these particles survive in the supernatant, the gradual depletion of CNTs and other carbonaceous species from the solution then drives the carbon-to-metal ratio back down. A peak in the carbon-metal ratios appears at intermediate times (~ 60 min) and forces ($\sim 40 \times 10^3$ g), where the most nanotubes are

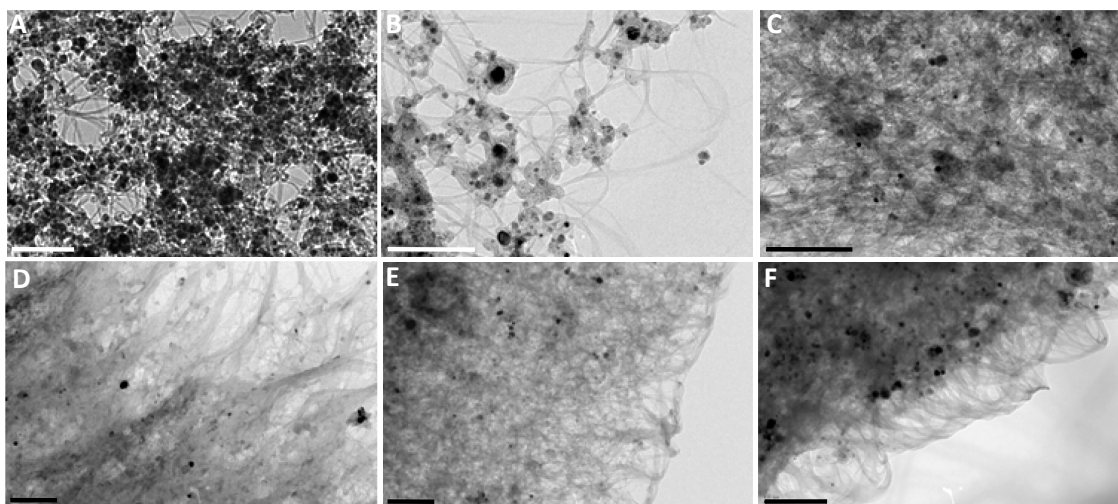


Figure 4.19: TEM images of as-produced CNTs (A, B) and of nanotube films produced from the supernatants of solutions centrifuged for 30 (C), 60 (D), 120 (E) and 180min (F) at $120 \times 10^3 \text{g}$. Scale bars are 200nm.

retained relative to metal impurities removed. Compared with previous centrifuge based purification studies the ‘optimal’ applied force observed here is around twice the value recommended in most purification protocols,^{98,101,355} although similar to others,⁹⁶ while it is far lower than the conditions utilised in some reports.^{274,356}

A significant number of the particles that are observed in the films are greater than 10nm in size even after 3 hours at $120 \times 10^3 \text{g}$, sometimes much larger, suggesting that while the metallic impurity content is greatly improved through centrifugation under intermediate conditions, it is certainly not the most effective means of removing the metal catalyst contaminants as observed for CNTs synthesised by other methods.²⁷⁴ It is also noteworthy that the analysis presented here pools contributions from non-nanotube carbonaceous material with that of CNTs, which also comprise a significant percentage of the starting material,¹⁰¹ thus the presented ratios reflect only the total carbon-metal content of each sample and not necessarily the CNT-metal ratio. While the carbon impurity content is visibly reduced in TEM images with increasing centrifugation time and force, there also remains a small amount of amorphous and particulate carbon present even after intense centrifugation.

Despite this, the non-oxidising nature of centrifugation allows for a reasonable level of purification without functionalising or damaging the nanotubes. The lowest metal content was observed for the sample centrifuged at $40 \times 10^3 \text{g}$ which contained half the amount of catalyst remaining at $120 \times 10^3 \text{g}$ for the same duration (i.e. half the metal content represented by Figure 4.19D) and with a corresponding decrease in metal

content of greater than 90% with respect to the as-produced material, suggesting that centrifugation is a viable route for purification of nanotube material. However, the conditions for which metallic catalyst particles are removed with the greatest efficiency do not correlate with the greatest level of nanotube individualisation. It is apparent that improved length and purity are obtained under relatively mild ultracentrifugation conditions, but greater intensity must be applied in order to obtain a large fraction of individually dispersed CNTs. Unfortunately, this means that optimising the percentage of individuals results in shorter nanotubes and an increased impurity content within the supernatant for dispersions prepared with a single centrifugation cycle.

One approach to further improve the purity of nanotube material is to utilise a two-stage centrifugation process, wherein the metal catalyst is removed in the sediment by a short initial step at high speed. The recovered supernatant is subjected to a second (much longer) centrifugation cycle which sediments the nanotubes and leaves the smallest amorphous carbon particles in the supernatant which is then discarded.²⁰⁰ The precipitated nanotubes may then be re-suspended by an additional sonication step. In a similar vein, by using step-wise centrifugation and collecting intermediate fractions nanotubes of differing length distributions may be obtained in the supernatant, as has been demonstrated with MWCNTs by Feng *et al.*³⁵⁷

4.3 Length Fractionation via Centrifugation

In an attempt to create nanotube populations that possess more well-defined length distributions, a sonicated sample (30min, 20% amplitude, 6.5mm tip) of arc CNTs at $0.5\text{mg}\cdot\text{mL}^{-1}$ in 50mL of 0.5% SDBS was centrifuged at $120\times 10^3\text{g}$ in the 70 Ti rotor for several iterations of varied duration and the supernatant and sediment fractions were collected separately for each phase. AFM images were collected from solutions spun-cast either directly from the supernatant as with prior studies or from precipitates that were diluted with SDBS solution and re-dispersed with brief (~2-5min) bath sonication as shown in Figure 4.20. UV-Vis-NIR spectra for each fraction were also recorded and these are displayed in Figure 4.21. An initial 20 minute cycle was used to eliminate the majority of the heavy catalyst particles (which were removed in the sedimented fraction along with a portion of the nanotubes as shown in Figure 4.20A). The optical spectrum of this fraction possesses a large background and broad, low-intensity CNT absorbance peaks which are consistent with a large percentage of impurities. The supernatant of the

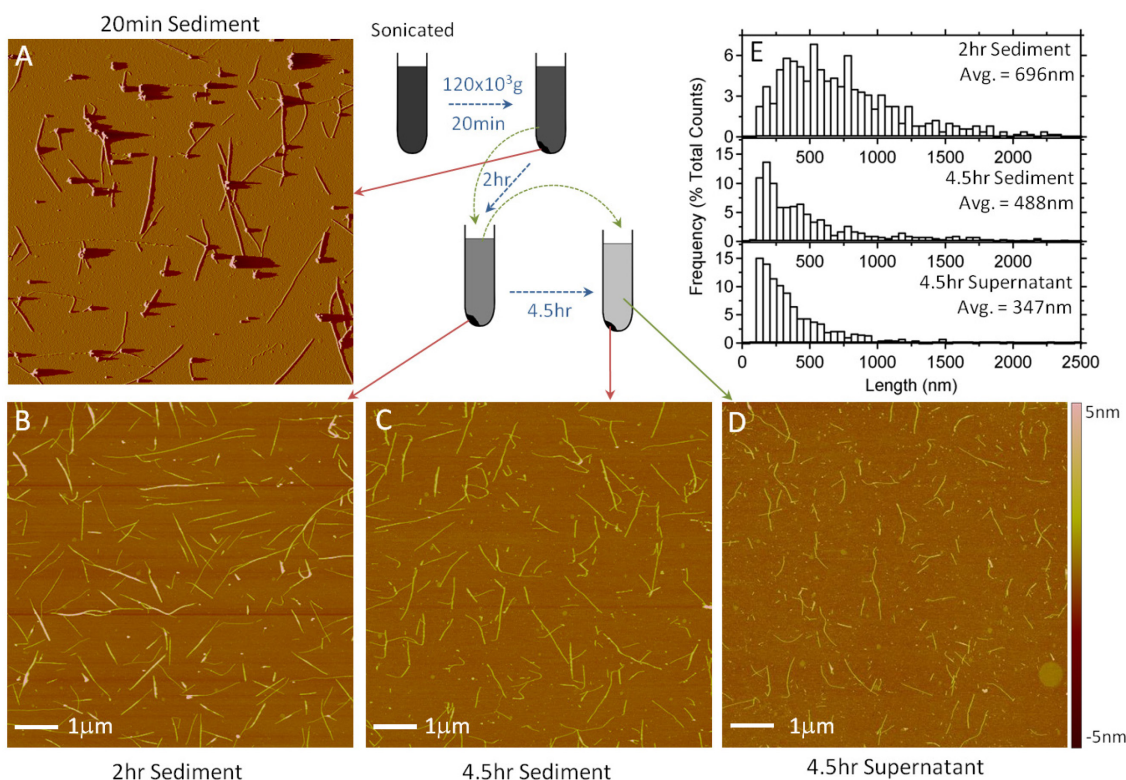


Figure 4.20: $8 \times 8 \mu\text{m}$ AFM images for fractionated solutions of arc CNTs in SDBS collected from the sediments of a dispersed sample after centrifuging for 20 minutes (A), 2 hours (B) and 4.5 hours (C) as well as from the supernatant after 4.5 hours (D) as indicated in the diagram. The image in (A) is an amplitude image while others were taken in height mode. Length distributions calculated from 3 such images for fractions (B), (C) and (D) are provided in (E).

initial cycle was reintroduced to the centrifuge for a second 100 minute run (2 hours total) which recovered longer nanotubes in the sediment, however this fraction also contains thicker CNT bundles which are evident in Figure 4.20B. The optical spectrum for this fraction exhibits a much lower background, although the nanotube peaks are significantly red-shifted due to the more aggregated nature of the dispersion. The final cycle was performed for 150 minutes (4.5 hours total), where nanotubes of intermediate length were deposited in the sediment as shown in Figure 4.20C, while the shortest nanotubes were retained in the supernatant (Figure 4.20D). The absorbance spectrum of the final supernatant is consistent with a large proportion of individualised nanotubes at a low concentration, showing well resolved fine structure as with similar samples analysed in Section 4.1.2. The AFM data and optical spectrum of the re-dispersed sediment in this instance are very similar to those recorded from the supernatants of solutions that were centrifuged for shorter durations, suggesting that precipitates may be

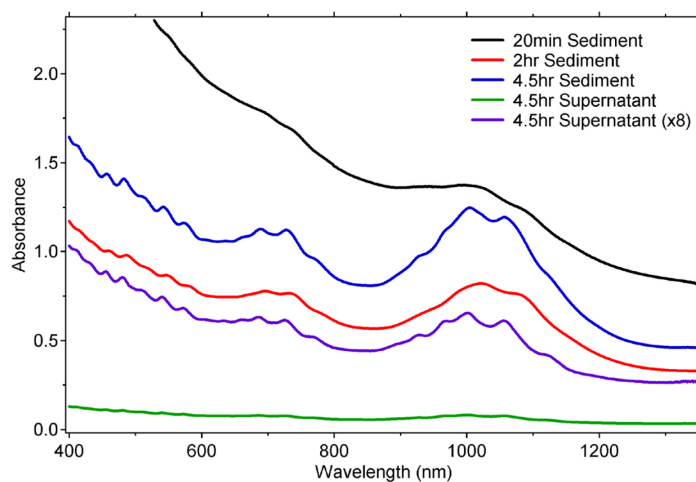


Figure 4.21: UV-Vis-NIR spectra for fractionated solutions of arc CNTs in SDBS collected from the re-dispersed sediments of a sample after centrifuging for 20 minutes, 2 hours and 4.5 hours as well as from the supernatant after 4.5 hours.

easily regenerated into high quality dispersions provided that they are kept in solution and are not allowed to dry out. Additionally, the amount of small particulates is visibly reduced in the two latter sediment fractions in contrast to the final supernatant, indicating that collection of such intermediate deposits is a feasible route to improved nanotube purification.

Length distributions and associated mean values for these samples are provided in Figure 4.20E, showing that objects in the sediment fraction after 2 hours of centrifugation are significantly longer on average than those in the two fractions recovered after 4.5 hours. While the mean value for the length distribution of the 4.5 hour supernatant sample is significantly lower than that of the 4.5hr sediment, the two distributions essentially overlap. Thus, while mean lengths of separated nanotube fractions can be significantly reduced, the separation by length that is achieved using water as the solvent medium is not capable of resolving discrete fractions that would be useful for further applications. To obtain such fractions using the centrifugation method it is necessary to use a gradient medium such as sucrose²⁰⁴ or iodixanol.^{205,358}

An experiment using a layered density gradient of sucrose was able to produce visible separation of dispersed nanotube material into a continuous distribution within the centrifuge tube, however the lengths of the CNTs in the fractionated gradient solutions were unable to be characterised by AFM as the nanotubes no longer adhered to the silicon substrate upon spin coating in sucrose solution. Further investigation into the length-fractionating ability of linear or stepped density gradients of sucrose are

warranted, although since length separation is not the ultimate aim of this study this avenue of research was not pursued.

Chapter 5

INFLUENCE OF SONICATION PARAMETERS ON DISPERSION PROPERTIES

As nanotubes within a bundle are tightly bound by van der Waals forces, significant energy input is required for them to be individualised (i.e. unbundled or separated from one another). Therefore, solutions of nanotubes are usually prepared with the aid of sonication, though the type (tip, bath, etc.), duration and intensity of ultrasound treatments reported for processing CNT dispersions are widely varied.³⁵⁹ It is important to characterise the ultrasonication process as this step critically influences the initial properties (length and bundle size) of the nanotube population.

5.1 Factors Affecting the Dispersion Process

Exfoliation of individual nanotubes from their bundles by a surfactant is postulated to occur through an ‘unzipping’ mechanism,¹³⁶ whereby ultrasonic agitation produces gaps between adjacent nanotubes at the end of a bundle, allowing surfactant molecules to adsorb onto the newly exposed surface. Surfactant adsorption propagates along the fissure, eventually splitting the bundle or separating an individual nanotube from the

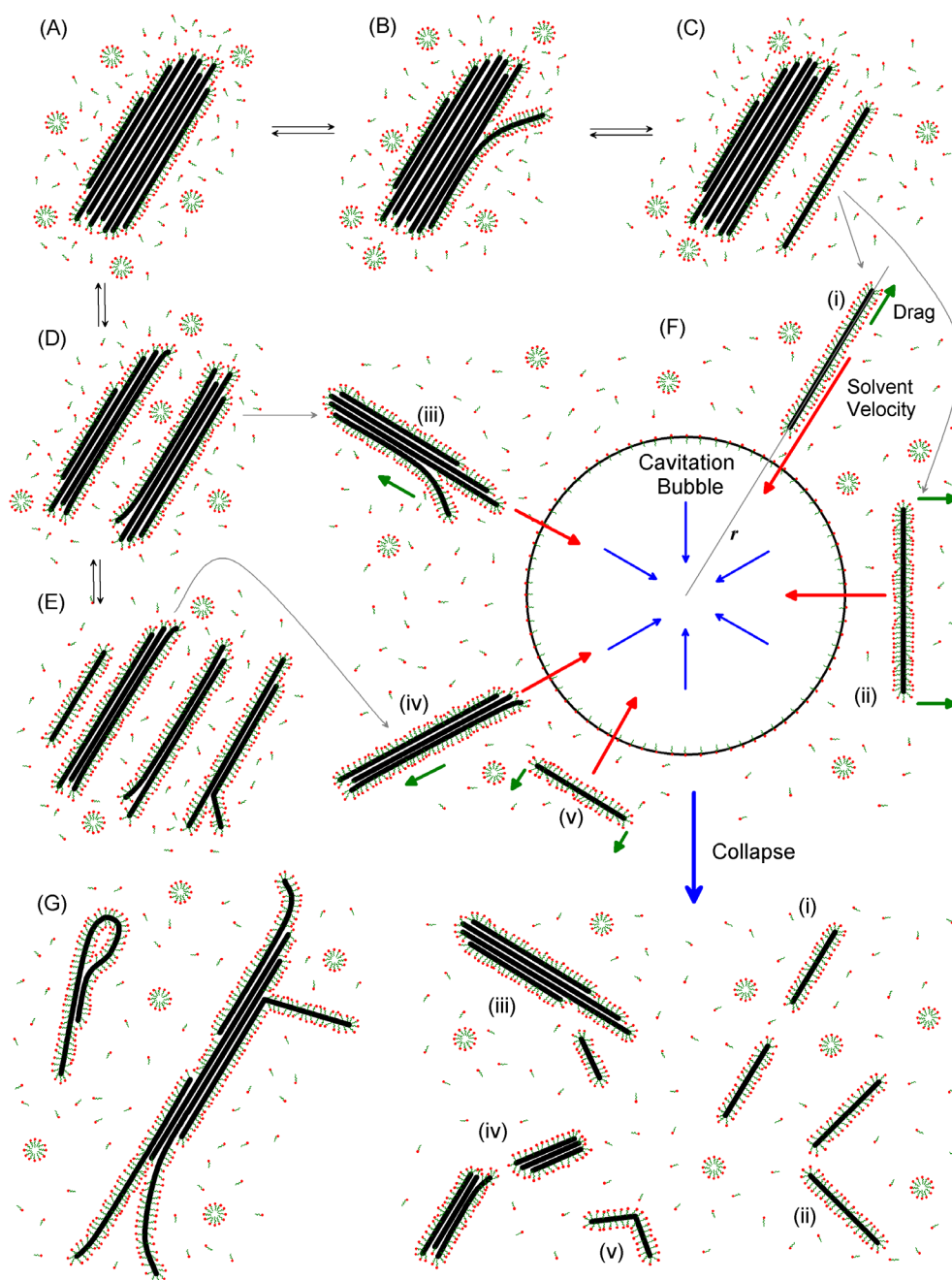


Figure 5.1: Speculative mechanisms involved in the dispersion of CNTs via cavitation: initial aggregates (A) are split by ‘unzipping’ of an individual (A→B→C) or division of separated bundles (A→D) which may be further exfoliated (D→E). These processes are reversible (re-aggregation; C,E→A). Shear forces associated with collapse of a microbubble (F) may induce scission (i and ii) or deformation (v) of individual nanotubes, while small (iv) or frayed bundles (iii) may also be cut into fragments. Additionally, individuals may self-associate, while partially exfoliated bundles are common (G).

aggregate (Figure 5.1A→C). Studies have demonstrated that ultrasonic processing of CNTs may result in significant defects, such as buckling, bending and dislocations,¹⁴¹ although most reports indicate that the sidewall damage to CNTs induced through mild

sonication conditions is minimal.^{108,133,345,360} However, exposure of CNTs to ultrasound does result in cutting of the nanotubes into increasingly shorter segments. This scission continues until a limit is ultimately reached as the rate of fragmentation reduces with particle size.^{328,361} The average length of the nanotubes in a dispersion has been shown to be reduced at a rate proportional to t^{-x} , where longer sonication times t produce nanotubes of progressively shorter lengths, although the measured value of the exponent x shows some variation between studies.^{138,139} It has also been suggested that nanotube bundles must first be broken up before scission of individual nanotubes can occur as illustrated by the sequence A→D→E in Figure 5.1,³²⁸ leading to a convolution of scission and debundling effects at short sonication times.³⁶¹ Additionally, nanotubes are likely to be preferentially cut at defect sites, whether they were present initially or induced by sonication, and it is suggested that the scission process is diameter dependent, with cleavage of larger diameter nanotubes being favoured.¹³⁷

The mechanism behind nanotube scission is thought to be due to fast collapsing cavitation bubbles that provide a high local solvent velocity, which in turn could potentially produce a shear force exceeding the tensile strength of the nanotube and thus cause its fragmentation as depicted in Figure 5.1F(i).^{138,139} However, more recent simulations have suggested that fracture by compressive atom ejection is the critical precursor mechanism of cutting SWCNTs with ultrasonication.³⁶² As opposed to fracture via bond-breaking tensile stress where nanotubes undergo scission if aligned normal to the bubble wall, it is proposed by Chew *et al.* that nanotubes are instead cut when oriented parallel to the interface. Here, the rapid flow of the water medium close to the bubble wall induces axial compressive forces on the nanotube through nanoscale drag, which causes the nanotube to buckle. This dynamic shell buckling can induce spontaneous ejection of a row of atoms from the graphitic structure, forming a fissure or crack along the nanotube circumference which may then be either closed by compression, creating a kink, or opened through tension to form a defect site at which scission occurs.³⁶² Thus, the nanotube depicted in Figure 5.1F(ii) may represent the more likely mechanism of scission.

As the size of the cavitation bubble is dependent on sonication parameters such as frequency and power, the extent of scission will consequently be determined by these experimental choices. Lower frequency ultrasound apparatus typically produce larger cavitation bubbles which create more intense forces as they collapse, thus imparting a greater amount of energy to the solution.³²⁸ Since tip/probe ultrasonicators typically

operate at lower frequencies than ultrasonic baths, more energy is delivered to the CNTs with the use of an ultrasonic tip, which increases the rate of fragmentation.¹²² The concentration of individually dispersed nanotubes has also been found to increase with applied ultrasonication power, although this is accompanied by a corresponding increase in the CNT defect density coupled with a reduction in the average length of the nanotubes.¹⁴⁰

Nanotube length has been shown to have a significant effect on the optical properties of nanotube ensembles,^{344,350,363} and since methods for evaluating the aggregation state of nanotube dispersions are often based on optical methods, the length distribution of the sample is a critical factor that must be considered. While in most instances longer nanotubes with preserved properties are desired, applications such as nematic liquid crystal production benefit from shortening of CNTs,³⁶⁴ thus analysis of dispersion processes to control the final dimensions of the nanotubes is important.

It is also possible that sonication in water may append oxygen containing functional groups to the nanotube sidewalls, or that some chemical functionalisation of the nanotube may occur through radicals produced from the dispersant.³⁶⁵ Recent results further suggest that molecular oxygen produced during sonication may act as a dopant and modify the chemical properties of CNTs.¹⁴³ These effects, along with those of aggregation and scission, make characterisation of CNT dispersions quite challenging.

Since many variables exist for the ultrasonic dispersion of CNTs, it is unsurprising that processing parameters vary significantly among reported literature.¹⁰⁴ Even in a simple time-dependent consideration with a fixed ultrasonic input signal, dispersion of nanotubes is a complicated process with many influential factors. However, ultrasonic energy may also be delivered at various frequencies and levels of intensity which further confounds analysis of sonication parameters. Since the properties of the final supernatant solution depend critically on this initial dispersion step, it is important to characterise the influence of the chosen sonication protocol on the resulting physical properties of the dispersion. Therefore, a study of the major controllable sonication variables involved with CNT dispersion has been performed in order to better understand the dispersion processes and hence find optimal values for the system involving arc discharge produced CNTs dispersed by SDBS. The influence of the sonication parameters of duration, input power and geometry have been examined by optical absorption measurements, Raman spectroscopy and AFM for both the bath and tip ultrasonicators, with results discussed in the following sections.

5.2 Duration of Ultrasound Exposure

5.2.1 UV-Vis NIR and Raman Spectroscopy

To examine the effect of sonication time on the resultant dispersions a series of samples of as-produced arc CNTs were prepared at a concentration of $0.5\text{mg}\cdot\text{mL}^{-1}$ in 0.5% SDBS and subjected to three different methods of ultrasonication. These were 10mL samples with the 5mm microtip, a single 50mL sample with the 6.5mm microtip and a solitary 110mL sample placed in the centre of the Elmasonic bath sonicator. Centrifugation parameters were fixed at $122\times 10^3\text{g}$ for 1 hour in each case and the resulting trends for the S_{22} areal absorbance, $S_{22}:\text{BG}$ ratio and S_{22} peak position are given in Figure 5.2. For bath sonication the amount of nanotubes in the supernatant continues to increase with time up to about 300 minutes, while saturation is realised at about 30 minutes for the 5mm tip. After 120 minutes the concentration is still climbing for the 6.5mm tip, though a similar levelling off is expected to occur at $\sim 150\text{-}180\text{min}$. The position of the S_{22} peak undergoes a blue-shift with increasing processing time in each case, essentially mirroring the peak area results, which is consistent with an increasingly disperse sample.

The changes in both the S_{22} resonance ratio and Raman D:G ratio shown in Figures 5.2C and D respectively suggest that the increase in dispersed CNT concentration is coupled to an increase in nanotube ‘damage’ caused through tube scission and possible sidewall defect generation. The D:G ratio continues to increase with processing time for each type of sonication, though much more rapidly for the tip-sonicated samples. The turning point in the resonance ratio corresponds to a greater increase in the background absorbance compared to that of the CNT peak, which may indicate an increase in damage to the sample; i.e. after a certain sonication time more defects are produced than nanotubes are being exfoliated. This occurs at $\sim 10\text{-}15$ minutes for the 5mm tip and ~ 60 minutes for the 6.5mm tip. The resonance ratio trend for bath sonicated samples levels out at about 60 minutes, where the turning point coincides with a minimum in the D:G ratio, however there is a subtle peak in the resonance ratio at approximately 180 minutes for this sample series. The concentration of CNTs at these times is well below that of the maximum obtained for each sample series, which may mean that the apparent increase in concentration with extended sonication is achieved through shortening of existing individual CNTs rather than through further exfoliation of bundles.

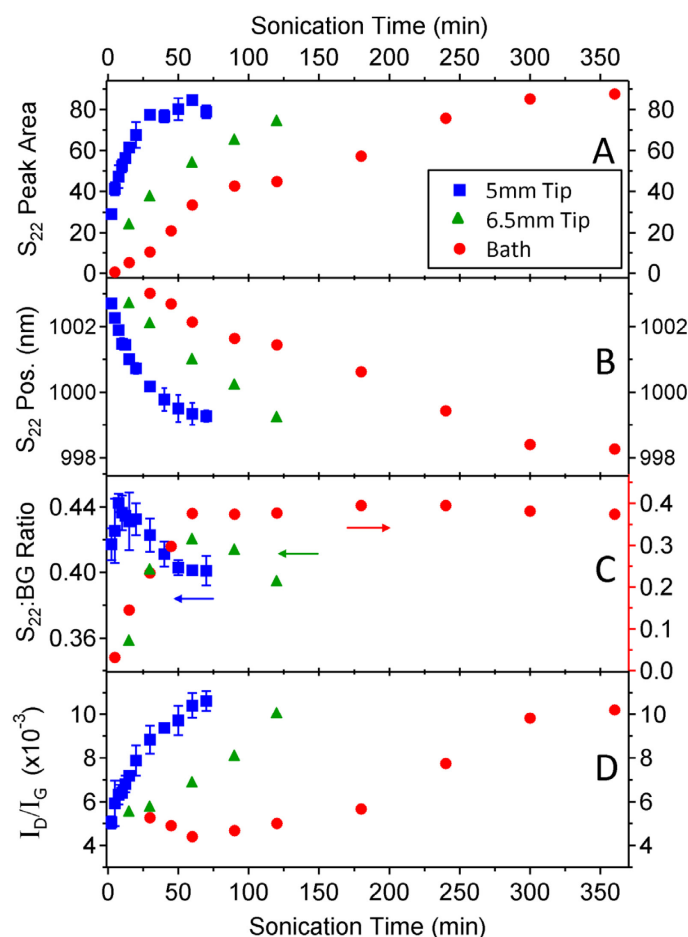


Figure 5.2: UV-Vis-NIR areal absorbances for the S_{22} peak (A) with corresponding peak positions (B) and peak-to-background absorbance ratios by area (C) for samples sonicated using a 5mm microtip (blue squares), 6.5mm microtip (green triangles) and an ultrasonic bath (red circles) for various durations. Raman I_D/I_G intensity ratios measured from solutions using a 2.33eV laser are also shown in (D). The two shortest time samples for the bath sonicated series were omitted from the peak position and I_D/I_G analysis due to exceptionally broad S_{22} peaks and low signal respectively.

The tip-sonicated dispersions possess a greater concentration of nanotubes after short processing times due to a more intense energy input with the probe sonicator apparatus.³⁶⁶ The two microtips were driven at 20% amplitude, delivering an approximate power of 8W to the solution in each case. For the 5mm tip repeat sets of individual 10mL samples were run and as such each point is an average of 2-4 samples, where error bars in Figure 5.2 denote standard deviations within the series. For both the 6.5mm tip and bath sonication series a large volume of solution was prepared and aliquots of 9.5mL were sequentially removed after the allocated times. This difference in sampling method may account for a portion of the observed variation in the rate of increase in CNT concentration with time between the two probe tips. However, Figure 5.3 compares these two series in terms of power delivered per volume of solution,

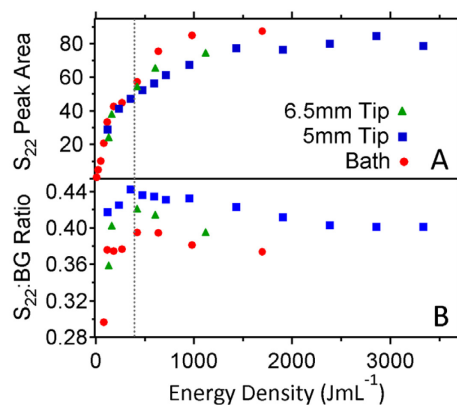


Figure 5.3: S_{22} areal absorbance (A) and peak-to-background absorbance ratios by area (B) for the 5mm (squares) and 6.5mm (triangles) microtips as well as the bath sonicated samples (circles) as a function of energy delivered to the solution. (Data have been normalised by sample volume to obtain energy density in $J \cdot mL^{-1}$).

where a similar dispersion performance is observed. The peak in the S_{22} :BG ratio now appears at the same position, approximately $400 J \cdot mL^{-1}$, suggesting this is the optimal energy input (at least for a fixed power of $\sim 8W$). It is evident that the volume of solution is an important parameter in controlling the supernatant CNT concentration of the resultant dispersion as it determines the overall energy density. Additionally, using the calibrated power output of $0.027W \cdot mL^{-1}$ for the bath sonicator (see Appendix A), the trends in areal absorbance and resonance ratio with energy density for this series become very similar to the tip-sonicated samples. This suggests that the energy input per volume of solution is an appropriate parameter for the control of dispersion which may be applied universally to various ultrasonic instruments.

5.2.2 AFM

AFM analysis shows that the average diameters for each sample within the 6.5mm tip and bath series are similar, which implies that the centrifugation step is the determining factor in defining the bundle size of nanotubes in the supernatant. Indeed, the distributions for both length and diameter change very little amongst the samples analysed (see Figure 5.4), however there is a subtle reduction in average length due to an increase in the number of shorter nanotubes through scission over time. The average lengths approach similar values with prolonged ultrasound exposure for both the 6.5mm tip and the ultrasonic bath (Figure 5.5A). It has been suggested that sonication parameters such as vessel geometry, pulsing rate and power affect only the time at

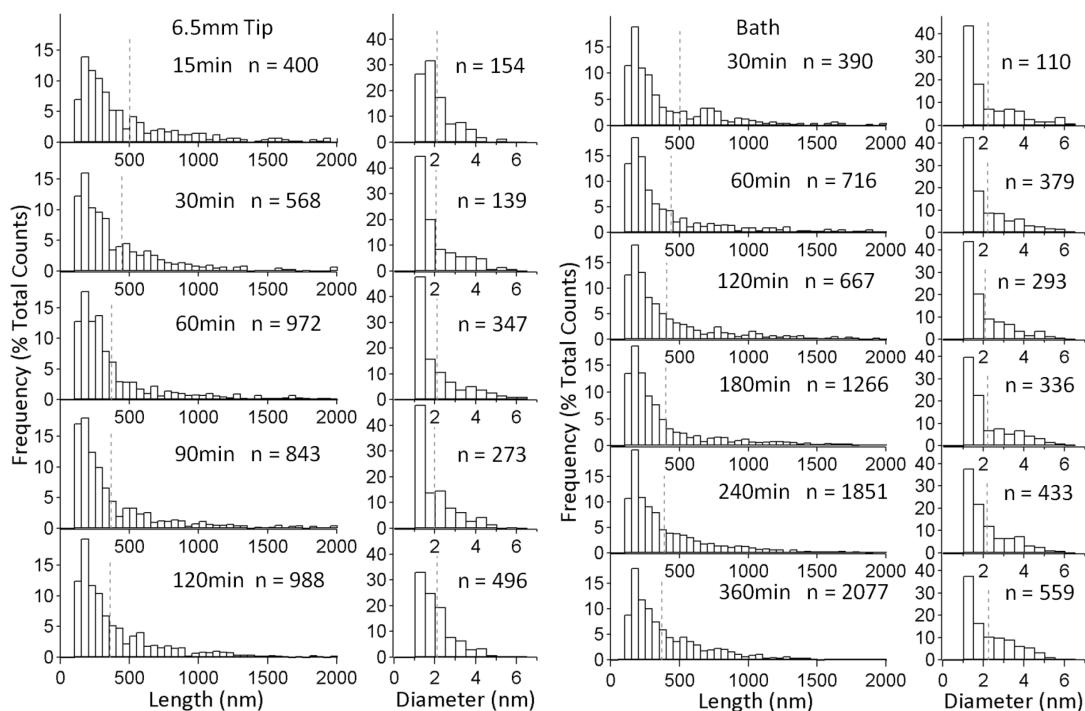


Figure 5.4: AFM length and diameter analyses for samples sonicated using a 6.5mm Ti microtip driven at 20% amplitude (left) and an ultrasonic bath (right) for different durations. Samples were centrifuged under identical conditions ($122 \times 10^3 g$ for 1hr). Grey dashed lines indicate mean values for the distributions, while n is the total population.

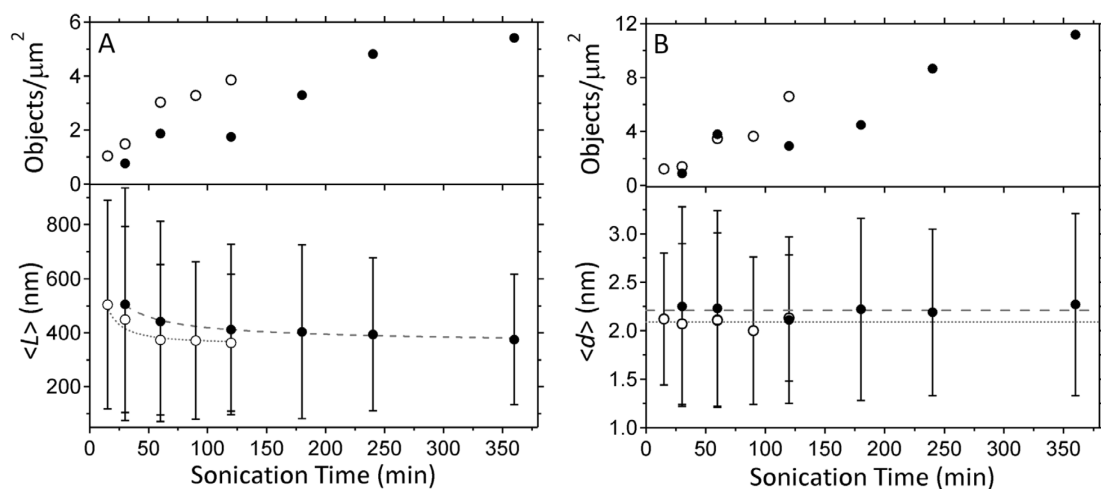


Figure 5.5: Average length (A) and diameter (B) of nanotube bundles as a function of sonication time determined by AFM for the 6.5mm microtip (open circles) and ultrasonic bath (solid circles). Dashed lines represent average overall diameters in panel (B) while in (A) these lines are fits of the form $\langle L \rangle = Ar^{-x}$ to the length data. Error bars depict average deviation from the mean.

which the terminal length for scission is achieved.³⁶¹ In this regard, tip sonication is far more efficient as the limiting length would be obtained much faster. The scission termination length (L_{lim}) has been reported to be approximately 100nm,¹³⁸ or alternatively to be between 50-200nm depending on the nanotube diameter.³⁶² Many

objects measured here were found to be shorter than 100nm in length, and although it is possible that some of these objects are forms of amorphous carbon, care was taken to only measure particles with a one-dimensional aspect ratio. Power-law fits of the form $\langle L \rangle = L_{\text{lim}} + At^{-x}$ (where A is a scalar fitting parameter) to the average values of the length distributions for both tip and bath sonication suggest L_{lim} to be approximately 360nm, however based on the results shown in Figure 5.4 the average length is expected to drop well below this value for extended processing times. Thus, the parameter L_{lim} is allowed to go to zero, and values for the exponent x are calculated to be 0.17 and 0.11 for the 6.5mm tip and bath sonication methods respectively. Previously estimated values of 0.5,¹³⁸ 0.45,³⁶⁷ and 0.21¹³⁹ have been reported (albeit for different types of CNT), which would suggest slower scission in this case, though since a highly polydisperse starting material was used here this comparison is not definitive. It is also impossible to deconvolute scission and exfoliation effects in this instance, as average length values are influenced both by the shortening of CNTs through cutting as well as the influx of longer CNT objects that may have been freshly cleaved from larger aggregates during sonication, which explains the underestimated rate of scission.

5.3 Effects of Nanotube Scission Due to Ultrasound Exposure

To more accurately determine the rate of scission for these suspensions under sonication a freshly prepared solution was exposed to additional ultrasound post-centrifugation. A 50mL sample of 0.5mg·mL⁻¹ arc CNTs in 0.5% SDBS was initially sonicated for 30 minutes at 20% amplitude (6.5mm tip) before centrifugation at 122x10³g for 1hr. This relatively low energy sonication step was designed to leave longer nanotubes in the initial supernatant, which was diluted 1:3 in 0.5% SDBS on collection. 15mL of this diluted dispersion was sonicated with the 5mm tip for an additional 260 minutes (290min total duration) with 0.3mL aliquots sequentially removed for analysis.

5.3.1 UV-Vis-NIR Spectroscopy

The absorbance spectrum of the bulk solution was collected with every aliquot removal and these spectra are shown in Figure 5.6A. It is evident that the background signal is significantly increased with extended exposure to ultrasonic irradiation. Linear background subtraction reveals that the nanotube absorbance peaks remain similar in

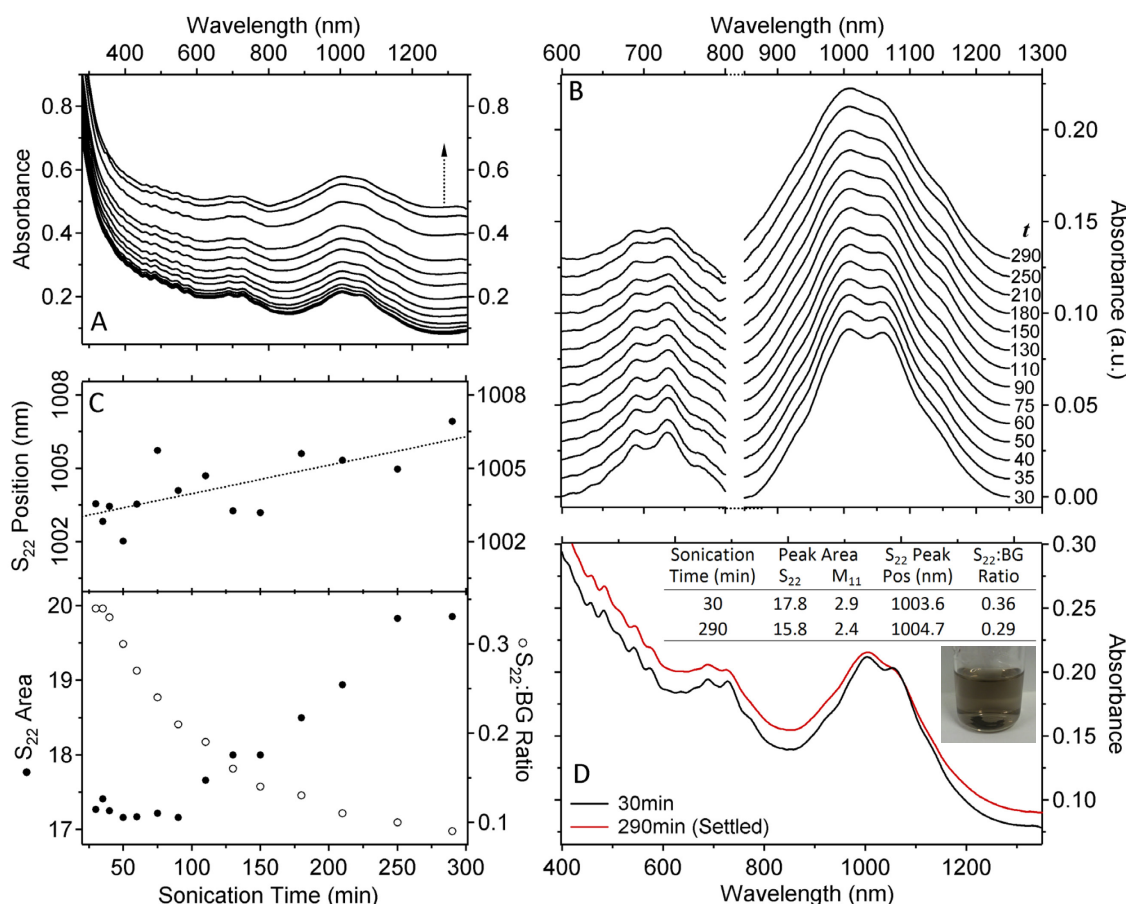


Figure 5.6: UV-Vis-NIR spectra of the bulk solution after each time interval (A) and the corresponding background subtracted M_{11} and S_{22} peak regions with vertical offsets of 0.01 (B). Evolution of the S_{22} peak position, areal absorbance and S_{22} :BG ratio over time are plotted in (C). Absorbance spectra of the original dispersion and the same solution after 260 additional minutes of sonication with 5 days of settling are provided in panel (D), while the inset shows the sediment that formed over this time frame.

intensity (Figure 5.6B) although there is a broadening and loss of fine structure within each band, which is the same behaviour observed when aggregation occurs. However, since it is unlikely that much re-bundling would occur during cavitation, the loss of spectral integrity with increased processing time observed here is believed to be due to defect generation along the sidewalls of the CNTs which would suppress and broaden optical excitations.³⁴⁷ The length of a nanotube is also expected to significantly influence its optical properties, perhaps even being the dominant factor,³⁶⁸ where longer nanotubes have been demonstrated to display enhanced optical properties since the bound excitons are localised along the nanotube length.³⁶³ Consequently, nanotube scission serves to degrade the optical properties through broadening and loss of intensity. Spectral broadening results in the increase in S_{22} area observed in Figure 5.6C, while the S_{22} :BG ratio decreases rapidly due to the increasing background. The

peak position was measured in each case and was found to effectively red-shift over time, though there is considerable scatter in the data. This scatter, along with the large increase in the background absorbance over time, is due to creation of dispersed particulates through erosion of the microtip.

The same cavitation process that is responsible for the dispersion of CNTs also acts to degrade the tip, eroding the titanium to form a pattern of circular pits in the (originally flat) surface. Over time, if left to expand, the pits become wider and much deeper, decreasing the amount of energy delivered to the solution. (Polishing of the tip back to a flat surface can restore dispersion power and slow the deterioration, but this reduces the length of the resonant tip and cannot be performed extensively). Ti particles are subsequently dispersed into the solution which results in a gradual increase in turbidity over the course of extended sonication. However, these particles are not stably dispersed and complete removal of titanium fragments is accomplished by centrifugation in most cases. Sedimentation of the particles occurs after several days of standing (see inset of Figure 5.6D), and the absorbance spectrum of the sample sonicated for an additional 260minutes after preparation (290min total) was observed to return to a similar level of background absorbance as the original dispersion after 5 days of incubation as shown in Figure 5.6D. After settling of the particles the S₂₂ peak position is shifted back towards its initial value, while the peak areas are now decreased with respect to the initial dispersion despite the increasing trend observed in Figure 5.6C. This would suggest that the increasing peak area and inflated red-shift are mostly a consequence of the overall absorption increase introduced by the presence of scattering particles.

Sonication has been demonstrated to cause fragmentation of both polymers²⁵³ and non-ionic surfactants,³⁶⁹ while sonochemical decomposition of SDBS has been shown to occur under ultrasonic irradiation at frequencies of 200kHz³⁷⁰, 363kHz³⁷¹, and 20kHz (albeit at much higher concentrations).^{372,373} However, analysis of sonicated SDBS solutions without CNTs showed no convincing evidence of surfactant degradation in these experiments. This assertion is based on optical absorbance measurements shown in Figure 5.7, where the SDBS absorbance peaks at 194, 224, 255, 261 and 267nm were not shifted or significantly altered in strength by either tip (20kHz) or bath (37kHz) sonication in any of the solutions analysed. These peaks are primarily associated with electronic transitions within the phenyl ring of the surfactant and therefore may not be the best indicators of degradation for the entire molecule, but a more thorough analysis is beyond the scope of this study. The occasional occurrence of a weak systematic

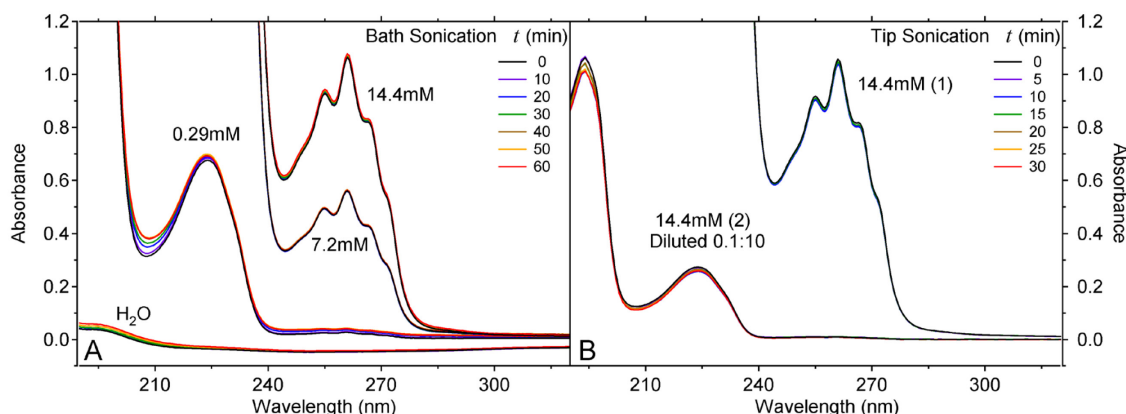


Figure 5.7: UV-Vis-NIR absorbance spectra for SDBS solutions sonicated using the bath (A) and tip (B) instruments. Spectra were collected using a 2mm path length quartz cuvette with the exception of 14.4mM (2) for which a standard 10mm cell was used. Note that 0.5wt% \approx 14.4mM.

background increase such as with the 0.29mM bath sonicated sample could indicate the formation of degraded SDBS particulates in an immiscible organic phase, however a similar (though diminished) effect was also present in water alone. Such an increase could arise due to interference from erosion of the vial wall or possibly due to residues remaining on the cuvette with repeated rinsing and drying during the experiment. In any case, changes in the absorbance background were minimal over SDBS peak wavelengths and insignificant over the spectral range of CNTs for all SDBS dispersions sonicated with both instruments. Therefore the microtip-erosion process is expected to be the sole cause of the background increase observed in Figure 5.6. The production of Ti particulates may then explain a previous report of a tip sonication-induced background absorbance increase that disappeared with settling, which was ascribed to particulates of SDBS proposed to form during sonication.³⁴⁷

5.3.2 AFM

Five AFM images of each dispersion aliquot were collected and representative images are displayed in Figure 5.8. The bundle diameter is not visibly different across each sample, thus it appears that the initial sonication-centrifugation dispersion process provided adequate individualisation of the CNTs and the fraction of individuals was not able to be improved by further ultrasonic processing. A number of the shorter objects found in the dispersion appear to be thin bundles even after several hours of ultrasound exposure, thus bundles may be fragmented in addition to individualised nanotubes.

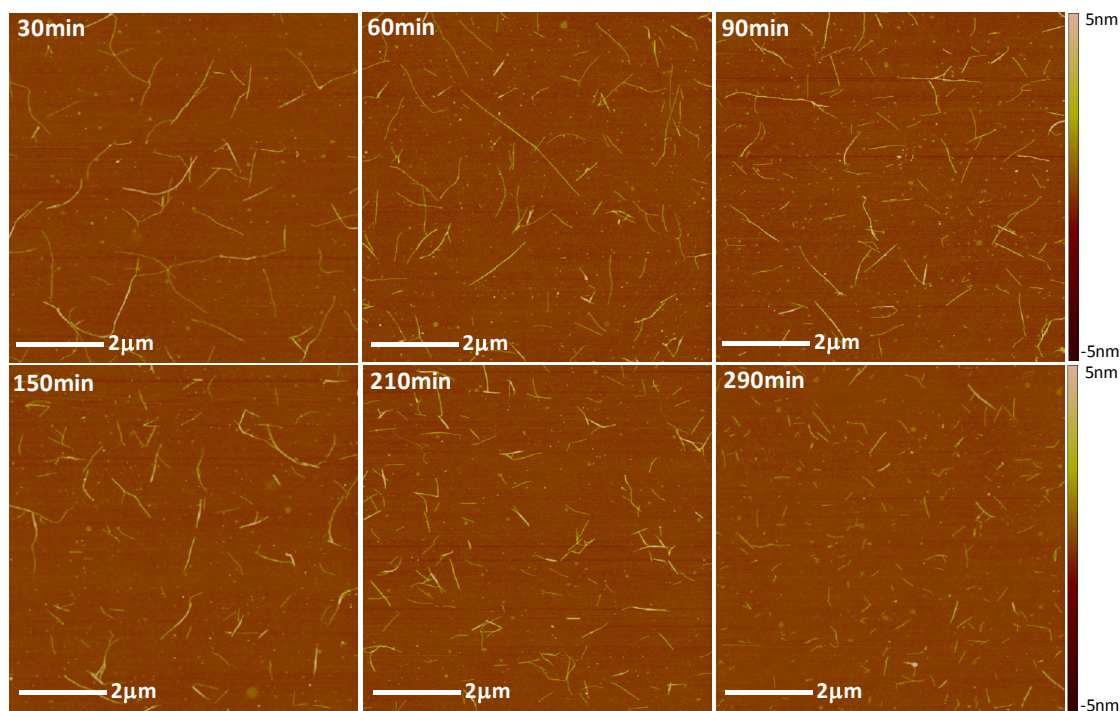


Figure 5.8: Representative $8 \times 8 \mu\text{m}$ AFM height images of the original solution (30min sample, top left), and the same sample after sonication for additional lengths of time with the 5mm microtip.

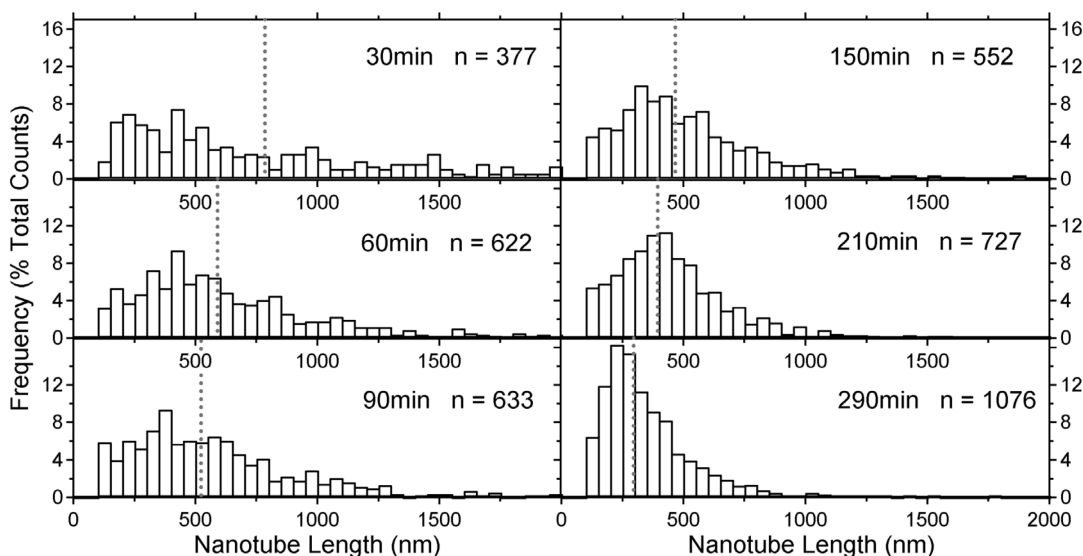


Figure 5.9: Length distributions measured from five $8 \times 8 \mu\text{m}$ AFM images for each time interval aliquot. Dotted lines denote mean values for the population in each case.

Figure 5.9 plots the corresponding length distributions measured from five AFM images for each aliquot. Although there is considerable variation in individual nanotube length, there is a clear systematic reduction in the mean length of the CNT ensemble over time. Note that in the length analysis objects less than 100nm long were excluded from the measurements due to difficulty in discriminating between CNTs and non-nanotube

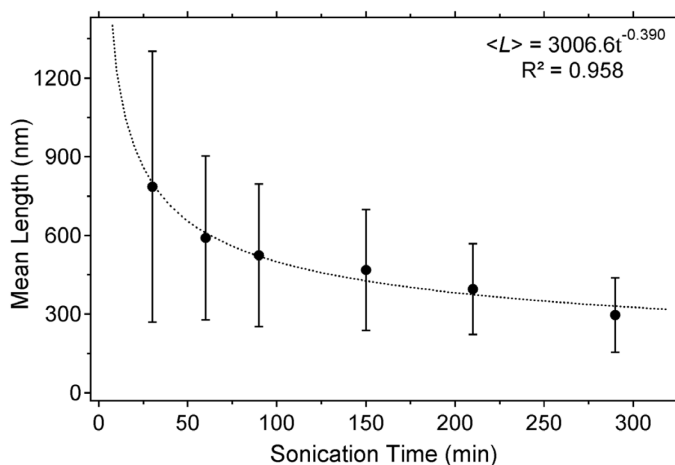


Figure 5.10: Fit of a power law to average lengths determined by AFM. Error bars depict average deviation from the mean value.

material within the resolution of the AFM images. The decrease in length is coupled with an increase in the number of objects as each (initially long) nanotube is cut into several pieces. A length of around 200-300nm appears to be favoured, with scission of nanotubes of this length becoming far less likely, despite the appearance of many shorter objects in previous distributions. A possible explanation may be found in the age of the sonicator tips, having already undergone a pitting-polishing cycle, which would reduce their energy transfer efficiency and thus the rate of scission. The condition of the tip must be kept in mind when comparing this data with prior results, as less power is applied to the sample with a worn tip than would be delivered through use of a pristine tip (see Section 5.5.3 and Appendix A for further details). The reduction of mean length in this case follows a power law with an exponent $x = 0.39 \pm 0.04$ when fit by Microsoft Excel (Figure 5.10), which is essentially an average of the three previously reported values that were quoted in Section 5.2.2.

5.3.3 Raman Spectroscopy

The Raman D:G ratio was determined for each aliquot from spectra acquired with 5x30 second accumulations at excitation energies of 1.58 and 2.33eV. For spectra collected with the green light source (2.33eV) the high resolution grating was used. After baseline subtraction the D and G bands were fit by two Lorentzian curves each using Fityk software and the integrated peak areas were used to calculate the D:G areal intensity ratio. Additional peaks fit to a background subtracted spectrum of a reference

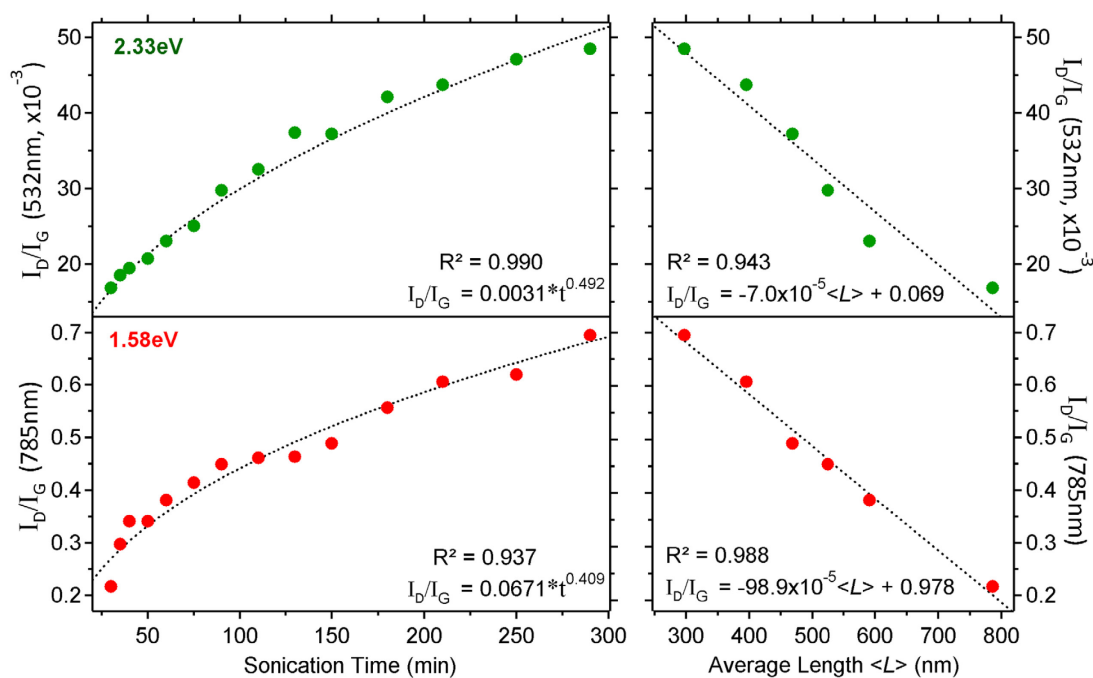


Figure 5.11: Power law fits to D:G values as a function of sonication time (left) and the linear relationship between D:G ratio and mean nanotube length determined by AFM (right) for excitation energies of 2.33eV (green, top) and 1.58eV (red, bottom).

SDBS solution were held constant for sample fits to remove contributions from water. The resulting D:G ratios are plotted in Figure 5.11, where these values increase with sonication time following a similar power law dependence to that observed for the average length. The best-fit values for the exponent were found to be $x = -0.41 \pm 0.03$ and -0.49 ± 0.01 for excitation energies in the red (1.58eV) and green (2.33eV) respectively, which are close to the value of -0.5 reported for CNTs sonicated in organic solvents.¹⁰⁴ The D:G ratio at 1.58eV shows very similar behaviour to the mean length measured by AFM ($x = 0.39$) and consequently the D:G ratio appears to scale linearly with the average length showing only a small amount of scatter. The values calculated at 2.33eV do not fit the linear relationship between D:G ratio and mean length to same level of agreement, however there is still a reasonably good correlation. This supports the assertion that the D:G ratio could be used to estimate the average length of a CNT sample,³⁴⁴ though it is expected that inclusion of longer nanotubes would result in this trend tending to a curve as the ratio approaches zero. Such estimations from this data or that from another source would rely on the nanotubes being in the same environmental state (i.e. dispersed in a surfactant or organic solvent, in a film, etc.) and that the D:G ratio be determined using an identical method of calculation, while CNTs possessing

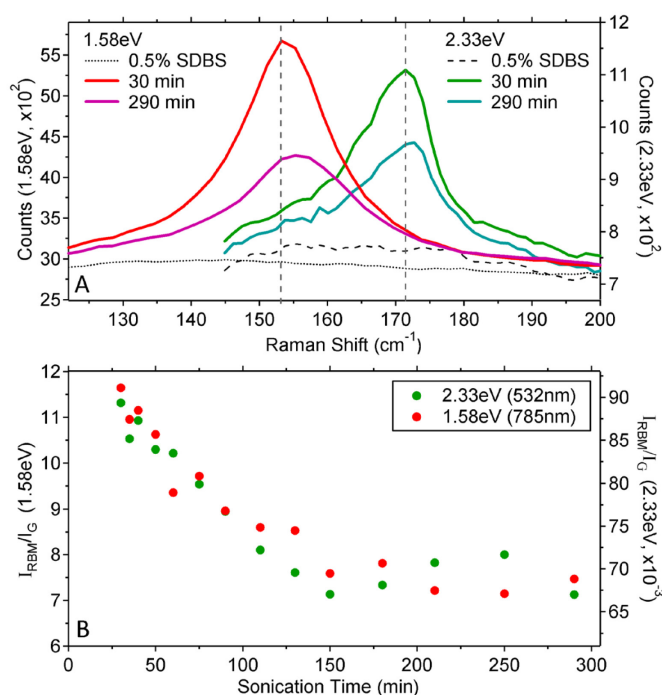


Figure 5.12: RBM spectra for the initial and final states of the sonicated dispersion generated at 2.33eV and 1.58eV excitation (A) and RBM:G ratios measured from each aliquot (B).

different diameter distributions would likely not conform to the same trend. Nonetheless, the D:G ratio offers a simple, rapid method of estimating the mean nanotube length provided a calibrated set of data exists for the samples of interest.

The radial vibration also decays with sonication time, and although a similar reduction of the G-mode occurs simultaneously, the RBM is quenched at a faster rate as evidenced by the RBM:G ratio, which is plotted as a function of sonication time in Figure 5.12. The RBM peak intensity decays reasonably quickly for the first two hours of additional sonication, after which little change in the ratio occurs. The behaviour is comparable between excitation energies which indicates that both smaller diameter semiconducting nanotubes (probed at 2.33eV) and larger diameter metallic CNTs (resonant at 1.58eV) are similarly affected by ultrasonication. However, the RBM peak also appears to undergo a subtle shift to higher energy with prolonged sonication which is more pronounced under 1.58eV excitation. This could indicate a slight preference for the scission of larger diameter nanotubes (assuming that more than one species of nanotube is resonant with each excitation energy and contributes to the RBM). The RBM of the ~1.59nm CNTs also exhibits a greater percentage decay in intensity over the 260 minute interval compared to that of the ~1.43nm CNTs (~50% reduction vs.

~40% respectively), which supports this assertion. This effect is potentially a result of the much larger initial intensity of the RBM peaks for larger nanotubes and should be treated with caution, though the preferential scission of larger diameter nanotubes has been previously reported for HiPCO nanotubes to a greater extent than is observed here.^{137,138} The possibility should also be noted that the slightly greater decay of the RBM for the larger diameter CNTs may be due to easier functionalisation or defect generation within the lattice structure of a metallic versus a semiconducting CNT, rather than a difference in diameter.

5.4 Containing Vessel Geometry and Tip Placement

The rapid oscillation of an ultrasonic tip produces a conical field within the fluid in which the solvent forms cavitation bubbles through nucleated boiling and collapse. A recirculating flow away from the tip and then back through this conical zone is induced by the cavitation and vibrations from the tip.³²⁸ The size of the field, as well as the flow velocity, depend on the solvent properties and energy input, however the geometry of the containing vessel and the position of the tip within the fluid also have an influence. Experiments to investigate the effect of the container diameter and tip placement within the sample were conducted using $0.5\text{mg}\cdot\text{mL}^{-1}$ arc CNTs dispersed in 0.5% SDBS (10min sonication at 20% amplitude) using the 6.5 and 5mm tips respectively. 10mL volumes were used for the depth study while 15mL volumes were used for the diameter study as the increasing width of the vessel lowers the immersion depth of the tip at fixed volume. These investigations revealed no direct correlation between the experimental geometry and the relative concentration of CNTs recovered in the supernatant as shown in Figure 5.13. Interestingly, the position of the tip appears to have only a minor influence on the overall dispersion, even when placed at the extremities, which may simply be a consequence of the small volume (10mL) and hence distances involved. However, there is a large deviation within the vessel diameter results that is greater than that observed for reproduction of a specific sample, thus this parameter does have a substantial influence. Note that the position of the tip was kept in the approximate centre of the solution for each different vessel diameter hence this variation is most likely related to changes in the energy density with variation in the geometry of the solution, although tip position and vessel diameter are convoluted in this case.

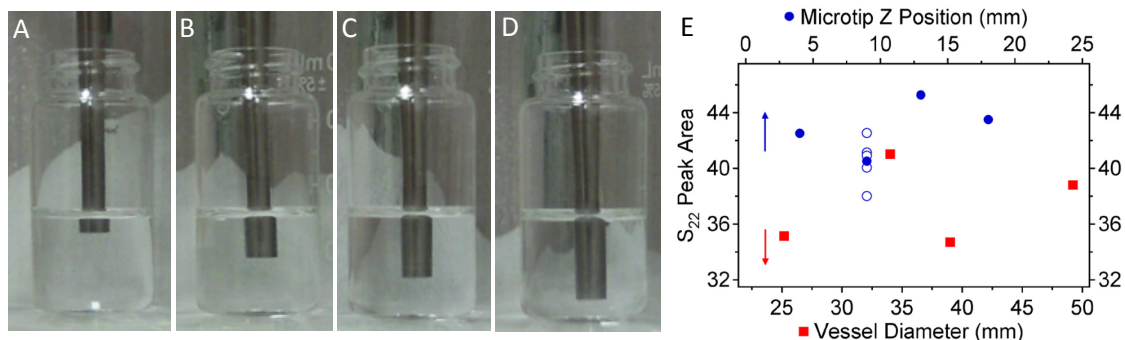


Figure 5.13: S_{22} peak areas from samples sonicated with the 5mm tip situated at different positions within the solution (with reference to the air-water interface, images A, B, C and D are 4, 9, 13 and 18mm respectively) are shown in (E) as blue circles. Open circles represent variation within 5 additional samples generated under identical conditions at position B. The 6.5mm tip was used to investigate 15mL solutions prepared in cylindrical containing vessels of varied diameter.

5.5 Applied Ultrasonic Power

5.5.1 Power Density

Previous studies have shown that increasing the power of sonication can lead to increased exfoliation, however it is also well known that increasing the energy input can increase the defect density induced by ultrasonic processing.¹⁴⁰ Thus, as with the sonication duration, applied power must provide a compromise between exfoliation and damage or fragmentation of the CNTs. A prior study has shown that a power of approximately 9W applied to 10mLs of solution provides the best such trade-off,¹⁴⁰ however this does not account for power density fluctuations with a change in volume. As discussed in Section 5.2.1 the different sonication apparatus performed comparatively in the energy density consideration suggesting that monitoring energy input in this manner is more appropriate than simply examining power.

To investigate the effect of power density three series of solutions of $0.5\text{mg}\cdot\text{mL}^{-1}$ arc CNTs in 0.5% SDBS having different fixed volumes of 25, 35 and 50mL were prepared via sonication using the 6.5mm tip at a selection of amplitudes, with centrifugation performed at $122\times 10^3\text{g}$ for an hour. The sonication time was fixed at 30min while the oscillation amplitude was varied from 20 to 40%, which is the maximum allowed by the instrument for a narrow tapered microtip. Again, as the same cavitation process acts to degrade the tip, the actual power delivered varies with the state of the probe surface. For

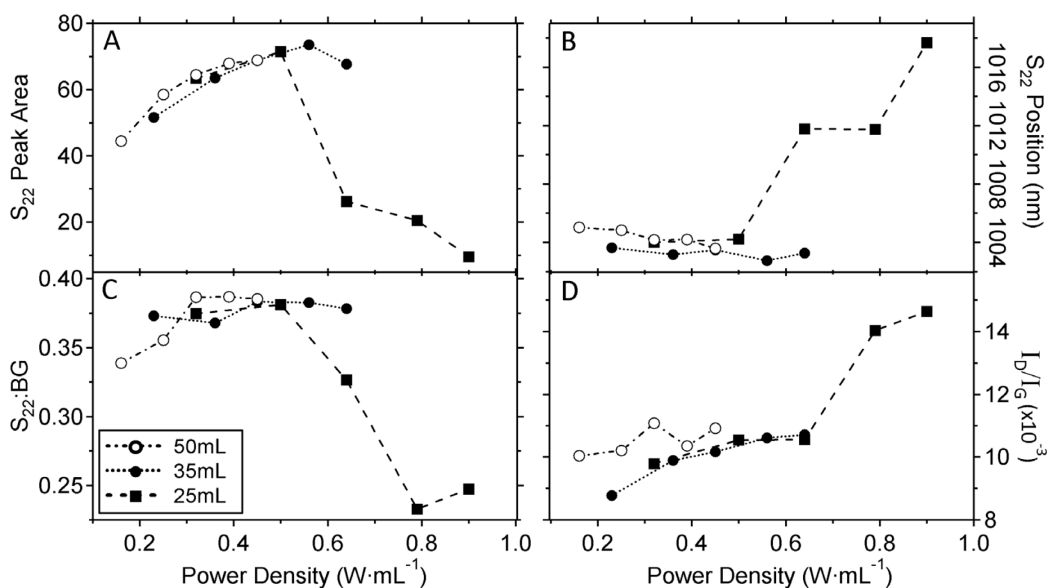


Figure 5.14: S_{22} areal absorbance (A), peak position (B) and resonance ratio (C) from UV-Vis-NIR spectra as a function of the input power density for solution volumes of 25, 35 and 50mL sonicated using various oscillation amplitudes of the 6.5mm tip. Raman D:G ratios measured from solution phase spectra at an excitation energy of 2.33eV are provided in (D).

the pristine tips, a setting of 20% amplitude corresponds to around 7-8W, while 40% is equivalent to ~21-23W according to calorimetric measurements. Values recorded on the instrument were calibrated to those of a pristine tip for the data presented in Figure 5.14 (see Appendix A). Figure 5.14A shows trends for the S_{22} areal absorbance for each sample series. Considering the 25mL samples, as the energy delivered to the system is increased from 0.32 to 0.50 $W \cdot mL^{-1}$ the amount of nanotubes remaining in the supernatant increases, while at 0.64 $W \cdot mL^{-1}$ a rapid decrease is observed followed by continued decay at higher power input. This change in yield is linked closely with the onset of foam formation at high power density; SDBS solutions were found to form stable foams under sonication at ~0.6 $W \cdot mL^{-1}$ and above for the 25mL volume. For the 35mL volumes only slight foam formation was observed for the highest applied power of 0.64 $W \cdot mL^{-1}$. No foam was formed in the 50mL samples, where a simple increase in CNT concentration in the supernatant with increasing power was observed. It is evident that the surfactant foaming is correlated with the power density applied to the solution during processing and that foaming reduces the amount of CNTs dispersed. However, no foam was produced at ~0.84 $W \cdot mL^{-1}$ for 10mL samples sonicated with the 5mm tip which suggests a simultaneous dependence on vessel geometry, i.e. for narrower

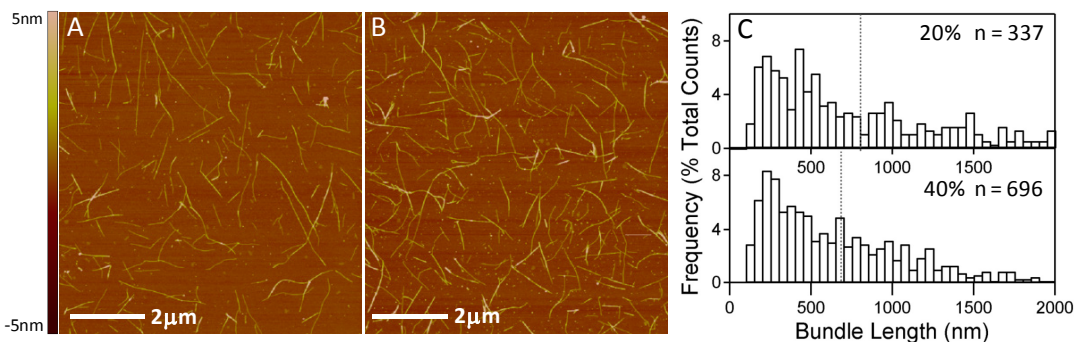


Figure 5.15: Representative AFM height images for CNTs dispersed in 50mL 0.5% SDBS using the 6.5mm microtip operating at tip amplitudes of 20% (A, $0.16W \cdot mL^{-1}$) and 40% (B, $0.45W \cdot mL^{-1}$), with associated length distributions (C).

containers the power density may be increased without inducing foam formation, although this would also depend on the immersion depth of the probe.²⁵²

Within the 35mL and 50mL series the trends in S_{22} peak position (blue-shifting) and $S_{22}:BG$ ratio (increasing) are consistent with improved dispersion with increasing power density up to the point at which foaming is observed. The Raman D:G ratio also increases with higher power input, however it is less pronounced in these series compared to the increases observed for prolonged ultrasound duration. Again, both average length and diameter of these dispersions are predominately controlled by the centrifugation step, though an increase in the number of short nanotubes is observed at higher power densities as shown in Figure 5.15. Length distributions for the 50mL samples sonicated at 20% ($0.16W \cdot mL^{-1}$) and 40% ($0.45W \cdot mL^{-1}$) amplitudes display a difference in mean length of around 120nm between the two samples as the rate of scission is increased at higher power density, although the concentration of nanotube objects is effectively doubled. While lower applied power will result in fewer defects and longer nanotubes, the exfoliation is less efficient and reduced concentrations of nanotubes will be retained in the supernatant. This is analogous to the case of sonication time, where the obtained CNT concentration and average bundle diameter must be at a compromise between the average length and defect density. Longer sonication times and greater power densities provide higher concentrations and better separation of individual nanotubes, however this comes at the expense of long tubes being cut into shorter, more damaged segments. From the results presented here, it appears that an input energy density of $0.6W \cdot mL^{-1}$ or lower applied for a sufficient duration to supply a total energy of $\sim 400J \cdot mL^{-1}$ to the solution represents favourable sonication conditions for preparing dispersions of arc CNTs in SDBS.

5.5.2 Surfactant Foaming in SDBS

The formation of surfactant foam reduces the efficiency of energy transfer to the liquid and prevents cavitation, thus impeding dispersion.^{252,366} This scenario is not ideal for the tip either, as it is almost equivalent to operating in air and should be avoided. Additionally, surfactant molecules are held at the interface of the bubble walls and are therefore unable to adsorb onto the nanotube surfaces. Methods to reduce foaming include use of a conical vessel, increasing the immersion depth of the probe and lowering the input power.^{252,366} However, with the liquid volumes involved in this work these options are not always possible, where foaming sometimes occurs at the lowest available power setting. It has also been suggested that the addition of a suitable antifoam agent could be used to suppress foaming and thus allow solutions of higher concentration to be produced.³⁷⁴ Thus, in an attempt to reduce the foaming of SDBS solutions at high sonication power two types of antifoam were introduced at both low (~0.05wt%) and high (~0.25wt%) concentrations. These antifoaming agents were Antifoam SE-15 (obtained from Sigma-Aldrich, a 10% emulsion of active silicone polymer and non-ionic emulsifiers) and Antifoam PE-M (obtained from Wako Pure, containing a polyether based molecule, poly(propylene glycol) monobutyl ether, of medium molecular weight). Figure 5.16 shows UV-Vis-NIR absorbance spectra for CNTs dispersed in solutions of 0.5% SDBS with and without addition of the antifoaming agents at an amplitude of 40%. For the silicone based antifoam the tip was extensively pitted (approx 50 hours of operation), while for the polyether antifoam the tip had been polished, hence the disparity in spectral shape and corresponding dispersion quality (greater foaming occurs with a polished tip, thus less material

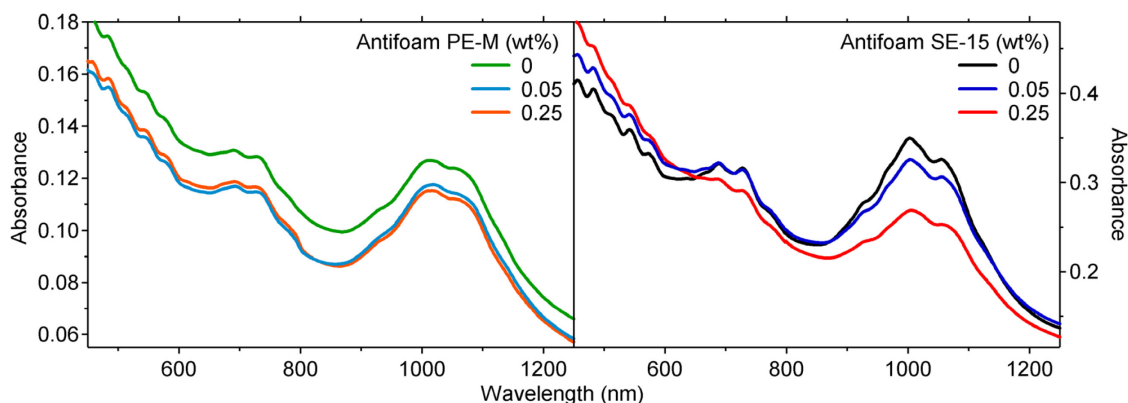


Figure 5.16: UV-Vis-NIR absorbance spectra for CNTs dispersed at 40% amplitude with the 5mm tip in the presence of two different antifoaming agents.

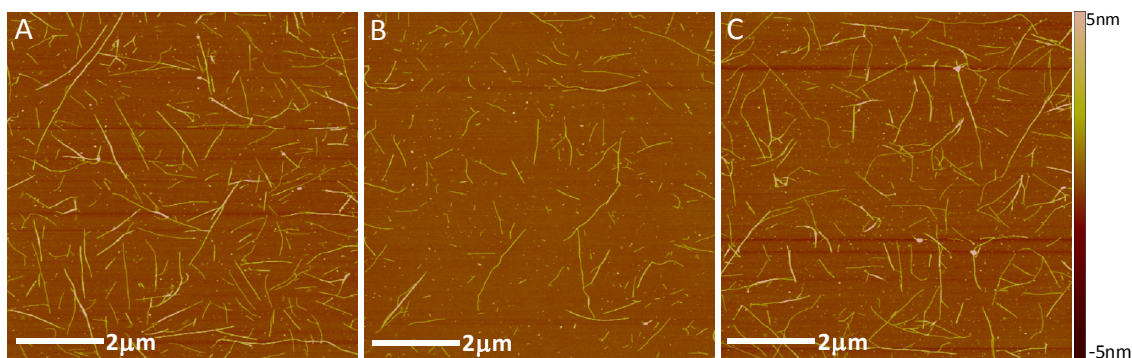


Figure 5.17: 8x8 μm AFM height images for a 50mL CNT dispersion processed at $0.25\text{W}\cdot\text{mL}^{-1}$ deposited from the original solution (A), deposited directly from a foam generated in this solution using an ultrasound input of $1.95\text{W}\cdot\text{mL}^{-1}$ (B), and of the dispersion after dissipation of the foam (C). The CNT concentration is reduced in the foam due to a lower volume being deposited compared to the liquid.

remains in the dispersion). It can be seen that the addition of Antifoam SE-15 reduces the amount of CNT dispersed, and increasing the antifoam concentration is actually detrimental to the surfactant's ability to suspend CNTs. Little to no improvement was seen for PE-M despite a previous report of this antifoam's effectiveness in the dispersion of CNTs in SDS,³⁷⁴ and repeated attempts produced a large variation in the results. Foam formation was not visibly suppressed for any of the dispersions containing either antifoam, even at concentrations equal to that of SDBS, thus this avenue of approach was abandoned. It is noted that the highest input power was used for these investigations hence there is a possibility that antifoaming agents may prevent foaming at lower input powers, however the addition of these materials is not an ideal solution, particularly as they may interfere with the dispersing power of the surfactant. It is instead preferable to reduce any instance of foaming by increasing the solution volume in order to lower the input power density.

It was also found that if a dispersion prepared with no foam formation in the initial sonication-centrifugation process is later exposed to ultrasound at a sufficient power density to induce foaming, the CNTs within the foam remain well dispersed as shown in Figure 5.17. In this instance a dense surfactant foam was generated in 5mL of the original CNT dispersion using 5min of sonication with the 5mm tip ($1.95\text{W}\cdot\text{mL}^{-1}$). A portion of the foam itself was transferred directly to a silicon substrate by spin coating as per the liquid samples (Figure 5.17B), while a second aliquot was removed from the bulk solution after the foam was depleted (Figure 5.17C). AFM images recorded from the recovered solution after the foam has dissipated are virtually indistinguishable from

those of the original dispersion (Figure 5.17A), while the optical absorption spectrum is also unchanged. This result shows that although foaming reduces dispersion of CNTs during the preparation phase, the formation of surfactant foams (at least in SDBS) does not destabilise the CNT dispersion once it has been generated.

5.5.3 Effect of Microtip Erosion on Applied Power

The difference in energy transfer efficiency between a tip with a flat, polished surface and the same tip with a pitted surface is illustrated in several ways in Figure 5.18. This figure compares dispersions of $0.5\text{mg}\cdot\text{mL}^{-1}$ arc CNTs in 0.5% SDBS prepared using the 5mm microtip (10mL, 10min duration, $122\times 10^3\text{g}$ for 1 hour) at various stages of its operational lifecycle. For comparative means these series are presented as a function of tip amplitude rather than delivered power as the latter is found to vary with the state of the tip. For samples of 10mL volume, a 20% amplitude setting equates to $\sim 0.8\text{W}\cdot\text{mL}^{-1}$, while 40% is equivalent to $\sim 2.3\text{W}\cdot\text{mL}^{-1}$ according to calorimetry measurements with a pristine tip.

The first series “initial” relates to the tip after a small number of experiments where its surface remains close to its as-received state. At this stage the power density delivered to the solution is quite high, thus foaming occurs instantaneously with tip amplitudes at or above 25% (and possibly lower, although it does not occur at 20%). The second series was performed after approximately 33 hours of cumulative operation of the microtip, where significant pitting of the surface has occurred. In comparison to the initial series, the S_{22} peak area (CNT concentration) is increased at amplitudes from 22-28% due to a shift in the onset of SDBS foaming to higher amplitudes. This is a consequence of the roughened surface of the tip that develops due to gradual erosion at the interface, resulting in a decrease in energy transfer between the tip and the liquid such that the actual energy delivered to the solution is lower than set on the instrument. Since the corrosion phenomena is amplified once nucleation of pitting sites occurs, further operation of the tip increases the depth of the pores etched into the microtip base at an increasing rate. Thus, after 52 hours of cumulative operation the tip is extensively pitted and the energy supplied to the solution is significantly decreased. This leads to a decrease in CNT concentration at low amplitudes. The foaming of SDBS is further shifted to still higher amplitude (although strong foaming still occurs at 40% amplitude), thus dispersion is greatest at intermediate amplitudes for the 52 hour series.

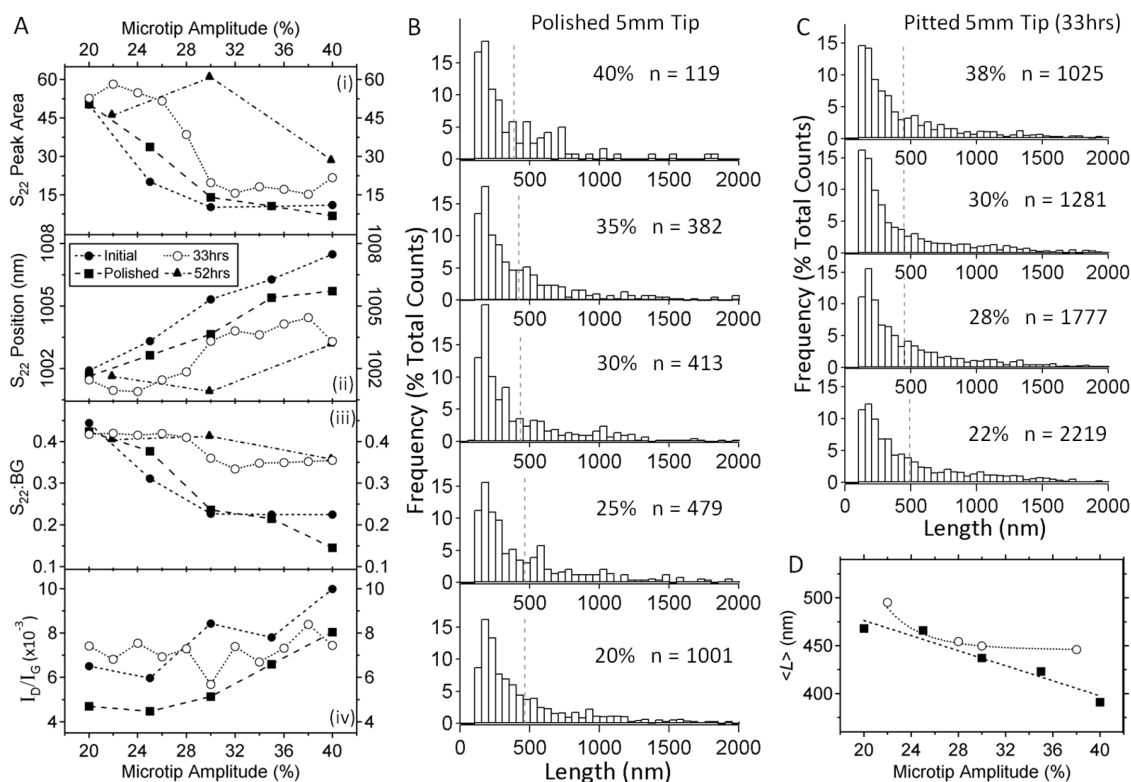


Figure 5.18: (A) UV-Vis-NIR absorbance and Raman spectroscopy analysis of arc CNTs dispersed in SDBS with the 5mm microtip at various stages of its lifetime (initial or essentially pristine tip, after 33hrs of cumulative operation, after 52hours of operation and after polishing to a flat surface); (i) S_{22} areal absorbance, (ii) S_{22} peak position, (iii) $S_{22}:BG$ ratio and (iv) Raman D:G Ratio as a function of sonication amplitude. Length distributions from AFM analysis of the polished-tip series and 33hr series are given in (B) and (C) respectively, while corresponding averages for the distributions are plotted in (D).

The final investigation was performed after the tip was mechanically planed back to a smooth surface on a lathe, removing close to 2mm of material. Polishing the microtip returns the trends observed in Figure 5.18 to a form similar to that of the initial series, however some energy conversion is lost with a change in length of the resonant tip. This process cannot be continually repeated as the transducer and microtip are tuned to a specific oscillation frequency and variation in the tip length may cause an overload in the piezoelectric system.

The 33 hour pitted tip and polished tip dispersion series were also analysed by AFM and their length distributions are provided in Figure 5.18. There is a decrease in mean CNT length that is less pronounced with the pitted surface in comparison to the polished one, which displays an essentially linear trend, however the lengths do not change significantly across either series. The concentration of nanotubes dispersed at high amplitude with the polished tip is quite low due to foam formation, although those

nanotubes that were dispersed were not considerably different in morphology (length and bundle size) to those observed at lower amplitudes.

Sonication intensity is known to affect the size of the cavitation microbubbles formed under ultrasonic irradiation, where larger bubbles are formed at higher input power.³⁷⁵ Here, the effect of increasing power appears to be more pronounced in creation of stable foams with the increased cavity size while the nanotubes themselves experience only a mild increase in scission. Although the formation of foam does not destabilise already suspended nanotubes, foaming is detrimental to dispersion efficiency and this regime should be avoided. The use of a pitted tip offers a method to reduce the power density delivered to low volume solutions, allowing foaming to be avoided, while still providing reasonably well dispersed CNTs in the centrifuged solution. The disadvantages of such an approach are that the actual input power will be considerably different to that set on the instrument and that tip erosion is an accelerating process. Thus, using a frequently polished tip is advisable, though for similar volumes and concentrations to those used in this work tip the lowest power settings must be used with a pristine tip to avoid generation of surfactant foams in SDBS.

Chapter 6

DECOMPOSITION OF ARYL DIAZONIUM SALTS IN AQUEOUS DISPERSANT SOLUTIONS

6.1 Dediazoniation Pathways and Reaction Mechanisms with CNTs

Figure 6.1 shows a number of reported mechanisms for the decomposition of diazonium salts in water, including reactions with the solvent, themselves and nanotubes should they be present. Dediazoniation of aryl diazonium salts in solution is known to follow two main mechanistic pathways, which may exist both simultaneously and competitively. The diazonium ion may undergo heterolytic dissociation into an aryl cation and molecular nitrogen (a), or alternatively if an electron is provided by a reducing agent dediazoniation may proceed through homolytic cleavage, yielding a reactive aryl radical and dinitrogen (b).³⁷⁶ The chemistry of decomposition is quite complex and not well understood due to the variety of reaction pathways available, including a large number of potential intermediates and eventual products (only a fraction of which are addressed in Figure 6.1).^{229,377} Consequently, the products obtained in dediazoniation reactions are highly sensitive to the type and position of the aryl substituent, the selected solvent, temperature, presence of any reducing agents and

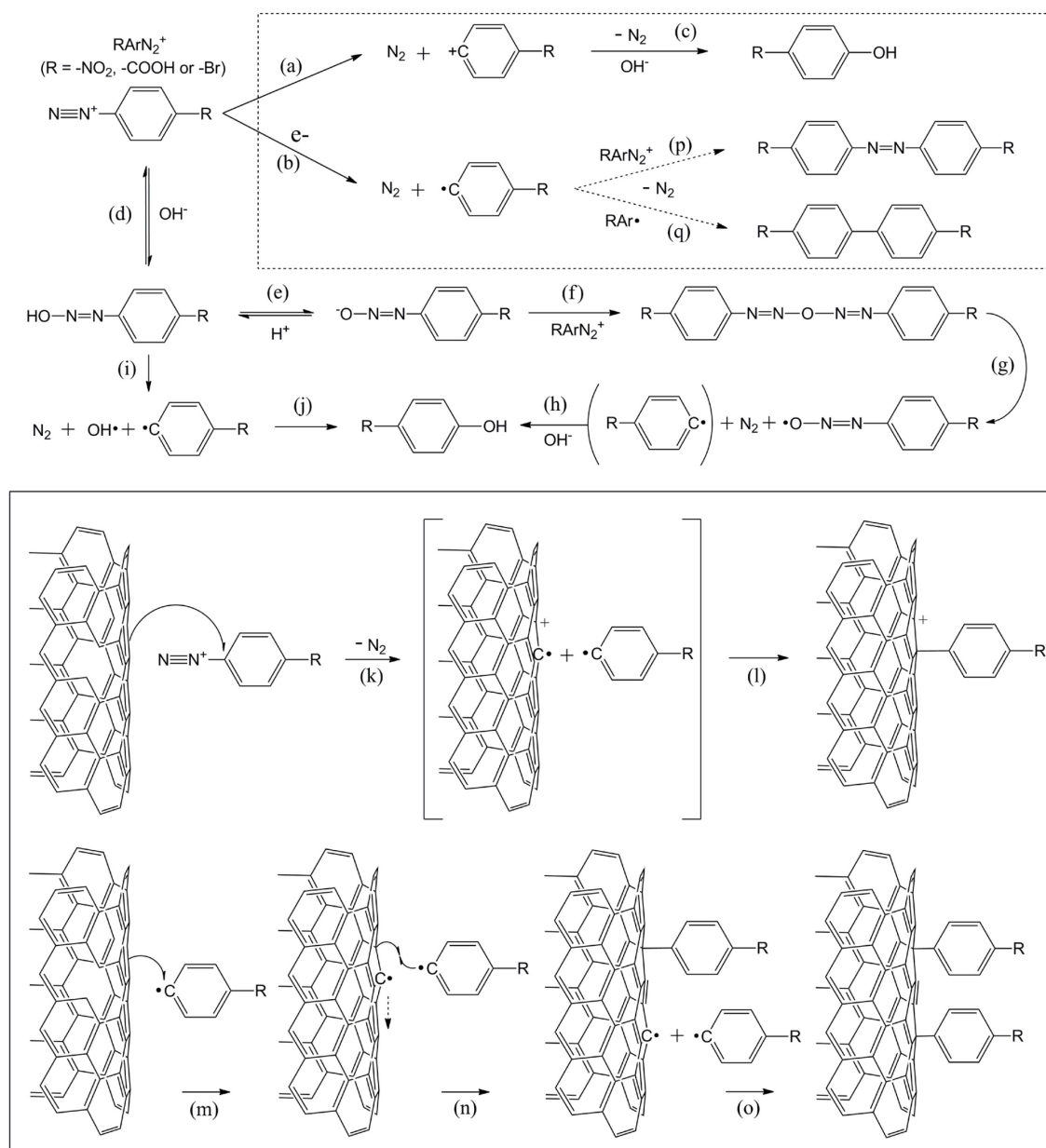


Figure 6.1: Decomposition and reaction pathways for diazonium salts in water and possible reaction mechanisms with a carbon nanotube.

exposure to light, among other conditions.³⁷⁷⁻³⁷⁹ Thermal dediazonation of aryl diazonium salts in water is expected to be dominated by heterolytic decomposition, where nitrogen loss generates an aryl cation that traps nucleophilic hydroxide ions, producing a phenol (c);³⁸⁰ however the presence of surfactant micelles may promote a shift in the relative amounts of decomposition products.^{379,381} It is also possible for the aryl radical to form the phenol product through various pathways (d→i→j) and (d→e→f→g→h), hence its presence does not necessarily reflect involvement of the cationic species.³⁷⁸ The cationic intermediate is expected to be responsible for extensive

polymerisation of aryl groups on the surface of CNTs that is sometimes observed,³⁸²⁻³⁸⁴ though the grafting density is not expected to be significantly greater than a monolayer for spontaneous reactions with single walled CNTs in solution.²⁴⁶ Other termination reactions involving the aryl radical include self-coupling to produce a biaryl (q) or reaction with a diazonium ion to form an azo compound (p). The production of a biaryl species is not often discussed for dediazonation in water, suggesting its prevalence is low, while the production of azo compounds when nanotubes are present has been reported to some extent.²⁴⁵ Compounds containing azo groups are often highly coloured and are referred to as azo dyes due to their use in industry as dyes and pigments,³⁸⁵ thus the presence of such products in solution would be expected to be accompanied by a colour change.

The reaction of diazonium salts with CNTs has been postulated to depend on electron transfer from the nanotube to the diazonium ion, which provides the basis for selectivity as metallic nanotubes donate electrons more readily.^{226,229} In this mechanistic description, the diazonium ion forms a charge transfer complex with the nanotube and extracts an electron, forming an aryl radical and nanotube-radical cation with the evolution of nitrogen gas (k). The aryl radical then forms a covalent linkage with the conjugated lattice of the nanotube, affording an aryl-CNT cation (l).²²⁶ The cationic species could potentially react with any nucleophile in solution, such as fluoride or water, however one study has suggested that the CNT-radical cation, if it is formed, receives an electron (possibly from the diazotate) thus generating a stabilised CNT-radical, as no evidence of nucleophilic attachment was found.²²⁹

While the reaction between diazonium salts and CNTs has been shown to depend on the formation of the aryl radical, i.e. homolytic decompositions, mechanistic studies have suggested that generation of the aryl radical does not necessarily require electron injection from the CNT itself, but rather reaction selectivity could depend on the faster reaction of metallic CNTs with aryl radicals produced in solution through formation-decomposition of diazohydroxides (d→i),³⁷⁸ diazotates and diazoanhydrides (d→e→f→g).^{229,246} In water under neutral to alkaline conditions diazotates can form and further react with the diazonium salt to produce electron rich diazoanhydrides, where these neutrally charged species may migrate into the surfactant micelle to complex with the CNT.^{229,245} The anhydride could then cleave to generate an aryl radical which would attack the conjugated lattice of the CNT sidewall (m). The process of aryl radical attack produces an adjacent radical site on the nanotube sidewall that may delocalise (n) such

that the reactivity of the nanotube is increased in the vicinity of a bonding event, allowing further attachment of aryl groups (o).²²⁹ In this manner the metallic nanotubes will be functionalised much faster than their semiconducting counterparts as once the reaction is initiated it is propagated by increased reactivity near defect sites created by the covalent attachment of aryl moieties. However, two delocalised radical sites on the same nanotube may also create a new double bond.

More recent studies have suggested that the reaction proceeds through a free radical chain mechanism where aryl-coupled CNT radicals are stable intermediates, and that metallic CNT radicals catalyse the reaction of semiconducting nanotubes.²⁴⁶ In this mechanistic description the metallic aryl-CNT radicals act to further reduce diazonium ions to aryl radicals rather than immediately coupling with a free radical in a termination reaction. Thus, the reduction of the diazonium ion at the CNT surface does not necessarily mean the generated aryl radical will react with the reducing CNT, as might be expected if the diazonium ion has initially formed a charge transfer complex with that nanotube.²⁴⁰ The implication that aryl and aryl-CNT radicals are free to diffuse throughout the solution independently suggests some importance of the dynamics of the dispersant solution itself and the particular dediazonation mechanisms operating within it. Previously, the role of the dispersant in the reaction mechanisms has been somewhat overlooked, though whether the dispersant affects the reaction through a change in dediazonation mechanism in solution or simply through steric or electrostatic screening of the nanotube sidewall is presently unknown. The major influence of the dispersant on the reaction is expected to be through differences in adsorption and environmental state at the surface of the nanotube, such as the difference between a tightly packed ionic surfactant and a loosely wrapped polymer, however changes in the decomposition pathways of the diazonium ion with the type of dispersant must also be considered. Thus, the effect of each dispersant on the dediazonation process in the absence of nanotubes was examined, as this was expected to affect the reaction rate of the diazonium compounds with CNTs and possibly the selectivity between electronic types.

6.2 Dediazonation in Dispersant Solutions

Kinetic studies of dediazonation reactions are known for their low reproducibility as slight changes in experimental conditions can alter the reaction rates, orders and products to a large extent.³⁸⁶ Indeed, large differences were observed for decay rates and

products for samples in the same dispersant analysed at different times (i.e. variable ambient temperature) and under different levels of light exposure, or even in containing vessels made of different material. However, comparison of samples treated in the same manner may still provide some insight into the different rates of decomposition experienced between dispersants.

6.2.1 Diazonium Materials

4-nitrobenzenediazonium tetrafluoroborate (nitro-BDTFB, Aldrich, 97%) and 4-bromobenzenediazonium tetrafluoroborate (bromo-BDTFB, Aldrich, 96%) salts as well as 4-aminobenzoic acid (Sigma, $\geq 99\%$) were purchased from Sigma-Aldrich (Sydney, Australia) and used as received. 4-carboxybenzenediazonium tetrafluoroborate (carboxy-BDTFB) was synthesised according to the general procedure described by Roe.³⁸⁷ Specifically, 4-aminobenzoic acid (13.72g; 0.1mol) was dissolved in a mixture of 48% fluoroboric acid (34mL) and distilled water (40mL). After cooling to 0°C, sodium nitrite (6.8g; 0.1mol) in distilled water (15mL) was added dropwise. The mixture was stirred for an additional 30 minutes and the thick precipitate was collected by vacuum filtration. The powder was purified by dissolving in a minimum amount of acetone and then flocculated by addition of diethyl ether. The product 4-carboxy-BDTFB was obtained as a pale orange powder (20.00g, 85%). All diazonium compounds were stored below 4°C in the dark to prevent their decomposition.

6.2.2 Decomposition in Water

The stability of the BDTFB salts under ambient laboratory conditions was first examined in water alone. Bromo-, nitro- and carboxy- benzenediazonium salts were added to 40mL of water in polypropylene vials at a concentration of approximately $15\mu\text{g}\cdot\text{mL}^{-1}$. These solutions were kept under ambient laboratory conditions and consequently were exposed to intermittent light over the course of the experiment. 3mL aliquots were transferred to quartz cells for UV-Vis analysis (Cary 50) and then returned to the vial after each measurement. A selection of the collected spectra are shown in Figure 6.2A, while their normalised spectra at the time of preparation are shown in Figure 6.2B. The bromo- salt exhibits a single peak centered at 292nm with a smaller absorbance feature at $\sim 220\text{nm}$. The nitro- salt possesses a large peak at 261nm

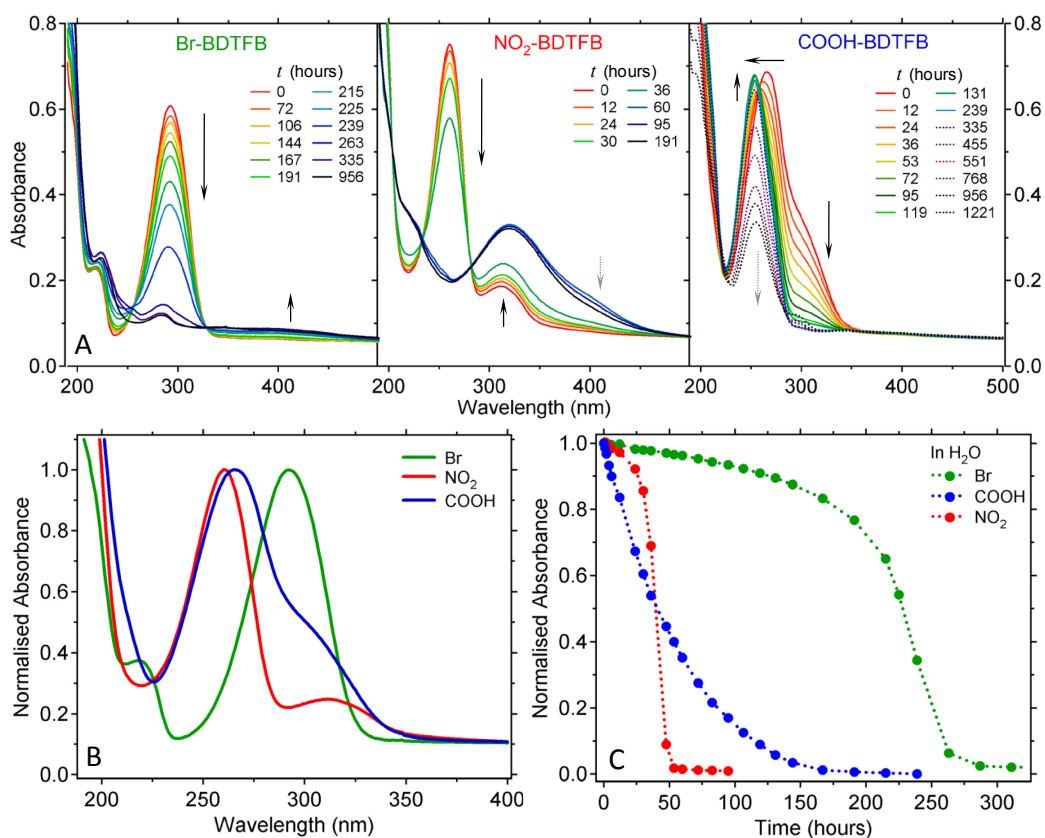


Figure 6.2: (A) UV-Vis absorption spectra for the decay of bromo- (left), nitro- (centre) and carboxy-BDTFB (right) salts over time at $\sim 0.015 \text{ mg mL}^{-1}$ in water under ambient laboratory conditions. Spectra for the initial solutions normalised to their peak maxima are shown in (B), while kinetic decay for each salt is plotted in (C) at wavelengths of 292, 261 and 300nm for bromo-, nitro- and carboxy- salts respectively.

with a broad shoulder of much lower intensity at around 312nm, consistent with the observations of others,³⁷⁸ while the carboxy- salt spectrum consists of a main peak at 266nm that has a large shoulder centered close to 309nm. In aqueous solution the major absorbance peaks that are associated with each species are observed to decay over time as the diazonium salt is converted to its decomposition products, as shown in Figure 6.2C. To produce these kinetic trends the absorbance at a fixed wavelength was normalised between the initial maximum value and a baseline zero value (taken as the point in time at which spectral variation ceases between several successive scans) before plotting these values as a function of time. Some small amount of intact diazonium salt may still be present in the final solution, although the concentration remaining is expected to be negligible.

The bromo- salt was the most stable of those studied, taking in excess of 250 hours to fully degrade. An initially slow period of decomposition was followed by a relatively

rapid decrease in diazonium concentration after about 200 hours for this salt. No major decomposition peaks arise, although there remains a small absorbance peak at ~282nm which displays minimal decay with further monitoring. This peak is likely due to bromophenol (~280-285nm^{388,389}) which is the expected major decomposition product of this salt. A broad absorbance centered at around 400nm also evolves, however its intensity is quite low. The intensity of this broad peak is also diminished at longer timescales, reaching a maximum at around the same time as the diazonium peak is fully depleted. The absorbance at longer wavelengths is expected to be due to a low incidence of azo-coupling with decomposition and serves to provide a slight yellowish colouring to the solution. It is likely that azo-coupling occurs simultaneously with decay of the diazonium salt resulting in increased absorbance over the range 350-450nm, although this peak is slowly lost at longer timescales suggesting that the azo products are also unstable and degrade over time.

The nitro- salt exhibits similar behaviour to the bromo-substituted compound with initially slow decay followed by a rapid drop in concentration, however it is far less stable and undergoes complete dediazonation within about 50 hours. In this case a major absorbance peak evolves at around 320nm which is expected to be due to the decomposition product nitrophenol.³⁹⁰ There is some increase in absorbance at longer wavelengths with a broad absorbance appearing around 350-450nm, which is again believed to be associated with assorted azo-coupled products (see Section 6.2.3), and again this absorbance band displays decreasing behaviour with extended time periods as was observed for the bromo- salt.

The initial peaks present in the absorbance spectrum of the carboxy- salt exhibit a relatively smooth decay over time, however growth of a secondary peak occurs at around 253nm which is assigned to the decomposition product hydroxybenzoic acid.³⁸⁸ This peak is convoluted with the primary diazonium peak at 266nm and prevents determination of the decay curve at this wavelength. Therefore the shoulder at 300nm was used to plot the decomposition of the carboxy- salt in Figure 6.2. Unlike the bromo- and nitro- salts no absorbance peaks develop at higher wavelengths, suggesting that the formation of azo compounds is not pronounced in this case. The peak at 253nm that develops as the peak at 266nm decays causes an apparent blue-shift of the absorbance maximum although with a small drop in intensity. By the time the shoulder at 300nm is entirely depleted (after roughly 170 hours) the absorbance strength of the decay peak matches that of the initial diazonium peak indicating essentially complete conversion to

the secondary product. The hydroxybenzoic acid absorbance peak is further found to decay at longer timescales with no additional peaks becoming apparent.

6.2.3 Decomposition in Various Dispersant Solutions

The dediazonation kinetics of both bromo- and nitro-BDFTB salts were examined in solutions containing 1wt% of each dispersant as shown in Figure 6.3. The rate of diazonium ion degradation was measured through depletion of the corresponding peaks in UV-visible absorbance spectra of the solutions, occurring at 261nm for nitro- and 292nm for bromo-BDFTB as discussed in Section 6.2.2. For Triton X-405 and SDBS, where the nitro-BDFTB peak is masked by surfactant absorption in the UV region, the rate of decay was measured by the rate of increase in absorbance from a corresponding major decomposition product. The nitro-substituted compound is less stable than the bromo- salt and decomposes much more rapidly, hence kinetic scans were taken with the sample enclosed in the spectrophotometer for nitro-BDFTB samples (i.e. in capped quartz cuvettes in the dark). As the bromo- salt takes much longer to decay, these samples were left in sealed polypropylene containers under ambient laboratory conditions and were thus exposed to daylight intermittently.

Large differences in stability are demonstrated between the different dispersants in Figure 6.3, where SDS and CTAB appear to stabilize both of the salts to a high degree with complete loss of the original diazonium peak taking longer than a month in each case. At the opposite end of the time scale, complete degradation of both salts in SCMC-90 was observed to take less than 3hrs. SC and DOC also show rapid dediazonation for both bromo- and nitro- substituents, while these salts displayed intermediate stability in both Triton X-405 and Brij S-100. Diazonium species in SDBS solution exhibited an initially rapid decay followed by a decrease in decomposition rate for both salts, although for the nitro- salt this may represent a conversion of products at longer timescales; in this instance the nitrophenol peak at 320nm developed first and was apparently converted to a product that absorbs at ~405nm (the evolution of which was used to plot the decay curve in Figure 6.3). Approximately the same degradation rate was shown for both salts in Tween 60, while in PVP much faster decay was displayed for the bromo- than for the nitro-BDFTB salt, which is attributed to illumination, temperature and container type differences between sample sets.

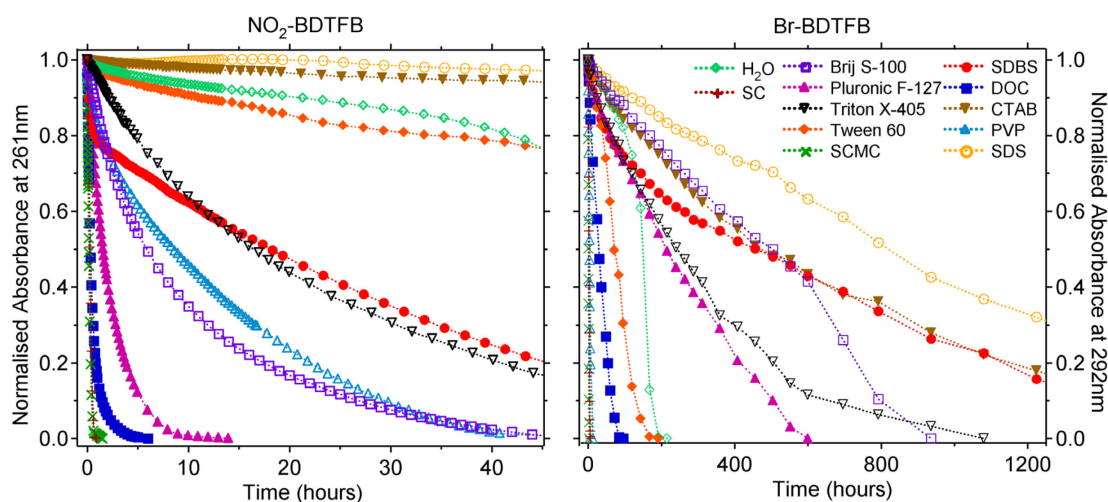


Figure 6.3: Decay of nitro-BDTFB (left) and bromo-BDTFB (right) salts over time at $\sim 0.015\text{mgmL}^{-1}$ in 1wt% of each dispersant as measured from UV-visible absorbance spectra. All solutions were kept under ambient conditions; however nitro-BDTFB samples were scanned in the spectrophotometer for the first 48 hours and thus decomposed in the dark.

The stability of the diazonium salts in each dispersant follows the trends $\text{SDS} > \text{CTAB} > \text{H}_2\text{O} > \text{Tween 60} > \text{Triton X-405} > \text{Brij S-100} > \text{PVP-55} > \text{SDBS} > \text{Pluronic F-127} > \text{DOC} > \text{SC} > \text{SCMC-90}$ for the nitro- salt and $\text{SDS} > \text{Brij S-100} > \text{CTAB} > \text{H}_2\text{O} > \text{Triton X-405} > \text{Pluronic F-127} > \text{SDBS} > \text{Tween 60} > \text{DOC} > \text{PVP-55} > \text{SC} > \text{SCMC-90}$ for the bromo- salt in order of increasing rate of decomposition. The similarity of these trends suggests that, for the most part, the dispersant affects the dediazonation mechanism more-or-less equivalently for each substituent. However, the effect of the individual dispersants on the mechanism is different in each case, as evidenced by the absorbance spectra of the degraded diazonium solutions.

The ratio of reaction products is significantly varied for solutions of nitro-BDTFB in each dispersant as shown in Figure 6.4, with each system yielding different decomposition compounds. The complex nature of dediazonation reactions makes assignment of the produced species via absorbance spectra extremely difficult and further analysis by additional techniques would be required to ascertain the exact composition of the reaction products. However, possible reaction products may be tentatively assigned through positions of their peak maxima. For the nitro- salt, nitrophenol at $\sim 320\text{nm}$ is expected to be present in most cases, although absorbance at this wavelength is only pronounced for water, Brij, CTAB and Tween solutions. The deprotonated form (nitrophenolate) strongly absorbs at $\sim 400\text{nm}$,³⁹⁰ however this species is not expected to be prevalent at neutral pH. The radical coupling product dinitro-

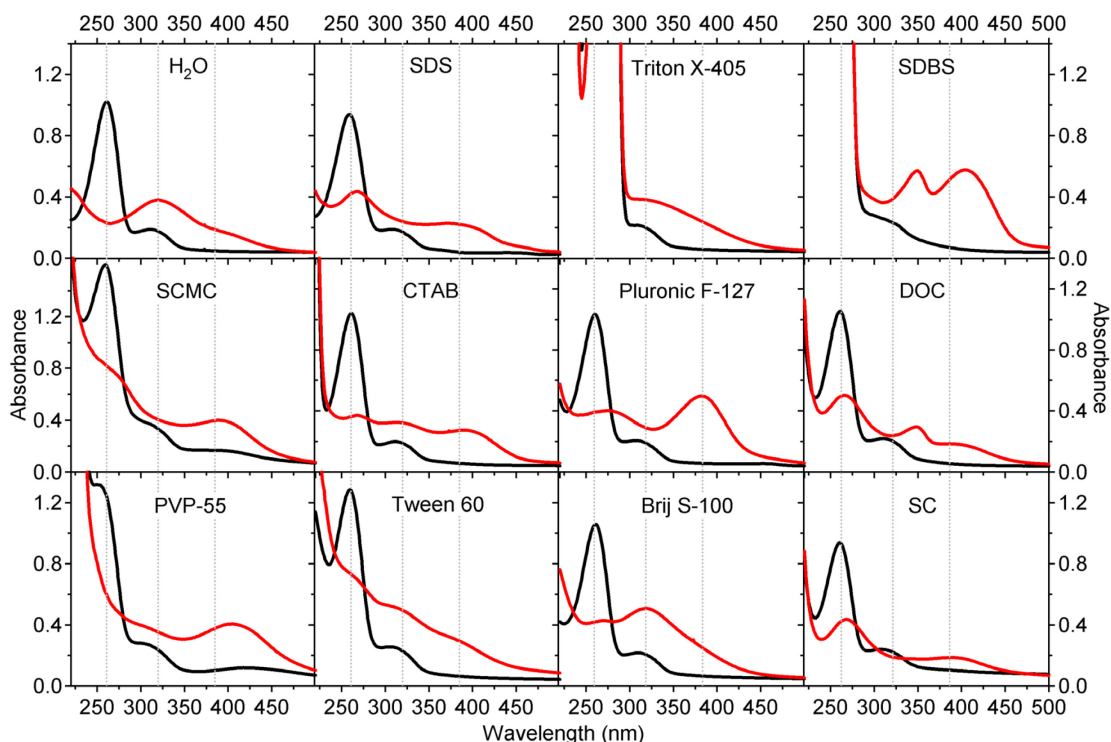


Figure 6.4: UV-Vis spectra of nitro-BDTFB in each dispersant (black) and the corresponding spectra after depletion of the diazonium peak (red). Dotted lines are drawn at 261, 320 and 385nm.

biphenyl absorbs at approximately 305nm,³⁹¹ a wavelength for which no appreciable peak is observed in any dispersant solution (except perhaps PVP), suggesting this product is not preferred in any of the studied systems. The most probable form of nitrobenzenediazotate has an absorbance peak at 330nm, which is not apparent in any of the dispersants, although this and other forms of the diazotate and diazohydroxide species are generally unstable intermediates of decomposition in aqueous solution.³⁹²

A previous analytical study of the decomposition products of 4-nitro-BDTFB in water has shown 4-nitrophenol along with 4-nitrobenzene and 4-hydroxybenzene-diazonium.³⁷⁸ Nitrobenzene absorbs at around 266nm in water³⁹³ and a peak at around 266-268nm was observed for DOC, SC, SDS and CTAB solutions, while SCMC and Tween also have absorbance bands that could be associated with this compound. Hydroxybenzene-diazonium, which absorbs at ~350nm, may be produced in the solution through nucleophilic substitution of the nitrite ion or an alternate pathway involving the diazotate ion as a nucleophile.³⁷⁸ Both SDBS and DOC show absorbance peaks at this wavelength. The coupling of this product with a nitrophenyl group could produce the azo dye 4-hydroxy-4'-nitroazobenzene, which possesses a major peak at around 385nm (in acetone),³⁸⁸ which could possibly account for the major peak in the

Pluronic solution. It is known that absorbance maxima shift depending on the polar microenvironment experienced by the molecule, thus peaks occurring at wavelengths slightly different to those listed may be related to the same compounds having undergone spectral shifts due to polarity differences in the enveloping micelles of each dispersant. The peak maximum for this particular azo dye has a variation of up to 30nm in solvents of differing polarity,³⁹⁴ hence peaks around 380-390nm could belong to this product in the various dispersants. Interestingly the compound 4-4'-dinitroazobenzene, which seems the most likely azo-coupled product for decomposition of nitro-BDTFB and absorbs at about 341nm (in chloroform),³⁹⁵ does not appear to be a major component for any of the resultant solutions. Thus, higher wavelength absorbances from 350-450nm may not be related to azo compounds formed solely from the diazonium salt, but rather from unknown products formed by reaction with the different dispersant molecules. Nitro-aromatic azo groups coupled with different organic substituents often have peaks in the 400-450nm range,³⁸⁸ and reactions of photo-generated aryl cations from diazonium salts have been shown to couple with π -nucleophiles of various forms.³⁹⁶

6.3 Effect of Dispersant Concentration

The decay of bromo- and nitro-BDTFB salts in Pluronic F-127 solutions of different concentrations was examined and the resulting UV-Vis spectra are shown in Figure 6.5, with an image of the degraded nitro-BDTFB solutions displayed in Figure 6.6. As nitro-BDTFB decays rapidly in solutions containing Pluronic the samples were contained in quartz cells inside the spectrometer for the entire duration of the experiment and therefore decomposed in the dark. Dediazonation of nitro-BDTFB in SDBS and SDS was also investigated and absorbance spectra for these samples are provided in Figure 6.7. In these solutions, as well as for bromo-BDTFB in Pluronic, the decay is much slower, hence the majority of decomposition occurred in polypropylene (SDBS) or soda glass (SDS and Pluronic with bromo-BDTFB) containers under ambient laboratory conditions.

Plots of the absorbance at fixed wavelength are provided in Figure 6.8 for the bromo-salt in Pluronic. The normalised absorbance from the diazonium peak at 292nm show some variation, where sharp drops in concentration between data points occur at

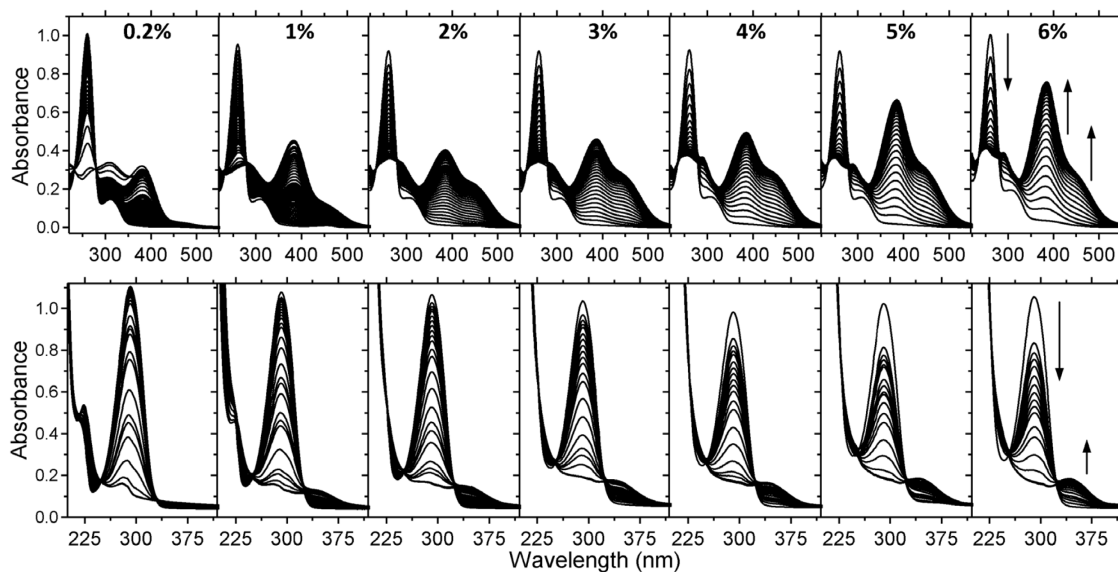


Figure 6.5: Evolution of absorbance spectra for $13.7\mu\text{g}\cdot\text{mL}^{-1}$ NO_2 -BDTFB (top) and Br-BDTFB at $15.6\mu\text{g}\cdot\text{mL}^{-1}$ (bottom) in different concentrations of Pluronic F-127 over time. The Pluronic spectrum was subtracted with the baseline in each case for the nitro salt but remains in the bromo- salt spectra, as evidenced by the red-shifting spectral cut-off with increasing Pluronic concentration.

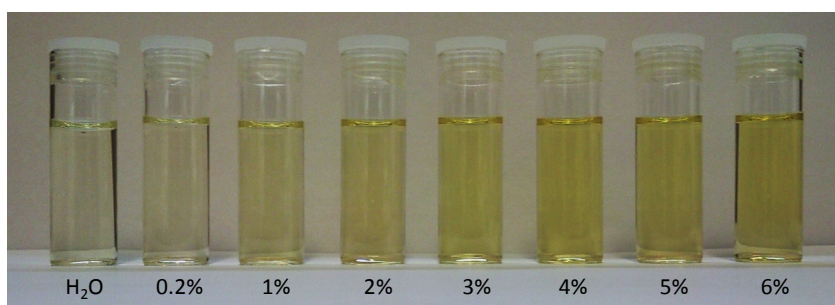


Figure 6.6: Change in solution colour for decomposition of nitro-BDTFB in different concentrations of Pluronic F-127.

roughly 12 hour intervals. Such irregularity in the decay curves may be explained by the rate of decomposition being slightly increased during daylight hours, probably due to the increase in room temperature, though the influence of light may also play a role. The decay of the diazonium peak is compared to the evolution of the absorbance at 341nm in each case. This peak is believed to be due to an azo-coupling product, however the absorbance maximum is significantly blue-shifted in Pluronic compared to the peak observed in water alone (occurring at around 395nm), therefore it is probable that a different decomposition product is forming when the dispersant is present. The formation of the decomposition product is certainly more prominent in Pluronic solution compared to water (Figure 6.2A), hence the presence of Pluronic causes a distinct change in the degradation pathways. This is made more evident by the increase in the

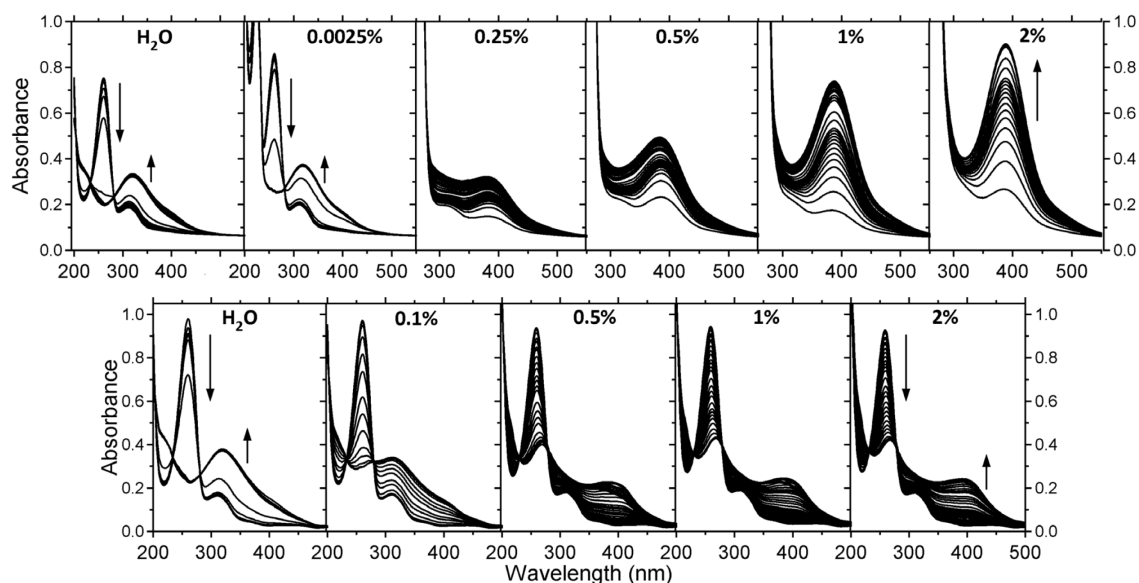


Figure 6.7: Evolution of absorbance spectra for $\text{NO}_2\text{-BDTFB}$ at $\sim 14 \mu\text{g}\cdot\text{mL}^{-1}$ in different concentrations of SDBS (top) and SDS (bottom) over time.

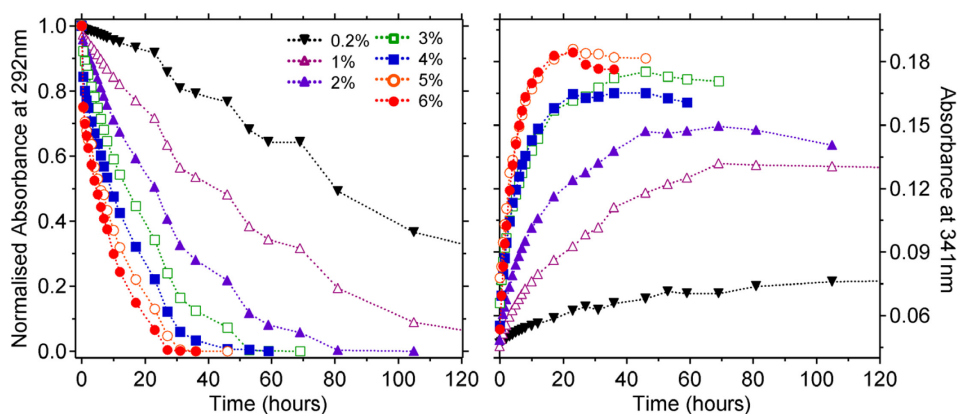


Figure 6.8: Decay of the bromo-BDTFB peak at 292nm over time at $15.6 \mu\text{g}\cdot\text{mL}^{-1}$ in different concentrations of Pluronic F-127 under ambient conditions (left). Absorbance increases at 341nm (possibly corresponding to azo product formation) are also shown for each case (right).

rate of dediazonation that occurs with increasing Pluronic concentration. Formation of the reaction product at 341nm is favoured with greater Pluronic content within the solution, while the bromophenol absorbance peak at 280nm (remaining after dediazonation) is decreased and becomes undetectable at Pluronic concentrations above 3%.

The decomposition of nitro-BDTFB in Pluronic, SDBS and SDS is similarly analysed in Figure 6.9, where the normalised absorbance for decay of the diazonium peak at 261nm is compared with the increase in absorbance due to decomposition products at around 385nm. Note that for SDBS the diazonium decay curve at 261nm is extrapolated by

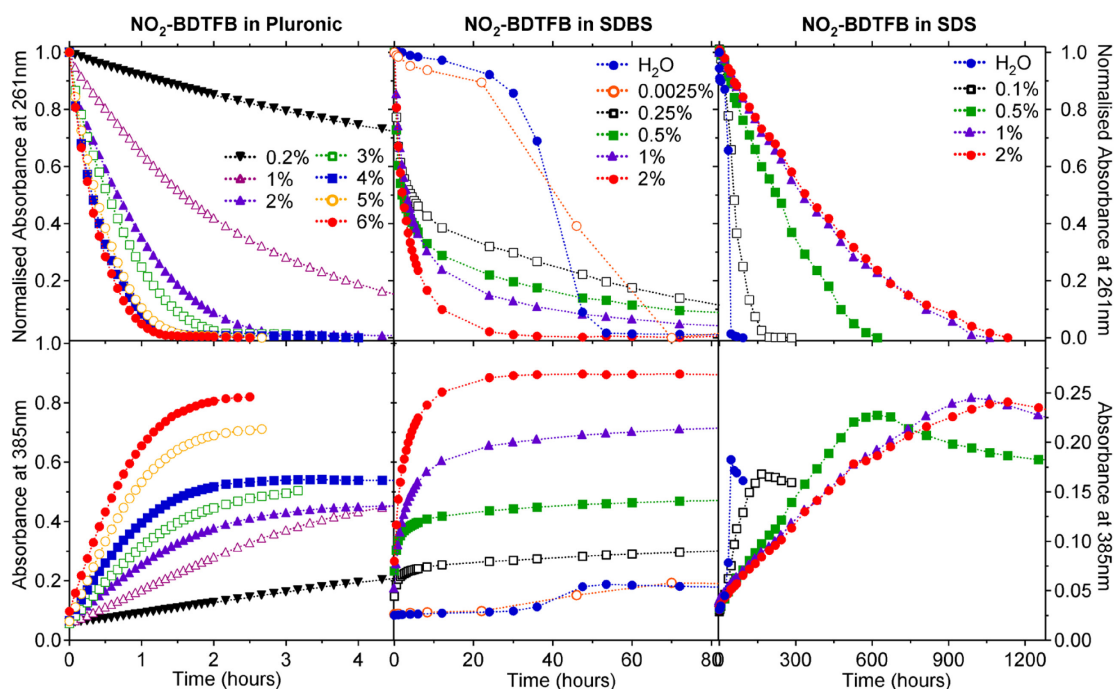


Figure 6.9: Decay of the nitro-BDTFB peak at 261nm over time at $\sim 14\mu\text{g}\cdot\text{mL}^{-1}$ in different concentrations of each dispersant for Pluronic, SDBS and SDS from left to right (top). Solutions in Pluronic were incubated in the spectrometer (dark) for the entirety of the run, while those in SDS and SDBS were exposed to ambient light. Absorbance increases at 385nm (potentially corresponding to azo product formation) are also shown for each case (bottom). The curves for SDBS at 261nm are approximated by transformation of the 385nm data as the diazonium peak is obscured by surfactant absorbance in this case.

inversion of the 385nm peak data as SDBS absorption masks the diazonium peak. For both SDBS and Pluronic there is a similar increase in the rate of nitro-BDTFB dediazonation with dispersant concentration as was observed with the bromo- salt in Pluronic. Again, the increased rate of diazonium peak loss is coupled to an increase in the concentration of products that absorb at higher wavelengths around 350-450nm. Solutions possessing greater absorbance over this region also display a more pronounced yellow colouration as shown for the nitro-BDTFB salt solutions after decomposition in Pluronic (Figure 6.6). Although the surfactant SDBS did not possess a large peak at 385nm in the previous analysis (see Figure 6.4), under these conditions decomposition in SDBS produces a peak at this wavelength while absorbance due to other products is not evident. This may suggest a significantly different decay mechanism being dominant when the solution is illuminated, or perhaps some influence from the containing vessel.

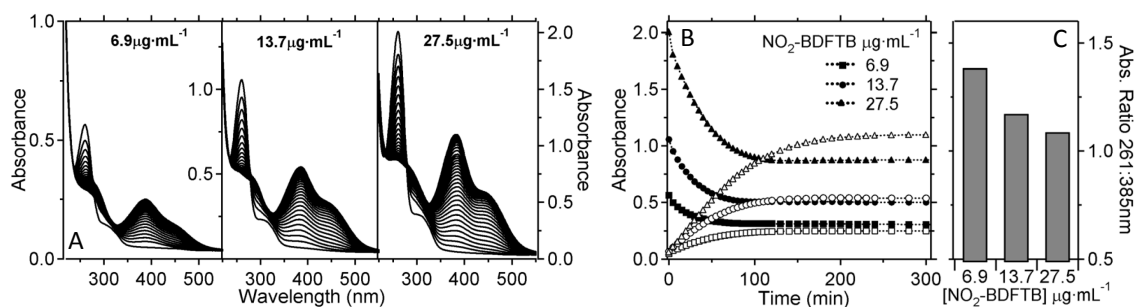


Figure 6.10: UV-Vis spectra for the decomposition of nitro-BDTFB in 4% Pluronic F-127 at different concentrations of the salt (A), evolution of the absorbance at wavelengths of 261nm (solid symbols) and 385nm (open symbols) over time (B), and the ratio of initial absorbance at 261 to final absorbance at 385nm for each diazonium concentration (C).

The decomposition products are slightly different for the SDS and Pluronic cases. Although both decayed solutions possess a broad absorbance peak at $\sim 385\text{nm}$, an additional absorbance peak centered at $\sim 460\text{nm}$ (which also appears to increase in intensity with the dispersant concentration) emerges in the spectra of Pluronic solutions. The absorbance due to decomposition products at both 385 and 460nm was also found to increase with diazonium concentration at a fixed Pluronic content, as shown in Figure 6.10. Since the prevalence of these products increases with the concentration of either Pluronic or the salt itself, it could be argued that the absorbance from 350-450nm is a result of coupling between the diazonium and the dispersant. However, since the peak at 385nm is consistent among SDS, SDBS and Pluronic, which have different structures, this does not seem likely. Regardless of their exact form, the increased prevalence of these products at higher concentrations of both Pluronic and SDS suggests that both dispersants promote the formation of azo compounds over other decomposition products. This would decrease the number of aryl radicals formed in solution as the azo groups are retained in the dyes and not liberated as molecular nitrogen. Even if the compounds did not contain azo groups and were a consequence of aryl linkage to the dispersant molecules, such a side-reaction would still reduce the effective diazonium concentration available for reaction with the nanotubes.

While peaks emerge in the same positions for nitro-BDTFB in SDS as with the other dispersants suggesting formation of similar decomposition products, this system displays a decreasing product formation rate at $\sim 385\text{nm}$ with increasing surfactant concentration. The dediazonation process takes much longer for SDS, requiring approximately 10 times as long as SDBS and almost 200 times longer than Pluronic for

| SDS | | Pluronic F-127 | | SDBS | |
|--------------|-------------|----------------|-------------|--------------|-------------|
| Conc. (wt %) | Solution pH | Conc. (wt %) | Solution pH | Conc. (wt %) | Solution pH |
| 2.0 | 6.56 | 1.0 | 6.57 | 2.0 | 8.19 |
| 1.0 | 6.57 | 2.0 | 6.75 | 1.0 | 8.36 |
| 0.5 | 6.66 | 3.0 | 6.73 | 0.5 | 8.47 |
| 0.1 | 6.65 | 4.0 | 6.73 | 0.1 | 8.62 |
| | | 5.0 | 6.74 | | |
| | | 6.0 | 6.76 | | |

Table 6.1: pH values for freshly prepared solutions containing various concentrations of SDS, SDBS and Pluronic F-127.

complete loss of the diazonium peak. Also, although there is a small increase in the amount of the diazonium converted to the decomposition products from 0.1 to 0.5% SDS, there is a lack of substantial increase in decay product with dispersant concentration as was observed for the other salt-dispersant combinations. These results suggest that SDS stabilises the diazonium salt to a significant extent and that the dediazonation mechanism is significantly different in this surfactant in comparison with SDBS and Pluronic (though there are subtle differences within each of the dispersant-salt systems in any case).

It is clear that the presence of a dispersant in the solution, and in particular its concentration, have a pronounced effect on the dediazonation of aryl diazonium salts. Shifts in decomposition pathways may be related to a change in functional form of the diazonium species with altered ionic strength or hydrogen ion activity. Alternatively, the increase in volume of the organic phase with increased surfactant concentration could provide a greater proportion of non-polar microenvironment with which the diazonium species would associate, allowing for an increase in azo-coupling interactions. Table 6.1 provides pH values measured for solutions containing various concentrations of SDS, SDBS and Pluronic as per the concentrations used in the previously discussed dediazonation analysis. It is apparent that the solution pH is not significantly altered with the dispersant concentration in either SDS or Pluronic, while very slight decreases in hydrogen ion activity were observed for SDBS. Since both Pluronic and SDBS show very similar decomposition behaviour (increasing dediazonation rate with increasing surfactant concentration), it seems more likely that it is the increase in available hydrophobic environment that is responsible for this effect rather than any change in pH or ionic strength. It remains to be determined whether the dediazonation rate in dispersant solution correlates with the selectivity of the reaction

with CNTs, however the reaction mechanism is likely to be further affected by the presence of nanotubes which would act as reducing agents.

6.4 Dediazonation in the Presence of CNTs

The effect of nanotubes on the dediazonation mechanics was investigated by incorporating a low concentration of CNTs into a dispersant solution. Nanotubes previously dispersed in Pluronic were added to a solution of 4% Pluronic F-127 at a concentration of approximately $1.3\text{mg}\cdot\text{mL}^{-1}$. The decomposition of nitro-BDTFB in this solution was monitored over time and compared to that of decay in the dispersant solution without CNTs as shown in Figure 6.11. It is apparent that the absorbance of decomposition products at $\sim 385\text{nm}$ increases in the presence of CNTs, thus azo-coupling appears to occur as a competitive reaction to nanotube functionalisation. The formation of azo compounds during dediazonation is a result of the aryl radical, which may be generated by electron transfer from the nanotubes.²²⁹ It is not surprising then that the addition of CNTs increases the prevalence of these products, and it is therefore likely that increasing the dispersant concentration would reduce the rate of nanotube functionalisation by increasing the yield of decomposition products over covalent addition of aryl moieties to the CNTs.

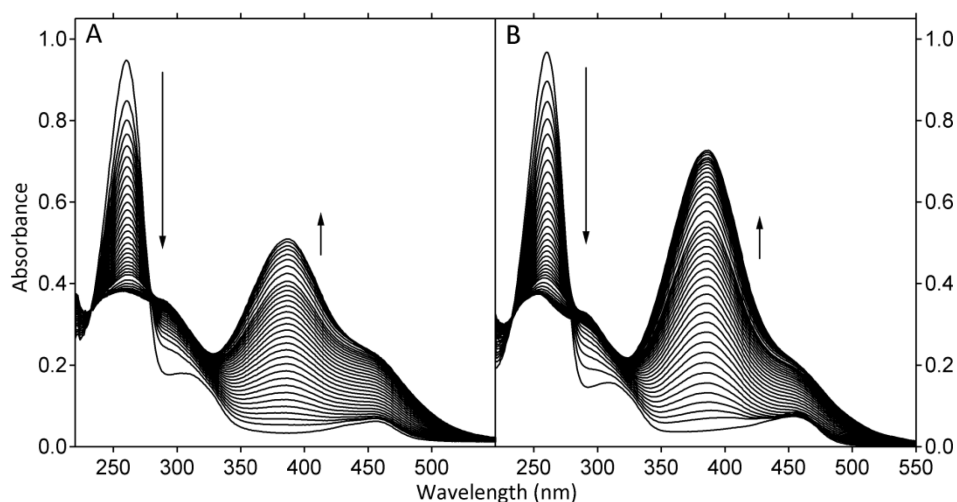


Figure 6.11: Absorbance spectra over time for $13.7\mu\text{g}\cdot\text{mL}^{-1}$ NO_2 -BDTFB in 4% Pluronic F-127 in the absence of CNTs (A) and with the addition of $1.3\mu\text{g}\cdot\text{mL}^{-1}$ CNTs (B). The spectrum of the nanotubes in (B) was subtracted with the baseline. The amount of decomposition product obtained (absorbing at $\sim 385\text{nm}$) was significantly greater in the presence of the nanotubes.

Chapter 7

REACTIONS OF CNTs WITH DIAZONIUM SALTS IN DISPERSANT SOLUTIONS

7.1 UV-Vis-NIR and Raman Analysis of CNT Dispersions

Once the dediazonation process was examined, the reaction between diazonium salts and CNTs in a variety of different dispersant systems was investigated. UV-Vis-NIR absorbance spectra of arc CNTs dispersed in each surfactant and polymer in which diazonium reactions were performed are shown in Figure 7.1. The particular dispersants employed here were chosen to provide a comparison between ionic, non-ionic and polymeric variants as well as for their proven ability to suspend these specific CNTs as demonstrated earlier in Chapter 3. Aqueous surfactant solutions were prepared at or slightly below their optimal concentrations or at the standard 1wt% where this value was not determined. Specifically, these concentrations were 0.5wt% for SDBS, 4.5wt% for Pluronic F-127, 3wt% for PVP-55, 1.6wt% for DOC, 3wt% for TX-405, 2wt% for Brij S-100 and 1wt% for CTAB, SDS, SCMC-90 and Tween-60. The dispersion protocol was chosen with reference to the results for SDBS dispersions presented earlier

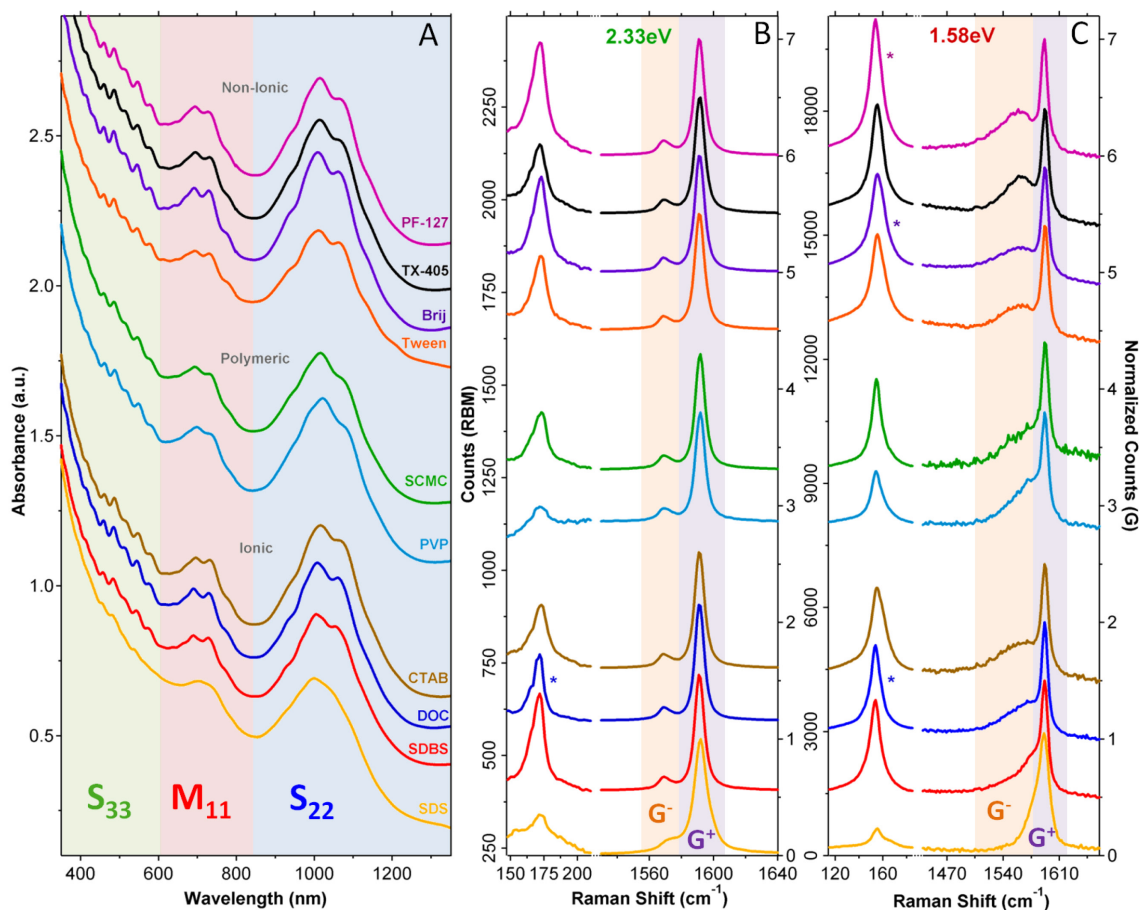


Figure 7.1: UV-Vis-NIR absorbance spectra of solutions diluted to equal CNT concentration (A) and Raman spectra generated at laser energies of 2.33eV (B) and 1.58eV (C) from the original solutions of arc CNTs in various dispersants. For Raman spectra, peaks associated with RBM modes (at low wavenumbers) are the raw spectra, while peaks associated with the G-band (at high wavenumbers) are normalised to their maximum intensity. Asterisks denote Raman spectra that are presented at 0.5x their original intensities.

in Chapters 4 and 5. Explicitly, 12.5mg of as-produced arc-CNT material was added to 25mL of dispersant solution and tip-sonicated at 20% amplitude for 30 minutes using the 6.5mm tip. This procedure delivers approximately $500\text{J}\cdot\text{mL}^{-1}$ of energy to the solution at a power level of $\sim 0.23\text{W}\cdot\text{mL}^{-1}$, a relatively mild sonication intensity that should provide sufficient energy for exfoliation while minimising scission of the nanotubes. Additionally, centrifugation was performed at $1\times 10^5\text{g}$ for 1 hour, a force slightly lower than that previously recognised as optimal for individualisation in SDBS, which would facilitate slight increases in nanotube length and concentration in the supernatant. The carbon to metal ratio should also be improved, although at the expense of incrementally larger bundles being present in the final solution. The use of

parameters shifted towards preservation of nanotube length was conducted as the electronic structure of the nanotubes is expected to be more accessible where the defect density is minimised (i.e. longer tube segments). The effect of the transition metals on the reaction is also unknown, and minimising their concentration should reduce any influence of residual nickel and yttrium particles.

The spectra presented in Figure 7.1 were recorded after dilution to approximately the same CNT concentration such that reagent concentrations would be similar between dispersants. As a consequence the spectral differences between dispersants are subtle, although there is some visible change in fine structure within the nanotube spectrum across the different suspensions. Most notably, SDS shows the least separation between absorptions from the different species, and a more aggregated state of the nanotubes is expected in this surfactant as previously discussed in Chapter 3. SDS was examined here primarily because selectivity for metallic nanotubes has been demonstrated in its prior use for diazonium reactions with HiPCO CNTs,^{226,240,243} and its inclusion was considered necessary for comparison.

Raman spectra for the CNT dispersions collected at excitation energies of 2.33 and 1.58eV are given in Figures 7.1B and C respectively, showing the RBM and G-band regions. The G-band spectra were normalised between the baseline and maximum intensity while RBM features are shown without normalisation to illustrate the variation in CNT concentration between the dispersants. At 2.33eV the G-band spectra are observed to be essentially identical for every dispersant, with the exception of SDS for which the separation between the G^+ and G^- bands is not as distinct. The Raman spectrum for PVP also sits on a weak fluorescent background that is produced by the polymer at this energy, a detail that is more apparent in the RBM spectrum (that has not been normalised). At 1.58eV the G^- band exhibits significant differences across the various dispersants in that the BWF lineshape appears far more pronounced for certain non-ionic surfactants. The Pluronic F-127, Brij S-100, Tween 60, CTAB and Triton X-405 spectra show a much more prominent G^- peak, while SDBS, PVP, SCMC and DOC exhibit weaker BWF components. In particular, the Pluronic and Triton X dispersions display greatly enhanced BWF features. The BWF shape of the G^- band has been shown to be related to surface plasmons that occur in bundles of metallic nanotubes, with the feature losing intensity for smaller bundles.²⁹⁵ These results suggest that SDBS and DOC are more effective for debundling CNTs than the non-ionic surfactants, which agrees with results reported previously in Section 3.1. However, the BWF feature may

be affected by charge transfer between the nanotube and dispersant molecules, where this component of the G-band is weakened when electron density is withdrawn from metallic nanotubes (and is conversely strengthened by donation).²⁹⁴ Consequently, even individualised nanotubes may display a prominent BWF peak and thus the effects of aggregation and molecular interactions on this Raman mode are convoluted.

The fact that SDS shows the least pronounced BWF component of all the dispersants may imply that metallic CNTs are well-dispersed in this surfactant, despite a particularly weak RBM band. Analysis of an SDS dispersion using atomic force microscopy (discussed earlier in Section 3.3.1) revealed that the CNTs were initially dispersed in small bundles which became progressively larger over several days. The BWF feature did not appear to increase in intensity as the CNTs aggregated (and note that the Raman spectrum in Figure 7.1 for SDS was taken two weeks after preparation of the solution). Thus, a more likely explanation is that the SDS molecules serve to localise electron density on the nanotube surface which results in a reduction of the BWF intensity, as has been observed with protonation of nanotube sidewalls in acidic media.²⁹⁶ Indeed, SDS has been suggested to act as a p-type dopant due to the electron withdrawing nature of the sulfate group.^{143,397} Therefore the weak nature of the BWF component that is seen in the Raman spectra of SDS dispersed CNTs at both excitation energies is ascribed to interaction between the nanotubes and the surfactant, rather than aggregation effects, and will be discussed in more detail in Section 7.4. A similar localisation or polarisation of charge may also be involved with the reduced BWF feature in SDBS, however this surfactant is expected to be much better at debundling the CNTs than SDS.¹²²

7.2 Methods of Measuring Selectivity

Reactions between the diazonium salts and arc CNTs in each dispersant solution were performed in capped quartz cuvettes in the dark and monitored by UV-Vis-NIR spectroscopy. In general, 0.1mL aliquots of diazonium salt in water were added to 3mL of CNT dispersion (to obtain a final volume of 3.1mL at the desired concentration) with scanning initiated immediately upon addition. An example set of absorbance spectra obtained over time is shown in Figure 7.2A for the reaction of 2mM bromo-BDTFB with nanotubes dispersed in 0.5% SDBS held at 27°C. Relative intensities of both the S₂₂ and M₁₁ absorbance peaks were recorded at a fixed wavelength for each spectrum

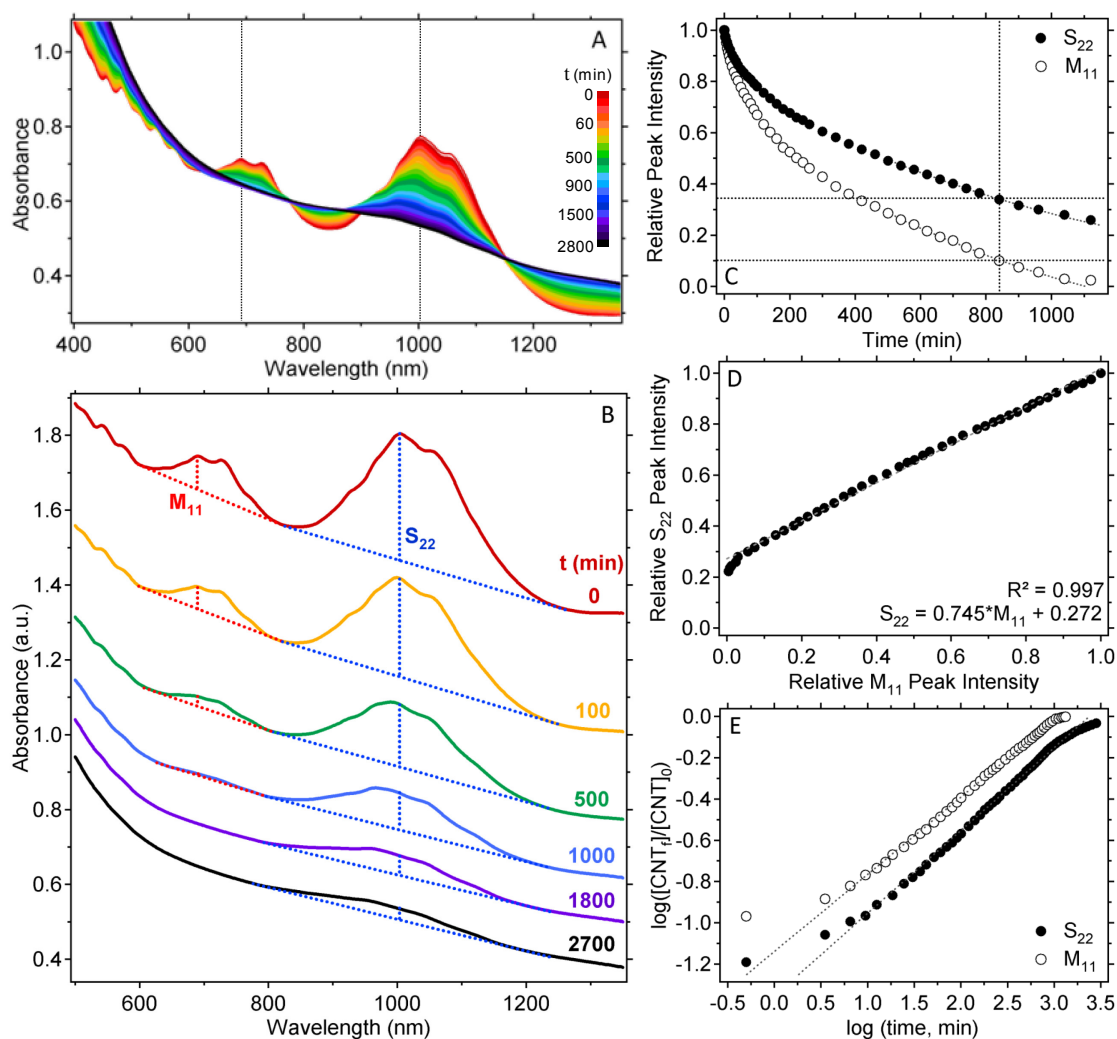


Figure 7.2: UV-Vis-NIR spectra recorded during the reaction between 2mM Br-BDTFB and CNTs dispersed in 0.5wt% SDBS at 27°C (A). Relative intensities were measured at fixed wavelengths corresponding to M_{11} and S_{22} peak maxima (approximately 689 and 1005nm respectively) after construction of linear baselines over each region (B) and then normalised relative to their initial values at $t = 0$ min. Evolution of the peak intensities over time is shown in the kinetic plot (C) where the percentage S_{22} peak remaining at 10% M_{11} is determined from partial polynomial fits and extrapolation to the vertical axis. The selectivity curve S_{22} vs. M_{11} is plotted in (D) where the inverse slope provides the selectivity factor. Grey lines in (E) represent fits of the power law $\log([CNT]_t/[CNT]_0) = \log(\beta) + \alpha \log(t)$ to adjusted data (see text for details).

using the intensity above a linear background as illustrated in Figure 7.2B. Specific wavelengths used for each dispersant system are provided in Table 7.1. Measurements were made using construction lines drawn manually in Igor Pro software as the background absorbance is highly variable, particularly for dispersants in which dediazonation products create a rising baseline towards lower wavelengths. To obtain kinetic data curves as per the example in Figure 7.2C measured intensity values were

| Dispersant | Concentration (wt %) | Solution pH | | [CNT] mg·mL ⁻¹ | D:G Ratio (2.33eV) | Peak λ (nm) | |
|------------------|-------------------------|-------------|--------|------------------------------|-----------------------|---------------------|-----------------|
| | | Neat | + CNTs | | | S ₂₂ | M ₁₁ |
| H ₂ O | - | 5.91 | - | - | - | - | - |
| SDBS | 0.5 | 8.45 | 8.56 | 0.024 | 0.0062 | 1005 | 689 |
| SDS | 1.0 | 6.66 | 7.64 | 0.027 | 0.0091 | 1001 | 704 |
| CTAB | 1.0 | 6.17 | 7.04 | 0.032 | 0.0066 | 1016 | 696 |
| DOC | 1.6 | 7.84 | 7.93 | 0.027 | 0.0062 | 1008 | 690 |
| SCMC | 1.0 | 7.01 | 7.62 | 0.063 | 0.0095 | 1016 | 693 |
| PVP | 3.0 | 3.88 | 4.76 | 0.040 | 0.0107 | 1022 | 698 |
| Triton X-405 | 3.0 | 3.30 | 3.73 | 0.029 | 0.0067 | 1014 | 695 |
| Brij S-100 | 2.0 | 4.13 | 6.38 | 0.031 | 0.0067 | 1009 | 692 |
| Tween 60 | 1.0 | 3.73 | 5.04 | 0.019 | 0.0081 | 1012 | 694 |
| Pluronic F-127 | 4.5 | 6.73 | 7.13 | 0.060 | 0.0057 | 1015 | 694 |

Table 7.1: pH values measured from (freshly prepared) dispersant solutions before and after addition of arc CNTs. The addition of CNTs results in the reduction of hydrogen ion activity in all systems, though the effect is more pronounced in the non-ionic dispersants. Concentrations of nanotubes in the original supernatant solutions for each dispersant are estimated from their absorbance at 850nm. D:G ratios calculated from 2.33eV spectra as well as positions of the S₂₂ and M₁₁ UV-Vis-NIR absorbance peak maxima tracked for each dispersant to create the kinetic data in Figure 7.3 are also provided.

normalised to the original intensity at $t = 0$ min and plotted as a function of elapsed time. Selectivity of the individual reactions was evaluated in three different ways in an attempt to determine the extent of preferential reaction of metallic over semiconducting nanotubes in each case. Firstly, the remaining S₂₂ peak intensity after the M₁₁ peak has been reduced to 10% of its original value (as the precise position of complete quenching is rather difficult to determine) was measured as depicted in Figure 7.2C. This provides an instantaneous measurement of the degree of semiconducting nanotube functionalisation as the metallic nanotubes are nearing complete coverage, but is not greatly affected by the drop in semiconducting intensity that occurs once the metallic CNTs are functionalised. Although the S₂₂ band is reportedly less sensitive to chemical changes than the S₁₁ peak group,^{18,242} it has been shown that these two bands decay at approximately the same rate for reactions with diazonium salts,²⁴⁶ hence the strength of the S₂₂ band should provide a good indication as to the extent of semiconducting nanotube functionalisation. By fitting polynomial splines to the data region where the M₁₁ curve crosses the 10% line the percentage of the S₂₂ peak remaining may be determined, and this value is measured as 33.8% for the example in Figure 7.2C. Where reactions did not go to completion percentage values could be estimated from extrapolated data in some cases (i.e. those for which the peak intensities continued to

decrease), although some reactions terminated before reaching a relative M_{11} intensity close to 10%.

As a second comparative measure, the relative peak height of the semiconducting CNTs was plotted as a function of that of metallic CNTs and subsequently fit using a linear regression. The entire available range is employed for this fit despite the non-linear nature of the selectivity curve in some cases, thus this method provides a more general evaluation of the overall reaction. The reciprocal slope of the linear fit is taken as a 'selectivity factor',²⁴⁶ where a selectivity factor of 1 indicates equal reaction rate between semiconducting and metallic species while values higher than 1 represent greater affinity for reaction with metallic nanotubes. Conversely, a value less than unity signifies preferential functionalisation of semiconducting CNTs. The selectivity curve for the bromo-BDTFB/arc CNT reaction is shown in Figure 7.2D. The linear correlation in this case is quite good, producing a slope of 0.745, which corresponds to a selectivity factor of approximately 1.34.

Finally, the functionalisation of CNTs by aryl diazonium salts has been previously shown to possess a power law dependence of the form $[CNT]_f = [CNT]_0 \beta t^\alpha$, where $[CNT]_f$ is the concentration of functionalised CNTs, $[CNT]_0$ is the initial concentration of CNTs and α and β are fitting parameters.²⁴⁶ Since the concentration of CNTs is linearly related to absorbance, the values of $[CNT]_0$ and $[CNT]_f$ may be directly substituted by measured absorbance intensities. The concentration of functionalised nanotubes is then estimated by the intensity difference $[CNT]_f = [CNT]_0 - [CNT]_t$, where $[CNT]_t$ is the relative intensity at time t . The scalar β and exponent α were consequently extracted from fits of $\log([CNT]_f/[CNT]_0) = \log(\beta) + \alpha \log(t)$ to the kinetic data as per the method of Schmidt *et al.*, as shown in Figure 7.2E for the example reaction. The ratios of $\alpha(M_{11})$ to $\alpha(S_{22})$ and $\beta(M_{11})$ to $\beta(S_{22})$ give an indication of the differences in reaction rate between the CNT electronic types.

7.3 Reactions in Different Dispersants

Dispersions of electric-arc CNTs in each surfactant or polymer were mixed with 2mM diazonium salt solutions and reacted at 27°C (within capped quartz cuvettes in the dark) for 24 hours or until all CNT related absorbance peaks had been completely bleached in the UV-Vis-NIR spectra. This concentration of diazonium should be sufficient to fully

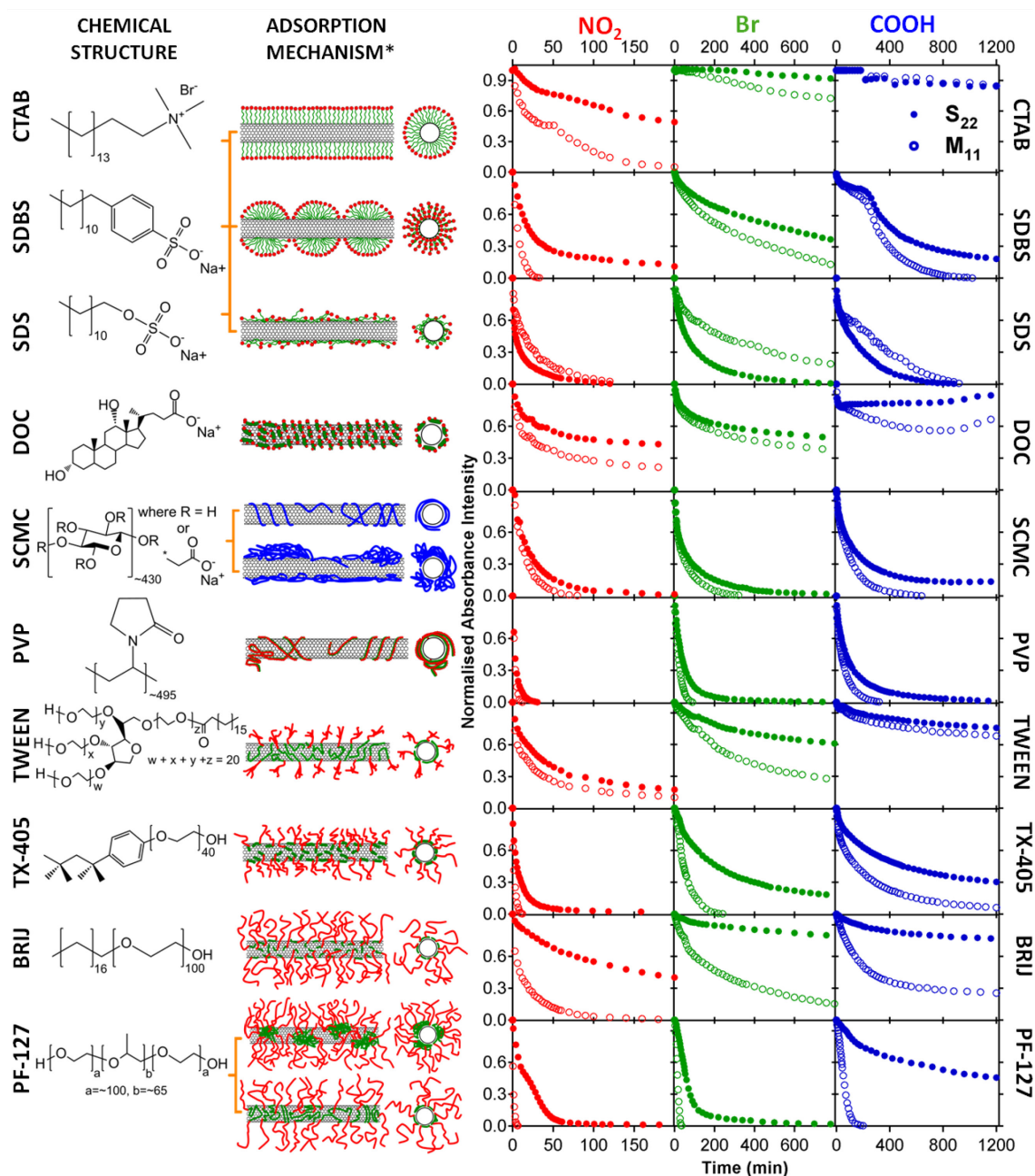


Figure 7.3: Chemical structures of each dispersant and some possible adsorption conformations for each type. Kinetic data for M_{11} (open circles) and S_{22} (full circles) absorbance peak suppression during reaction with 2mM of nitro-, bromo- and carboxy-BDTFB at 27°C is shown (right) for each dispersant. *Adsorption mechanisms are schematic only, i.e. are not to scale and do not reflect accurate packing densities, representing only those conformations that have been previously reported in literature for surfactants of that type. Red sections represent hydrophilic segments, while green sections are hydrophobic.

functionalise all of the nanotubes present in solution, while reactions were performed at the natural pH of the dispersions as per values provided in Table 7.1. The natural pH of most CNT dispersions is close to neutral, with the exceptions of Tween 60 and Triton

X-405 which possess relatively high hydrogen ion activities (5.0 and 3.7 respectively) and SDBS which has a slightly alkaline pH (~8.6). Kinetic data for reactions performed with three different aryl diazonium salts are shown in Figure 7.3, along with the structures of the dispersants. Possible adsorption conformations for each dispersant on the CNT surface are reproduced from Section 3.1.1 for convenience, depicting differences in the local environment experienced by the diazonium reagents. The type of dispersant has a significant influence on the reaction as evidenced by the variety of kinetic curves displayed in Figure 7.3, possibly due to differences in surface density or ‘wrapping’ configuration, charge or chemical nature. The general trend of the reaction rates was expected to follow the relative electron withdrawing ability of the BDTFB salts in each dispersant. For the aryl salts bearing different functional groups in the *para* position, this can be expressed in terms of their σ_p Hammett parameters which are approximately 0.78 for NO₂, 0.45 for COOH and 0.23 for Br.³⁹⁸ However, even though the decomposition of the three salts in water alone follows this expected trend (see Section 6.2.2), here the reaction rate follows the trend nitro>bromo>carboxy in each dispersant which is more consistent with the carboxy- salt reacting in its dissociated form ($\sigma_p \sim -0.1$).

Selectivity curves for each reaction are presented in Figure 7.4, while the calculated selectivity factors are given in Figure 7.5 for comparison. Also plotted in Figure 7.5 are the remaining S₂₂ percentages determined at 10% of the original M₁₁ intensity. It is apparent from these two values that there is large difference in the selectivity of the reaction across the various dispersants. The instantaneous S₂₂% remaining at 10% M₁₁ values show a greater spread than the selectivity factors which are between 1 and 2 for most reactions. However, the trend in both values is essentially the same across the dispersant range, so although the curved nature of the selectivity data below ~10% M₁₁ intensity observed for some reactions does lower the measured selectivity factors in those instances, this does not seem to significantly bias the results. The high molecular weight polymers PVP and SCMC show fast loss of absorbance peaks for both CNT electronic types with minimal separation of their reaction rates and hence return selectivity factors close to 1. The non-ionic dispersants Tween 60 and Triton X-405 along with ionic SDBS, CTAB and DOC also return relatively low selectivity factors where they could be determined, although for certain dispersant-salt combinations (such as bromo-BDTFB with CTAB and Triton X-405) the metallic CNTs are functionalised

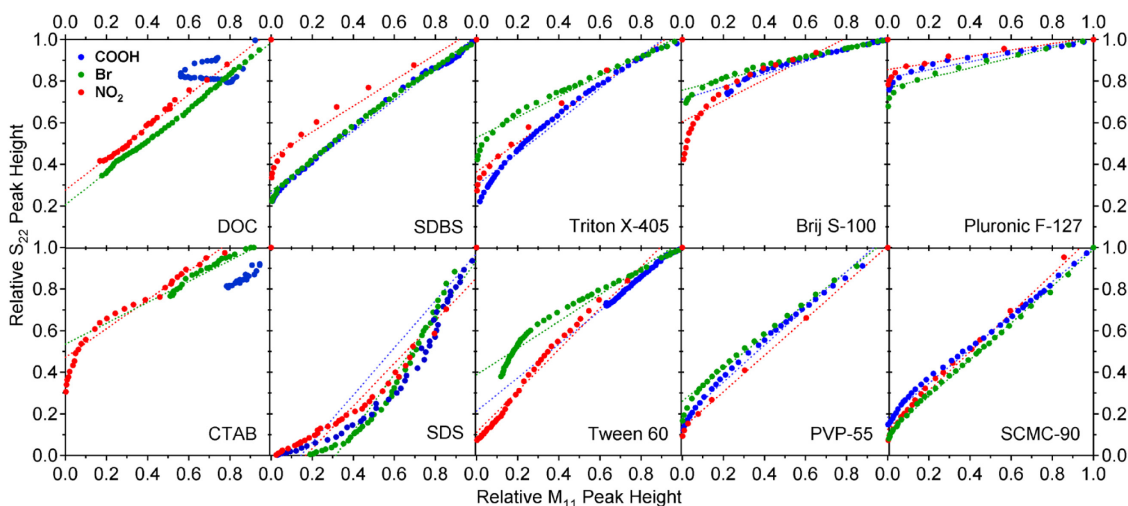


Figure 7.4: Selectivity curves with linear fits for each salt and dispersant combination. The semiconducting relative absorbance peak height is plotted as a function of that from metallic species.

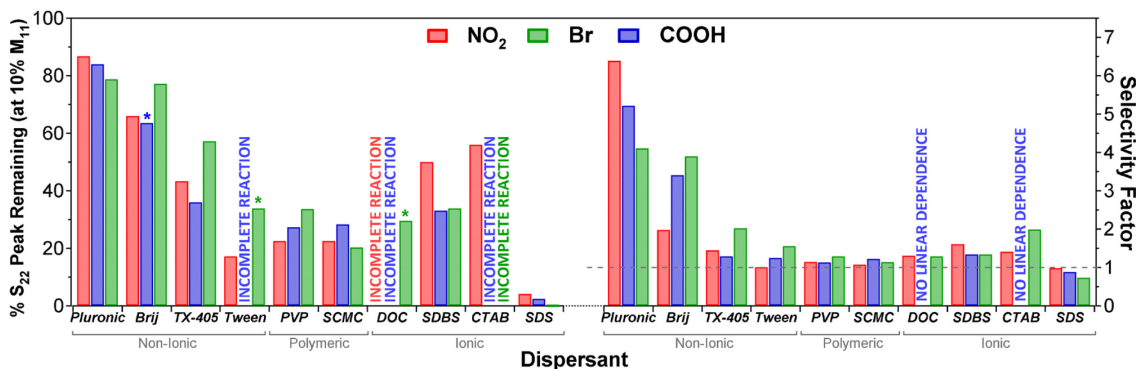


Figure 7.5: Percentage of the S_{22} UV-Vis-NIR absorbance peak remaining after reduction of the M_{11} peak to 10% of its original intensity for each dispersant and diazonium salt (left) and selectivity factors extracted from Figure 7.4 (right). Asterisks indicate values extrapolated from kinetic data (where possible) for reactions that did not completely quench the M_{11} peak.

at a rate close to double that of the semiconducting species. Brij S-100 and Pluronic F-127 showed the best selectivity, with the Pluronic block-copolymer being the superior performer in both forms of measurement. SDS was the only surfactant for which the selectivity factor was less than unity, showing the least preference for metallic CNT functionalisation of all the dispersant systems studied.

The three different salts produce similar selectivity values in each individual dispersant, suggesting that the type of dispersant is more influential than the functional group of the diazonium species. Although the selectivity trend in the case of Pluronic follows the order of Hammet parameters for the different diazonium salts, which is consistent with results reported in a previous study using this surfactant,²⁴⁶ this was not generally the

case for the other dispersants. It is noted that the reactivity (and stability) of diazonium salts is not always expected to obey a Hammett-type relationship.^{376,399}

Overall, there is no definitive correlation between the dediazonation rates observed in the dispersants alone as discussed in Chapter 6 (Section 6.2.3) and the selectivity parameters calculated here. Both the most stable (SDS) and least stable (SCMC) dispersants for the diazonium ion species provide poor selectivity of nanotube functionalisation. Given the complexities of dediazonation reactions, this is not an entirely surprising result. The effect of variation in dediazonation rate with dispersant concentration (discussed in Section 6.3) means that the decomposition curves analysed previously in Figure 6.3 do not necessarily represent an accurate rate of decay where concentrations different to 1% were used to disperse CNTs. However, the time-frame for dediazonation of the salts differs so greatly between the various dispersants that the magnitude of any concentration-induced shifts is not likely to alter the decomposition rates to an extent that would produce a definitive correlation between the dediazonation rates in the neat dispersants and the respective reaction selectivities.

Intuitively, selectivity should be enhanced by complete individualisation of the CNTs, thus it might be expected that those dispersants that do not exfoliate the CNTs well would display the least difference in reaction rate between metallic and semiconducting species. The CNT dispersions were prepared using sonication followed by ultracentrifugation, which should produce solutions containing mostly individuals and small bundles of nanotubes. All solutions were processed equivalently, thus any differences in selectivity are more than likely associated with the dispersant-diazonium interaction, however the bundling state of the nanotubes is also a factor which is inconsistent across the dispersant range. Although the intensity of the BWF component in the Raman G-band suggests that dispersion in Pluronic F-127, Brij S-100 and Triton X-405 produces more bundled suspensions, these three surfactants demonstrate the greatest selectivity. These surfactants all possess long polyethylene oxide (PEO) chains as their hydrophilic segments, which may imply that this type of structure is conducive to better selective functionalisation. However, although Tween-60 also has PEO based hydrophilic segments (albeit in shorter, branched chains) it does not provide such good selectivity. The surfactants SDBS and DOC which were expected to provide the greatest fraction of individual nanotubes in solution appear to provide marginal selectivity at best, suggesting that the extent of individualisation of the CNTs has less influence than the nature of the dispersant itself.

| Dispersant | Nitro | | | | | | Bromo | | | | | | Carboxy | | | | | |
|----------------|-----------------|---------|-----------------|---------|---------------------------------------|---------------|-----------------|---------|-----------------|---------|---------------------------------------|---------------|-----------------|---------|-----------------|---------|---------------------------------------|---------------|
| | M ₁₁ | | S ₂₂ | | (M ₁₁)/(S ₂₂) | | M ₁₁ | | S ₂₂ | | (M ₁₁)/(S ₂₂) | | M ₁₁ | | S ₂₂ | | (M ₁₁)/(S ₂₂) | |
| | α | β | α | β | α/α | β/β | α | β | α | β | α/α | β/β | α | β | α | β | α/α | β/β |
| Pluronic F-127 | 0.19 | 0.74 | 0.53 | 0.12 | 0.36 | 0.16 | 1.04 | 0.031 | 1.04 | 0.008 | 1.00 | 0.26 | 0.81 | 0.022 | 0.58 | 0.011 | 1.41 | 0.50 |
| Brij S-100 | 0.12 | 0.60 | 0.37 | 0.09 | 0.32 | 0.15 | 0.46 | 0.050 | 0.35 | 0.022 | 1.31 | 0.43 | 0.53 | 0.031 | 0.41 | 0.016 | 1.31 | 0.53 |
| Triton X-405 | 0.36 | 0.48 | 0.69 | 0.12 | 0.52 | 0.25 | 0.76 | 0.031 | 0.68 | 0.017 | 1.11 | 0.57 | 0.29 | 0.140 | 0.42 | 0.042 | 0.69 | 0.30 |
| Tween 60 | 0.17 | 0.43 | 0.30 | 0.20 | 0.55 | 0.46 | 0.49 | 0.033 | 0.46 | 0.020 | 1.06 | 0.62 | 0.28 | 0.050 | 0.32 | 0.026 | 0.85 | 0.53 |
| SDBS | 0.28 | 0.42 | 0.36 | 0.21 | 0.79 | 0.51 | 0.37 | 0.073 | 0.40 | 0.044 | 0.93 | 0.61 | 0.26 | 0.063 | 0.27 | 0.048 | 0.97 | 0.75 |
| PVP | 0.20 | 0.65 | 0.32 | 0.47 | 0.62 | 0.72 | 0.48 | 0.144 | 0.53 | 0.089 | 0.91 | 0.62 | 0.36 | 0.169 | 0.39 | 0.110 | 0.91 | 0.65 |
| SCMC | 0.27 | 0.37 | 0.28 | 0.31 | 0.95 | 0.85 | 0.35 | 0.193 | 0.35 | 0.162 | 0.98 | 0.84 | 0.32 | 0.163 | 0.32 | 0.132 | 1.00 | 0.81 |
| DOC | 0.13 | 0.46 | 0.17 | 0.29 | 0.73 | 0.62 | 0.23 | 0.154 | 0.26 | 0.113 | 0.91 | 0.74 | - | - | - | - | - | - |
| CTAB | 0.27 | 0.24 | 0.29 | 0.13 | 0.92 | 0.53 | 0.74 | 0.002 | 0.84 | 0.0005 | 0.88 | 0.21 | - | - | - | - | - | - |
| SDS | 0.14 | 0.53 | 0.12 | 1.31 | 1.17 | 1.17 | 0.13 | 0.349 | 0.17 | 0.356 | 0.78 | 1.02 | 0.08 | 0.447 | 0.13 | 0.415 | 0.63 | 0.93 |

Table 7.2: Parameters for the power law fits to the transformed data (see Appendix C). Ratios between metallic and semiconducting parameters are given as an indication of selectivity.

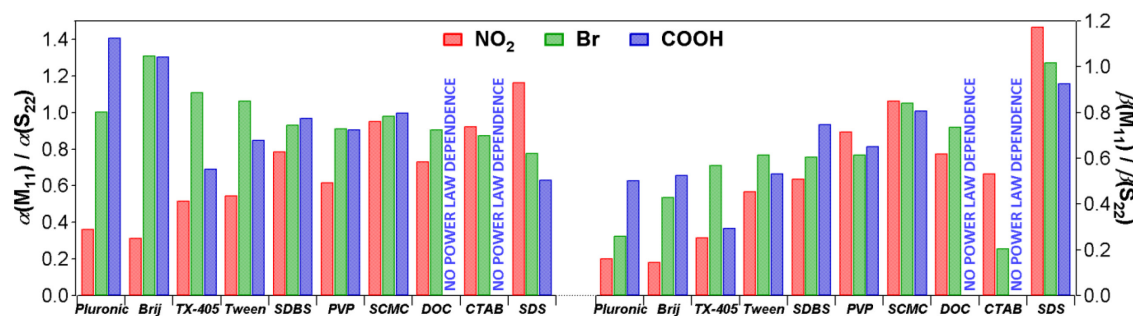


Figure 7.6: Ratios of the fitting parameters α (left) and β (right) for the M₁₁ and S₂₂ UV-Vis-NIR absorbance peaks for each combination of dispersant and diazonium salt (from Table 7.2).

In contrast to the selectivity factors and percentage values where the different salts produced similar values in each individual dispersant, the power law fitting parameter ratios (Table 7.2 and Figure 7.6) serve to highlight differences in the reaction rates for the different salts within each dispersant. Those that showed the best selectivity, i.e. Brij and Pluronic, have a larger spread of ratio values between the different aryl substituents than the worst performers SCMC and PVP. This would tend to suggest that the PEO containing dispersants allow a more unperturbed interaction between the diazonium molecule and the nanotube surface, which would account for the superior selectivity observed with these dispersions.

Differences in reactivity have previously been ascribed to variation in the permeability of the adsorbed layer between the micellar structures of ionic surfactants and disordered polymer wrapping,²⁴⁵ where functionalisation is expected to be facilitated more by the latter mechanism as the nanotube sidewall is more accessible. Both ionic surfactants and long chain polymers provided relatively poor selectivity in these results, though the permeability of the dispersant layer cannot be ignored as a contributing factor. In long polymeric dispersants such as PVP and SCMC the reaction is possibly rate limited by

the dediazonation of the diazonium salt species, which is reasonably fast in these dispersants as discussed in Section 6.2.3, hence the reaction is rapid and non-selective. In ionic, more densely packed dispersants the reaction may be limited by diffusion of aryl radicals to the CNT surface. This would slow the reaction and allow for selective interactions to occur, but at the same time the nanotube electron density is screened by a densely packed layer possessing a surface charge that would reduce the ability of the diazonium ion to adsorb to the CNT sidewall. The better selectivity provided by Pluronic and Brij polymers may represent a middle ground, with a more permeable layer that still provides a significant diffusion barrier. Two different conformations have been proposed for the micelle formation of PEO containing block copolymers with CNTs,⁴⁰⁰ one involving loosely adsorbed polymer chains and another involving a layered core-shell model where the hydrophobic chains in contact with the nanotubes could be hydrated to a significant degree. This could potentially allow easier diffusion of the diazonium ion into the hydrophobic interface and thus access to the electronic states of the CNTs.

For certain combinations of diazonium salt with DOC, Tween-60 and CTAB the reaction did not go to completion (i.e. peaks associated with CNTs were not completely quenched). In the case of CTAB and carboxy-BDTFB this is likely due to interaction between the amine headgroup of CTAB and the carboxylic acid of the diazonium salt, which would reduce the number of aryl groups that are free to associate with the CNT surface. For DOC, in all cases the solution was found to be slightly turbid after the reaction, sometimes containing a gelatinous precipitate, which could imply a reaction between the diazonium and this surfactant, or possibly polymerisation of the aryl species. In addition, reactions of a chloro-BDTFB salt with CNTs dispersed by sodium cholate (SC) have shown that SC blocks the covalent bond from forming between the aryl group and the nanotube under alkaline conditions.²⁴⁰ As SC and DOC are similar in structure (differing only by a single hydroxyl group), this may explain why reactions performed in DOC are comparatively slow, and in the case of carboxy-BDTFB why the intensity of the absorbance peaks is regained after an initial decrease, even for the metallic nanotubes.

Based on previous reports in literature^{240,401} and the behaviour observed in the DOC system, it is expected that within the process of forming the covalent aryl linkage an initial non-covalent charge-transfer complex adsorption suppresses the UV-Vis-NIR peaks, and it has been shown that bromo-BDTFB is a p-type dopant when non-

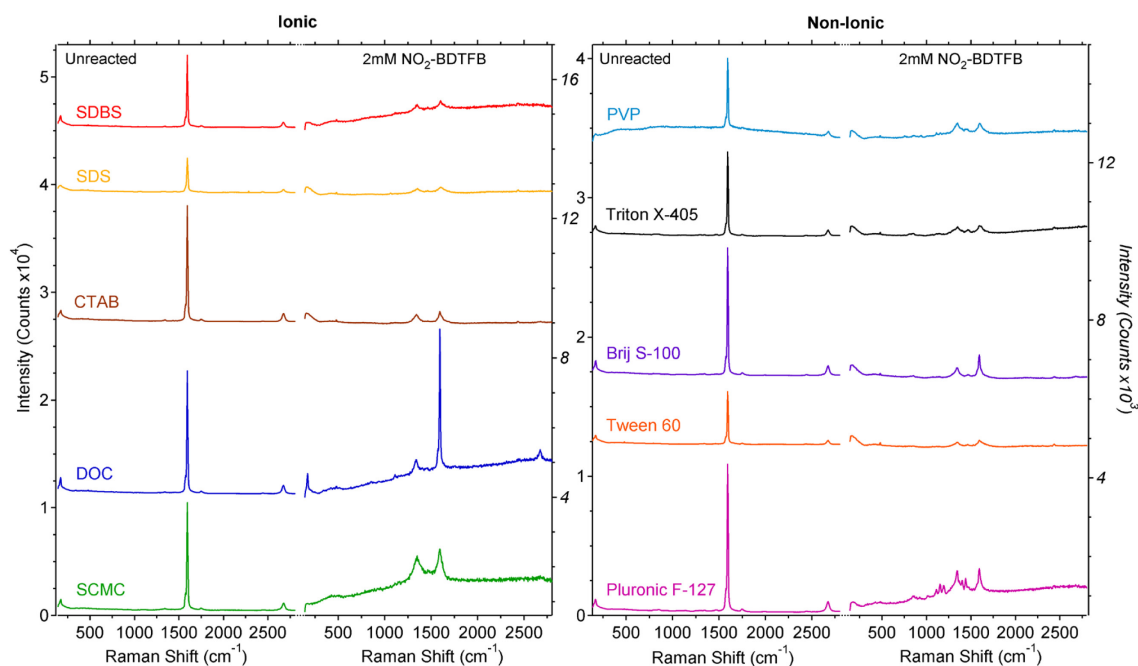


Figure 7.7: Raman spectra recorded at 2.33eV excitation for arc CNTs in each ionic (left) and non-ionic (right) dispersant before and after reaction with 2mM NO₂-BDTFB (5 days after addition), showing an increase in D:G ratio in all cases.

covalently adsorbed to the graphene lattice.⁴⁰² Consequently, the kinetic data presented in Figure 7.3 may represent only adsorption of the diazonium species and not actual disruption of the conjugated lattice induced by formation of a covalent bond, though covalent bonding has been shown to occur for most aryl diazonium salt reactions.^{229,246} In an effort to ascertain whether covalent bonding occurs in each of the dispersant systems studied here, the reaction between dispersed CNTs and 2mM NO₂-BDTFB was probed using Raman spectroscopy. Spectra for the as-produced dispersions and for the same solutions 5 days after addition of the diazonium reagent are shown in Figure 7.7. At a concentration of 2mM the diazonium salt is in excess, thus all CNTs should be completely functionalised in the ideal case. Large D:G ratio increases, which are associated with covalent bond formation,^{237,241} are displayed by all dispersant systems. The D:G ratio approached 1 for all dispersants except for DOC which shows a considerably less attenuated nanotube spectrum after the reaction, consistent with inhibited covalent functionalisation of the CNTs in this surfactant. Since reactions in DOC are likely to be non-covalent in nature in addition to their low selectivity, this dispersant is not an ideal choice for performing reactions between CNTs and diazonium salts.

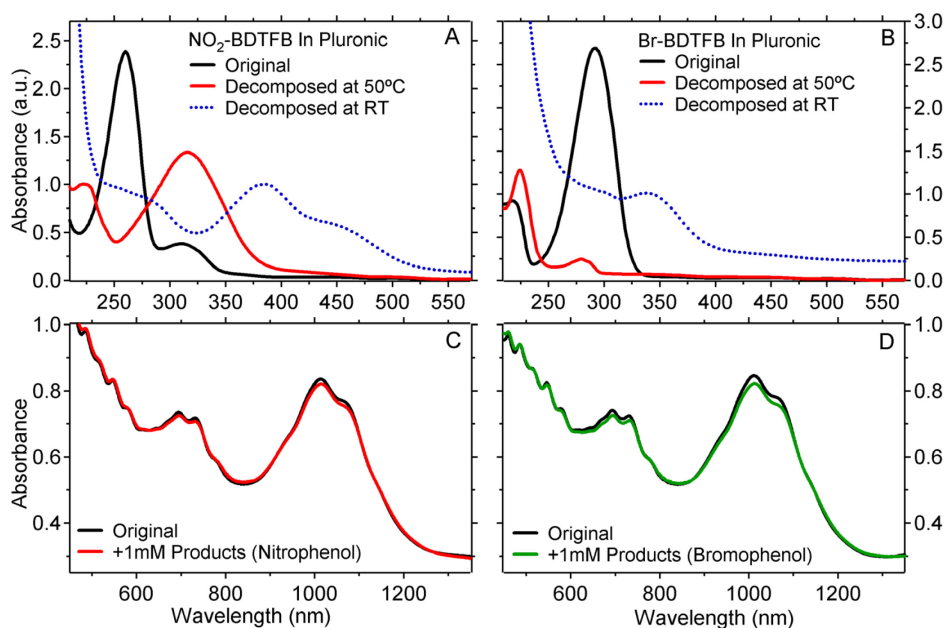


Figure 7.8: UV-Vis-NIR absorption spectra for NO₂-BDTFB (A) and Br-BDTFB (B) salts (black lines) and their thermal decomposition products in water with 4.5% Pluronic at 50°C (red lines). Decomposition was performed at high diazonium concentration (2M) and a dilution of 1:40 in water was made before recording of these spectra. Spectra from dediazonation in 4% Pluronic at room temperature and low concentration (Section 6.3) are also overlaid (blue dotted lines, scaled up), to illustrate differences in the degradation products; the absorption edge below 250nm is due to the higher concentration of Pluronic polymer in these two undiluted samples. The thermal decomposition products were added at a concentration of 1mM to solutions of CNTs in 4.5% Pluronic and monitored for 20 hours to probe for molecular interactions. Original spectra and those recorded after 20 hours of incubation are shown in (C) for NO₂-BDTFB and in (D) for Br-BDTFB.

To test the sensitivity of the nanotube absorbance spectra to adsorption of some other organic species present in the reaction mixture, the thermal decomposition products of dediazonation for both bromo- and nitro-BDTFB were produced by heating solutions of the salts in Pluronic until the diazonium peaks in the UV-Vis spectra had disappeared. The products of this thermal decomposition were found to be primarily nitrophenol and bromophenol as shown in Figures 7.8A and B, despite the presence of the Pluronic dispersant which was shown in Chapter 6 to encourage the formation of other products. Aliquots of these solutions were added to CNT solutions dispersed by Pluronic F-127 and monitored for 20 hours. Minimal spectral changes were observed in both cases, as displayed in Figures 7.8C and D, where both the S₂₂ and M₁₁ absorbance peaks were similarly affected by addition of the dediazonation products. Therefore, loss of the CNT absorbance peak intensities observed for diazonium salt addition is more

likely to be due to surface adsorption of the diazonium ion or covalent attachment of an aryl group rather than interaction with other organic products that are present in the solution. However, the thermally-decomposed solutions contained larger fractions of the phenol derivatives than the room temperature controls from Chapter 6, which were observed to contain different decomposition products that were also found in CNT-containing solutions. These additional products could potentially adsorb to the nanotube and undergo a charge transfer as has been suggested to occur for nitro-aromatic species such as nitrophenol,⁴⁰³ although since nitrophenol itself is observed to have a minimal effect here it is not expected that other (stable) products would have a significant influence on the nanotube absorbance spectrum.

Interestingly, metallic nanotubes were found to react faster than semiconducting nanotubes for every dispersant except SDS where the selectivity is reversed. This result was unexpected as several studies have previously reported metallic nanotube selectivity for this surfactant, although these reactions were performed under alkaline conditions (pH 10).^{226,227,240} This effect might be explained as with the intensity of the BWF feature in this surfactant; if the SDS molecule partially withdraws electron density from the CNT, then the electrons will no longer be readily available to interact with the diazonium salt. The observed inverse selectivity trend implies that SDS reduces the electron density of metallic CNTs to such an extent that the diazonium salts have preferential affinity for the semiconducting nanotubes, particularly in the case of bromo-BDTFB. Since selectivity has been demonstrated in SDS under alkaline conditions, the discrepancy of this system was investigated further by performing reactions in SDS dispersions with increased hydroxide concentrations.

7.4 Effect of pH in SDS, SDBS and Pluronic Dispersions

7.4.1 Arc Nanotubes

Increasing the pH of an SDS dispersion from 7.6 to 11 (using 1M NaOH) resulted in a strong increase in absorbance intensity for both the M₁₁ and S₂₂ peaks in the UV-Vis-NIR spectrum as shown in Figure 7.9A. This change in absorbance was coupled with an increase in the scattering intensity of the Raman RBM and G modes at excitation energies of both 2.33eV and 1.58eV (Figures 7.9B and C, respectively). The G⁻ peak

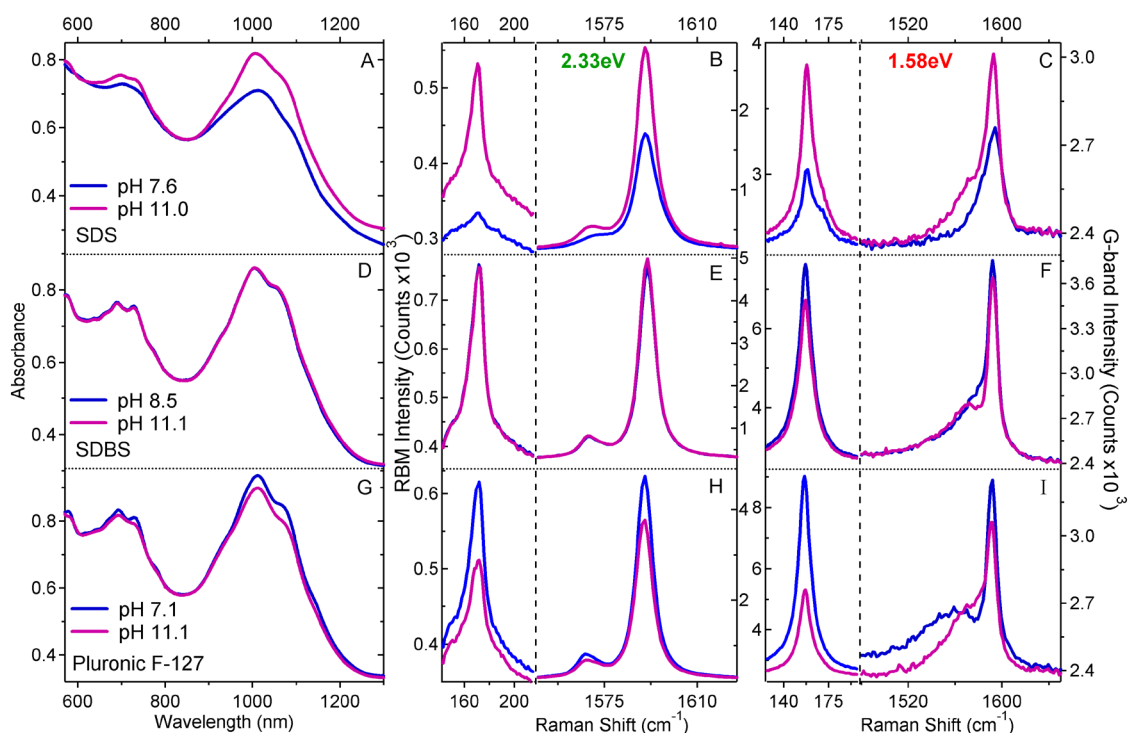


Figure 7.9: UV-Vis-NIR absorbance spectra for arc-CNTs dispersed in 1% SDS (A), 0.5% SDBS (D) and 4.5% Pluronic F-127 (G) at both natural pH and pH ~11. Unmodified Raman spectra at 2.33eV excitation are shown for the same dispersions in (B) for SDS, (E) for SDBS and (H) for Pluronic, where semiconducting nanotubes are resonant. Raman spectra collected using an excitation energy of 1.58eV are given in panels (C) for SDS, (F) for SDBS and (I) for Pluronic, exciting predominantly metallic CNTs.

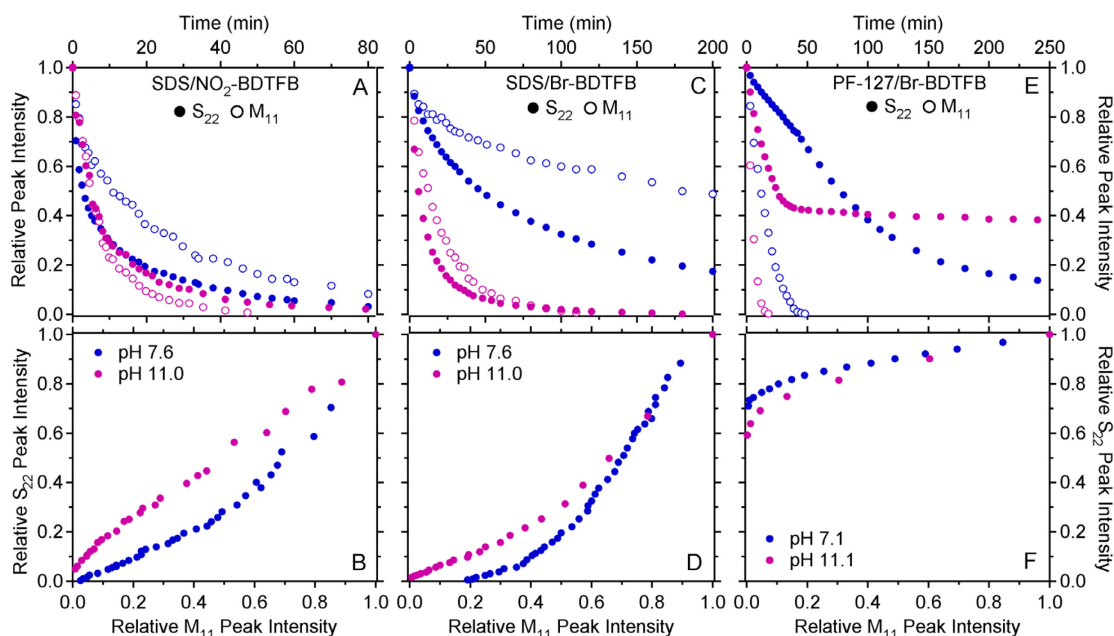


Figure 7.10: Kinetics of S₂₂ (circles) and M₁₁ (open circles) peaks for reactions of 2mM NO₂-BDTFB (A) and 2mM Br-BDTFB (C) with CNTs in SDS as well as 1mM Br-BDTFB with CNTs in Pluronic (E) at natural pH and pH 11. Selectivity curves for these reactions are given in (B), (D) and (F) respectively.

also became more prominent at both excitation energies upon addition of NaOH with a small BWF feature developing at 1.58eV. Similar trends were also observed for HiPCO nanotubes dispersed in SDS, and will be discussed momentarily in Section 7.4.2. These changes could be related to either nanotube aggregation or charge transfer, both of which may induce spectral shifts and variation in linewidth and intensity.^{296,404}

As mentioned in Section 7.1, the effects of charge transfer and aggregation on the Raman-active modes of CNTs are convoluted. To reiterate, the BWF feature of the G-band is known to be sensitive to molecular interactions as well as the nanotube aggregation state, and it is suggested that any partial withdrawal of electron density weakens this component of the G-band while injection strengthens it.²⁹⁴ Metallic nanotubes in contact with one-another may share fractional electron density, which would lead to the increased BWF intensity observed in bundles of metallic CNTs.²⁹⁵ Previously, changes in the BWF component of the G⁻ band for CNTs dispersed in DNA have been ascribed both to aggregation (where debundling reportedly increases the intensity of this feature but reduces the linewidth)⁴⁰⁵ and to selective p-doping interactions between the DNA strand and metallic CNTs (which weakens the BWF feature for metallic nanotubes but has a negligible impact for semiconducting species).⁴⁰⁶ A reversible blue-shift of the BWF component with increasing pH has been documented for acid addition (charge localisation through protonation) in SDS-dispersed HiPCO CNTs at 2.33eV.⁴⁰⁷ Narrowing and blue-shifting of the BWF component have also been observed for HiPCO nanotubes dispersed in single-stranded DNA with protonation by hydrogen peroxide, where the interaction with H₂O₂ is reversible on addition of NaOH.⁴⁰⁸ In summary, both nanotube aggregation and charge delocalisation may strengthen (broaden) the BWF feature, while exfoliation of CNTs and charge localisation weaken it.

The enhancement of the BWF component with hydroxide addition observed for an SDS dispersion in Figure 7.9C may therefore be ascribed to aggregation of the nanotubes, however dispersions of bundled CNTs generally produce lower absorbance and Raman intensities. Thus, the increase in optical absorbance at alkaline pH is contradictory to this argument. AFM images of SDS dispersions at both natural pH and pH 11 were also found to be indistinguishable from one another. Consequently, the broadening and shift of the G⁻ peak is deemed to be related to charge localisation on the CNT surface. It has been shown previously that p-doping of CNTs by SDS molecules may occur in sonicated aqueous dispersions,¹⁴³ while theoretical calculations have demonstrated

charge transfer occurs between a (5,5) nanotube and molecules possessing electron-accepting sulfate headgroups with sodium counterions.⁴⁰⁹ Similarly, the surfactant Nafion (which also possesses a sulfonate group) has shown the ability to suppress the Raman G^- peak due to protonation of the nanotube sidewalls.⁴¹⁰

The increase in optical absorbance and Raman scattering intensities for SDS dispersions with NaOH addition observed in Figure 7.9 are concordant with an increase in the available electron density as both UV-Vis-NIR and Resonance Raman spectroscopies probe electronic transitions. Thus it appears that hydroxide addition reduces the strength of the interaction between SDS and the nanotubes, freeing electrons and thus increasing the absorbance and scattering intensities by returning the band-structure to a near undoped state. Intuitively, the strength of the interaction is expected to be greater for metallic CNTs,⁴⁰⁶ however absorbance and Raman spectra shown here suggest semiconducting CNTs are also significantly affected. Although studies have shown the morphology of SDS adsorption depends strongly on surfactant concentration and nanotube diameter,^{317,411} this interaction would be more likely to occur if the molecules are adsorbed parallel to the CNT sidewall as opposed to in a tails-on conformation such that the sulfate headgroup is located in close proximity to the nanotube surface.

In light of these results, the diazonium reaction was re-examined in SDS at pH 11. In contrast to the results obtained at natural pH, the diazonium reaction between CNTs and nitro-BDTFB in SDS displayed slight preferential reaction for metallic CNTs at pH 11 as shown in Figures 7.10A and B. These results support the assertion that SDS is involved with charge localisation on the CNT surface, whereas at alkaline pH the influence of the sulfate group is diminished allowing the diazonium species to extract electrons. However, although the selectivity of bromo-BDTFB was further directed towards equal rates of reaction it remained in favour of semiconducting nanotubes as shown in Figures 7.10C and D.

The possibility also exists that the nanotube electron density is not altered by SDS itself and that these changes in reaction rate and optical spectra are due to interaction with protons, adsorbed oxygen or water molecules that may access the CNT surface and polarize electron density, suggested to be possible due to the permeability of the SDS layer.⁴¹² However, if this were the case, loosely wrapped polymers such as SCMC and PVP might be expected to possess similarly attenuated BWF features at their natural pH. In Figure 7.1 SDS clearly shows the narrowest line shape for the G^- peak at 1.58eV in comparison with all of the other surfactants, implying that the charge localization

interaction observed in SDS is dependent on the surfactant itself. Additionally, if this effect were related to desorption of protons from the nanotube sidewalls a similar pH response would be expected in the absorbance and Raman spectra of CNTs dispersed by other surfactants. The effect of pH on the spectra of Pluronic and SDBS dispersions was also investigated, where these represent the opposite end of the selectivity scale to SDS and an intermediate control, respectively. Both of these systems displayed different behaviour to that of SDS.

As shown in Figure 7.9D, the UV-Vis-NIR absorbance spectrum for SDBS-dispersed arc CNTs is essentially unaltered by the addition of NaOH save for slight red-shifts of the M_{11} and S_{22} peak maxima of $\sim 0.6\text{nm}$ and $\sim 0.8\text{nm}$ respectively, consistent with this surfactant providing greater protection of the nanotube against the influence of pH.⁴¹³ The Raman spectra at 2.33eV are also unchanged (Figure 7.9E), while at 1.58eV the RBM and G^+ signals are slightly reduced in intensity with the G^- band becoming more resolved (Figure 7.9F). It is probable that in this instance the addition of NaOH results in a slight re-aggregation of the CNTs that is virtually undetectable in the absorption spectrum but is sufficient to induce changes in the G^- peak. This is thought to be the most likely mechanism to describe the behaviour observed here, although the possibility that partial charge localisation also occurs for metallic CNTs within this system cannot be ruled out.

Increasing the pH of a Pluronic-based nanotube dispersion results in a decrease in the optical absorption intensity as shown in Figure 7.9G, along with a reduction of the Raman RBM and G-band intensities at both 2.33eV (Figure 7.9H) and 1.58eV (Figure 7.9I). The BWF component of the G-band at 1.58eV in this case is narrowed and shifted to higher energy, which correlates with withdrawal of electron density from the metallic nanotubes. Again, this may be attributed either to exfoliation of bundles or to a charge transfer or localisation interaction with the dispersant. As reduction in optical absorbance and Raman scattering intensities are not normally associated with improved dispersion, these results imply that the Pluronic polymer donates fractional electron density to the metallic CNTs and that this interaction is disturbed by the addition of NaOH. PEO chains have been suggested to form weak $n-\pi$ donor-acceptor complexes with the fullerene C_{60} , where composites may be stabilised by electron transfer between the n -orbital of the PEO ether oxygen and the fullerene π -system.⁴¹⁴ Such an interaction with nanotubes might explain the spectral changes with increased pH observed here.

Additionally, for a reaction between 1mM bromo-BDTFB and CNTs in Pluronic F-127 performed at pH 11 the metallic nanotube selectivity was decreased (Figures 7.10E and F) and the reaction was much more rapid, reaching completion in approximately half the time taken in the natural dispersion. The fact that reactions in both SDS and Pluronic occur more rapidly at alkaline pH is likely due to the increase in diazotate formation at high pH, where a corresponding increase in aryl radical concentration would be associated with the cleavage of this molecule and related species. While this alone could explain the decrease in selectivity due to an increase in aryl radical formation as will be discussed in Section 7.5, such a decrease may also support the notion that addition of hydroxide ions disrupts the PEO-CNT complex and thus reduces the effective electron density of the CNTs, possibly through an increase in hydrogen bonding.

An implication of this proposed surfactant-CNT interaction is that the enhanced BWF components observed in Figure 7.1 for the PEO containing polymers Pluronic and Triton X (as well as Brij and Tween to a lesser extent) do not signify a more aggregated suspension, but rather the occurrence of charge transfer between PEO chains and CNTs. This would explain why the G⁻ band of these dispersants is significantly more intense than in other systems (despite showing similar absorbance spectra) and also account for their superior selectivity. Although both Triton X and Tween 60 dispersions displayed lower selectivity than for CNTs in either Pluronic or Brij, this is probably related to the higher hydrogen ion activity in the former dispersants in their natural state (see Table 7.1) which would likely alter the form of the diazonium species in solution. A further corollary of this result is that the hydrophilic PEO chains in Brij and Triton X interact with the nanotube surface and therefore must be in close proximity to the interface rather than being entirely extended into the aqueous phase. This would tend to suggest that the core-shell model for adsorption of PEO containing polymers is not an accurate description of the system in these cases. For Pluronic F-127 dispersions, where the hydrophobic polypropylene oxide block also contains an ether oxygen, the potential for donation of electron density would be greatly increased. This could explain why the magnitude of selectivity factors measured for reactions in this dispersant are always much greater than those recorded in other systems.

7.4.2 HiPCO nanotubes in SDS

Figure 7.11A shows absorbance spectra of HiPCO CNTs dispersed in SDS under natural conditions along with volumes of the same solution for which the pH was altered. Addition of 1M NaOH was used to increase the pH to 11.0, whereas 0.1M HCl was added to decrease the pH to 4.6. Under acidic conditions the absorbance peaks of both metallic and semiconducting species are significantly weakened. This effect is known to occur due to protonation of the CNT sidewall which localises valence electrons, and is suggested to be mediated by surface adsorbed oxygen.⁴⁰⁷

Conversely, with an increase in pH the absorbance peaks become stronger, particularly for the S_{11} transition of the larger diameter semiconducting nanotubes. This is coupled with an overall increase in Raman scattering intensity for each of the major nanotube peaks (RBM, G and G') at both excitation energies as was observed for arc nanotubes in the previous section. Notably, the RBM intensities of CNTs with larger diameters undergo a greater enhancement than those with smaller diameters (regardless of their electronic type) after an increase in pH, as shown in Figure 7.12. This is consistent with the greater increase in optical absorbance for larger diameter nanotubes from 1100-1300nm compared to that from smaller diameters around 900-1100nm seen in Figure 7.11A. The fact that the RBM features of larger diameter nanotubes are weaker in SDS than in SDBS has previously been ascribed to the preferential solubilisation of large diameter CNTs by SDBS,³²³ however the pH-based recovery of their intensity would suggest that these species are indeed dispersed. This result implies that SDS interacts more strongly with the electronic structure of nanotubes possessing smaller band gaps, which explains why arc CNTs appeared to be far less disperse than the HiPCO variety through examination of their optical spectra in Section 3.1.3 even though SDS actually suspends both types of nanotube to a reasonable degree.

As shown in Figure 7.11, at 2.33eV excitation where primarily metallic CNTs are probed a red-shift and increase in width of the G^- peak with respect to the natural dispersion is observed following addition of NaOH, while no change in width of the G-band was observed at 1.58eV where mostly semiconducting nanotubes are resonant. This change in the G^- band implies a partial increase in the electron density for the metallic CNTs upon the addition of NaOH. As previously discussed, this potentially occurs through nanotube aggregation, disruption of charge localisation by the surfactant or direct interaction of the hydroxide with the CNTs or surface adsorbed oxygen. If the

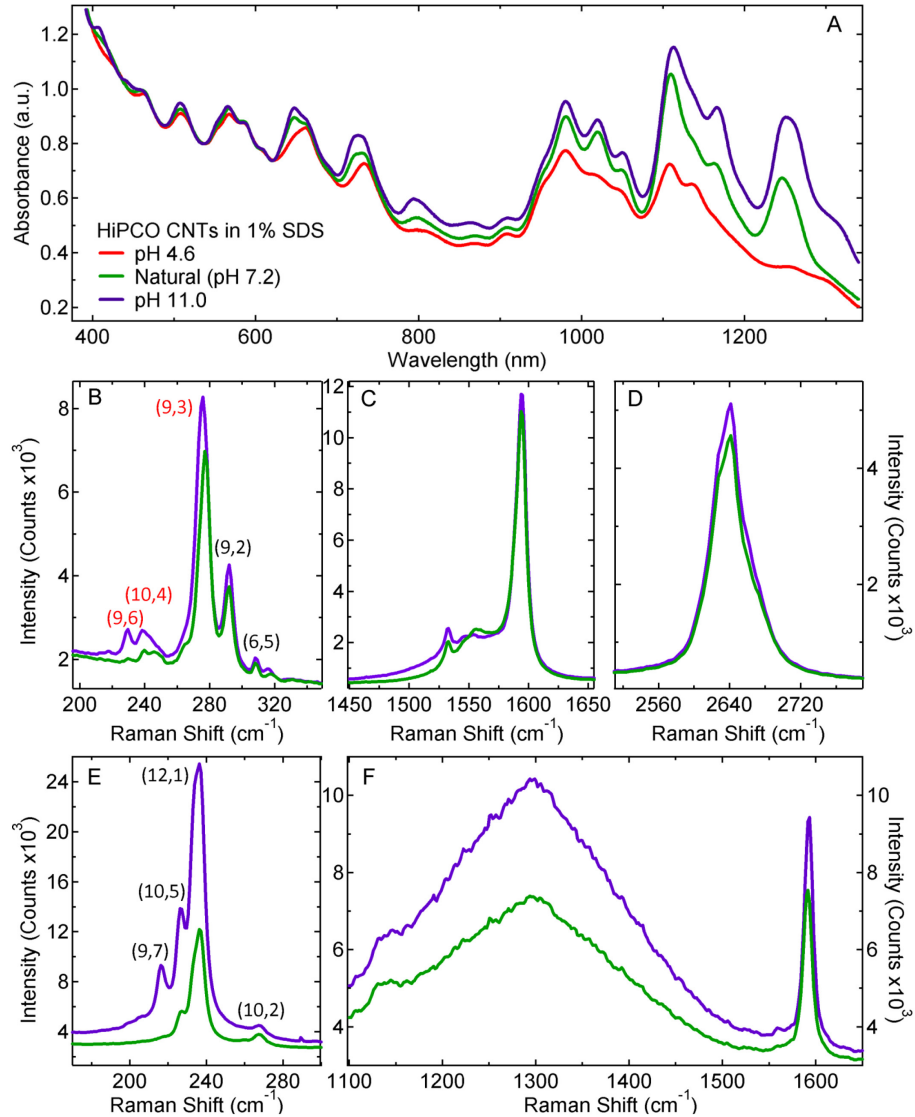


Figure 7.11: UV-Vis-NIR absorbance spectra for HiPCO CNTs in 1% SDS at different pH levels (A); Raman spectra of the RBM (B), G-band (C) and G' mode (D) regions for dispersions at natural pH and pH 11 for an excitation energy of 2.33eV; Raman spectra of the RBM (E) and G-band (F) regions at an excitation energy of 1.58eV. Assignments of dominant RBM peaks were made according to data from several sources (see Appendix B) with semiconducting species labelled in black and metallic CNTs indicated in red.

G⁻ peak broadening was due to aggregation of the nanotubes the optical absorbance peaks would be expected to decrease and red-shift. While slight red-shifting of the peaks does occur for some of the larger diameter semiconducting species, as with the arc CNT dispersions absorbance peaks from all nanotube types increased in intensity. Also, the linewidth of the G' band is reportedly not sensitive to changes in pH, but is decreased with improved solubilisation of the nanotubes.⁴⁰⁴ As the spectral shape of the

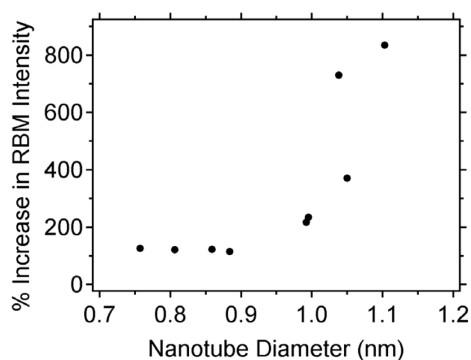


Figure 7.12: Percentage increase in the RBM intensity at pH 11 with respect to the natural solution for the major RBM contributing species identified in Figure 7.11.

G' band did not undergo a shift with NaOH addition in Figure 7.11D (only a slight increase in intensity), it suggests that the aggregation state of the dispersion is unaltered. Another strong indicator of the nanotubes remaining dispersed is evident in Figure 7.11F, where at 1.58eV excitation the fluorescence peak at a shift of 1300cm^{-1} is enhanced at high pH rather than quenched as would be expected for aggregated nanotubes, especially since photoluminescence is highly sensitive to bundling.³²⁹ (This peak essentially masks the D band for HiPCO CNTs and is due to a photon of 1.42eV, which corresponds to a phonon-assisted radiative recombination of an exciton in the (6,4) nanotube.⁴¹⁵ Other species exhibit similar photoluminescence peaks as discussed in Section 1.1.3, however these occur at energies outside of the range detected by the Raman instrument). Thus, considering the cumulative evidence of the results for both arc and HiPCO type CNTs, it is quite conclusive that the spectral changes in SDS dispersions that accompany hydroxide addition are not aggregation related.

Despite the prevalence of the use of SDS for nanotube dispersion, the charge transfer effects that occur in this surfactant are rarely (if ever) addressed, particularly where the role of the surfactant molecule is concerned. Blackburn *et al.* have previously reported that increasing the pH of laser ablation produced CNTs also dispersed in 1wt% SDS did not result in modification of the G' band BWF component (at 1.96eV excitation, which would excite metallic CNTs in their sample as 2.33eV does here for HiPCO nanotubes) or an increase in the S₁₁ absorbance peaks,²⁹⁴ both of which were clearly observed here (with multiple repetitions). A further experiment confirmed that the same effects occurred in a dispersion of HiPCO CNTs in 1% SDS in the solvent D₂O. The discrepancy between the results reported here and those of Blackburn *et al.* cannot

currently be explained, although the concentration of hydroxide used in this case (pH 11) was higher than that adopted in their experiment (pH 10).

7.5 Influence of Reaction Temperature, Diazonium Concentration and Dispersant Concentration

In an attempt to maximise the selectivity, experiments were performed to examine the influence of some other controllable experimental factors on these reactions. As Pluronic was identified as the dispersant capable of providing the greatest selectivity this system was chosen and utilised for the majority of further studies. A solution of arc CNTs in 4.5% Pluronic F-127 was used in successive reactions with bromo-BDTFB where the diazonium concentration and reaction temperature were varied. Additional experiments were performed with the dispersant concentration varied and the temperature and diazonium concentration held constant for both Pluronic and SDBS. The kinetic data for all of these reactions are presented in Appendix D. Selectivity factors, $S_{22\%}$ percentages remaining at 10% M_{11} intensity and power law fitting parameter ratios calculated from the experimental data are provided in Figure 7.13 for comparison. Selectivity is clearly improved by minimising both diazonium concentration (Figure 7.13A) and temperature (Figure 7.13B), which corresponds to a slower reaction in each case. Keeping the diazonium concentration low has been previously shown to be important in obtaining selectivity between electronic types,²²⁶ and contrary to a recent study that found little difference in selectivity with diazonium concentration²⁴⁶ it is clear from these results that the selectivity factor decreases significantly with an increasing amount of diazonium reagent. Increasing the temperature of the reaction comparatively has much less influence on the selectivity, however at temperatures below $\sim 24^{\circ}\text{C}$ there is some slight improvement in each of the analysis parameters.

Perhaps more interesting is the influence of the surfactant concentration on the reaction selectivity. As previously stated, the surfactant concentrations used in the dispersant study had been optimised for CNT concentration in the final solution when suspending the nanotubes, though this may not result in an optimised selectivity due to a potential shift in dediazonation mechanics with dispersant concentration. According to the analysis of reactions of both bromo- and nitro-BDTFB with CNTs performed in

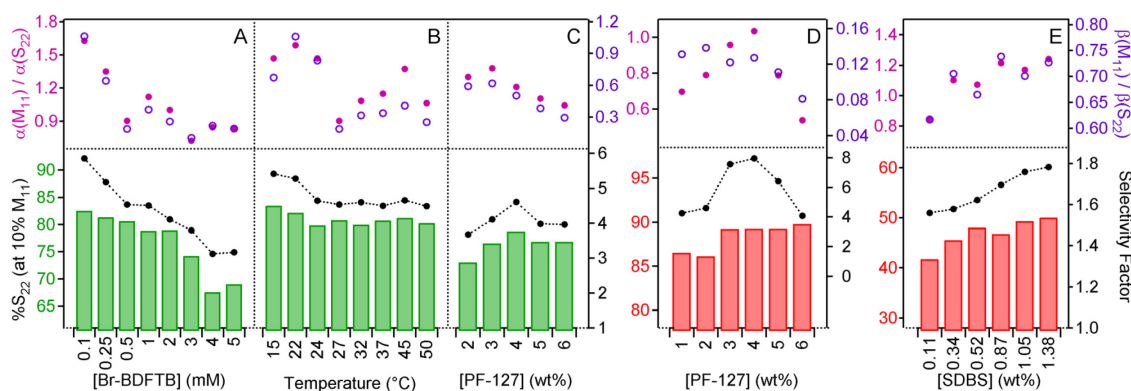


Figure 7.13: Results for kinetic studies with varying experimental parameters; Br-BDFTB concentration varied with CNTs in 4.5% Pluronic F-127 at 27°C (A); 0.5mM Br-BDFTB with CNTs in 4.5% Pluronic F-127 at different temperatures (B); 3mM Br-BDFTB with CNTs dispersed in various concentrations of Pluronic F-127 at 27°C (C); 0.3mM NO₂-BDFTB with CNTs dispersed in various concentrations of Pluronic F-127 at 27°C (D); and 0.5mM NO₂-BDFTB with CNTs in various concentrations of SDBS at 27°C (E). Analysis of percentage S₂₂ UV-Vis-NIR absorbance peak remaining at 10% M₁₁ is shown (bars), along with calculated selectivity factors (joined circles) and ratios of the fitting parameters α and β for the M₁₁ and S₂₂ UV-Vis-NIR absorbance peaks (closed and open circles, respectively).

different concentrations of Pluronic F-127 (Figures 7.13C and D respectively) the best selectivity occurs at around 4wt% of the dispersant. The ‘optimised’ dispersant concentration for Pluronic F-127 was previously determined to be ~5wt%, though a slightly lowered 4.5% was used in experiments here to avoid the flocculating regime that exists at concentrations above this value. Thus, selectivity appears to be improved at a dispersant concentration that is only slightly removed from that which obtains the best dispersion for the case of Pluronic F-127.

Reactions of NO₂-BDFTB with CNTs in different concentrations of SDBS (Figure 7.13E) were performed as a comparison with a dispersant that did not show evidence of charge transfer to the CNTs. The selectivity in this system was also improved at higher SDBS concentrations over the studied range (which was again chosen to avoid the threshold of attractive depletion effects), hence such behaviour is not unique to the Pluronic system. In this case the selectivity factor did not pass through a maximum, possibly as the concentration range for SDBS used here does not fully encompass the dispersion peak as it does for Pluronic. The reason for the increase in selectivity with dispersant concentration is postulated to be related to the decomposition of the diazonium salt in solution.

Since in Figure 7.13A it is shown that lower concentrations of diazonium provide a higher selectivity in reaction with carbon nanotubes, it is proposed that using higher concentrations of dispersant reduces the reactive diazonium concentration through promotion of azo-coupling (or formation of other degradation products) over nanotube functionalisation, thus lowering the number of free aryl-radicals and increasing the selectivity as observed in Figure 7.13E for increasing SDBS content. For Pluronic solutions, once the concentration is raised above 4-5%, attractive depletion effects come into play, causing the CNTs to re-aggregate in larger clusters which could explain the reduction in selectivity at higher concentrations, resulting in the selectivity peak at 4% Pluronic observed in Figures 7.13C and D. The micelles of block co-polymers are also particularly sensitive to concentration and temperature,⁴¹⁶ which may have an affect with increasing Pluronic concentration, although in Figure 7.13B increasing temperature did not appear to have an adverse effect on the obtained selectivity.

7.6 Stepwise Additions for Improved Selectivity

As selectivity is improved by lowering the diazonium concentration, preferential functionalisation is best achieved through stepwise additions of reagent to the CNT solution.²²⁶ This is illustrated in Figure 7.14, where 13 μ L aliquots of 7.3mM nitro-BDTFB were added to 9mL of CNTs dispersed at $\sim 43\mu\text{g}\cdot\text{mL}^{-1}$ in 4.5% Pluronic F-127 and allowed to react for 48 hours between additions (approximately 0.01mM diazonium salt per aliquot). Some aggregation of the CNTs likely occurred over this time frame, although the absorbance spectrum of the original bulk solution was unchanged at the final addition. Initially the M_{11} peaks are noticeably reduced with only slight changes in the S_{22} absorbance, although the more functionalised the metallic nanotubes become the greater the subsequent loss of the S_{22} peak absorbance is for each addition. This is coupled with a gradual broadening of the S_{22} band (Figure 7.14A), which is consistent with a small degree of functionalisation of the semiconducting nanotubes.²³⁹ In Figure 7.14D there appears to be three separate domains for the selectivity of the reaction, which can be considered in terms of the percentage of the M_{11} peak remaining. The first region from 100-50% is characterised by minimal change to the S_{22} peaks with rapid loss of the metallic absorbance. From 50-10% there is a greater change to the S_{22} band with each addition, since the metallic nanotubes are now considerably functionalised

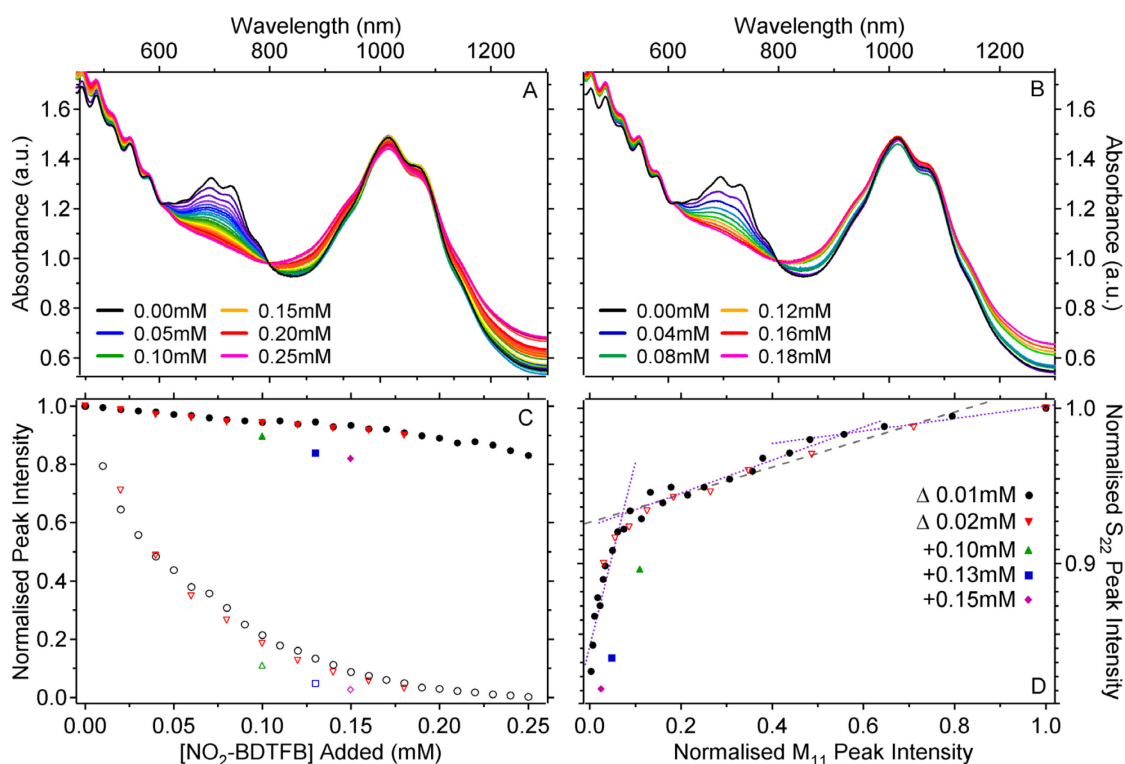


Figure 7.14: UV-Vis-NIR spectra (equalised at 800nm) for arc CNTs dispersed in 4.5% Pluronic F-127 and functionalised by consecutive additions of 0.01mM (A) and 0.02mM (B) NO₂-BDTFB made every 48hours; (C) Evolution of the M₁₁ (open symbols) and S₂₂ (closed symbols) relative peak intensities with each addition from the spectra in frames A (circles) and B (inverted triangles), showing also peak heights obtained from single additions of 0.1mM (triangles), 0.13mM (squares) and 0.15mM (diamonds) NO₂-BDTFB to separate volumes of the same parent CNT solution; (D) Selectivity curve for the 0.01mM and 0.02mM stepwise additions as well as single addition points as per panel C. Linear fits to regions 0.0-0.09, 0.1-0.5 and 0.5-1.0 are shown (dotted lines) to illustrate decreasing selectivity with increasing number of additions, while the overall fit (dashed line) from 0.05-1.0 gives a selectivity factor of 11.26.

and the diazonium ions begin coupling to the semiconducting nanotubes with greater frequency. Below 10% M₁₁, the reaction is preferential to semiconducting nanotubes, which suggests that absolute bleaching of the metallic absorbance peaks is only possible with significant levels of semiconducting nanotube functionalisation. The selectivity factor determined from a fit of the 100-5% region was ~11.3, which is comparable to that achieved via in situ generation of aryl radicals from diazoesters.⁴¹⁷ Reactions performed using single additions show significantly reduced selectivity, though additions made in 0.02mM increments (Figure 7.14B) resulted in an essentially identical selectivity curve, suggesting that below a critical concentration per addition selectivity is no longer improved.

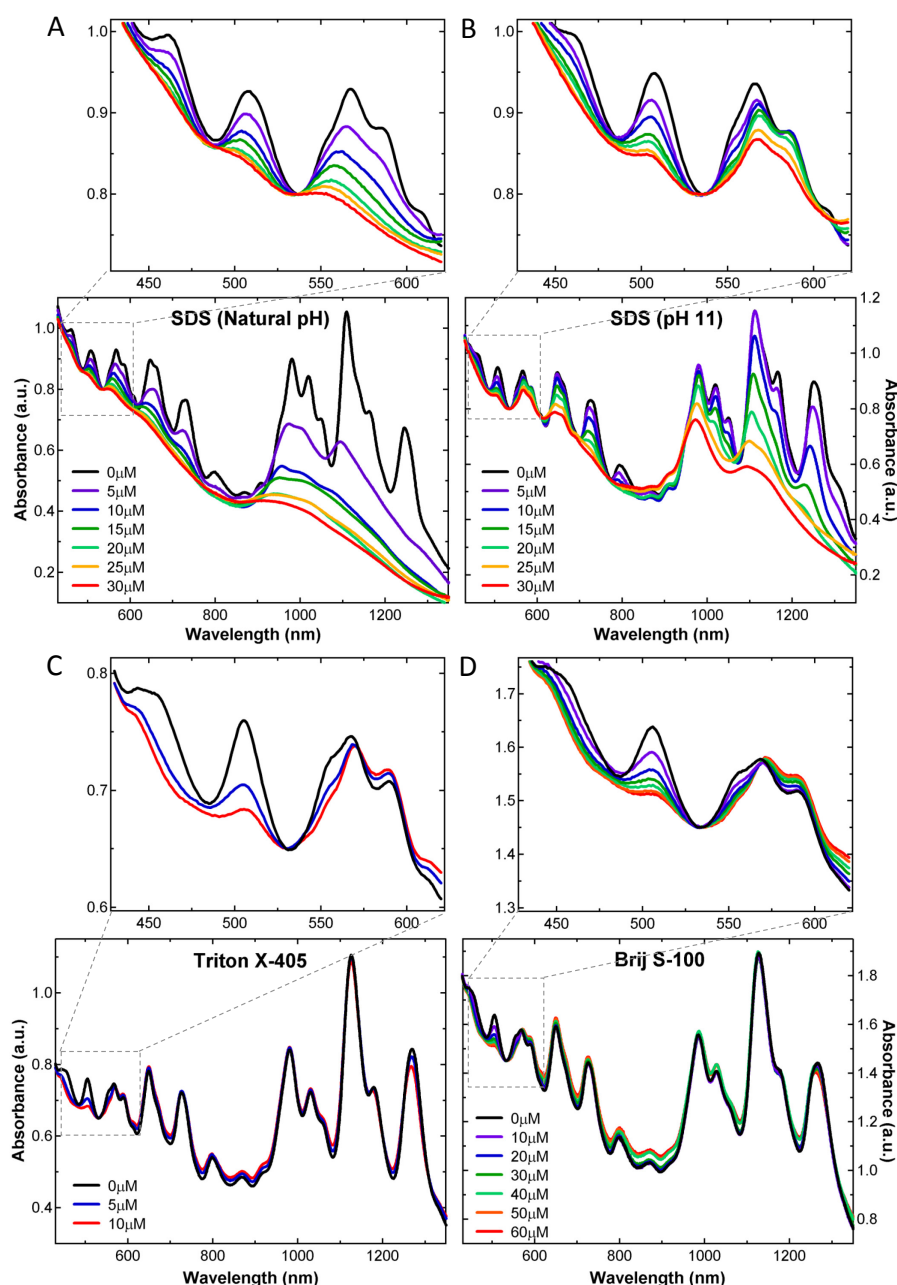


Figure 7.15: UV-Vis-NIR spectra for sequential additions of NO_2 -BDTFB in H_2O made to dispersions of HiPCO CNTs in 1% SDS at natural pH (~ 7.2) (A), 1% SDS at pH 11 (B), 3% Triton X-405 (C) and 2% Brij S-100 (D). The region corresponding to M_{11} peaks has been expanded in each case.

Previous results have shown that Pluronic F-127 is not a good dispersant for smaller diameter nanotubes, i.e. those produced by the HiPCO method, however the surfactants Brij S-100 and Triton X-405 provide much better dispersions of HiPCO CNTs (see Section 3.1.3). As these dispersants displayed some degree of selectivity with the arc nanotubes they were used to compare the reaction between the two different diameter distributions, while the SDS-HiPCO system was also evaluated as this is the basis

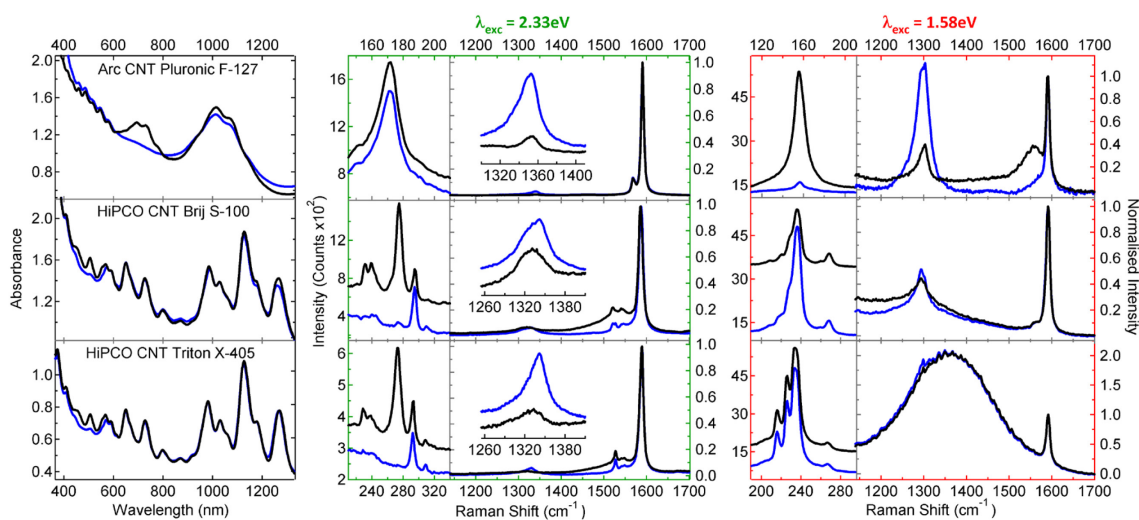


Figure 7.16: UV-Vis-NIR spectra (left panel) for arc CNTs in 4.5% Pluronic F-127, HiPCO CNTs in 2% Brij S-100 and HiPCO CNTs in 3% Triton X-405 with Raman spectra generated from the same solutions at 2.33eV (centre panel) and 1.58eV (right panel). As in Figure 7.1, G (1600cm^{-1}) and D band (1350cm^{-1}) spectra were normalised to the G^+ -peak, while RBM regions ($100\text{-}350\text{cm}^{-1}$) are as-collected spectra. Black curves are original dispersions while blue curves are solutions reacted with 0.15mM, 0.06mM and 0.01mM $\text{NO}_2\text{-BDTFB}$ for Pluronic, Brij and Triton X samples respectively.

system for literature comparison. Absorbance spectra for sequential additions of nitro-BDTFB to HiPCO CNTs dispersed in SDS at natural pH and pH 11 are shown in Figures 7.15A and B, while those for HiPCO nanotubes dispersed in Triton X-405 and Brij S-100 are given in Figures 7.15C and D respectively. Both the Brij and Triton X dispersants are able to provide decent selectivity, where the metallic absorbance peaks are bleached while the semiconducting peaks remain largely unchanged. These two systems show vastly superior selectivity over the surfactant SDS at natural pH where for the latter both metallic and semiconducting peaks are depleted simultaneously. As observed for arc CNTs, increasing the pH of the SDS system to 11 vastly improves the selectivity of the reaction for metallic nanotubes, however the two PEO-containing dispersants clearly provide better selectivity than SDS in any case.

Figure 7.16 shows UV-Vis-NIR and Raman spectra for initial and final selectively functionalised dispersions using the nitro-BDTFB salt for three of the different systems analysed; arc CNTs in Pluronic (0.15mM single diazonium addition), HiPCO CNTs in Brij S-100 (0.01mM additions to 0.06mM) and HiPCO CNTs in Triton X-405 (.005mM additions to 0.01mM). The metallic absorbance peaks are mostly depleted in each case, while the semiconducting peaks remain close to their original intensity. There appears to be a slightly greater loss of semiconducting peak intensity for Brij than for Triton X,

and it is noted that more than nominal semiconducting functionalisation occurred with the Pluronic sample as the diazonium was not added stepwise but rather in a single addition.

As previously noted, for the arc CNT distribution semiconducting CNTs are in resonance when excited at 2.33eV while metallic nanotubes are resonant at 1.58eV. Thus, the loss of RBM intensity for the arc nanotubes at 1.58eV is attributed to the sidewall attachment of aryl moieties to metallic nanotubes and is accompanied by loss of the BWF feature in the G-band and a significant increase in the D:G ratio at this excitation energy. The increase in the Raman D-band suggests that the loss of UV-Vis-NIR absorbance is related to covalent attachment rather than adsorption and charge transfer from the diazonium ion species, while loss of the BWF feature also supports the notion that metallic CNTs are being functionalised. Conversely, at 2.33eV a mild increase in the D:G ratio is observed but otherwise very little change between the initial and functionalised spectra is evident, indicating a low degree of functionalisation for the semiconducting nanotube species. The extent of semiconducting functionalisation would be expected to be slightly lower if the diazonium reagent had been added in stepwise additions.

For HiPCO CNTs, the excitation relationship is reversed; the resonant optical transitions at 1.58eV belong to semiconducting species while mostly metallic nanotubes are probed at 2.33eV. Assignments of the RBMs of HiPCO nanotube species are made in Appendix B, where the (9,6), (10,4) and (9,3) metallic CNTs were identified as being resonant at 2.33eV with RBM frequencies of 228, 237 and 272 cm^{-1} respectively. As these nanotubes are not armchair species they possess a strong BWF feature in the G-band of their Raman spectra.²⁹³ Also resonant at this excitation energy are the (9,2) and (6,5) semiconducting nanotubes with RBMs at 291 and 308 cm^{-1} . With the addition of diazonium salt the breathing modes of the metallic nanotubes are depleted in both the Brij and Triton X systems while those of the two semiconducting nanotubes remain strong with little to no loss of scattering intensity, supporting the UV-Vis-NIR absorbance results. Again, the D:G ratio is increased by the functionalisation of the metallic species, while the BWF component of the G-band is significantly reduced in both cases which is consistent with the perturbation of the metallic nanotube structure. At 1.58eV only semiconducting species are resonant and the RBM peaks for these nanotubes are not significantly altered by the addition of diazonium salt in either the Brij or Triton X dispersants. The G-band of the semiconducting species is also

unchanged, however there is again some small increase in the D band for both systems which again indicates functionalisation of the semiconducting nanotubes. The extent of this functionalisation is limited, especially in the Triton X solutions where the Raman spectra of the original and functionalised samples essentially overlap. There is a larger D band increase for semiconducting nanotubes in the Brij dispersant, although the RBMs are, if anything, slightly greater in intensity after functionalisation has occurred, suggesting minimal perturbation of the semiconducting nanotube structures.

The Brij-HiPCO system contains considerably more bundled CNTs than the Triton X dispersed sample, which is evidenced by a slight red-shift for peaks in the optical absorbance spectra of the Brij sample relative to Triton X. The appearance of a fluorescence peak from the (6,4) nanotube at 1.58eV excitation also suggests the presence of individualised CNTs in the Triton X sample, which was not observed in the Brij based dispersion. This fluorescence peak was not significantly quenched by diazonium addition, which offers further support for the low level of functionalisation imparted to the semiconducting species.²⁴⁵ Further evidence for the less bundled state of the Triton X dispersion is found in the increased separation of the RBM peaks at 1.58eV compared to Brij, coupled with the lower RBM intensity from the (10,2) nanotube at 267cm^{-1} . The RBM of this species is known to be sensitive to nanotube aggregation as increased inter-nanotube contact shifts the optical transition of the (10,2) CNT further into resonance at this excitation energy.⁴¹⁸ Nevertheless, the metallic nanotubes were still able to be selectively functionalised to a reasonable degree in the Brij dispersion despite its more aggregated nature.

Overall, selective functionalisation of metallic nanotubes for both the arc and HiPCO diameter distributions has been demonstrated to a degree that suggests separation of the two electronic types using diazonium functionalisation is feasible. Use of the PEO-containing dispersants Pluronic F-127 for arc CNTs and Triton X-405 for HiPCO nanotubes should provide the means to greatly improve separation yields comparative to SDS based reactions as the reaction selectivity is found to be much greater in the former dispersants.

Chapter 8

CONCLUSIONS AND FUTURE DIRECTIONS

A variety of different surfactants and polymers for the dispersion of carbon nanotubes in aqueous solution were examined in this work. It was shown that the quality of the dispersion will depend on the type of surfactant or polymer as well as the properties of the CNTs under investigation. All of the dispersants studied here were able to suspend raw arc nanotube material to some degree, although the anionic surfactant SDBS and the bile salt DOC were identified as the most effective for nanotube individualisation and long-term stability. DOC was determined to possess the strongest hydrophobic interaction with the nanotube surface out of all the dispersants studied. The commonly utilised surfactant SDS was found to be a relatively poor dispersant for arc-type nanotubes showing a significant level of aggregation within 72 hours of preparing the dispersion, whereas SDBS and DOC provided relatively good dispersion stability over a period of several months. For smaller diameter HiPCO nanotubes the discrepancy was greater between dispersive agents, with smaller ionic surfactants including SDBS, DOC, SC and SDS exhibiting superior performance. The improved stability of SDS with smaller diameter nanotubes highlights the fact that an effective dispersant for CNTs produced by a certain technique may not necessarily perform well for those prepared by

another method (that possess a different diameter distribution). Indeed, the dispersants PVP-10, PVP-55, Triton X-100 and Pluronic-F127 did not suspend HiPCO CNTs nearly as well as the larger diameter arc nanotubes.

The concentration of the surfactant was found to be a more influential parameter on the resultant dispersion than the ratio of surfactant to CNT material by mass for both DOC and SDBS. A clear maximum in the amount of nanotubes recovered in the supernatant was found to exist at approximate concentrations of 0.5% for SDBS and 1.6% for DOC. Dispersions analysed for SDBS showed that increasing the surfactant concentrations above these optimal values is detrimental as it leads to flocculation of the CNTs. This concentration-dependent aggregation is expected to be due to attractive depletion interactions between the dispersed nanotubes and the increasing volume of free surfactant micelles. Since the surfactant concentration determines the concentration of micelles in the solution, which would mediate attractive depletion interactions, this is a vital parameter. Optimal concentrations for dispersion of arc nanotubes were also determined for the dispersants Triton X-405, Brij S-100, Pluronic F-127 and PVP-55 as 3, 2, 5 and 3% respectively.

The two step sonication-centrifugation dispersion protocol was thoroughly analysed for dispersions of arc-CNTs in SDBS as a model system in order to characterise the properties of the nanotube ensemble in the supernatant. The large number of variables involved in dispersion may be altered to produce solutions containing a range of CNT concentrations, average lengths and aggregated states. The ability to manipulate such dispersions invariably results in a compromise between these three qualities. Increasing centrifugation time, force and temperature was able to increase the fraction of individual nanotubes present at the cost of a reduced CNT concentration and mean length. Centrifugation parameters appear to have a more pronounced effect on the dispersion properties over those of sonication, as the choice of applied force and duration defines the fraction of the sample remaining in the final supernatant. Centrifugation at $\sim 40 \times 10^3 \text{g}$ was found to provide the best metallic impurity removal, while $\sim 120 \times 10^3 \text{g}$ for 1-2 hours affords the best compromise between concentration, aggregation state and average length of the nanotube ensemble for the arc-CNT/SDBS system. Purification of CNTs may be enhanced by collecting an intermediate fraction, where a short initial step may remove heavier impurities while a longer secondary cycle can leave smaller particulate matter suspended.

Increasing sonication time was found to produce higher concentrations of CNTs with reduced bundle size, however scission greatly reduces the mean length of the population where both the tip and bath instruments generated a considerable amount of nanotube fragmentation. Since probe tips accomplish dispersion more efficiently without appearing to damage the nanotubes to any appreciable degree their use is preferred, although the energy density input should be minimised to reduce nanotube fragmentation and any instance of surfactant foaming. The use of antifoam agents was unable to suppress the formation of foams in SDBS dispersions under intense sonication, however CNTs were observed to remain suspended within foams generated from established dispersions. The input energy density was found to correlate with the dispersion quality more so than either duration or power alone, and trends built on this parameter were consistent across both the tip and bath instruments. Based on the studies performed in this work, optimal dispersion may be accomplished using a tip sonicator operating at low power density ($\sim 0.5\text{-}0.6\text{W}\cdot\text{mL}^{-1}$ or below) for a sonication time sufficient to deliver an overall energy density of around $400\text{-}500\text{J}\cdot\text{mL}^{-1}$. The mean nanotube length was found to scale proportional to $t^{-0.39}$ when exposed to ultrasound for an extended period, while the Raman D:G ratios followed a corresponding power law increase such that the relationship between mean length and D:G Ratio was approximately linear for both 1.58 and 2.33eV excitation.

Using the results of the dispersion analysis, a set of parameters was chosen that corresponded to nanotubes of reasonable length (around 600nm) and concentration ($0.025\text{mg}\cdot\text{mL}^{-1}$) but intermediate aggregation state (average bundle size $\sim 2.6\text{nm}$). The solutions were processed at low power to minimise nanotube scission and sidewall defect generation which would perturb the electronic structure of the CNTs and potentially reduce the selectivity of the diazonium reaction. The selectivity of the reactions between three different aryl diazonium salts and CNTs enveloped by a variety of dispersants was then probed via a kinetic study of their UV-Vis-NIR absorbance spectra. Non-ionic surfactants containing long polyethylene oxide hydrophilic groups, such as Pluronic F-127 and Brij S-100 were found to provide the best selectivity for arc type nanotubes, while ionic surfactants were generally unfavourable in this respect. This is suggested to be due to partial donation of electron density from the PEO containing polymers to the CNTs which encourages the preferential reaction with metallic nanotubes. Conversely, molecular interactions between nanotubes and the surfactant SDS are found to cause localisation of charge on the CNT surface, leading to inverse

selectivity of the diazonium reaction at its natural pH. Increasing the pH was found to improve or completely reverse the selectivity trend in this dispersant. The charge extraction effect of the SDS molecule is a finding that should receive further attention, particularly due to the prevalence of SDS as a dispersant for nanotubes in the literature where this phenomenon could be misinterpreted as CNT aggregation. In particular, the interaction of SDS with CNTs was found to deplete the electron density of larger diameter nanotubes to a greater extent than those of smaller diameter, which may lead to the degree of dispersion being underestimated in the SDS/arc CNT system when analysis is based on optical spectra alone. (Although there is some aggregation in this CNT-surfactant system, the surfactant-nanotube charge transfer interaction reduces the intensity of the of the optical absorbance spectrum such that level of aggregation appears greater than it actually is).

Diazonium salt concentration and solution temperature were found to affect the selectivity and rate of the reaction simultaneously. Minimising both of these parameters significantly improved the selectivity of the reaction in Pluronic F-127 dispersions. Although no direct correlation was observed between the diazonium ion degradation rate and the measured selectivity for each dispersant, the dispersant concentration was found to influence the reaction due to shifts in the dediazonation mechanism and the corresponding products. In solutions of Pluronic F-127 and SDBS the formation of highly coloured products is favoured at high dispersant concentration. This reduces the concentration of aryl radicals available for coupling with the CNTs and thus increases the selectivity of the reaction. The best rate separation between metallic and semiconducting arc-type nanotubes was observed in Pluronic F-127 dispersions of ~4 wt% using low concentrations (≤ 0.01 mM) of nitro-BDTFB added stepwise at temperatures below 24°C. HiPCO CNTs were also able to be selectively functionalised in both Brij S-100 and Triton X-405, though Triton X-405 was found to provide better individualisation of the smaller diameter nanotubes. Thus, utilising these optimal conditions and providing certain combinations of dispersant, diazonium salt and CNT diameter populations, it is possible to selectively functionalise metallic nanotubes to a high degree without significant coupling to semiconducting nanotubes. These results suggest that separation of CNTs by electronic type via the diazonium functionalisation method could be significantly improved. Failing separation, such reactions may be applied to any system that may benefit from the suppression of metallic nanotube characteristics.

Using CNTs dispersed in Pluronic, transparent thin films of nanotubes may be created through vacuum filtration. A comparison between pristine and nitro-BDTFB functionalised nanotubes in such films has shown a significant difference in the photoresponse of p-n junction type photovoltaic devices in which they are incorporated, although the performance of these materials in initial tests was not equal to that of nanotubes electronic-type separated by dielectrophoresis. Further work may concentrate on refining integration of the films into the photovoltaic cell and investigating alternate processing methods in order to improve the photoresponse of these particular devices.

However, the primary objective remains physical separation of the metallic and semiconducting nanotube types. This may be possible using the nitro-BDTFB functionalised material through reactions of the nitro group, possibly through reduction to an amine before further chemistry can be applied. Unfortunately, this requires relatively harsh conditions which may not be able to be performed in the Pluronic dispersion without destabilising it. Initial attempts to use Bechamp reduction (addition of HCl in the presence of iron powder) in an aqueous solution did not prove successful; despite proving to be resilient to the acidic conditions initially, the suspension was eventually destabilised.

A more accessible route may be to use the carboxy-BDTFB salt as the functional handle. Although this reagent was not quite as effective as the nitro-BDTFB salt it still produced a high degree of selectivity when used with Pluronic dispersions. The carboxyl addend would open up a variety of options for further chemical attachment, which may facilitate eventual separation of the two nanotube types. The most straight forward method would be to selectively functionalise metallic CNTs with the carboxy-BDTFB salt and subsequently attach a long chained alkyl-amine through a condensation reaction (forming an amide bond). This would then enable extraction of the functionalised metallic species in an organic solvent, while the semiconducting nanotubes would be anticipated to remain in the immiscible phase. If successful, this method could possibly provide a cheaper and simpler alternative to DGU and gel chromatography based techniques for bulk separation of nanotubes by electronic type, simply because the amount of equipment required to implement these other techniques (swing-bucket rotors, chromatographic columns) as well as the cost of related consumables (density gradient or gel media, centrifuge tubes etc.) are likely to be higher than for an industrial scale solvent extraction method to produce the same quantity of CNT material.

Aqueous dispersions of nanotubes may be used to deposit CNT films onto a substrate through drop casting, spray casting or contact printing, allowing for versatility in terms of the type of surface and target application. As these films are transparent when applied in a thin layer they possess the potential to replace other transparent conductors such as indium-tin oxide coatings. Such dispersions may also afford CNT materials being incorporated as conductive and reinforcing filler materials into polymer gels or ceramics. However, the properties of the nanotube dispersion will affect the overall performance of any novel material or device fabricated via these pathways, and therefore control of the initial dispersion phase of the process is important. The results presented within this work identify certain variables that may be used to produce CNT dispersions of high quality and thus lend themselves to further applications. Separation of CNTs by electronic type will afford the ability to produce high performance devices containing nanotubes as, for example, interconnects (metallic CNTs) and transistors (semiconducting CNTs), using dispersions enriched in these species. Indeed, it is inevitable that separated CNT material, both conducting and semiconducting, will be a part of future technology, and these separated materials are on the way to becoming commercially available through continued research efforts.

Appendix A

CALIBRATION OF SONICATOR POWER BY CALORIMETRY

The ultrasonic power output for the Sonics VCX 750W was measured at each amplitude setting for both the 5mm and 6.5mm microtips at the end of their experimental lifetime. As these apparatus have been used extensively prior to the calibration experiment, having been eroded and subsequently polished back to a smooth surface twice each, the output power is not expected to be equal to that of a pristine tip. Therefore a new 6.5mm microtip was purchased for calibration purposes.

The calorimetric method was employed to determine the output power for each tip. Specifically, the temperature increase imparted to a known volume of water held in a foam-insulated polypropylene container was measured using a Hanna Instruments HI 9063 thermometer with a K-type thermocouple which was immersed towards the base of the vial (away from the probe tip). Container lids were modified to allow insertion of the probe and thermocouple lead while still providing a cover to prevent excessive evaporation. 10 and 30mL volumes of water were used for the 5 and 6.5mm microtips respectively, with individual sample masses recorded prior to each run. Readings were taken in 10 second intervals for 3 minutes at tip amplitudes of 20, 25, 30, 35 and 40% as

set on the instrument, except for the 5mm tip where measurement was stopped when the temperature exceeded 55°C. At least two runs were performed at each amplitude setting, hence the resulting calibration curves use mean power values from 2-3 repetitions.

Figure A.1A shows the temperature increase over time recorded at each amplitude for the pristine 6.5mm tip. The power delivered by the probe was calculated from a linear fit to each series using the equation

$$P = \frac{dT}{dt} \cdot M \cdot C_p \quad (\text{A.1})$$

where P is the power, dT/dt is the slope of the temperature rise over time, M is the mass of water analysed and C_p is the specific heat capacity for water. Over the range of temperatures involved here, the heat capacity for water is taken as $4.18\text{J}(\text{g}\cdot\text{K})^{-1}$. Calorimetric power values were compared to the power output recorded by the energy monitor on the instrument itself, i.e. the energy delivered to the probe, to produce a calibration curve (Figure A.1D). This process was repeated for the worn 6.5mm tip used in the experiments, with temperature results for this tip shown in Figure A.1C and the calibration curve plotted alongside that of the pristine tip. Note that ‘worn’ refers to a tip that has been pitted through normal operation and then mechanically planed back to a smooth surface, as per the cycle shown in Figure A.1B. The data shown here for worn tips were recorded with a recently polished surface and should provide a reasonable transfer of power to the solution. However, since polishing changes the length of the resonant microtip the delivered calorimetric power is slightly reduced, as evidenced by the vertical shift of the calibration curve between the pristine and worn 6.5mm tips. All power values reported in the main text are derived from the pristine tip calorimetry data and thus may slightly overestimate the actual power delivered to the samples. Lateral deviations between the pristine and worn 6.5mm tip calibration curves reflect the uncertainty in the amplitude knob position between the two experiments, as selecting the appropriate power setting is somewhat ambiguous with the manual controls of the instrument.

The power output of the 5mm tip was also measured by calorimetry (Figure A.1E) and compared to the instrumental readings (Figure A.1F). There is a much more rapid temperature increase in this instance as a large amount of energy is provided to the low volumes within a short time frame. This led to some evaporative and sputtered loss of volume which would be a source of error for this series (and is the most likely cause of

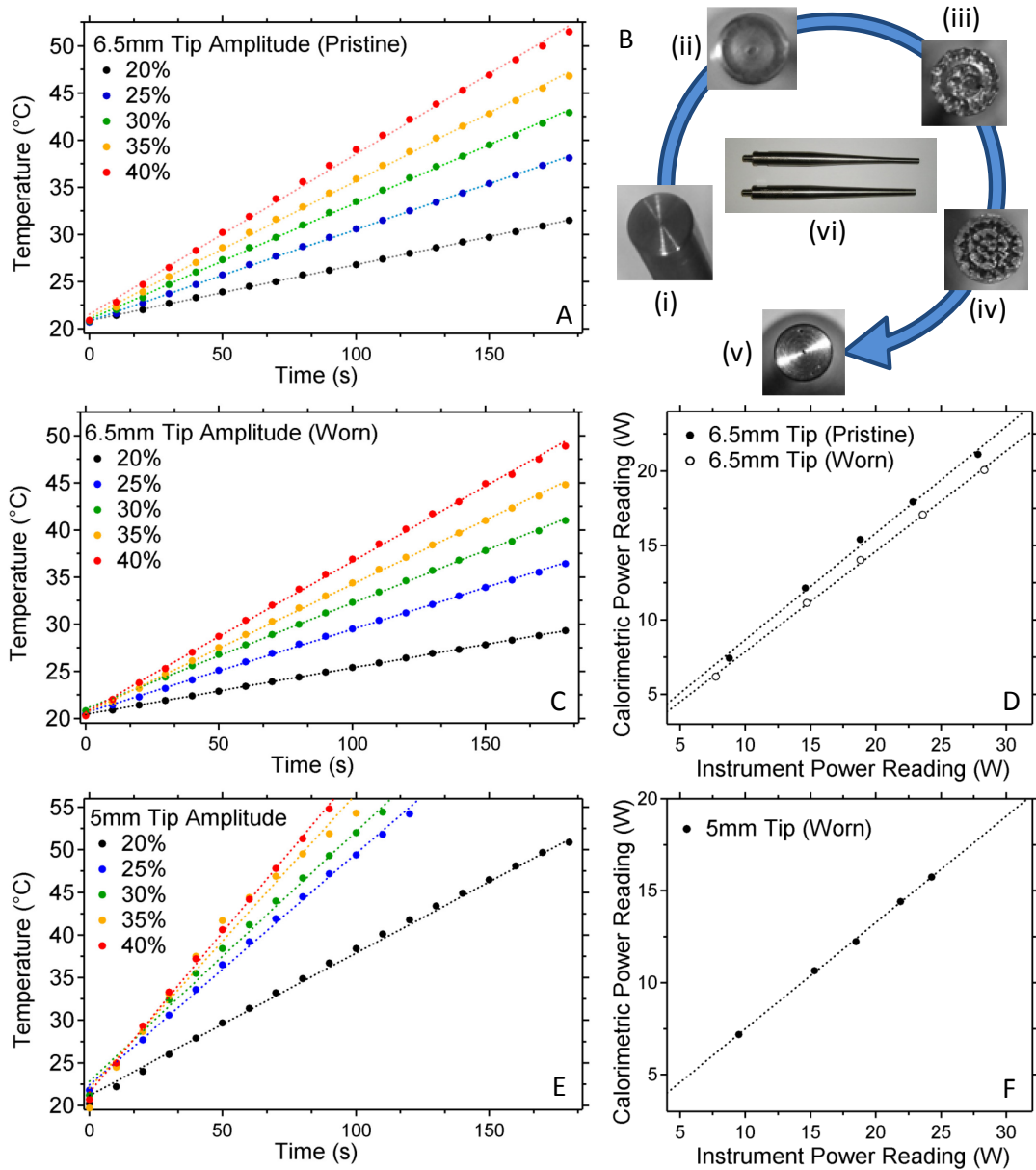


Figure A.1: Calorimetric calibration of the ultrasonic power output for the Sonics VCX 750W instrument. The temperature rise for 30mL volumes of water at various tip amplitudes for the pristine 6.5mm tip is shown in (A) and for the worn 6.5mm tip in (B), with power calibration curves for both the pristine and worn tips given in (D). Temperature data for the worn 5mm tip at different amplitudes is provided in panel (E) with the associated calibration curve displayed in frame (F). The diagram (B) depicts the life cycle of the 5mm microtip. The pristine tip (i) starts showing mild pitting (ii) after short periods of operation, which becomes extensive (iii) if allowed to progress. The image (iv) is the extensively pitted tip after filing back the outer layer, showing the regular pattern formed by ultrasonic erosion of the surface. Mechanical polishing of the tip can return the surface to its pristine condition (v). The image (vi) shows the 5mm (top) and 6.5mm (bottom) microtips from a side-on view.

the small degree of scatter and non-linearity in the data), however there is still a well-defined relationship between the calorimetrically determined power and the value

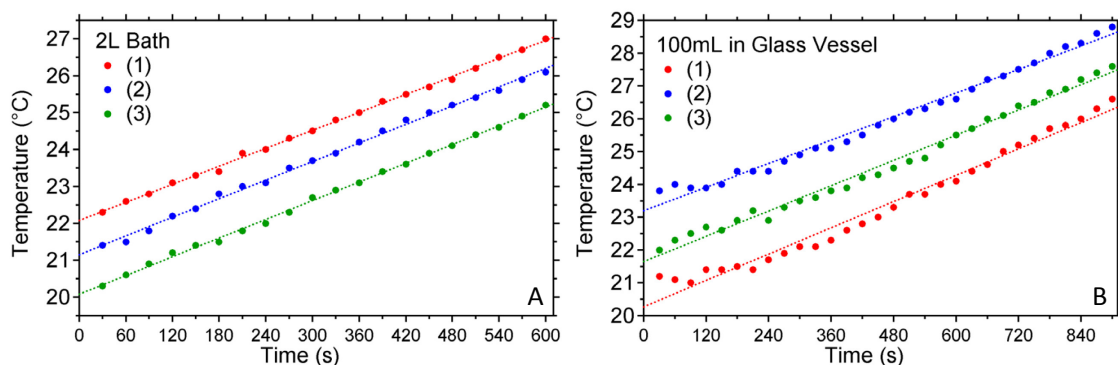


Figure A.2: Calorimetric calibration of the ultrasonic power output for the Elmasonic S30H bath sonicator. The temperature rise for 2L volumes of water held directly by the bath is shown in (A), while that of 100mL volumes held in Schott glass vials is presented in (B). The three iterations are offset by $\pm 1^\circ\text{C}$ for clarity.

provided by the control electronics for this tip. The calorimetric power provided by the 5mm tip was reduced by a greater amount with respect to the instrument value in comparison to the 6.5mm tip, particularly at higher amplitudes, which is probably related to the age of the tips as the 5mm tip was worn down to a much greater extent.

The power output of the bath sonicator was measured in a similar fashion. The instrument has a 37kHz output signal and is quoted by the manufacturer as having an effective ultrasonic power of 80W. When the bath is filled by 2L of water (73% of maximum capacity), the power output is measured as 69.6W averaged over several repetitions as shown in Figure A.2A. This is slightly lower than the expected 80W, however not all of the ultrasonic energy is converted to heat; some is also lost through vibrations of the apparatus, while thermal losses to the environment would also lower the calorimetrically determined value. Such systematic errors would also be present in the tip sonicator calibrations, although thermal insulation was employed in that experiment to reduce the uncertainty. The value of $\sim 70\text{W}$ is significantly higher than any power output recorded by the probe sonicator, however the energy is distributed throughout a much larger solution volume in case of the bath instrument. The output power for the bath corresponds to approximately $0.035\text{W}\cdot\text{mL}^{-1}$, which is far lower than the power densities provided by the tip sonicator ($\sim 0.2\text{-}1\text{W}\cdot\text{mL}^{-1}$). Additionally, the power delivered directly to the bath must also be transmitted through the vessel containing the sample, which would result in further loss of energy. To better estimate the power delivered to the nanotube samples the temperature rise of 100mLs of water held inside a Schott glass vial (100mL designated capacity) was recorded several times

as presented in Figure A.2B. The results returned a power output of 2.66W, or approximately $0.027\text{W}\cdot\text{mL}^{-1}$, which equates to about 76% of the power delivered to the bath itself. This measurement was made with the vial held in the centre of the bath by a clamp. Changing the depth of immersion (internal fluid level of the vial with respect to the bath) or type of container would probably result in a small difference in the energy imparted to the sample solution, while changing the level of the bath itself can have some influence. When the bath was filled with 2.4L of water the power output measured directly from the bath was somewhat lower, with a value of about $0.028\text{W}\cdot\text{mL}^{-1}$. However, perhaps the most precarious variation in the power density is found with the position of the sample within the bath. For both the direct measurements and those taken from within a vial described previously the position of the thermocouple was in the approximate geometric centre of the bath. Although the bath temperature is likely to be relatively uniform, the ultrasonic field distribution is not, and the dispersion of nanotubes was observed to be highly dependent on the position of the vial within the bath.

A foam float capable of holding up to 12 samples was inserted into the bath (Figure A.3C), with 8 vials containing 15mL of $0.5\text{mg}\cdot\text{mL}^{-1}$ as-produced arc CNTs in 1% SDBS situated in the positions indicated in Figures A.3E-H. The dispersions were monitored periodically by extracting 0.3mL of the liquid, diluting this aliquot 1:10 in surfactant solution and measuring the absorbance spectrum. The change in absorbance at 1000nm over time for each position is shown in Figure A.3A, where the different locations show clear variation in the amount of nanotube dispersion. The absorbance at 1000nm is colour-mapped by a gradient onto the vial positions in Figures A.3E-H to highlight the discrepancy in sonication power across the bath. The centre position provides the greatest intensity, where the vial at position 6 fractured after approximately 1 hour of sonication. Samples at positions 5, 7 and 8 appeared to receive approximately the same level of ultrasonic power input based on the absorbance at 1000nm, however after centrifugation at $40\times 10^3\text{g}$ there was a significant difference between the absorbance spectra of the supernatant solutions of these 3 samples (Figure A.3B). It was found that the centrifugation process is able to differentiate between solutions that are dispersed to different degrees even though most of the sonicated solutions reach the same level of absorbance at 1000nm and are indistinguishable after a period of time. The positions 5 and 7 appear to provide much better dispersion than the others, while positions 4 and 5 are intermediates. Positions 1 and 3 provided quite poor dispersion

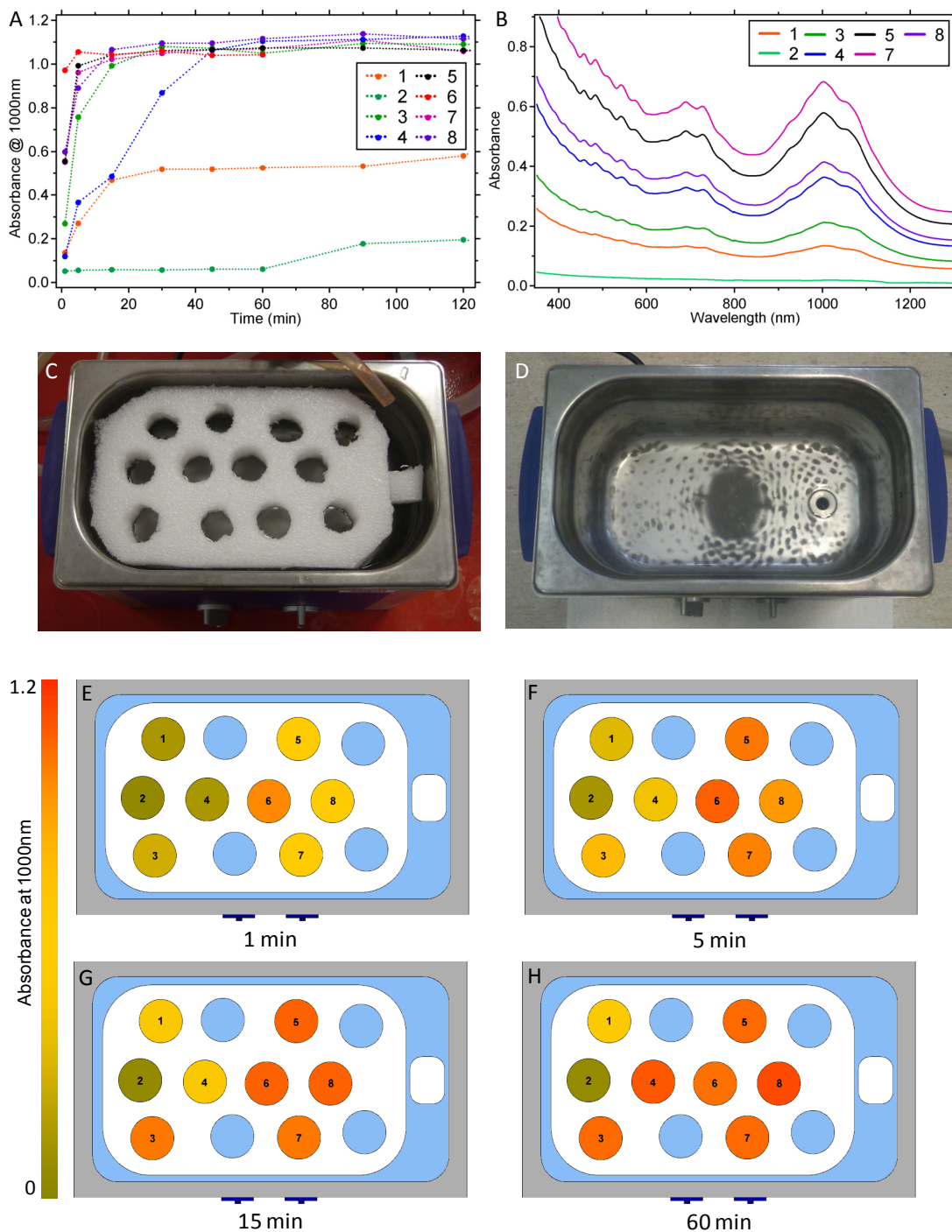


Figure A.3: Dispersion of arc CNTs in 1% SDBS using the Elmasonic S30 H ultrasonicator; (A) evolution of the absorbance at 1000nm for nanotube solutions held in vials in different positions within the bath, with absorbance spectra for each sample after 180minutes of sonication followed by centrifugation at $40 \times 10^3 g$ (B). Positions 1-8 in the foam float (C) are depicted in the diagrams E-H where the colour map relates the strength of the absorbance at 1000nm to the location in the bath after 1min (E), 5min (F), 15min (G) and 60min (H). The bath sonicator is pictured in (D), showing etching marks due to erosion of the metal surface. The darker regions indicate greater ultrasonic intensity.

and the solution placed at position 2 was barely dispersed at all. This suggests a non-uniform distribution of ultrasonic power within the bath with the greatest intensity in the centre and the weakest intensity towards the central edge.

The ultrasonic bath instrument is used extensively, hence over time a pattern developed on the base of the metal bath where the surface has been eroded by cavitation in a similar manner as the ultrasonic microtips in the probe sonicator case (Figure A.3D). Comparing these markings to the vial positions, it can be seen that where the pattern is at its darkest (such as positions 4-8) there is good dispersion, though positions 4 and 8 appear to lie over nodal points and as such the dispersion is reduced at these locations. The corner positions 1 and 3 reside over areas that show minor erosion of the metal housing, while position 2 sits over a region showing only very weak patterning. As the dispersion efficiency in the positions 1-8 correlates well with the erosion pattern, it is expected that the markings on the base are a good indication of the power distribution throughout the entire depth of the bath. Consequently, the lateral position of the sample is a determining factor of the overall energy input, and any comparison between samples in a series is only valid if they are sonicated in the same bath position. Thus, one of the only advantages the bath sonication method offers over that of tip sonication; the ability to process multiple samples at once; is not really valid for experiments where the input power density is desired to remain constant.

As a final note, an experiment to analyse the power distribution over all 12 sample positions was performed using vials containing 50mg of anhydrous ferric oxide powder in 15mL of water. These were placed into the float in two different orientations as shown in Figure A.4 and the optical density of the obtained solutions was colour

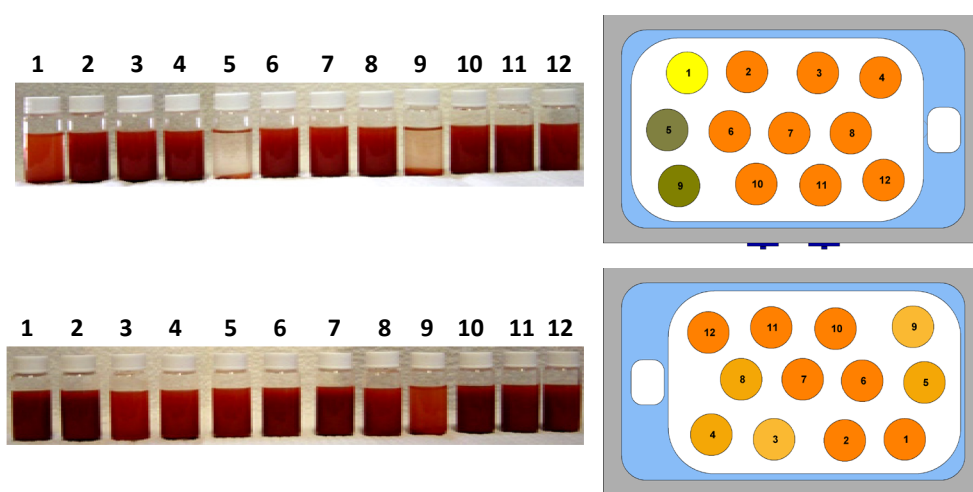


Figure A.4: Power distribution within the bath determined using iron oxide in water situated in all 12 sample positions of the foam float in two different orientations.

mapped onto the respective positions. Again, the extent of dispersion was reasonably consistent with the pattern on the base of the bath plate, with dispersion over the drain edge being much better than the opposite side. Hence, not only is the ultrasonic power distribution non-uniform within the bath, it is also asymmetric.

Appendix B

DECONVOLUTION OF ABSORBANCE SPECTRA FOR SPECIES ASSIGNMENT

The (n, m) species present in the arc and HiPCO nanotube materials may be elucidated through fitting of the optical absorbance spectra. Although photoluminescence spectroscopy would be a preferable technique for determining the constituent species, an appropriate instrument was not available for this kind of measurement. Deconvolution of the absorbance spectra, while not as precise, may identify the major species present in a particular sample based on positions of individual absorbance peaks. Species assignments were made primarily using the data provided by Weisman and Bachilo which was produced from dispersions of HiPCO CNTs in sodium dodecyl sulphate, with an error on the order $\sim 2\%$ expected for dispersions in different surfactants.³⁹

By comparing the optical absorbance spectrum to a Kataura plot of transition energies vs. nanotube diameters the range of possible CNT diameters within the sample may be estimated from the width of the S_{11} and S_{22} absorbance bands.³⁶ Since the reference values were measured by photoluminescence only semiconducting nanotubes could be included in the analysis, however the metallic tubes are assumed to be of similar

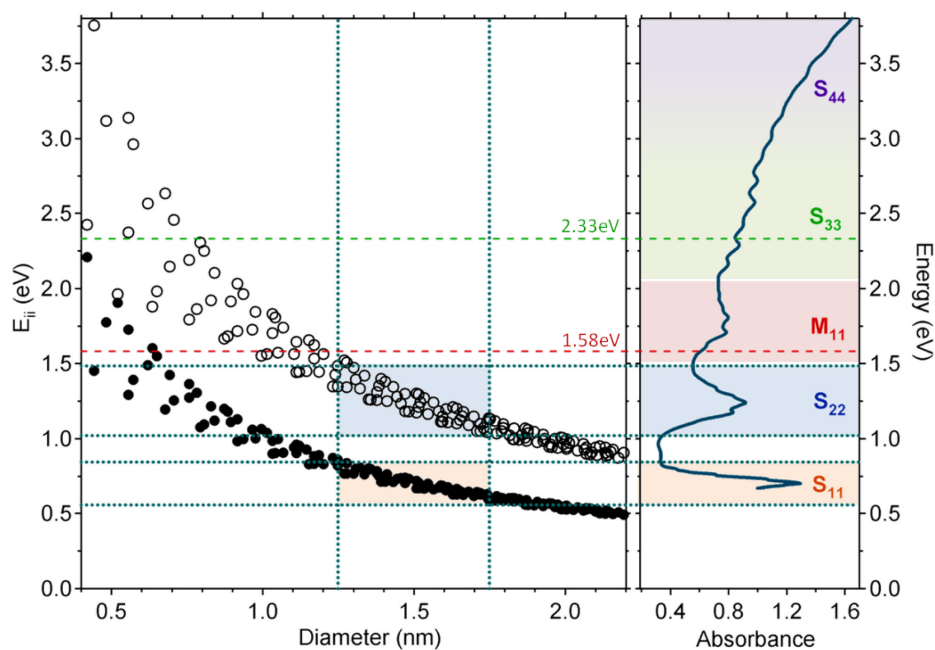


Figure B.1: Kataura plot reproduced from the data of Weisman & Bachilo (left), showing semiconducting S_{11} (solid circles) and S_{22} (open circles) optical transitions. The UV-Vis-NIR spectrum of arc CNTs in D_2O and 1% SDBS is shown (right) with blue dotted lines indicating boundaries for the observed S_{11} and S_{22} absorbance bands and the limits of the expected corresponding nanotube diameters. Red and green dashed lines represent the two laser excitation energies of the Raman instrument.

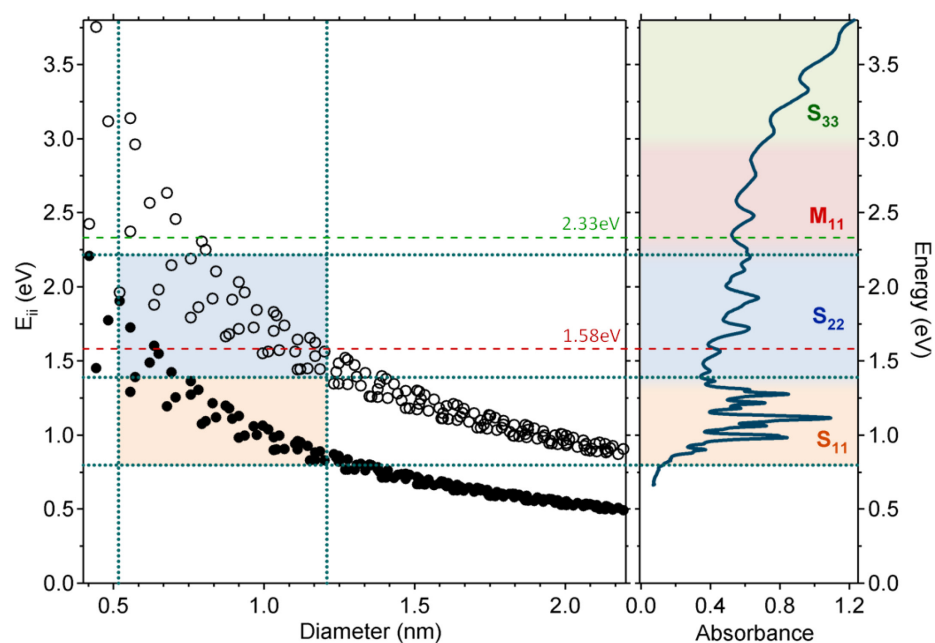


Figure B.2: Kataura plot as in Figure B.1 (left) with the UV-Vis-NIR absorbance spectrum of HiPCO CNTs in D_2O and 1% SDBS (right). Blue dotted lines indicate boundaries for the observed S_{11} and S_{22} absorbance bands and the range of possible diameters responsible for these optical transitions.

dimensions as the synthesis method generally defines the diameter range of the sample. The S_{11} and S_{22} absorbance bands of the arc nanotubes potentially include transitions

from a large number of nanotube species from 1.25-1.75nm in diameter (Figure B.1), though not all of these are expected to actually be present in the sample. Through a similar analysis, it is estimated that the optical transitions for HiPCO nanotubes arise from nanotubes having diameters around 0.5-1.2nm (Figure B.2).

A more specific estimation of the CNT species present was made through fitting of the optical absorbance spectra. For arc CNTs this was done using a sample of the raw nanotube material dispersed in 0.5% SDBS ($0.5\text{mg}\cdot\text{mL}^{-1}$, 50mL solution sonicated for 30min at 22% amplitude with the 6.5mm microtip, centrifuged for 1 hour at $\sim 120\times 10^3\text{g}$). To remove contributions to the background from other sources, some of the suspended CNTs were reacted with an excess of 4-bromo-BDTFB to completely bleach the optical transitions.²⁴² This material was filtered over a $0.22\mu\text{m}$ PTFE membrane, rinsed thoroughly with H_2O and resuspended in SDBS to generate a background spectrum which was then subtracted. A further baseline removal of the form $A = ae^{-b\lambda}$ with $b = 0.00155$ was also performed to account for the intrinsic absorption background from metallic nanotubes.³⁴⁷ These background signals are shown in Figure B.3 along with the original spectrum before baseline subtraction.

A sample of arc CNTs dispersed in the same manner but centrifuged for 6 hours was also examined, where the spectrum was multiplied by a scalar (x5) to match the absorbance intensity of the 1 hour sample at 800nm. The same background subtraction was then applied to this sample, as shown in Figure B.3. Fits of 10 Lorentzian peaks to the S_{22} regions of the 1 and 6 hour spectra were calculated using Fityk software (freeware, v. 0.97). Although 11 peaks could be fit to the S_{33} region, the highest energy peaks could potentially correspond to S_{44} transitions, while data for these higher order transitions are not available in the literature for comparison in any case. Assignments of metallic nanotube absorbance peaks are also lacking for nanotubes larger than 1.3nm in diameter, thus only the S_{22} peak fits are used to estimate the presence of certain species for the arc nanotubes. Fits to the spectra of both the 1 and 6 hour samples are provided in Figure B.3. Peak positions and species assignments are provided in Figure B.4. Some ambiguity exists within the fit as peak widths were allowed to vary, however consideration of both samples allows a reasonable estimate of the CNT species present to be made by comparison to the data of Weisman & Bachilo.³⁹ The diameters of the assigned nanotubes vary between about 1.25-1.73nm while the major candidate species (possessing the largest Lorentzian peaks) have diameters around 1.5nm, which is the

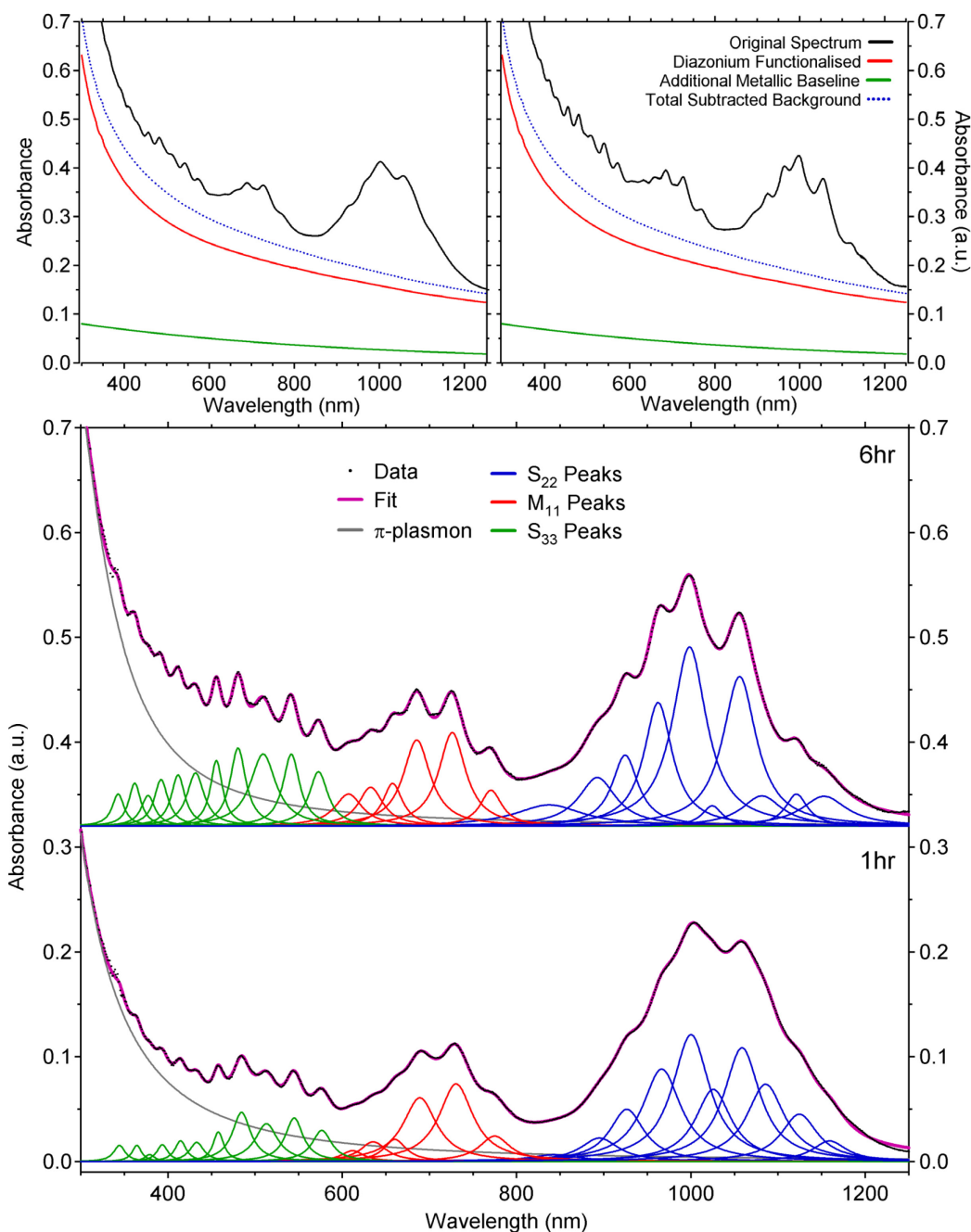


Figure B.3: UV-Vis-NIR spectra for arc CNTs in 0.5% SDBS in water (black lines) after centrifugation for 1hr (left) and 6hrs (right). The re-suspended diazonium functionalised nanotube spectrum used for initial background subtraction is displayed in both frames (red line) while the additional calculated background is also shown (green line). Fits of Lorentzian peaks to the background-subtracted spectra are given in the bottom panel.

expected average diameter value for the ensemble. The individual peaks for all species exhibit a slight blue-shift with increased centrifugation time due to the change in aggregation state as bundles are removed, which is consistent with expectations.

| Peak Group | Peak Position (nm) | | Shift (nm) | Energy (eV) | | Most Likely | d (nm) | Assignment* | | | |
|------------|--------------------|--------|------------|-------------|-------|-------------|--------|---------------|-----------|--------|---------------|
| | 1hr | 6hr | | 1hr | 6hr | | | E_{22} (eV) | Alternate | d (nm) | E_{22} (eV) |
| S22 | 1159.2 | 1152.9 | 6.3 | 1.070 | 1.075 | (15,10) | 1.730 | 1.072 | (15,11) | 1.795 | 1.071 |
| S22 | 1124.5 | 1121.1 | 3.4 | 1.103 | 1.106 | (17,6) | 1.641 | 1.102 | (18,4) | 1.611 | 1.109 |
| S22 | 1085.8 | 1081.5 | 4.3 | 1.142 | 1.146 | (14,9) | 1.594 | 1.148 | (17,7) | 1.697 | 1.149 |
| S22 | 1058.6 | 1055.9 | 2.8 | 1.171 | 1.174 | (16,5) | 1.508 | 1.175 | (15,7) | 1.546 | 1.165 |
| S22 | 1025.7 | 1024.5 | 1.2 | 1.209 | 1.210 | (12,10) | 1.515 | 1.210 | (19,3) | 1.641 | 1.201 |
| S22 | 1000.1 | 998.4 | 1.7 | 1.240 | 1.242 | (16,6) | 1.564 | 1.240 | (13,9) | 1.521 | 1.243 |
| S22 | 966.5 | 962.4 | 4.1 | 1.283 | 1.288 | (11,10) | 1.440 | 1.280 | (18,2) | 1.515 | 1.294 |
| S22 | 926.5 | 924.6 | 1.9 | 1.338 | 1.341 | (13,5) | 1.278 | 1.344 | (12,7) | 1.321 | 1.333 |
| S22 | 895.2 | 892.7 | 2.5 | 1.385 | 1.389 | (10,9) | 1.307 | 1.395 | (16,3) | 1.405 | 1.381 |
| S22 | 843.3 | 837.5 | 5.8 | 1.470 | 1.480 | (11,7) | 1.248 | 1.484 | (14,4) | 1.300 | 1.472 |
| M11 | 775.0 | 770.7 | 4.3 | 1.600 | 1.609 | | | | | | |
| M11 | 730.6 | 726.2 | 4.4 | 1.697 | 1.707 | | | | | | |
| M11 | 689.0 | 685.5 | 3.5 | 1.799 | 1.809 | | | | | | |
| M11 | 660.4 | 657.9 | 2.6 | 1.877 | 1.885 | | | | | | |
| M11 | 635.6 | 632.7 | 2.9 | 1.951 | 1.960 | | | | | | |
| M11 | 611.8 | 607.3 | 4.5 | 2.027 | 2.042 | | | | | | |
| S33 | 576.6 | 572.8 | 3.8 | 2.150 | 2.165 | | | | | | |
| S33 | 544.8 | 541.6 | 3.3 | 2.276 | 2.289 | | | | | | |
| S33 | 513.0 | 509.2 | 3.8 | 2.417 | 2.435 | | | | | | |
| S33 | 484.5 | 480.4 | 4.1 | 2.559 | 2.581 | | | | | | |
| S33 | 457.9 | 455.7 | 2.2 | 2.708 | 2.721 | | | | | | |
| S33 | 433.1 | 431.8 | 1.3 | 2.863 | 2.872 | | | | | | |
| S33 | 414.5 | 411.7 | 2.8 | 2.991 | 3.012 | | | | | | |
| S33 | 393.7 | 392.2 | 1.5 | 3.149 | 3.161 | | | | | | |
| S33 | 379.1 | 377.2 | 1.9 | 3.270 | 3.287 | | | | | | |
| S33 | 364.4 | 362.0 | 2.4 | 3.403 | 3.425 | | | | | | |
| S33 | 344.4 | 342.9 | 1.5 | 3.600 | 3.616 | | | | | | |

*Based on Weisman & Bachilo, *Nano Lett.* 2003, **3** (9),1235-8.

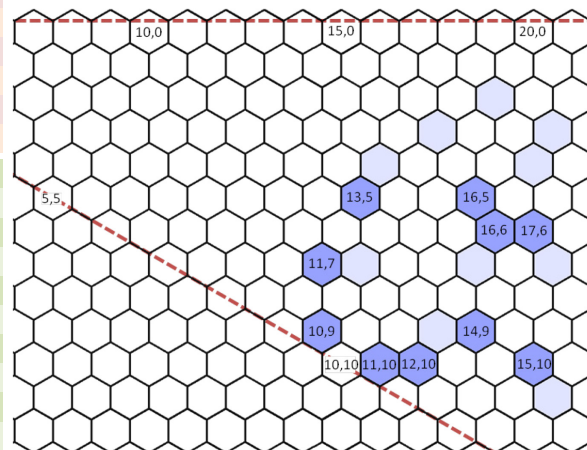


Figure B.4: Species assignments for arc CNTs in SDBS centrifuged for both 1 and 6 hours at $\sim 120 \times 10^3 g$. Diameters were calculated using a carbon-carbon bond length of 0.144nm. The most probable species are marked in colour on the irreducible wedge of the graphene lattice.

Analysis of HiPCO nanotubes was also performed for a dispersion in D_2O with 1% SDBS ($0.5 \text{ mg} \cdot \text{mL}^{-1}$ CNTs, 10mL solution sonicated for 20 min at 22% amplitude with the 5mm microtip, centrifuged for 2 hours at $\sim 122 \times 10^3 g$; diluted 1:2 in D_2O on collection). In this instance only a calculated background was subtracted as shown in the upper frame of Figure B.5, with parameters $a = 1.1$ and $b = 0.00155$. The spectrum was fit with a number of Lorentzian bands pertaining to various S_{11} , S_{22} , M_{11} and S_{33} transitions. Since the HiPCO nanotubes have smaller diameters the energies of the optical transitions are more disperse and more species are identifiable, though the bands overlap somewhat which increases uncertainty in the assignments. Again, comparative data for higher order transitions is presently unavailable, however energy gaps for metallic nanotubes in the HiPCO distribution have been analysed in a number of studies.^{286,419,420} Metallic species are assigned here based on the preferential bleaching of these transitions during reactions with diazonium salts, which indicates their metallic nature, although S_{22} transitions for species identified in the S_{11} region also appear within

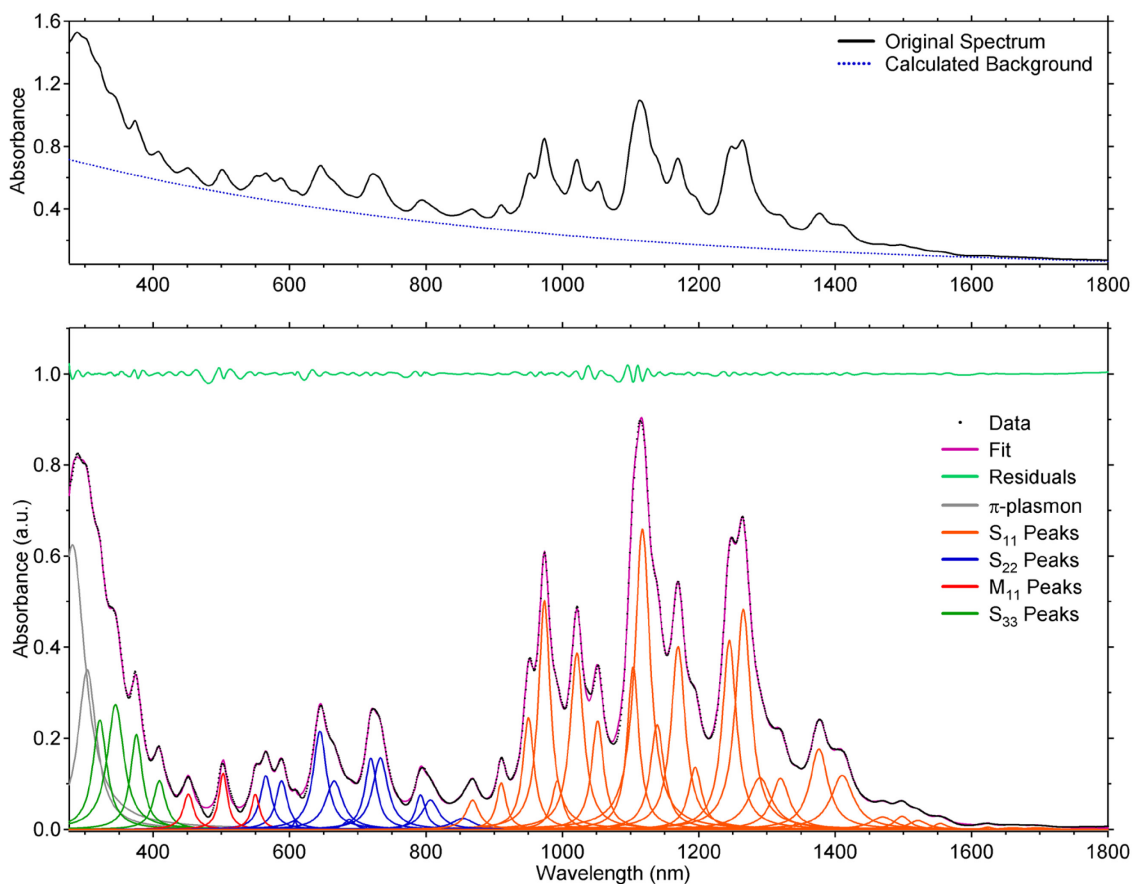


Figure B.5: UV-Vis-NIR spectra for HiPCO CNTs in 1% SDBS in D₂O (black line) and the calculated background used for subtraction (dotted blue line). Fits of Lorentzian peaks to the background-subtracted spectra are given in the bottom panel.

this energy range. Chirality assignments for the fits in Figure B.5 are provided in Figure B.6. Although a large number of species are identified by their individual absorbance peaks here, more are probably present in the sample. Those marked as ‘alternative’ assignments are likely to be additional contributors to the spectrum, while other species with diameters within the range 0.5-1.2nm are most certainly present even though their absorbance peaks could not be strictly resolved. Indeed, the spectrum of HiPCO nanotubes has been fit with up to 57 species (39 semiconducting, 18 metallic),²⁴² all within a similar area of the irreducible graphene wedge.³⁷ Thus, although a particular nanotube chirality may not be marked on the lattice in Figure B.6, it may still be present in the sample as long as it lies within the expected region. This was made apparent by deconvolution of the RBM regions for HiPCO nanotubes as shown in Figure B.7, which revealed at least 7 other species not marked as primary assignments in Figure B.6 to be present in the solution. Assignment of the RBM peaks in Figure B.7 is based on a combination of data from several sources,^{39,239,286,290,418,419,421} with excitation energies

| Peak Group | Peak Position | | Assignment | | | | | | | |
|------------|---------------|-------|---------------------|--------|-----------------------------|----------------------|-----------|--------|----------------------|----------------------|
| | (nm) | (eV) | Most Likely (n,m) | d (nm) | E ₁₁ (eV) | E ₂₂ (eV) | Alternate | d (nm) | E ₁₁ (eV) | E ₂₂ (eV) |
| S11 | 1623 | 0.764 | (16,0) | 1.270 | 0.764 | 1.521 | (14,4) | 1.300 | 0.764 | 1.472 |
| - | - | - | - | - | - | - | (15,2) | 1.278 | 0.764 | 1.508 |
| S11 | 1554 | 0.798 | (10,9) | 1.307 | 0.797 | 1.390 | (17,0) | 1.350 | 0.799 | 1.261 |
| S11 | 1521 | 0.815 | (11,7) | 1.248 | 0.818 | 1.484 | - | - | - | - |
| S11 | 1498 | 0.828 | (13,3) | 1.170 | 0.828 | 1.631 | (12,5) | 1.201 | 0.829 | 1.559 |
| - | - | - | - | - | - | - | (14,1) | 1.153 | 0.826 | 1.657 |
| S11 | 1469 | 0.844 | (10,8) | 1.24 | 0.844 | 1.428 | - | - | - | - |
| S11 | 1410 | 0.879 | (9,8) | 1.170 | 0.879 | 1.533 | - | - | - | - |
| S11 | 1376 | 0.901 | (12,2) | 1.041 | 0.901 | 1.810 | (10,6) | 1.111 | 0.900 | 1.644 |
| S11 | 1344 | 0.923 | (12,4) | 1.145 | 0.924 | 1.447 | - | - | - | - |
| S11 | 1320 | 0.939 | (9,7) | 1.103 | 0.937 | 1.569 | - | - | - | - |
| S11 | 1290 | 0.961 | (14,0) | 1.111 | 0.957 | 1.443 | - | - | - | - |
| S11 | 1265 | 0.980 | (8,7) | 1.032 | 0.981 | 1.702 | (11,1) | 0.916 | 0.980 | 2.032 |
| S11 | 1245 | 0.996 | (9,5) | 0.976 | 0.999 | 1.848 | (10,3) | 0.936 | 0.993 | 1.963 |
| - | - | - | - | - | - | - | (10,5) | 1.050 | 0.992 | 1.577 |
| S11 | 1195 | 1.038 | (11,3) | 1.014 | 1.036 | 1.564 | - | - | - | - |
| S11 | 1170 | 1.060 | (12,1) | 0.995 | 1.060 | 1.552 | (8,6) | 0.966 | 1.058 | 1.727 |
| S11 | 1140 | 1.088 | (9,2) | 0.806 | 1.090 | 2.251 | - | - | - | - |
| S11 | 1117 | 1.110 | (8,4) | 0.840 | 1.116 | 2.105 | - | - | - | - |
| S11 | 1104 | 1.123 | (9,4) | 0.916 | 1.126 | 1.716 | - | - | - | - |
| S11 | 1052 | 1.179 | (10,2) | 0.884 | 1.177 | 1.683 | - | - | - | - |
| S11 | 1021 | 1.214 | (7,5) | 0.829 | 1.211 | 1.921 | - | - | - | - |
| S11 | 992 | 1.250 | (7,3) | 0.706 | 1.250 | 2.457 | - | - | - | - |
| S11 | 974 | 1.273 | (6,5) | 0.757 | 1.270 | 2.187 | - | - | - | - |
| S11 | 950 | 1.305 | (8,3) | 0.782 | 1.303 | 1.863 | - | - | - | - |
| S11 | 910 | 1.362 | (9,1) | 0.757 | 1.359 | 1.794 | - | - | - | - |
| S11 | 866 | 1.432 | (6,4) | 0.692 | 1.420 | 2.146 | - | - | - | - |
| S22 | 854 | 1.452 | (14,0)/(12,4) | - | - | - | - | - | - | - |
| S22 | 806 | 1.538 | (9,8)/(16,0) | - | - | - | - | - | - | - |
| S22 | 792 | 1.565 | (9,7)/(12,1)/(11,3) | - | - | - | - | - | - | - |
| S22 | 733 | 1.691 | (8,7)/(10,2) | - | - | - | - | - | - | - |
| S22 | 719 | 1.724 | (9,4) | - | - | - | - | - | - | - |
| S22 | 688 | 1.802 | (12,2)/(9,1) | - | - | - | - | - | - | - |
| S22 | 665 | 1.864 | (8,3)/(9,5) | - | - | - | - | - | - | - |
| S22 | 644 | 1.925 | (7,5) | - | - | - | - | - | - | - |
| S22 | 608 | 2.039 | (11,1) | - | - | - | - | - | - | - |
| S22 | 588 | 2.109 | (8,4) | - | - | - | - | - | - | - |
| S22 | 565 | 2.194 | (6,5) | - | - | - | - | - | - | - |
| M11 | 550 | 2.254 | (9,6) | 1.038 | E ₁₁ = 2.23-2.25 | - | - | - | - | - |
| M11 | 503 | 2.465 | (8,5) | 0.902 | E ₁₁ = 2.43-2.47 | - | - | - | - | - |
| M11 | 452 | 2.743 | (6,6) | 0.825 | E ₁₁ = 2.69-2.71 | - | - | - | - | - |
| S33 | 409 | 3.031 | - | - | - | - | - | - | - | - |
| S33 | 375 | 3.306 | - | - | - | - | - | - | - | - |
| S33 | 345 | 3.594 | (6,5) | - | - | - | - | - | - | - |
| S33 | 322 | 3.850 | - | - | - | - | - | - | - | - |

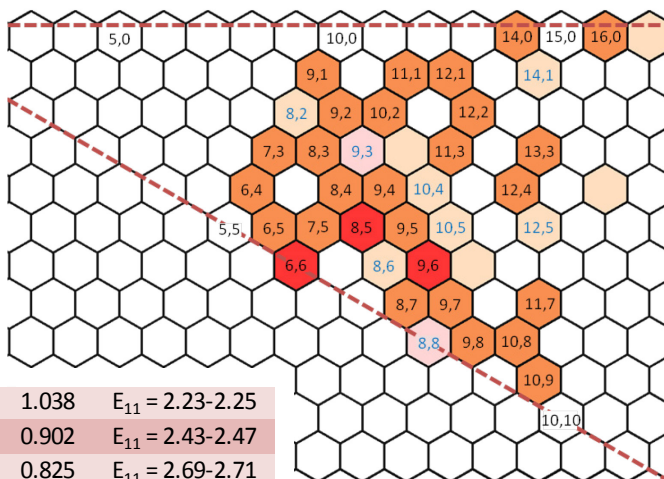
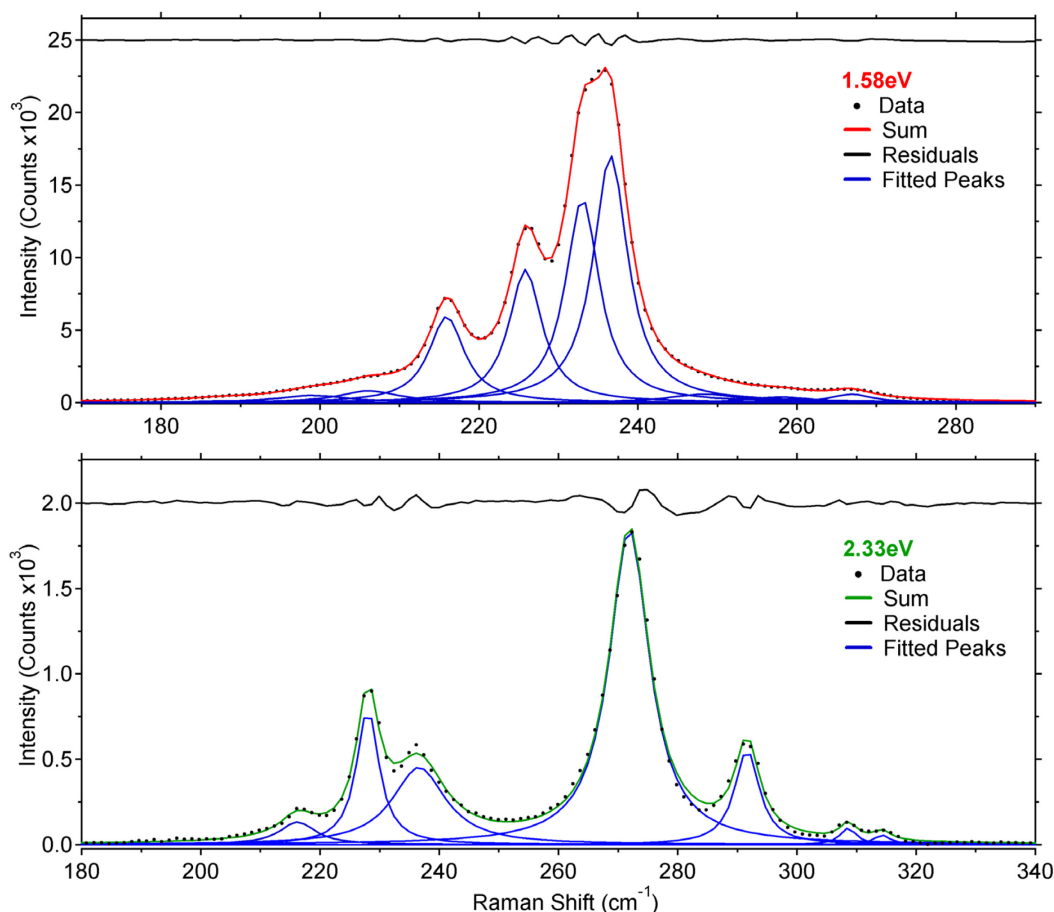


Figure B.6: Species assignments for HiPCO CNTs in SDBS. Diameters were calculated using a carbon-carbon bond length of 0.144nm. The most probable species are marked in colour on the irreducible wedge of the graphene lattice.



| 2.33eV | | | | 1.58eV | | | |
|-------------------------|------------------|--------|--------------------------|-------------------------|------------------|--------|--------------------------|
| RBM (cm ⁻¹) | Assignment (n,m) | d (nm) | Resonant Transition (eV) | RBM (cm ⁻¹) | Assignment (n,m) | d (nm) | Resonant Transition (eV) |
| 216 | (8,8) | 1.100 | M ₁₁ 2.23 | 190 | (11,7) | 1.248 | S ₂₂ 1.47 |
| 228 | (9,6) | 1.038 | M ₁₁ 2.25 | 199 | (12,5) | 1.201 | S ₂₂ 1.56 |
| 237 | (10,4) | 0.992 | M ₁₁ 2.24 | 206 | (14,1) | 1.153 | S ₂₂ 1.66 |
| 272 | (9,3) | 0.859 | M ₁₁ 2.40 | 216 | (9,7) | 1.103 | S ₂₂ 1.55 |
| 291 | (9,2) | 0.806 | S ₂₂ 2.28 | 226 | (10,5) | 1.050 | S ₂₂ 1.56 |
| 308 | (6,5) | 0.757 | S ₂₂ 2.18 | 233 | (11,3) | 1.014 | S ₂₂ 1.55 |
| 314 | (8,2) | 0.728 | M ₁₁ 2.53 | 237 | (12,1) | 0.995 | S ₂₂ 1.54 |
| - | - | - | - | 248 | (8,6) | 0.966 | S ₂₂ 1.72 |
| - | - | - | - | 258 | (9,4) | 0.916 | S ₂₂ 1.71 |
| - | - | - | - | 267 | (10,2) | 0.884 | S ₂₂ 1.69 |

Figure B.7: Fits of Lorentzian peaks to the RBM regions of Raman spectra recorded from HiPCO CNTs in 0.5% SDBS in water at energies of 1.58 and 2.33eV using the high-resolution gratings. Assignments of the RBM peaks are provided in the table along with the energies of the optical transition excited by the laser. Diameters were calculated using a carbon-carbon bond length of 0.144nm.

quoted from Maultzsch *et al.*²⁸⁶ The newly identified species include the (8,8) and (10,4) nanotubes which have transition energies virtually indistinguishable from that of the (9,6) nanotube in the absorbance spectrum. This is just one example of overlapping transition energies, which is a common occurrence where so many different species of

nanotube are involved. All HiPCO nanotubes for which spectral signatures were identified in either Raman or UV-Vis-NIR spectra are marked on the graphene lattice in Figure B.6. Although other species are expected to be present and contribute to the optical spectra of the nanotube ensemble, these are the major species of which the HiPCO material is composed. This provides a reasonable picture of the specific nanotube chiralities that would be interacting with the different dispersants and diazonium salts within the experiments discussed in the main text.

Appendix C

SUPPLEMENTARY DATA FOR SONICATION

STUDIES

Absorbance spectra for samples of arc CNTs dispersed at $0.5\text{mg}\cdot\text{mL}^{-1}$ in 0.5% SDBS that were prepared by sonication for various durations (using both the probe and bath ultrasound apparatus) are displayed in Figure C.1. Specifically, for the 5mm microtip these samples were individually prepared 10mL solutions, while sequential aliquot removal from single samples of 50 and 110mL volume was performed for the 6.5mm microtip and bath series respectively. Centrifugation parameters were fixed at $122\times 10^3\text{g}$ for 1 hour in each case. These sample series are analysed in detail in Chapter 5, Section 5.2, where trends in the S_{22} semiconducting absorbance bands (areal absorbance, peak-to-background ratio and position of the maximum) and their implications are discussed. These parameters were also measured for the absorbance band due to metallic nanotube species (M_{11} , occurring at around 687nm for arc CNTs in SDBS) and their values are plotted alongside the semiconducting peak data in Figure C.2 for comparison. Trends in areal absorbance for the metallic peak are essentially identical in comparison with the semiconducting data for each sample series, while the evolution of the M_{11} peak-to-background ratio and position with sonication time is also very similar to that of the

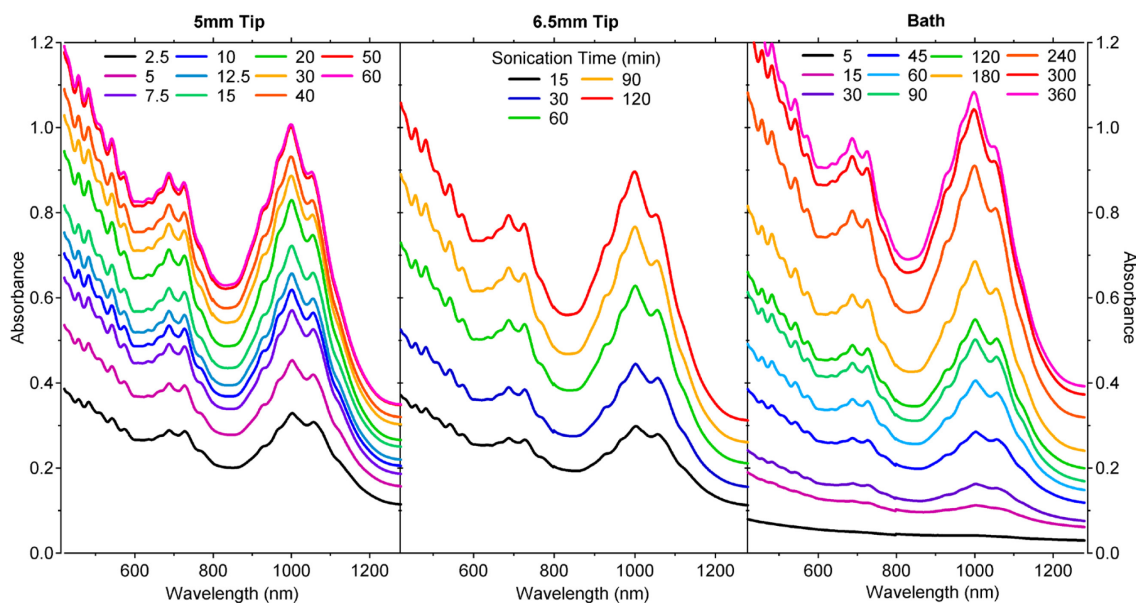


Figure C.1: UV-Vis-NIR spectra for arc CNTs in 0.5% SDBS prepared by sonication for various durations using the 5mm microtip (left), 6.5mm microtip (centre) and ultrasonic bath (right).

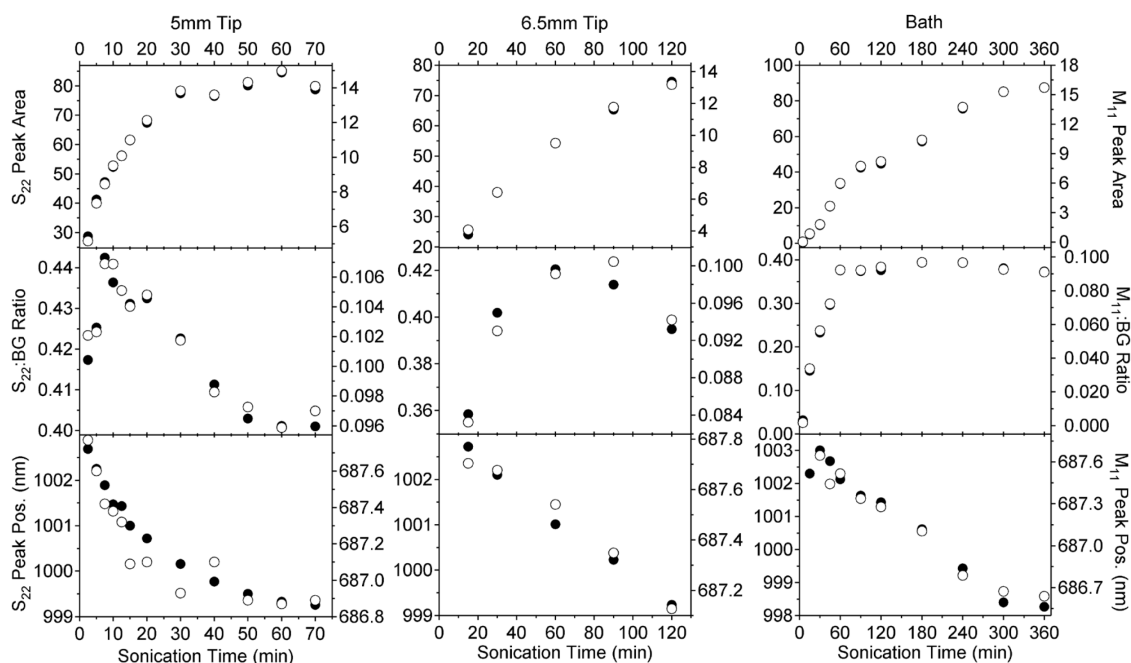


Figure C.2: Comparison between trends in areal absorbance, peak-to-background ratio and position of the maximum for both the semiconducting (S₂₂, solid circles) and metallic (M₁₁, open circles) absorbance bands.

semiconducting peak in each case. As the two peaks scale equivalently, this tends to suggest that sonication affects nanotubes of both electronic types to an equal extent.

The metallic peak was also assessed for all other experiments within the main text where the S₂₂ peak was analysed, and in all cases the trends between the M₁₁ and S₂₂

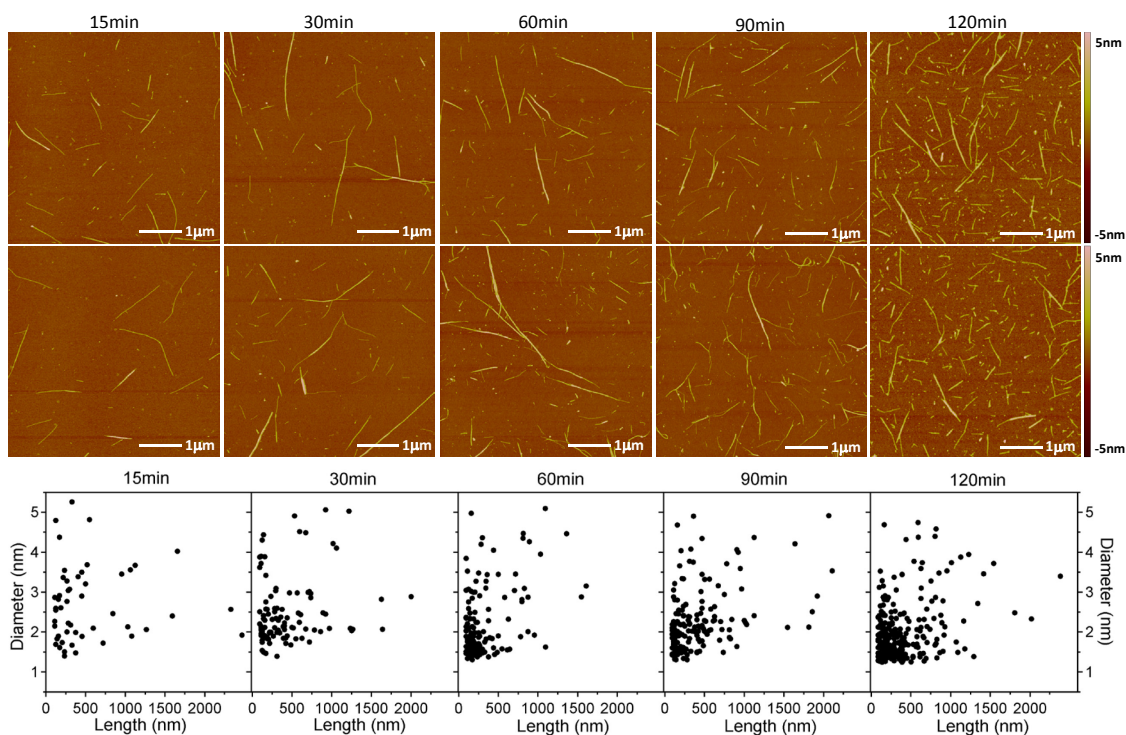


Figure C.3: 5x5μm AFM height images for dispersions of arc CNTs in SDBS sonicated using the 6.5mm tip for various durations. Two images are shown for each time interval. Length vs. diameter distributions recorded from a single 8x8μm image for each sample are also shown (bottom).

bands were very closely matched. Consequently, the S_{22} band alone was used to evaluate absorbance spectra as this provided sufficient data for comparison of dispersion state between samples in a series.

Each of the sonicated sample series presented above were also analysed by AFM, where mean values for nanotube dimensions within a sample were obtained from separately recorded distributions of length and diameter, as discussed in Chapter 5, Section 5.2. An alternative analysis for the 6.5mm tip-sonicated sample series is presented in Figure C.3, where the length and diameter of nanotube objects were measured simultaneously from a single image for each sample. In this method of assessment it becomes more obvious that extended exposure to ultrasound increases the concentration of nanotube objects in the dispersion, while the dimensions of these objects are reduced over time. However, although the distributions become more congested at shorter lengths and smaller diameters, some larger objects are always present at longer lengths and larger diameters for all samples. This is due to the simultaneous effects of debundling and scission that occur with cavitation. The continuous debundling of larger aggregates in

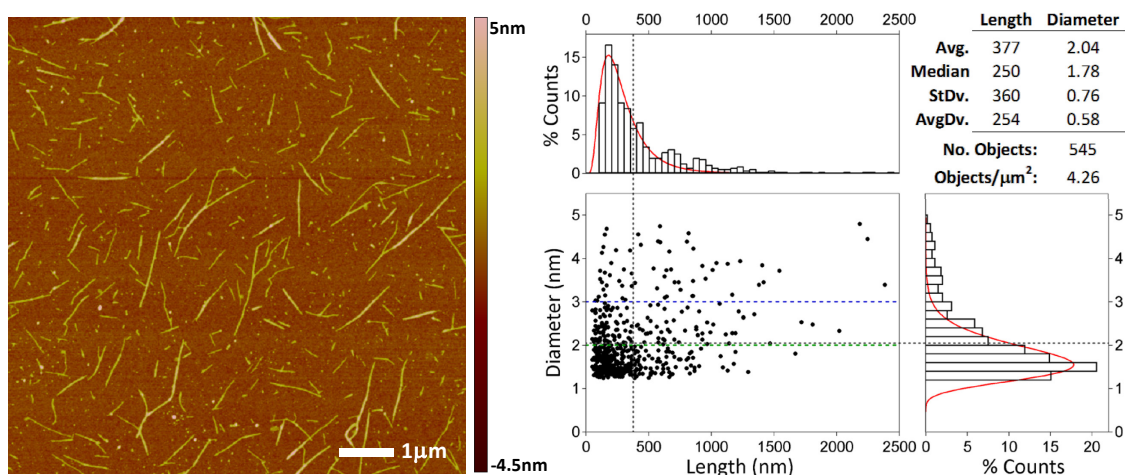


Figure C.4: An $8 \times 8 \mu\text{m}$ AFM height image for a dispersion of arc CNTs in 0.5% SDBS sonicated for 120 minutes with the 6.5mm microtip and centrifuged at $122 \times 10^3 \text{g}$ for 1 hour (left). The associated length and diameter distributions recorded from two such images are also shown (right).

the bulk solution allows larger bundles to be present in the centrifuged supernatant even after extended periods of sonication, while both of these effects serve to increase the concentration of nanotube objects in the supernatant.

Length and diameter distributions for the sample sonicated for 120 minutes are provided in Figure C.4. In comparison with the dispersion produced by 10 minutes of sonication with the 5mm tip that was similarly analysed in Figure 4.7 (Chapter 4, Section 4.1.4), this dispersion shows a significantly reduced number of long objects with diameters on the order of a single nanotube. Also, the number of short objects with diameters corresponding to bundles of several tubes is considerably increased in the 120 minute sample. Therefore, in addition to supporting the established reduction in CNT length with sonication time, the results presented here suggest that large bundles are also broken into shorter lengths by cavitation and that this is a frequent occurrence. Consequently, the use of prolonged sonication times does not guarantee that the CNTs will be exfoliated, only that the mean length will be significantly reduced. This again supports the use of short-to-intermediate ultrasound durations for the preparation of CNT dispersions that contain individualised nanotubes of reasonable length.

Appendix D

KINETIC DATA FOR DIAZONIUM REACTIONS

Figure D.1 shows the power law fits for the kinetic data obtained for reactions of the three different diazonium salts in each dispersant from which the parameters α and β quoted in the main text (Chapter 7, Section 7.3) were extracted.

Further figures in this appendix contain plots of relative peak intensities against time for the experimental studies presented in Chapter 7, Section 7.5, where diazonium reactions were performed with dispersions of arc CNTs in Pluronic F-127 and SDBS. Selectivity curves and the linear fits from which selectivity factor values were calculated are shown for each series, while data converted to the power-law form and associated fits are also provided for each data set.

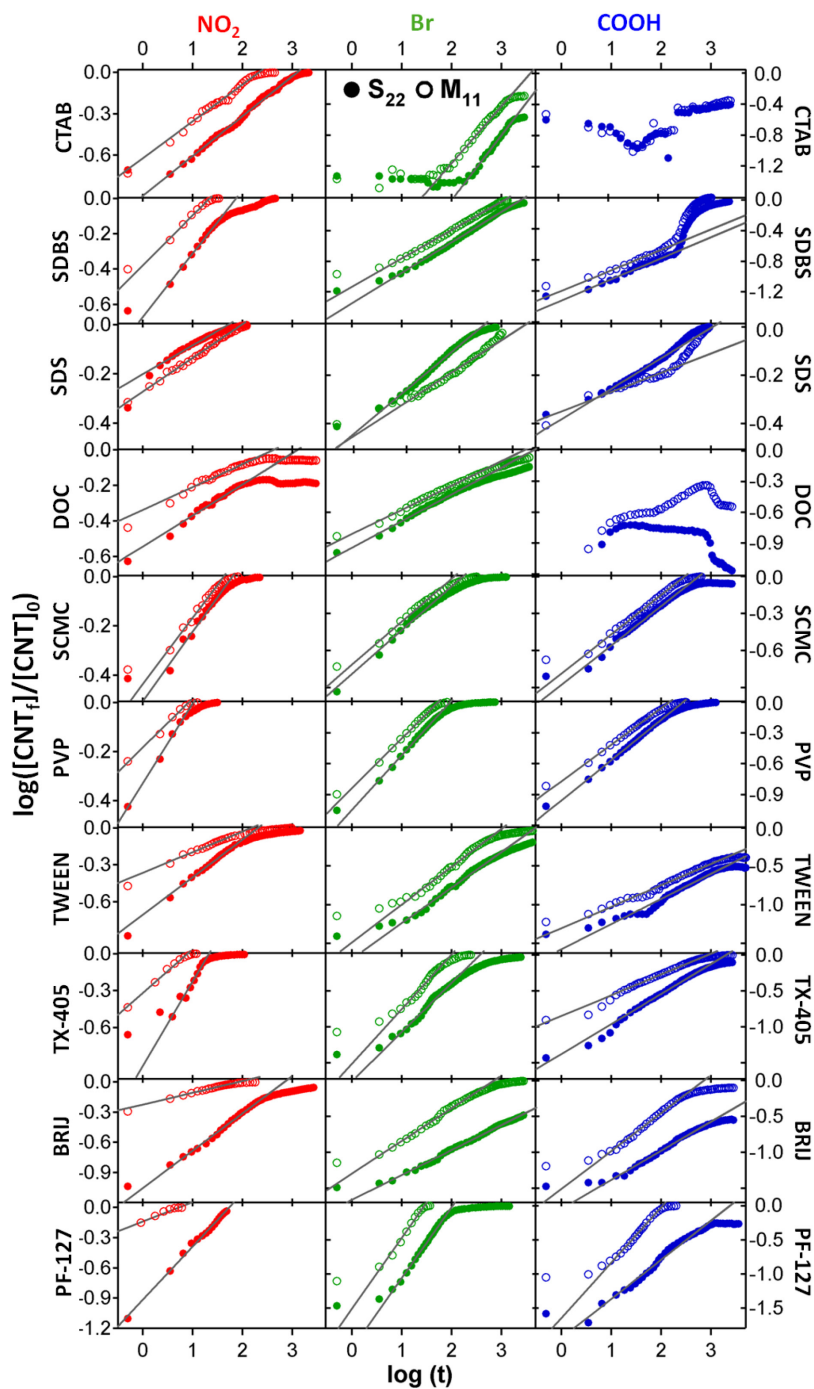


Figure D.1: Relative peak heights for both M₁₁ and S₂₂ UV-Vis-NIR absorbance peaks of CNTs in different dispersants reacting with Br⁻, NO₂⁻ and COOH⁻-BDTFB salts. Grey lines represent fits of the power law $\log([\text{CNT}]_t)/[\text{CNT}]_0 = \log(\beta) + \alpha \log(t)$ to each data set.

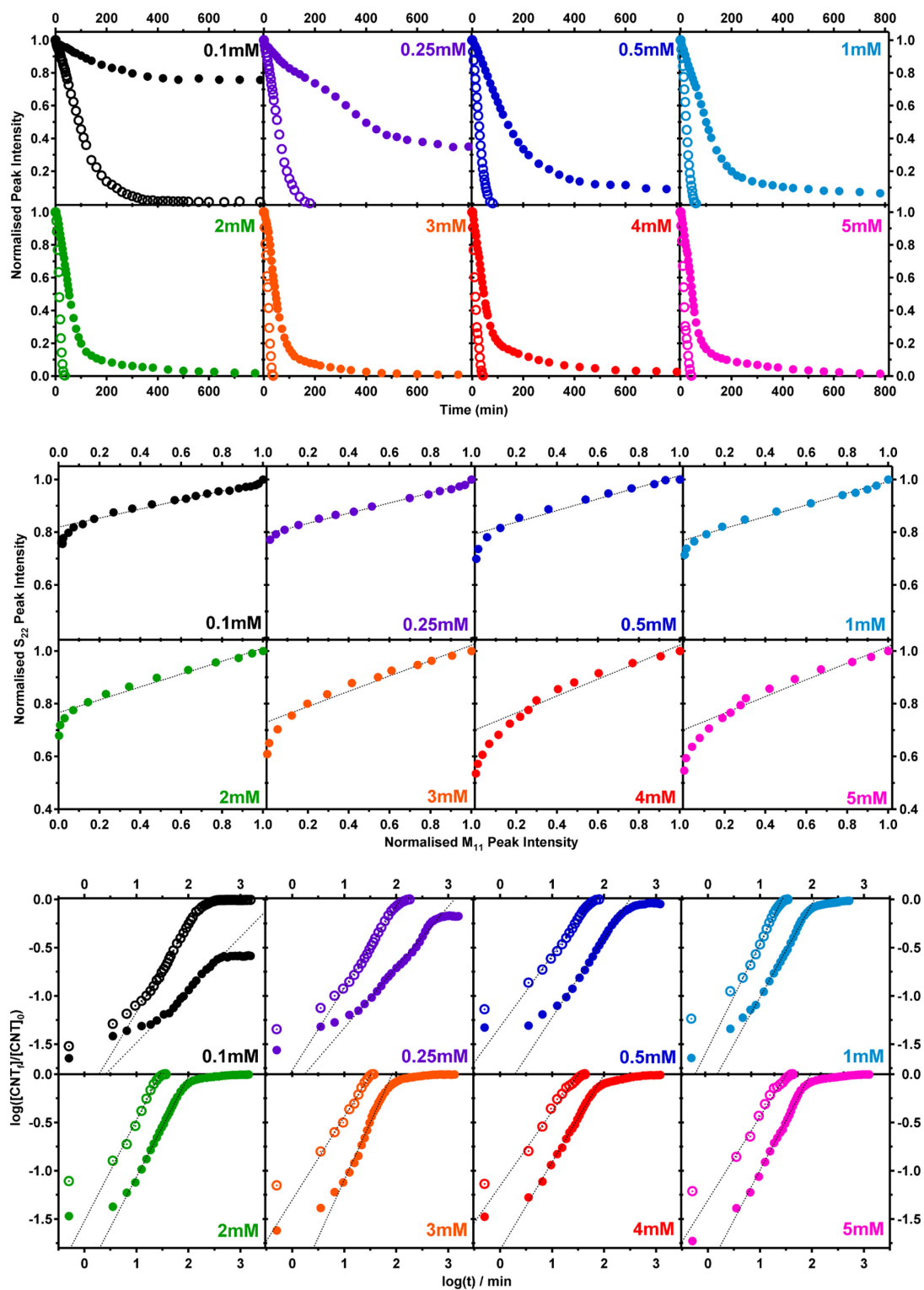


Figure D.2: Kinetic data (top) and selectivity curves (centre) for reaction of Br-BDTFB at different concentrations with CNTs in 4.5% Pluronic F-127 at 27°C. The same data with power law fits is presented in the bottom panel. Open and solid circles for top and bottom frames represent the metallic M_{11} and semiconducting S_{22} peaks respectively.

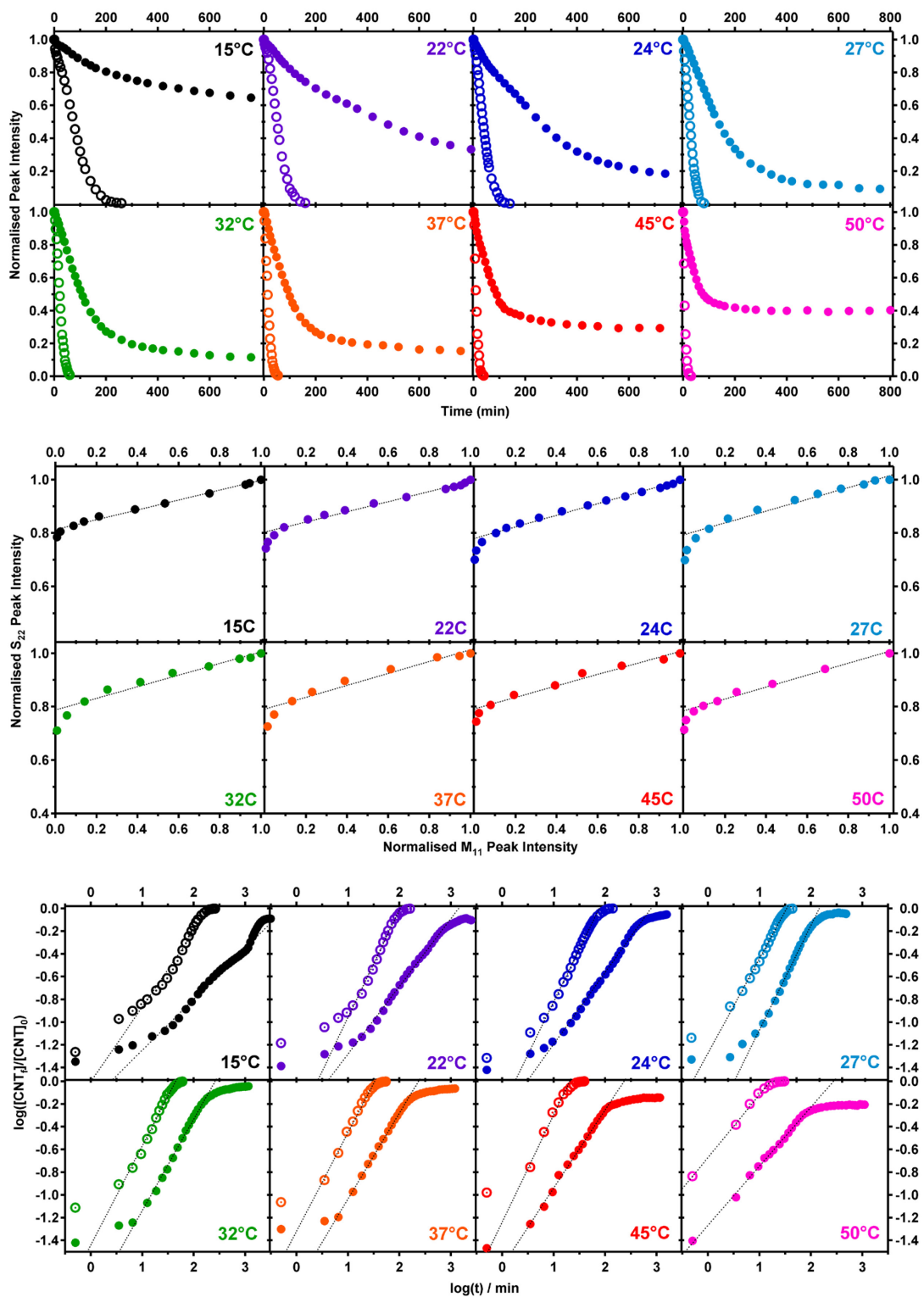


Figure D.3: Kinetic data (top) and selectivity curves (centre) for the reaction of 0.5mM Br-BDTFB with CNTs in 4.5% Pluronic F-127 at different temperatures. The same data with power law fits is presented in the bottom panel. Open and solid circles for top and bottom frames represent the metallic M_{11} and semiconducting S_{22} peaks respectively.

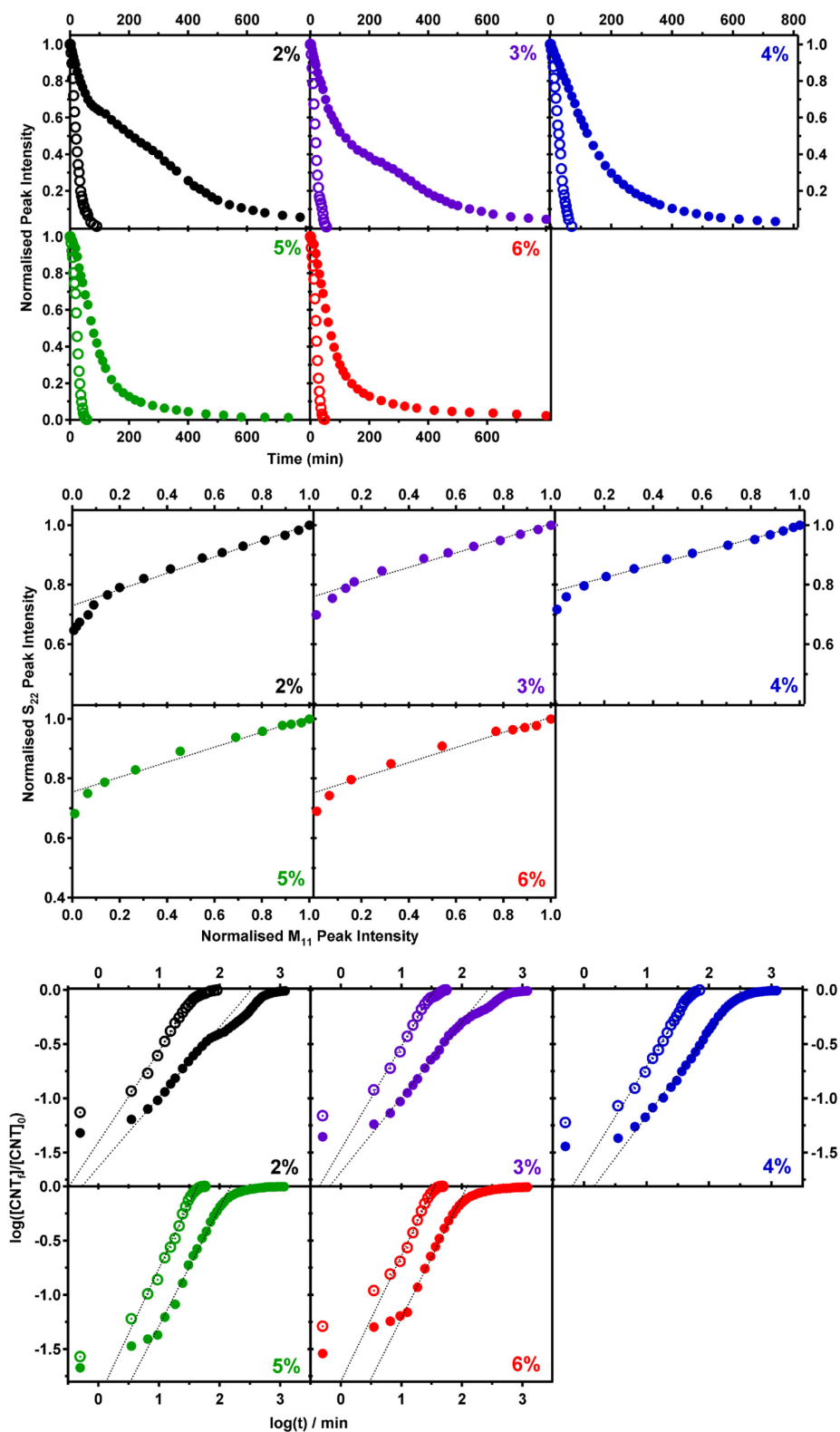


Figure D.4: Kinetic data (top) and selectivity curves (centre) for reaction of 3mM Br-BDTFB with CNTs in different concentrations of Pluronic F-127 at 27°C. The same data with power law fits is presented in the bottom panel. Open and solid circles for top and bottom frames represent the metallic M_{11} and semiconducting S_{22} peaks respectively.

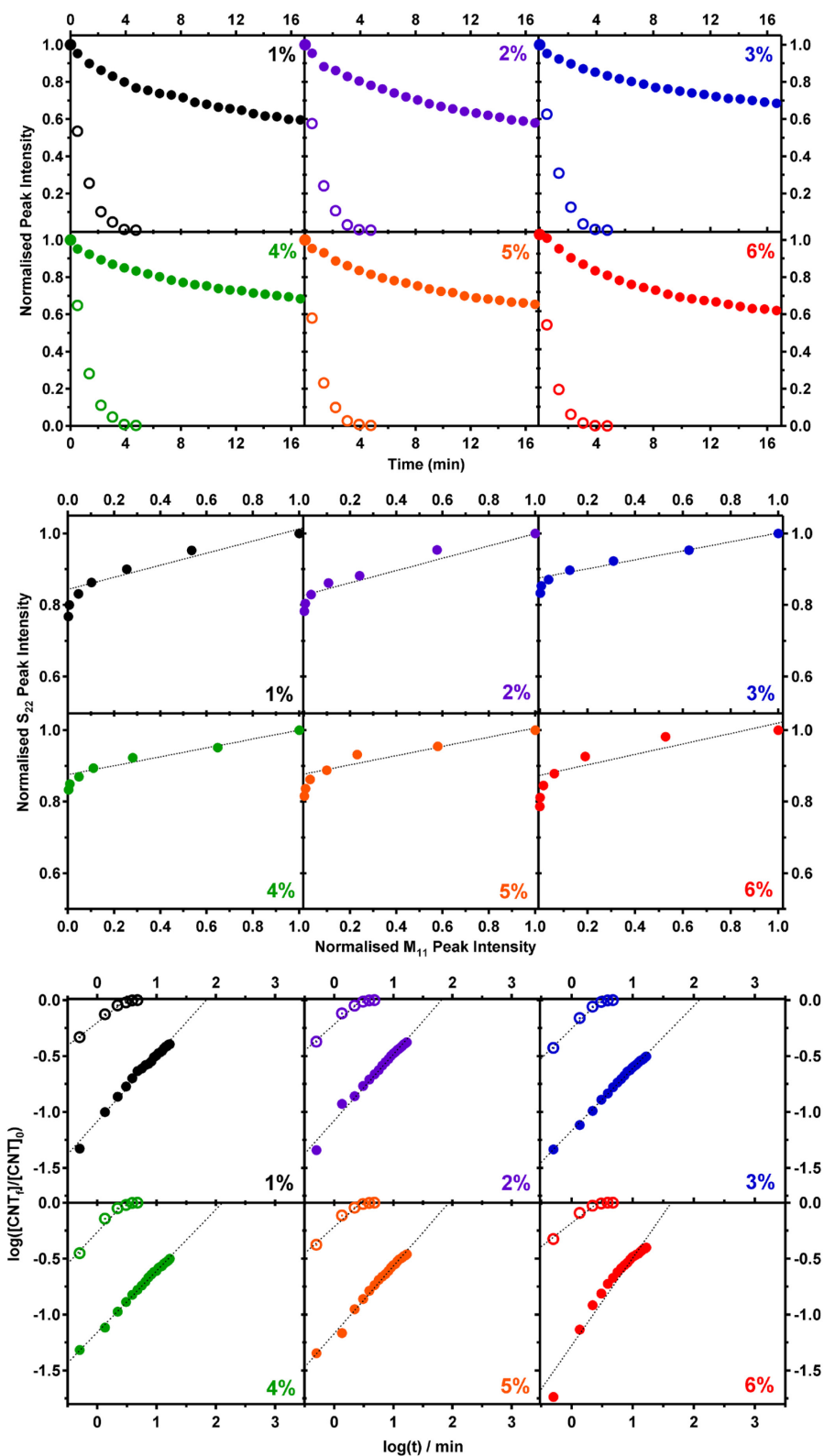


Figure D.5: Kinetic data (top) and selectivity curves (centre) for reaction of 0.3mM NO₂-BDTFB with CNTs in different concentrations of Pluronic F-127 at 27°C. The same data with power law fits is presented in the bottom panel. Open and solid circles for top and bottom frames represent the metallic M₁₁ and semiconducting S₂₂ peaks respectively.

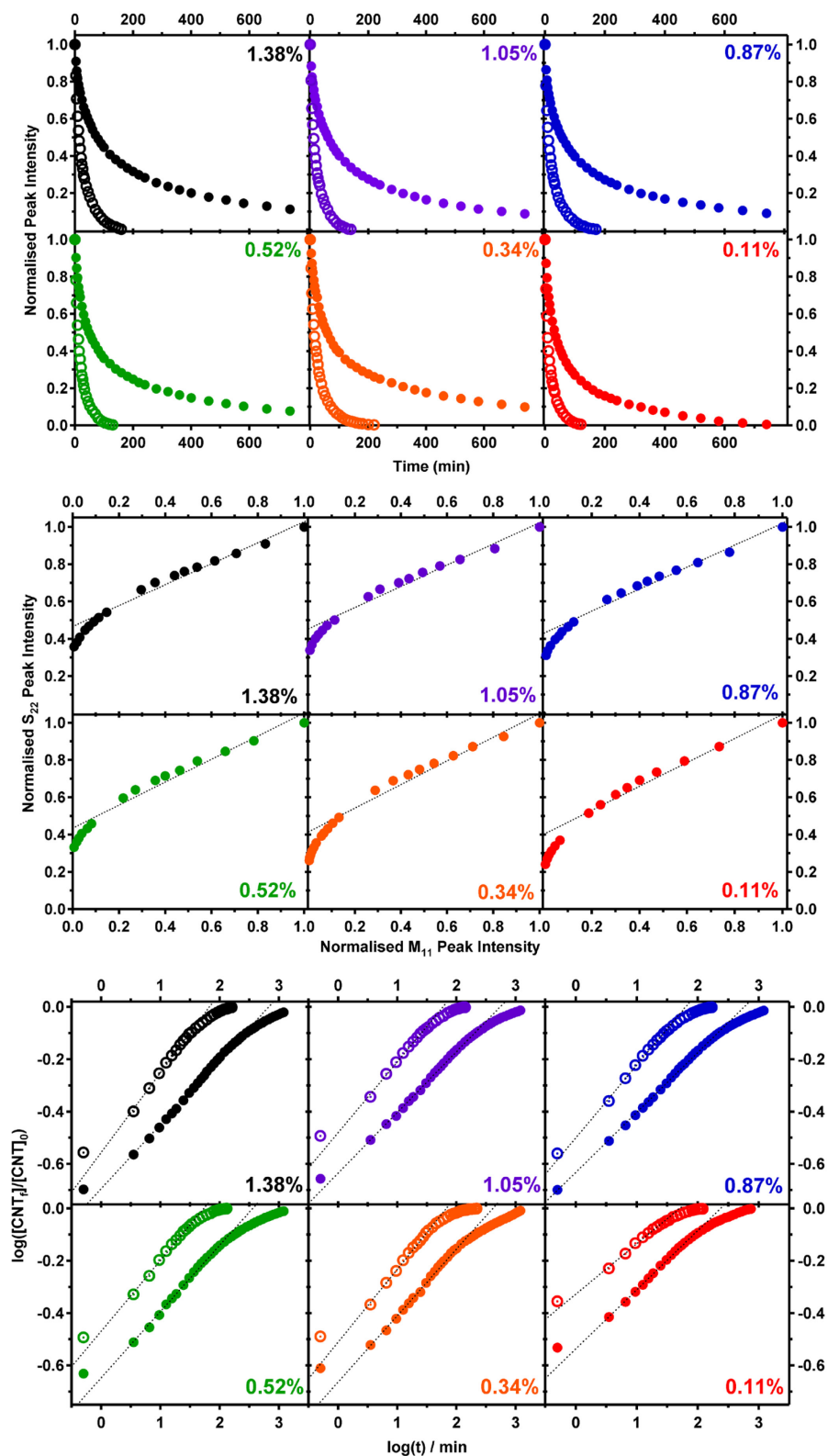


Figure D.6: Kinetic data (top) and selectivity curves (centre) for reaction of 0.5mM NO_2 -BDTFB with CNTs in different concentrations of SDBS at 27°C. The same data with power law fits is presented in the bottom panel. Open and solid circles for top and bottom frames represent the metallic M_{11} and semiconducting S_{22} peaks respectively.

BIBLIOGRAPHY

1. Schnorr, J. M.; Swager, T. M., Emerging Applications of Carbon Nanotubes. *Chem. Mater.* **2011**, *23* (3), 646-657.
2. Hersam, M. C., Progress towards monodisperse single-walled carbon nanotubes. *Nat. Nanotechnol.* **2008**, *3* (7), 387 - 394.
3. Monthieux, M.; Kuznetsov, V. L., Who should be given the credit for the discovery of carbon nanotubes? *Carbon* **2006**, *44* (9), 1621-1623.
4. Iijima, S., Helical microtubules of graphitic carbon. *Nature* **1991**, *354* (6348), 56-58.
5. Radushkevich, L. V.; Lukyanovich, V. M., O Strukture Ugleroda, Obrazujucesja Pri Termiceskom Razlozenii Okisi Ugleroda Na Zeleznom Kontakte. *Journal of Physical Chemistry of Russia* **1952**, *26*, 88-95.
6. Wiles, P. G.; Abrahamson, J., Carbon Fibre Layers on Arc Electrodes I: Their Properties and Cool Down Behaviour. *Carbon* **1978**, *16*, 341-349.
7. Abrahamson, J.; Wiles, P. G.; Rhoades, B. L., Structure of carbon fibres found on carbon arc anodes. *Carbon* **1999**, *37* (11), 1873-1874.
8. Oberlin, A.; Endo, M.; Koyama, T., Filamentous growth of carbon through benzene decomposition. *J. Cryst. Growth* **1976**, *32*, 335-349.
9. Iijima, S.; Ichihashi, T., Single-shell carbon nanotubes of 1-nm diameter. *Nature* **1993**, *363* (6430), 603-605.
10. Bethune, D. S.; Klang, C. H.; de Vries, M. S.; Gorman, G.; Savoy, R.; Vazquez, J.; Beyers, R., Cobalt-catalysed growth of carbon nanotubes with single-atomic-layer walls. *Nature* **1993**, *363* (6430), 605-607.
11. Zhao, X.; Liu, Y.; Inoue, S.; Suzuki, T.; Jones, R. O.; Ando, Y., Smallest Carbon Nanotube Is 3Å in Diameter. *Phys. Rev. Lett.* **2004**, *92* (12), 125502.
12. Smalley, R. E.; Yakobson, B. I., The future of the fullerenes. *Solid State Commun.* **1998**, *107* (11), 597-606.
13. Zheng, L. X.; O'Connell, M. J.; Doorn, S. K.; Liao, X. Z.; Zhao, Y. H.; Akhadow, E. A.; Hoffbauer, M. A.; Roop, B. J.; Jia, Q. X.; Dye, R. C.; Peterson, D. E.;

- Huang, S. M.; Liu, J.; Zhu, Y. T., Ultralong single-wall carbon nanotubes. *Nat. Mater.* **2004**, *3* (10), 673-676.
14. Hamada, N.; Sawada, S.-i.; Oshiyama, A., New one-dimensional conductors: Graphitic microtubules. *Phys. Rev. Lett.* **1992**, *68* (10), 1579.
 15. Strano, M. S., Carbon nanotubes: Sorting out left from right. *Nat. Nanotechnol.* **2007**, *2* (6), 340-341.
 16. Dresselhaus, M. S.; Dresselhaus, G.; Saito, R., Physics of carbon nanotubes. *Carbon* **1995**, *33* (7), 883-891.
 17. Saito, R.; Fujita, M.; Dresselhaus, G.; Dresselhaus, M. S., Electronic structure of chiral graphene tubules. *Appl. Phys. Lett.* **1992**, *60* (18), 2204-2206.
 18. Liu, C.-H.; Zhang, H.-L., Chemical approaches towards single-species single-walled carbon nanotubes. *Nanoscale* **2010**, *2* (10), 1901-1918.
 19. Dresselhaus, M. S.; Dresselhaus, G.; Saito, R.; Jorio, A., Raman spectroscopy of carbon nanotubes. *Phys. Rep.* **2005**, *409* (2), 47-99.
 20. Saito, R.; Dresselhaus, G.; Dresselhaus, M. S., *Physical Properties of Carbon Nanotubes*. Imperial College Press: London, 1998.
 21. Ouyang, M.; Huang, J. L.; Lieber, C. M., Fundamental Electronic Properties and Applications of Single-Walled Carbon Nanotubes. *Acc. Chem. Res.* **2002**, *35* (12), 1018-1025.
 22. Saito, R.; Dresselhaus, G.; Dresselhaus, M. S., Trigonal warping effect of carbon nanotubes. *Phys. Rev. B* **2000**, *61* (4), 2981.
 23. "Electronic Band Structure of a Single-Walled Carbon Nanotube by the Zone-Folding Method" and "Graphene Brillouin Zone and Electronic Energy Dispersion", from the Wolfram Demonstrations Project; contributors: J. Alfonsi; V. Gavryushin: <http://demonstrations.wolfram.com/> (accessed 29-06-2011).
 24. Odom, T. W.; Huang, J. L.; Kim, P.; Lieber, C. M., Structure and Electronic Properties of Carbon Nanotubes. *J. Phys. Chem. B* **2000**, *104* (13), 2794-2809.
 25. Avouris, P., Carbon nanotube electronics. *Chem. Phys.* **2002**, *281* (2-3), 429-445.
 26. An, K. H.; Lee, Y. H., Electronic-Structure Engineering of Carbon Nanotubes. *NANO: Brief Reports and Reviews* **2006**, *1* (2), 115-138.
 27. Dresselhaus, M. S.; Dresselhaus, G.; Jorio, A., Unusual Properties and Structure of Carbon Nanotubes. *Ann. Rev. Mater. Res.* **2004**, *34* (1), 247-278.
 28. Blase, X.; Benedict, L. X.; Shirley, E. L.; Louie, S. G., Hybridization effects and metallicity in small radius carbon nanotubes. *Phys. Rev. Lett.* **1994**, *72* (12), 1878.
 29. Ouyang, M.; Huang, J.-L.; Cheung, C. L.; Lieber, C. M., Energy Gaps in "Metallic" Single-Walled Carbon Nanotubes. *Science* **2001**, *292* (5517), 702-705.
 30. White, C. T.; Mintmire, J. W., Fundamental Properties of Single-Wall Carbon Nanotubes. *J. Phys. Chem. B* **2005**, *109* (1), 52-65.
 31. Carlson, L. J.; Krauss, T. D., Photophysics of Individual Single-Walled Carbon Nanotubes. *Acc. Chem. Res.* **2008**, *41* (2), 235-243.
 32. Maruyama, S. Resonant Raman (Kataura plot and 1D electronic DOS of carbon nanotubes). <http://www.photon.t.u-tokyo.ac.jp/~maruyama/kataura/kataura.html> (accessed 20/10/2011).
 33. White, C. T.; Mintmire, J. W., Density of states reflects diameter in nanotubes. *Nature* **1998**, *394* (6688), 29-30.
 34. Charlier, J. C.; Lambin, P., Electronic structure of carbon nanotubes with chiral symmetry. *Phys. Rev. B* **1998**, *57* (24), R15037.
 35. Hagen, A.; Hertel, T., Quantitative Analysis of Optical Spectra from Individual Single-Wall Carbon Nanotubes. *Nano Lett.* **2003**, *3* (3), 383-388.

36. Kataura, H.; Kumazawa, Y.; Maniwa, Y.; Umez, I.; Suzuki, S.; Ohtsuka, Y.; Achiba, Y., Optical properties of single-wall carbon nanotubes. *Synthetic Met.* **1999**, *103* (1-3), 2555-2558.
37. Bachilo, S. M.; Strano, M. S.; Kittrell, C.; Hauge, R. H.; Smalley, R. E.; Weisman, R. B., Structure-Assigned Optical Spectra of Single-Walled Carbon Nanotubes. *Science* **2002**, *298* (5602), 2361-2366.
38. O'Connell, M. J.; Bachilo, S. M.; Huffman, C. B.; Moore, V. C.; Strano, M. S.; Haroz, E. H.; Rialon, K. L.; Boul, P. J.; Noon, W. H.; Kittrell, C.; Ma, J.; Hauge, R. H.; Weisman, R. B.; Smalley, R. E., Band Gap Fluorescence from Individual Single-Walled Carbon Nanotubes. *Science* **2002**, *297* (5581), 593-596.
39. Weisman, R. B.; Bachilo, S. M., Dependence of Optical Transition Energies on Structure for Single-Walled Carbon Nanotubes in Aqueous Suspension: An Empirical Kataura Plot. *Nano Lett.* **2003**, *3* (9), 1235-1238.
40. Kane, C. L.; Mele, E. J., Ratio Problem in Single Carbon Nanotube Fluorescence Spectroscopy. *Phys. Rev. Lett.* **2003**, *90* (20), 207401.
41. Wang, F.; Dukovic, G.; Brus, L. E.; Heinz, T. F., The Optical Resonances in Carbon Nanotubes Arise from Excitons. *Science* **2005**, *308* (5723), 838-841.
42. Ando, T., Excitons in carbon nanotubes. *J. Phys. Soc. Jap.* **1997**, *66* (4), 1066-1073.
43. Perebeinos, V.; Tersoff, J.; Avouris, P., Scaling of Excitons in Carbon Nanotubes. *Phys. Rev. Lett.* **2004**, *92* (25), 257402.
44. Spataru, C. D.; Ismail-Beigi, S.; Benedict, L. X.; Louie, S. G., Excitonic Effects and Optical Spectra of Single-Walled Carbon Nanotubes. *Phys. Rev. Lett.* **2004**, *92* (7), 077402.
45. Zhao, H.; Mazumdar, S., Electron-Electron Interaction Effects on the Optical Excitations of Semiconducting Single-Walled Carbon Nanotubes. *Phys. Rev. Lett.* **2004**, *93* (15), 157402.
46. Ma, Y.-Z.; Valkunas, L.; Bachilo, S. M.; Fleming, G. R., Exciton Binding Energy in Semiconducting Single-Walled Carbon Nanotubes. *J. Phys. Chem. B* **2005**, *109* (33), 15671-15674.
47. Maultzsch, J.; Pomraenke, R.; Reich, S.; Chang, E.; Prezzi, D.; Ruini, A.; Molinari, E.; Strano, M. S.; Thomsen, C.; Lienau, C., Exciton binding energies in carbon nanotubes from two-photon photoluminescence. *Phys. Rev. B* **2005**, *72* (24), 241402.
48. Dresselhaus, M. S.; Dresselhaus, G.; Saito, R.; Jorio, A., Exciton Photophysics of Carbon Nanotubes. *Annu. Rev. Phys. Chem.* **2007**, *58* (1), 719-747.
49. Wang, F.; Cho, D. J.; Kessler, B.; Deslippe, J.; Schuck, P. J.; Louie, S. G.; Zettl, A.; Heinz, T. F.; Shen, Y. R., Observation of Excitons in One-Dimensional Metallic Single-Walled Carbon Nanotubes. *Phys. Rev. Lett.* **2007**, *99* (22), 227401-4.
50. Samsonidze, G. G.; Saito, R.; Kobayashi, N.; Gruneis, A.; Jiang, J.; Jorio, A.; Chou, S. G.; Dresselhaus, G.; Dresselhaus, M. S., Family behavior of the optical transition energies in single-wall carbon nanotubes of smaller diameters. *Appl. Phys. Lett.* **2004**, *85* (23), 5703-5705.
51. Avouris, P.; Freitag, M.; Perebeinos, V., Carbon-nanotube photonics and optoelectronics. *Nat. Photon.* **2008**, *2* (6), 341-350.
52. Lüer, L.; Hoseinkhani, S.; Polli, D.; Crochet, J.; Hertel, T.; Lanzani, G., Size and mobility of excitons in (6, 5) carbon nanotubes. *Nat. Phys.* **2009**, *5* (1), 54-58.

53. Cagnet, L.; Tsyboulski, D. A.; Rocha, J.-D. R.; Doyle, C. D.; Tour, J. M.; Weisman, R. B., Stepwise Quenching of Exciton Fluorescence in Carbon Nanotubes by Single-Molecule Reactions. *Science* **2007**, *316* (5830), 1465-1468.
54. Liu, T.; Xiao, Z., Exact and Closed Form Solutions for the Quantum Yield, Exciton Diffusion Length, and Lifetime to Reveal the Universal Behaviors of the Photoluminescence of Defective Single-Walled Carbon Nanotubes. *J. Phys. Chem. C* **2011**, *115* (34), 16920-16927.
55. Siitonen, A. J.; Tsyboulski, D. A.; Bachilo, S. M.; Weisman, R. B., Dependence of Exciton Mobility on Structure in Single-Walled Carbon Nanotubes. *J. Phys. Chem. Lett.* **2010**, *1* (14), 2189-2192.
56. Haddon, R. C., Chemistry of the Fullerenes: The Manifestation of Strain in a Class of Continuous Aromatic Molecules. *Science* **1993**, *261* (5128), 1545-1550.
57. Niyogi, S.; Hamon, M. A.; Hu, H.; Zhao, B.; Bhowmik, P.; Sen, R.; Itkis, M. E.; Haddon, R. C., Chemistry of Single-Walled Carbon Nanotubes. *Acc. Chem. Res.* **2002**, *35* (12), 1105-1113.
58. Haddon, R. C.; Scuseria, G. E.; Smalley, R. E., C240 - The most chemically inert fullerene? *Chem. Phys. Lett.* **1997**, *272* (1-2), 38-42.
59. Ebbesen, T. W.; Ajayan, P. M., Large-scale synthesis of carbon nanotubes. *Nature* **1992**, *358* (6383), 220-222.
60. Journet, C.; Maser, W. K.; Bernier, P.; Loiseau, A.; de la Chapelle, M. L.; Lefrant, S.; Deniard, P.; Lee, R.; Fischer, J. E., Large-scale production of single-walled carbon nanotubes by the electric-arc technique. *Nature* **1997**, *388* (6644), 756-758.
61. Guo, T.; Nikolaev, P.; Thess, A.; Colbert, D. T.; Smalley, R. E., Catalytic growth of single-walled nanotubes by laser vaporization. *Chem. Phys. Lett.* **1995**, *243* (1-2), 49-54.
62. Thess, A.; Lee, R.; Nikolaev, P.; Dai, H.; Petit, P.; Robert, J.; Xu, C.; Lee, Y. H.; Kim, S. G.; Rinzler, A. G.; Colbert, D. T.; Scuseria, G. E.; Tomanek, D.; Fischer, J. E.; Smalley, R. E., Crystalline Ropes of Metallic Carbon Nanotubes. *Science* **1996**, *273* (5274), 483-487.
63. Cassell, A. M.; Raymakers, J. A.; Kong, J.; Dai, H., Large Scale CVD Synthesis of Single-Walled Carbon Nanotubes. *J. Phys. Chem. B* **1999**, *103* (31), 6484-6492.
64. Endo, M.; Takeuchi, K.; Igarashi, S.; Kobori, K.; Shiraishi, M.; Kroto, H. W., The production and structure of pyrolytic carbon nanotubes (PCNTs). *J. Phys. Chem. Solids* **1993**, *54* (12), 1841-1848.
65. Dai, H.; Rinzler, A. G.; Nikolaev, P.; Thess, A.; Colbert, D. T.; Smalley, R. E., Single-wall nanotubes produced by metal-catalyzed disproportionation of carbon monoxide. *Chemical Physics Letters* **1996**, *260* (3-4), 471-475.
66. Jose-Yacaman, M.; Miki-Yoshida, M.; Rendon, L.; Santiesteban, J. G., Catalytic growth of carbon microtubules with fullerene structure. *Appl. Phys. Lett.* **1993**, *62* (2), 202-204.
67. Journet, C.; Bernier, P., Production of carbon nanotubes. *Appl. Phys. A-Mater.* **1998**, *67* (1), 1-9.
68. Nessim, G. D., Properties, synthesis, and growth mechanisms of carbon nanotubes with special focus on thermal chemical vapor deposition. *Nanoscale* **2010**, *2* (8), 1306-1323.
69. Terranova, M. L.; Sessa, V.; Rossi, M., The World of Carbon Nanotubes: An Overview of CVD Growth Methodologies. *Chem. Vapor Depos.* **2006**, *12*, 315-325.

70. Wang, J.-T.; Chen, C.; Ohno, K.; Wang, E.; Chen, X.-L.; Wang, D.-S.; Mizuseki, H.; Kawazoe, Y., Atomistic nucleation and growth mechanism for single-wall carbon nanotubes on catalytic nanoparticle surfaces. *Nanotechnology* **2010**, *21* (11), 115602.
71. Dai, H., Carbon nanotubes: opportunities and challenges. *Surf. Sci.* **2002**, *500*, 218–241.
72. Joselevich, E.; Dai, H.; Liu, J.; Hata, K.; Windle, A., Carbon Nanotube Synthesis and Organization. In *Carbon Nanotubes*, Springer Berlin / Heidelberg: 2008; Vol. 111, pp 101-164.
73. Hou, P.-X.; Liu, C.; Cheng, H.-M., Purification of carbon nanotubes. *Carbon* **2008**, *46* (15), 2003-2025.
74. Nikolaev, P.; Bronikowski, M. J.; Bradley, R. K.; Rohmund, F.; Colbert, D. T.; Smith, K. A.; Smalley, R. E., Gas-phase catalytic growth of single-walled carbon nanotubes from carbon monoxide. *Chem. Phys. Lett.* **1999**, *313* (1-2), 91-97.
75. Duque, J. G.; Parra-Vasquez, A. N. G.; Behabtu, N.; Green, M. J.; Higginbotham, A. L.; Price, B. K.; Leonard, A. D.; Schmidt, H. K.; Lounis, B.; Tour, J. M.; Doorn, S. K.; Cognet, L.; Pasquali, M., Diameter-Dependent Solubility of Single-Walled Carbon Nanotubes. *ACS Nano* **2010**, *4* (6), 3063-3072.
76. Kitiyanan, B.; Alvarez, W. E.; Harwell, J. H.; Resasco, D. E., Controlled production of single-wall carbon nanotubes by catalytic decomposition of CO on bimetallic Co-Mo catalysts. *Chem. Phys. Lett.* **2000**, *317* (3-5), 497-503.
77. Lolli, G.; Zhang, L.; Balzano, L.; Sakulchaicharn, N.; Tan, Y.; Resasco, D. E., Tailoring (n,m) Structure of Single-Walled Carbon Nanotubes by Modifying Reaction Conditions and the Nature of the Support of CoMo Catalysts. *J. Phys. Chem. B* **2006**, *110* (5), 2108-2115.
78. Li, Y.; Mann, D.; Rolandi, M.; Kim, W.; Ural, A.; Hung, S.; Javey, A.; Cao, J.; Wang, D.; Yenilmez, E.; Wang, Q.; Gibbons, J. F.; Nishi, Y.; Dai, H., Preferential Growth of Semiconducting Single-Walled Carbon Nanotubes by a Plasma Enhanced CVD Method. *Nano Lett.* **2004**, *4* (2), 317-321.
79. Qu, L.; Du, F.; Dai, L., Preferential Syntheses of Semiconducting Vertically Aligned Single-Walled Carbon Nanotubes for Direct Use in FETs. *Nano Lett.* **2008**, *8* (9), 2682-2687.
80. Liu, Q.; Ren, W.; Chen, Z.-G.; Wang, D.-W.; Liu, B.; Yu, B.; Li, F.; Cong, H.; Cheng, H.-M., Diameter-Selective Growth of Single-Walled Carbon Nanotubes with High Quality by Floating Catalyst Method. *ACS Nano* **2008**, *2* (8), 1722-1728.
81. Hata, K.; Futaba, D. N.; Mizuno, K.; Namai, T.; Yumura, M.; Iijima, S., Water-Assisted Highly Efficient Synthesis of Impurity-Free Single-Walled Carbon Nanotubes. *Science* **2004**, *306* (5700), 1362-1364.
82. Park, T.-J.; Banerjee, S.; Hemraj-Benny, T.; Wong, S. S., Purification strategies and purity visualization techniques for single-walled carbon nanotubes. *J. Mater. Chem.* **2006**, *16* (2), 141-154.
83. Pumera, M., Carbon Nanotubes Contain Residual Metal Catalyst Nanoparticles even after Washing with Nitric Acid at Elevated Temperature Because These Metal Nanoparticles Are Sheathed by Several Graphene Sheets. *Langmuir* **2007**, *23* (11), 6453-6458.
84. Monthieux, M.; Smith, B. W.; Burtiaux, B.; Claye, A.; Fischer, J. E.; Luzzi, D. E., Sensitivity of single-wall carbon nanotubes to chemical processing: an electron microscopy investigation. *Carbon* **2001**, *39* (8), 1251-1272.

85. Rinzler, A. G.; Liu, J.; Dai, H.; Nikolaev, P.; Huffman, C. B.; Rodríguez-Macías, F. J.; Boul, P. J.; Lu, A. H.; Heymann, D.; Colbert, D. T.; Lee, R. S.; Fischer, J. E.; Rao, A. M.; Eklund, P. C.; Smalley, R. E., Large-scale purification of single-wall carbon nanotubes: process, product, and characterization. *Appl. Phys. A-Mater.* **1998**, *67* (1), 29-37.
86. Dillon, A. C.; Gennett, T.; Jones, K. M.; Alleman, J. L.; Parilla, P. A.; Heben, M. J., A Simple and Complete Purification of Single-Walled Carbon Nanotube Materials. *Adv. Mater.* **1999**, *11* (16), 1354-1358.
87. Hu, H.; Zhao, B.; Itkis, M. E.; Haddon, R. C., Nitric Acid Purification of Single-Walled Carbon Nanotubes. *J. Phys. Chem. B* **2003**, *107* (50), 13838-13842.
88. Chiang, I. W.; Brinson, B. E.; Smalley, R. E.; Margrave, J. L.; Hauge, R. H., Purification and Characterization of Single-Wall Carbon Nanotubes. *J. Phys. Chem. B* **2001**, *105* (6), 1157-1161.
89. Landi, B. J.; Ruf, H. J.; Evans, C. M.; Cress, C. D.; Raffaele, R. P., Purity Assessment of Single-Wall Carbon Nanotubes, Using Optical Absorption Spectroscopy. *J. Phys. Chem. B* **2005**, *109* (20), 9952-9965.
90. Arepalli, S.; Nikolaev, P.; Gorelik, O.; Hadjiev, V. G.; Holmes, W.; Files, B.; Yowell, L., Protocol for the characterization of single-wall carbon nanotube material quality. *Carbon* **2004**, *42* (8-9), 1783-1791.
91. Tchoul, M. N.; Ford, W. T.; Lolli, G.; Resasco, D. E.; Arepalli, S., Effect of Mild Nitric Acid Oxidation on Dispersability, Size, and Structure of Single-Walled Carbon Nanotubes. *Chem. Mater.* **2007**, *19* (23), 5765-5772.
92. Kim, Y.; Luzzi, D. E., Purification of Pulsed Laser Synthesized Single Wall Carbon Nanotubes by Magnetic Filtration. *J. Phys. Chem. B* **2005**, *109* (35), 16636-16643.
93. Wiltshire, J. G.; Li, L. J.; Khlobystov, A. N.; Padbury, C. J.; Briggs, G. A. D.; Nicholas, R. J., Magnetic separation of Fe catalyst from single-walled carbon nanotubes in an aqueous surfactant solution. *Carbon* **2005**, *43* (6), 1151-1155.
94. Bonard, J.-M.; Stora, T.; Salvétat, J.-P.; Maier, F.; Stöckli, T.; Duschl, C.; Forró, L.; Heer, W. A. d.; Châtelain, A., Purification and size-selection of carbon nanotubes. *Adv. Mater.* **1997**, *9* (10), 827-831.
95. Nepal, D.; Kim, D. S.; Geckeler, K. E., A facile and rapid purification method for single-walled carbon nanotubes. *Carbon* **2005**, *43* (3), 660-662.
96. Ryabenko, A. G.; Dorofeeva, T. V.; Zvereva, G. I., UV-Vis-NIR spectroscopy study of sensitivity of single-wall carbon nanotubes to chemical processing and Van-der-Waals SWNT/SWNT interaction. Verification of the SWNT content measurements by absorption spectroscopy. *Carbon* **2004**, *42* (8-9), 1523-1535.
97. Vichchulada, P.; Shim, J.; Lay, M. D., Non-oxidizing Purification Method for Large Volumes of Long, Undamaged Single-Walled Carbon Nanotubes. *J. Phys. Chem. C* **2008**, *112* (49), 19186-19192.
98. Ansón-Casaos, A.; González-Domínguez, J. M.; Martínez, M. T., Separation of single-walled carbon nanotubes from graphite by centrifugation in a surfactant or in polymer solutions. *Carbon* **2010**, *48* (10), 2917-2924.
99. Ansón-Casaos, A.; Gonzalez, M.; Gonzalez-Dominguez, J. M.; Martinez, M. T., Influence of Air Oxidation on the Surfactant-Assisted Purification of Single-Walled Carbon Nanotubes. *Langmuir* **2011**, *27* (11), 7192-7198.
100. Hu, H.; Yu, A.; Kim, E.; Zhao, B.; Itkis, M. E.; Bekyarova, E.; Haddon, R. C., Influence of the Zeta Potential on the Dispersability and Purification of Single-Walled Carbon Nanotubes. *J. Phys. Chem. B* **2005**, *109* (23), 11520-11524.

101. Yu, A.; Bekyarova, E.; Itkis, M. E.; Fakhrutdinov, D.; Webster, R.; Haddon, R. C., Application of Centrifugation to the Large-Scale Purification of Electric Arc-Produced Single-Walled Carbon Nanotubes. *J. Am. Chem. Soc.* **2006**, *128* (30), 9902-9908.
102. Shelimov, K. B.; Esenaliev, R. O.; Rinzler, A. G.; Huffman, C. B.; Smalley, R. E., Purification of single-wall carbon nanotubes by ultrasonically assisted filtration. *Chem. Phys. Lett.* **1998**, *282* (5-6), 429-434.
103. Girifalco, L. A.; Hodak, M.; Lee, R. S., Carbon nanotubes, buckyballs, ropes, and a universal graphitic potential. *Phys. Rev. B* **2000**, *62* (19), 13104.
104. Cheng, Q.; Debnath, S.; Gregan, E.; Byrne, H. J., Ultrasound-Assisted SWNTs Dispersion: Effects of Sonication Parameters and Solvent Properties. *J. Phys. Chem. C* **2010**, *114* (19), 8821-8827.
105. Ausman, K. D.; Piner, R.; Lourie, O.; Ruoff, R. S.; Korobov, M., Organic Solvent Dispersions of Single-Walled Carbon Nanotubes: Toward Solutions of Pristine Nanotubes. *J. Phys. Chem. B* **2000**, *104* (38), 8911-8915.
106. Landi, B. J.; Ruf, H. J.; Worman, J. J.; Raffaele, R. P., Effects of Alkyl Amide Solvents on the Dispersion of Single-Wall Carbon Nanotubes. *J. Phys. Chem. B* **2004**, *108* (44), 17089-17095.
107. Bahr, J. L.; Mickelson, E. T.; Bronikowski, M. J.; Smalley, R. E.; Tour, J. M., Dissolution of small diameter single-wall carbon nanotubes in organic solvents? *Chem. Commun.* **2001**, (2), 193-194.
108. Giordani, S.; Bergin, S. D.; Nicolosi, V.; Lebedkin, S.; Kappes, M. M.; Blau, W. J.; Coleman, J. N., Debundling of Single-Walled Nanotubes by Dilution: Observation of Large Populations of Individual Nanotubes in Amide Solvent Dispersions. *J. Phys. Chem. B* **2006**, *110* (32), 15708-15718.
109. Bergin, S. D.; Sun, Z.; Streich, P.; Hamilton, J.; Coleman, J. N., New Solvents for Nanotubes: Approaching the Dispersibility of Surfactants. *J. Phys. Chem. C* **2010**, *114* (1), 231-237.
110. Itzhak, R.; Raichman, D.; Shahar, Z.; Frey, G. L.; Frey, J.; Yerushalmi-Rozen, R., Tailoring Triblock Copolymers for Dispersion of Individual, Pristine, Single-Walled Carbon Nanotubes in Organic Solvents. *J. Phys. Chem. C* **2010**, *114* (9), 3748-3753.
111. Hasan, T.; Tan, P. H.; Bonaccorso, F.; Rozhin, A. G.; Scardaci, V.; Milne, W. I.; Ferrari, A. C., Polymer-Assisted Isolation of Single Wall Carbon Nanotubes in Organic Solvents for Optical-Quality Nanotube Polymer Composites. *J. Phys. Chem. C* **2008**, *112* (51), 20227-20232.
112. Vaisman, L.; Wagner, H. D.; Marom, G., The role of surfactants in dispersion of carbon nanotubes. *Adv. Colloid Interfac.* **2006**, *128-130*, 37-46.
113. Kharisov, B. I.; Kharissova, O. V.; Leija Gutierrez, H.; Ortiz Mendez, U., Recent Advances on the Soluble Carbon Nanotubes. *Ind. Eng. Chem. Res.* **2009**, *48* (2), 572-590.
114. Wang, H., Dispersing carbon nanotubes using surfactants. *Curr. Opin. Colloid In.* **2009**, *14* (5), 364-371.
115. Shin, J.-Y.; Premkumar, T.; Geckeler, Kurt E., Dispersion of Single-Walled Carbon Nanotubes by Using Surfactants: Are the Type and Concentration Important? *Chem. Eur. J.* **2008**, *14* (20), 6044-6048.
116. Haggemueller, R.; Rahatekar, S. S.; Fagan, J. A.; Chun, J.; Becker, M. L.; Naik, R. R.; Krauss, T.; Carlson, L.; Kadla, J.; Trulove, P.; Fox, D.; DeLong, H.; Fang, Z.; Kelley, S. O.; Gilman, J. W., Comparison of the Quality of Aqueous

- Dispersions of Single Wall Carbon Nanotubes Using Surfactants and Biomolecules. *Langmuir* **2008**, *24* (9), 5070-5078.
117. White, B.; Banerjee, S.; O'Brien, S.; Turro, N. J.; Herman, I. P., Zeta-Potential Measurements of Surfactant-Wrapped Individual Single-Walled Carbon Nanotubes. *J. Phys. Chem. C* **2007**, *111* (37), 13684-13690.
 118. Sun, Z.; Nicolosi, V.; Rickard, D.; Bergin, S. D.; Aherne, D.; Coleman, J. N., Quantitative Evaluation of Surfactant-stabilized Single-walled Carbon Nanotubes: Dispersion Quality and Its Correlation with Zeta Potential. *J. Phys. Chem. C* **2008**, *112* (29), 10692-10699.
 119. Ishibashi, A.; Nakashima, N., Individual Dissolution of Single-Walled Carbon Nanotubes in Aqueous Solutions of Steroid or Sugar Compounds and Their Raman and Near-IR Spectral Properties. *Chem. Eur. J.* **2006**, *12* (29), 7595-7602.
 120. Wenseleers, W.; Vlasov, I. I.; Goovaerts, E.; Obratsova, E. D.; Lobach, A. S.; Bouwen, A., Efficient Isolation and Solubilization of Pristine Single-Walled Nanotubes in Bile Salt Micelles. *Adv. Funct. Mater.* **2004**, *14* (11), 1105-1112.
 121. Moore, V. C.; Strano, M. S.; Haroz, E. H.; Hauge, R. H.; Smalley, R. E.; Schmidt, J.; Talmon, Y., Individually Suspended Single-Walled Carbon Nanotubes in Various Surfactants. *Nano Lett.* **2003**, *3* (10), 1379-1382.
 122. Islam, M. F.; Rojas, E.; Bergey, D. M.; Johnson, A. T.; Yodh, A. G., High Weight Fraction Surfactant Solubilization of Single-Wall Carbon Nanotubes in Water. *Nano Lett.* **2003**, *3* (2), 269-273.
 123. Rastogi, R.; Kaushal, R.; Tripathi, S. K.; Sharma, A. L.; Kaur, I.; Bharadwaj, L. M., Comparative study of carbon nanotube dispersion using surfactants. *J. Colloid Interface Sci.* **2008**, *328* (2), 421-428.
 124. Sinani, V. A.; Gheith, M. K.; Yaroslavov, A. A.; Rakhnyanskaya, A. A.; Sun, K.; Mamedov, A. A.; Wicksted, J. P.; Kotov, N. A., Aqueous Dispersions of Single-wall and Multiwall Carbon Nanotubes with Designed Amphiphilic Polycations. *J. Am. Chem. Soc.* **2005**, *127* (10), 3463-3472.
 125. Nish, A.; Hwang, J.-Y.; Doig, J.; Nicholas, R. J., Highly selective dispersion of single-walled carbon nanotubes using aromatic polymers. *Nat. Nanotechnol.* **2007**, *2* (10), 640-646.
 126. Xin, X.; Xu, G.; Zhao, T.; Zhu, Y.; Shi, X.; Gong, H.; Zhang, Z., Dispersing Carbon Nanotubes in Aqueous Solutions by a Starlike Block Copolymer. *J. Phys. Chem. C* **2008**, *112* (42), 16377-16384.
 127. Gong, H.; Xu, G.; Liu, T.; Pang, J.; Dou, W.; Xin, X., Synthesis of block polyethers with various structures and their application in dispersing single-walled carbon nanotubes. *Colloid Polym. Sci.* **2011**, *289* (8), 933-942.
 128. Di Meo, E. M.; Di Crescenzo, A.; Velluto, D.; O'Neil, C. P.; Demurtas, D.; Hubbell, J. A.; Fontana, A., Assessing the Role of Poly(ethylene glycol-bl-propylene sulfide) (PEG-PPS) Block Copolymers in the Preparation of Carbon Nanotube Biocompatible Dispersions. *Macromolecules* **2010**, *43* (7), 3429-3437.
 129. Fujigaya, T.; Nakashima, N., Methodology for Homogeneous Dispersion of Single-walled Carbon Nanotubes by Physical Modification. *Polym. J.* **2008**, *40* (7), 577-589.
 130. Backes, C.; Schmidt, C. D.; Rosenlehner, K.; Hauke, F.; Coleman, J. N.; Hirsch, A., Nanotube Surfactant Design: The Versatility of Water-Soluble Perylene Bisimides. *Adv. Mater.* **2010**, *22* (7), 788-802.
 131. Zheng, M.; Jagota, A.; Semke, E. D.; Diner, B. A.; McLean, R. S.; Lustig, S. R.; Richardson, R. E.; Tassi, N. G., DNA-assisted dispersion and separation of carbon nanotubes. *Nat. Mater.* **2003**, *2* (5), 338-342.

132. Edri, E.; Regev, O., "Shaken, Not Stable": Dispersion Mechanism and Dynamics of Protein-Dispersed Nanotubes Studied via Spectroscopy. *Langmuir* **2009**, *25* (18), 10459-10465.
133. Liu, Y.; Gao, L.; Zheng, S.; Wang, Y.; Sun, J.; Kajiura, H.; Li, Y.; Noda, K., Debundling of single-walled carbon nanotubes by using natural polyelectrolytes. *Nanotechnology* **2007**, *18* (36), 365702.
134. Alpatova, A. L.; Shan, W.; Babica, P.; Upham, B. L.; Rogensues, A. R.; Masten, S. J.; Drown, E.; Mohanty, A. K.; Alocilja, E. C.; Tarabara, V. V., Single-walled carbon nanotubes dispersed in aqueous media via non-covalent functionalization: Effect of dispersant on the stability, cytotoxicity, and epigenetic toxicity of nanotube suspensions. *Water Res.* **2010**, *44* (2), 505-520.
135. Dror, Y.; Pyckhout-Hintzen, W.; Cohen, Y., Conformation of Polymers Dispersing Single-Walled Carbon Nanotubes in Water: A Small-Angle Neutron Scattering Study. *Macromolecules* **2005**, *38* (18), 7828-7836.
136. Strano, M. S.; Moore, V. C.; Miller, M. K.; Allen, M. J.; Haroz, E. H.; Kittrell, C.; Hauge, R. H.; Smalley, R. E., The Role of Surfactant Adsorption during Ultrasonication in the Dispersion of Single-Walled Carbon Nanotubes. *J. Nanosci. Nanotechnol.* **2003**, *3* (1/2), 81-86.
137. Heller, D. A.; Mayrhofer, R. M.; Baik, S.; Grinkova, Y. V.; Usrey, M. L.; Strano, M. S., Concomitant Length and Diameter Separation of Single-Walled Carbon Nanotubes. *J. Am. Chem. Soc.* **2004**, *126* (44), 14567-14573.
138. Hennrich, F.; Krupke, R.; Arnold, K.; RojasStutz, J. A.; Lebedkin, S.; Koch, T.; Schimmel, T.; Kappes, M. M., The Mechanism of Cavitation-Induced Scission of Single-Walled Carbon Nanotubes. *J. Phys. Chem. B* **2007**, *111* (8), 1932-1937.
139. Lucas, A.; Zakri, C.; Maugey, M.; Pasquali, M.; Schoot, P. v. d.; Poulin, P., Kinetics of Nanotube and Microfiber Scission Under Sonication. *J. Phys. Chem. C* **2009**, *113* (48), 20599-20605.
140. Vichchulada, P.; Cauble, M. A.; Abdi, E. A.; Obi, E. I.; Zhang, Q.; Lay, M. D., Sonication Power for Length Control of Single-Walled Carbon Nanotubes in Aqueous Suspensions Used for 2-Dimensional Network Formation. *J. Phys. Chem. C* **2010**, *114* (29), 12490-12495.
141. Lu, K. L.; Lago, R. M.; Chen, Y. K.; Green, M. L. H.; Harris, P. J. F.; Tsang, S. C., Mechanical damage of carbon nanotubes by ultrasound. *Carbon* **1996**, *34* (6), 814-816.
142. Niyogi, S.; Hamon, M. A.; Perea, D. E.; Kang, C. B.; Zhao, B.; Pal, S. K.; Wyant, A. E.; Itkis, M. E.; Haddon, R. C., Ultrasonic Dispersions of Single-Walled Carbon Nanotubes. *J. Phys. Chem. B* **2003**, *107* (34), 8799-8804.
143. Moonosawmy, K. R.; Kruse, P., Cause and Consequence of Carbon Nanotube Doping in Water and Aqueous Media. *J. Am. Chem. Soc.* **2010**, *132* (5), 1572-1577.
144. Banerjee, S.; Hemraj-Benny, T.; Wong, S. S., Routes Towards Separating Metallic and Semiconducting Nanotubes. *J. Nanosci. Nanotechnol.* **2005**, *5* (6), 841-855.
145. Krupke, R.; Hennrich, F., Separation Techniques for Carbon Nanotubes. *Adv. Eng. Mater.* **2005**, *7* (3), 111-116.
146. Rao, C. N. R.; Voggu, R.; Govindaraj, A., Selective generation of single-walled carbon nanotubes with metallic, semiconducting and other unique electronic properties. *Nanoscale* **2009**, *1* (1), 96-105.
147. Bonaccorso, F., Debundling and Selective Enrichment of SWNTs for Applications in Dye-Sensitized Solar Cells. *Int. J. Photoenergy* **2010**, 14.

148. Zhang, Y.; Zheng, L., Towards chirality-pure carbon nanotubes. *Nanoscale* **2010**, 2 (10), 1919-1929.
149. Lu, F.; Meziani, M. J.; Cao, L.; Sun, Y.-P., Separated Metallic and Semiconducting Single-Walled Carbon Nanotubes: Opportunities in Transparent Electrodes and Beyond. *Langmuir* **2011**, 27 (8), 4339-4350.
150. Zhang, H.; Wu, B.; Hu, W.; Liu, Y., Separation and/or selective enrichment of single-walled carbon nanotubes based on their electronic properties. *Chem. Soc. Rev.* **2011**, 40 (3), 1324-1336.
151. Fagan, J. A.; Bauer, B. J.; Hobbie, E. K.; Becker, M. L.; Hight Walker, A. R.; Simpson, J. R.; Chun, J.; Obrzut, J.; Bajpai, V.; Phelan, F. R.; Simien, D.; Huh, J. Y.; Migler, K. B., Carbon Nanotubes: Measuring Dispersion and Length. *Adv. Mater.* **2011**, 23, 338-348.
152. Collins, P. G.; Arnold, M. S.; Avouris, P., Engineering Carbon Nanotubes and Nanotube Circuits Using Electrical Breakdown. *Science* **2001**, 292 (5517), 706-709.
153. Wei, D.; Liu, Y.; Cao, L.; Zhang, H.; Huang, L.; Yu, G.; Kajiura, H.; Li, Y., Selective Electrochemical Etching of Single-Walled Carbon Nanotubes. *Adv. Funct. Mater.* **2009**, 19 (22), 3618-3624.
154. Hassanien, A.; Tokumoto, M.; Umek, P.; Vrbanic, D.; Mozetic, M.; Mihailovic, D.; Venturini, P.; Pejovnik, S., Selective etching of metallic single-wall carbon nanotubes with hydrogen plasma. *Nanotechnology* **2005**, 16 (2), 278-281.
155. Zhang, G.; Qi, P.; Wang, X.; Lu, Y.; Li, X.; Tu, R.; Bangsaruntip, S.; Mann, D.; Zhang, L.; Dai, H., Selective Etching of Metallic Carbon Nanotubes by Gas-Phase Reaction. *Science* **2006**, 314 (5801), 974-977.
156. Yang, C.-M.; An, K. H.; Park, J. S.; Park, K. A.; Lim, S. C.; Cho, S.-H.; Lee, Y. S.; Park, W.; Park, C. Y.; Lee, Y. H., Preferential etching of metallic single-walled carbon nanotubes with small diameter by fluorine gas. *Phys. Rev. B* **2006**, 73 (7), 075419-7.
157. An, K. H.; Yang, C.-M.; Lee, J. Y.; Lim, S. C.; Kang, C.; Son, J.-H.; Jeong, M. S.; Lee, Y. H., A diameter-selective chiral separation of single-wall carbon nanotubes using nitronium ions. *J. Electron. Mater.* **2006**, 35 (2), 235-242.
158. Miyata, Y.; Maniwa, Y.; Kataura, H., Selective Oxidation of Semiconducting Single-Wall Carbon Nanotubes by Hydrogen Peroxide. *J. Phys. Chem. B* **2006**, 110 (1), 25-29.
159. Wang, L.; Xiong, Y.; Wu, Z.; Duong, B.; Seraphin, S.; Xin, H.; Chen, L., Demetalization of single-walled carbon nanotube thin films with microwave irradiation. *Appl. Phys. A-Mater.* **2011**, 102 (2), 401-406.
160. Qiu, H.; Maeda, Y.; Akasaka, T., Facile and Scalable Route for Highly Efficient Enrichment of Semiconducting Single-Walled Carbon Nanotubes. *J. Am. Chem. Soc.* **2009**, 131 (45), 16529-16533.
161. Gomez, L. M.; Kumar, A.; Zhang, Y.; Ryu, K.; Badmaev, A.; Zhou, C., Scalable Light-Induced Metal to Semiconductor Conversion of Carbon Nanotubes. *Nano Lett.* **2009**, 9 (10), 3592-3598.
162. Liu, J.; Rinzler, A. G.; Dai, H.; Hafner, J. H.; Bradley, R. K.; Boul, P. J.; Lu, A.; Iverson, T.; Shelimov, K.; Huffman, C. B.; Rodriguez-Macias, F.; Shon, Y.-S.; Lee, T. R.; Colbert, D. T.; Smalley, R. E., Fullerene Pipes. *Science* **1998**, 280 (5367), 1253-1256.
163. Peng, H.; Alvarez, N. T.; Kittrell, C.; Hauge, R. H.; Schmidt, H. K., Dielectrophoresis Field Flow Fractionation of Single-Walled Carbon Nanotubes. *J. Am. Chem. Soc.* **2006**, 128 (26), 8396-8397.

164. Ohmori, S.; Saito, T.; Shukla, B.; Yumura, M.; Iijima, S., Fractionation of Single Wall Carbon Nanotubes by Length Using Cross Flow Filtration Method. *ACS Nano* **2010**, *4* (7), 3606-3610.
165. Doorn, S. K.; Fields, R. E.; Hu, H.; Hamon, M. A.; Haddon, R. C.; Selegue, J. P.; Majidi, V., High Resolution Capillary Electrophoresis of Carbon Nanotubes. *J. Am. Chem. Soc.* **2002**, *124* (12), 3169-3174.
166. Doorn, S. K.; Strano, M. S.; O'Connell, M. J.; Haroz, E. H.; Rialon, K. L.; Hauge, R. H.; Smalley, R. E., Capillary Electrophoresis Separations of Bundled and Individual Carbon Nanotubes. *J. Phys. Chem. B* **2003**, *107* (25), 6063-6069.
167. Vetcher, A. A.; Srinivasan, S.; Vetcher, I. A.; Abramov, S. M.; Kozlov, M.; Baughman, R. H.; Levene, S. D., Fractionation of SWNT/nucleic acid complexes by agarose gel electrophoresis. *Nanotechnology* **2006**, *17* (16), 4263-4269.
168. Krupke, R.; Hennrich, F.; v.Lohneysen, H.; Kappes, M. M., Separation of Metallic from Semiconducting Single-Walled Carbon Nanotubes. *Science* **2003**, *301* (5631), 344-347.
169. Krupke, R.; Hennrich, F.; Kappes, M. M.; v.Lohneysen, H., Surface Conductance Induced Dielectrophoresis of Semiconducting Single-Walled Carbon Nanotubes. *Nano Lett.* **2004**, *4* (8), 1395-1399.
170. Krupke, R.; Linden, S.; Rapp, M.; Hennrich, F., Thin Films of Metallic Carbon Nanotubes Prepared by Dielectrophoresis. *Adv. Mater.* **2006**, *18* (11), 1468-1470.
171. Lee, D. S.; Kim, D. W.; Kim, H. S.; Lee, S. W.; Jhang, S. H.; Park, Y. W.; Campbell, E. E. B., Extraction of semiconducting CNTs by repeated dielectrophoretic filtering. *Appl. Phys. A-Mater.* **2005**, *80* (1), 5-8.
172. Kim, Y.; Hong, S.; Jung, S.; Strano, M. S.; Choi, J.; Baik, S., Dielectrophoresis of Surface Conductance Modulated Single-Walled Carbon Nanotubes Using Catanionic Surfactants. *J. Phys. Chem. B* **2006**, *110* (4), 1541-1545.
173. Shin, D. H.; Kim, J.-E.; Shim, H. C.; Song, J.-W.; Yoon, J.-H.; Kim, J.; Jeong, S.; Kang, J.; Baik, S.; Han, C.-S., Continuous Extraction of Highly Pure Metallic Single-Walled Carbon Nanotubes in a Microfluidic Channel. *Nano Lett.* **2008**, *8* (12), 4380-4385.
174. Duesberg, G. S.; Muster, J.; Krstic, V.; Burghard, M.; Roth, S., Chromatographic size separation of single-wall carbon nanotubes. *Appl. Phys. A-Mater.* **1998**, *67* (1), 117-119.
175. Arnold, K.; Hennrich, F.; Krupke, R.; Lebedkin, S.; Kappes, M. M., Length separation studies of single walled carbon nanotube dispersions. *Phys. Status Solidi B* **2006**, *243* (13), 3073-3076.
176. Farkas, E.; Elizabeth Anderson, M.; Chen, Z.; Rinzler, A. G., Length sorting cut single wall carbon nanotubes by high performance liquid chromatography. *Chem. Phys. Lett.* **2002**, *363* (1-2), 111-116.
177. Huang, X.; McLean, R. S.; Zheng, M., High-Resolution Length Sorting and Purification of DNA-Wrapped Carbon Nanotubes by Size-Exclusion Chromatography. *Anal. Chem.* **2005**, *77* (19), 6225-6228.
178. Zheng, M.; Jagota, A.; Strano, M. S.; Santos, A. P.; Barone, P.; Chou, S. G.; Diner, B. A.; Dresselhaus, M. S.; McLean, R. S.; Onoa, G. B.; Samsonidze, G. G.; Semke, E. D.; Usrey, M.; Walls, D. J., Structure-Based Carbon Nanotube Sorting by Sequence-Dependent DNA Assembly. *Science* **2003**, *302* (5650), 1545-1548.
179. Strano, M. S.; Zheng, M.; Jagota, A.; Onoa, G. B.; Heller, D. A.; Barone, P. W.; Usrey, M. L., Understanding the Nature of the DNA-Assisted Separation of Single-Walled Carbon Nanotubes Using Fluorescence and Raman Spectroscopy. *Nano Lett.* **2004**, *4* (4), 543-550.

180. Tu, X.; Manohar, S.; Jagota, A.; Zheng, M., DNA sequence motifs for structure-specific recognition and separation of carbon nanotubes. *Nature* **2009**, *460* (7252), 250-253.
181. Tu, X.; Hight Walker, A. R.; Khripin, C. Y.; Zheng, M., Evolution of DNA Sequences Toward Recognition of Metallic Armchair Carbon Nanotubes. *J. Am. Chem. Soc.* **2011**, *133* (33), 12998-13001.
182. Chattopadhyay, D.; Galeska, I.; Papadimitrakopoulos, F., A Route For Bulk Separation Of Semiconducting From Metallic Single-Wall Carbon Nanotubes. *J. Am. Chem. Soc.* **2003**, *125* (11), 3370-3375.
183. Samsonidze, G. G.; Chou, S. G.; Santos, A. P.; Brar, V. W.; Dresselhaus, G.; Dresselhaus, M. S.; Selbst, A.; Swan, A. K.; Unlu, M. S.; Goldberg, B. B.; Chattopadhyay, D.; Kim, S. N.; Papadimitrakopoulos, F., Quantitative evaluation of the octadecylamine-assisted bulk separation of semiconducting and metallic single-wall carbon nanotubes by resonance Raman spectroscopy. *Appl. Phys. Lett.* **2004**, *85* (6), 1006-1008.
184. Maeda, Y.; Kanda, M.; Hashimoto, M.; Hasegawa, T.; Kimura, S.; Lian, Y.; Wakahara, T.; Akasaka, T.; Kazaoui, S.; Minami, N.; Okazaki, T.; Hayamizu, Y.; Hata, K.; Lu, J.; Nagase, S., Dispersion and Separation of Small-Diameter Single-Walled Carbon Nanotubes. *J. Am. Chem. Soc.* **2006**, *128* (37), 12239-12242.
185. Maeda, Y.; Kimura, S. i.; Kanda, M.; Hirashima, Y.; Hasegawa, T.; Wakahara, T.; Lian, Y.; Nakahodo, T.; Tsuchiya, T.; Akasaka, T.; Lu, J.; Zhang, X.; Gao, Y.; Yu, Y.; Nagase, S.; Kazaoui, S.; Minami, N.; Shimizu, T.; Tokumoto, H.; Saito, R., Large-Scale Separation of Metallic and Semiconducting Single-Walled Carbon Nanotubes. *J. Am. Chem. Soc.* **2005**, *127* (29), 10287-10290.
186. Maeda, Y.; Takano, Y.; Sagara, A.; Hashimoto, M.; Kanda, M.; Kimura, S.-i.; Lian, Y.; Nakahodo, T.; Tsuchiya, T.; Wakahara, T.; Akasaka, T.; Hasegawa, T.; Kazaoui, S.; Minami, N.; Lu, J.; Nagase, S., Simple purification and selective enrichment of metallic SWCNTs produced using the arc-discharge method. *Carbon* **2008**, *46* (12), 1563-1569.
187. Niyogi, S.; Boukhalfa, S.; Chikkannanavar, S. B.; McDonald, T. J.; Heben, M. J.; Doorn, S. K., Selective Aggregation of Single-Walled Carbon Nanotubes via Salt Addition. *J. Am. Chem. Soc.* **2007**, *129* (7), 1898-1899.
188. Chen, Z.; Du, X.; Du, M. H.; Rancken, C. D.; Cheng, H. P.; Rinzler, A. G., Bulk Separative Enrichment in Metallic or Semiconducting Single-Walled Carbon Nanotubes. *Nano Lett.* **2003**, *3* (9), 1245-1249.
189. Bonaccorso, F.; Hasan, T.; Tan, P. H.; Sciascia, C.; Privitera, G.; Di Marco, G.; Gucciardi, P. G.; Ferrari, A. C., Density Gradient Ultracentrifugation of Nanotubes: Interplay of Bundling and Surfactants Encapsulation. *J. Phys. Chem. C* **2010**, *114* (41), 17267-17285.
190. Arnold, M. S.; Stupp, S. I.; Hersam, M. C., Enrichment of Single-Walled Carbon Nanotubes by Diameter in Density Gradients. *Nano Lett.* **2005**, *5* (4), 713-718.
191. Arnold, M. S.; Green, A. A.; Hulvat, J. F.; Stupp, S. I.; Hersam, M. C., Sorting carbon nanotubes by electronic structure using density differentiation. *Nat. Nanotechnol.* **2006**, *1* (1), 60-65.
192. Wei, L.; Wang, B.; Goh, T. H.; Li, L. J.; Yang, Y.; Chan-Park, M. B.; Chen, Y., Selective Enrichment of (6,5) and (8,3) Single-Walled Carbon Nanotubes via Cosurfactant Extraction from Narrow (n,m) Distribution Samples. *J. Phys. Chem. B* **2008**, *112* (10), 2771-2774.

193. Antaris, A. L.; Seo, J.-W. T.; Green, A. A.; Hersam, M. C., Sorting Single-Walled Carbon Nanotubes by Electronic Type Using Nonionic, Biocompatible Block Copolymers. *ACS Nano* **2010**, *4* (8), 4725-4732.
194. Zhao, P.; Einarsson, E.; Xiang, R.; Murakami, Y.; Maruyama, S., Controllable Expansion of Single-Walled Carbon Nanotube Dispersions Using Density Gradient Ultracentrifugation. *J. Phys. Chem. C* **2010**, *114* (11), 4831-4834.
195. Chernov, A. I.; Obraztsova, E. D., Metallic single-wall carbon nanotubes separated by density gradient ultracentrifugation. *Phys. Status Solidi B* **2009**, *246* (11-12), 2477-2481.
196. Miyata, Y.; Yanagi, K.; Maniwa, Y.; Kataura, H., Optical Evaluation of the Metal-to-Semiconductor Ratio of Single-Wall Carbon Nanotubes. *J. Phys. Chem. C* **2008**, *112* (34), 13187-13191.
197. Fleurier, R.; Lauret, J.-S.; Lopez, U.; Loiseau, A., Transmission Electron Microscopy and UV-vis-IR Spectroscopy Analysis of the Diameter Sorting of Carbon Nanotubes by Gradient Density Ultracentrifugation. *Adv. Funct. Mater.* **2009**, *19* (14), 2219-2223.
198. Duque, J. G.; Densmore, C. G.; Doorn, S. K., Saturation of Surfactant Structure at the Single-Walled Carbon Nanotube Surface. *J. Am. Chem. Soc.* **2010**, *132* (45), 16165-16175.
199. Ghosh, S.; Bachilo, S. M.; Weisman, R. B., Advanced sorting of single-walled carbon nanotubes by nonlinear density-gradient ultracentrifugation. *Nat. Nanotechnol.* **2010**, *5* (6), 443-450.
200. Yanagi, K.; Iitsuka, T.; Fujii, S.; Kataura, H., Separations of Metallic and Semiconducting Carbon Nanotubes by Using Sucrose as a Gradient Medium. *J. Phys. Chem. C* **2008**, *112* (48), 18889-18894.
201. Feng, Y.; Miyata, Y.; Matsuishi, K.; Kataura, H., High-Efficiency Separation of Single-Wall Carbon Nanotubes by Self-Generated Density Gradient Ultracentrifugation. *J. Phys. Chem. C* **2011**, *115* (5), 1752-1756.
202. Stürzl, N.; Hennrich, F.; Lebedkin, S.; Kappes, M. M., Near Monochiral Single-Walled Carbon Nanotube Dispersions in Organic Solvents. *J. Phys. Chem. C* **2009**, *113* (33), 14628-14632.
203. Tabakman, S. M.; Welsher, K.; Hong, G.; Dai, H., Optical Properties of Single-Walled Carbon Nanotubes Separated in a Density Gradient: Length, Bundling, and Aromatic Stacking Effects. *J. Phys. Chem. C* **2010**, *114* (46), 19569-19575.
204. Deng, X.; Xiong, D.; Wang, H.; Chen, D.; Jiao, Z.; Zhang, H.; Wu, M., Bulk enrichment and separation of multi-walled carbon nanotubes by density gradient centrifugation. *Carbon* **2009**, *47* (6), 1608-1610.
205. Fagan, J. A.; Becker, M. L.; Chun, J.; Hobbie, E. K., Length Fractionation of Carbon Nanotubes Using Centrifugation. *Adv. Mater.* **2008**, *20* (9), 1609-1613.
206. Sun, X.; Zaric, S.; Daranciang, D.; Welsher, K.; Lu, Y.; Li, X.; Dai, H., Optical Properties of Ultrashort Semiconducting Single-Walled Carbon Nanotube Capsules Down to Sub-10 nm. *J. Am. Chem. Soc.* **2008**, *130* (20), 6551-6555.
207. Green, A.; Duch, M.; Hersam, M., Isolation of single-walled carbon nanotube enantiomers by density differentiation. *Nano Res.* **2009**, *2* (1), 69-77.
208. Cambré, S.; Wenseleers, W., Separation and Diameter-Sorting of Empty (End-Capped) and Water-Filled (Open) Carbon Nanotubes by Density Gradient Ultracentrifugation. *Angew. Chem. Int. Edit.* **2011**, *50* (12), 2764-2768.
209. Fagan, J. A.; Huh, J. Y.; Simpson, J. R.; Blackburn, J. L.; Holt, J. M.; Larsen, B. A.; Walker, A. R. H., Separation of Empty and Water-Filled Single-Wall Carbon Nanotubes. *ACS Nano* **2011**, *5* (5), 3943-3953.

210. Green, A. A.; Hersam, M. C., Nearly Single-Chirality Single-Walled Carbon Nanotubes Produced via Orthogonal Iterative Density Gradient Ultracentrifugation. *Adv. Mater.* **2011**, *23* (19), 2185-2190.
211. Tanaka, T.; Jin, H.; Miyata, Y.; Fujii, S.; Suga, H.; Naitoh, Y.; Minari, T.; Miyadera, T.; Tsukagoshi, K.; Kataura, H., Simple and Scalable Gel-Based Separation of Metallic and Semiconducting Carbon Nanotubes. *Nano Lett.* **2009**, *9* (4), 1497-1500.
212. Liu, H.; Nishide, D.; Tanaka, T.; Kataura, H., Large-scale single-chirality separation of single-wall carbon nanotubes by simple gel chromatography. *Nat. Commun.* **2011**, *2*, 309.
213. Liu, H.; Feng, Y.; Tanaka, T.; Urabe, Y.; Kataura, H., Diameter-Selective Metal/Semiconductor Separation of Single-wall Carbon Nanotubes by Agarose Gel. *J. Phys. Chem. C* **2010**, *114* (20), 9270-9276.
214. Moshhammer, K.; Hennrich, F.; Kappes, M., Selective suspension in aqueous sodium dodecyl sulfate according to electronic structure type allows simple separation of metallic from semiconducting single-walled carbon nanotubes. *Nano Res.* **2009**, *2* (8), 599-606.
215. Silvera-Batista, C. A.; Scott, D. C.; McLeod, S. M.; Ziegler, K. J., A Mechanistic Study of the Selective Retention of SDS-Suspended Single-Wall Carbon Nanotubes on Agarose Gels. *J. Phys. Chem. C* **2011**, *115* (19), 9361-9369.
216. Liu, C.-H.; Liu, Y.-Y.; Zhang, Y.-H.; Wei, R.-R.; Li, B.-R.; Zhang, H.-L.; Chen, Y., Selective interaction of a soluble pentacene derivative with metallic single-walled carbon nanotubes. *Chem. Phys. Lett.* **2009**, *471* (1-3), 97-102.
217. Marquis, R.; Greco, C.; Sadokierska, I.; Lebedkin, S.; Kappes, M. M.; Michel, T.; Alvarez, L.; Sauvajol, J.-L.; Meunier, S.; Mioskowski, C., Supramolecular Discrimination of Carbon Nanotubes According to Their Helicity. *Nano Lett.* **2008**, *8* (7), 1830-1835.
218. Voggu, R.; Rao, K. V.; George, S. J.; Rao, C. N. R., A Simple Method of Separating Metallic and Semiconducting Single-Walled Carbon Nanotubes Based on Molecular Charge Transfer. *J. Am. Chem. Soc.* **2010**, *132* (16), 5560-5561.
219. Liu, C.-H.; Liu, Y.-Y.; Zhang, Y.-H.; Wei, R.-R.; Zhang, H.-L., Tandem extraction strategy for separation of metallic and semiconducting SWCNTs using condensed benzenoid molecules: effects of molecular morphology and solvent. *Phys. Chem. Chem. Phys.* **2009**, *11* (33), 7257-7267.
220. Wang, W.; Fernando, K. A. S.; Lin, Y.; Mezziani, M. J.; Veca, L. M.; Cao, L.; Zhang, P.; Kimani, M. M.; Sun, Y. P., Metallic Single-Walled Carbon Nanotubes for Conductive Nanocomposites. *J. Am. Chem. Soc.* **2008**, *130* (4), 1415-1419.
221. Ju, S.-Y.; Doll, J.; Sharma, I.; Papadimitrakopoulos, F., Selection of carbon nanotubes with specific chiralities using helical assemblies of flavin mononucleotide. *Nat. Nanotechnol.* **2008**, *3* (6), 356-362.
222. Saito, K.; Troiani, V.; Qiu, H.; Solladie, N.; Sakata, T.; Mori, H.; Ohama, M.; Fukuzumi, S., Nondestructive Formation of Supramolecular Nanohybrids of Single-Walled Carbon Nanotubes with Flexible Porphyrinic Polypeptides. *J. Phys. Chem. C* **2007**, *111* (3), 1194-1199.
223. Banerjee, S.; Wong, S. S., Selective Metallic Tube Reactivity in the Solution-Phase Osmylation of Single-Walled Carbon Nanotubes. *J. Am. Chem. Soc.* **2004**, *126* (7), 2073-2081.
224. Yoonmi Lee; Ki-Seok Jeon; Hyunseob Lim; Hyeon Suk Shin; Seung Min Jin; Hye Ryung Byon; Yung Doug Suh; Hee Cheul Choi, Silencing of Metallic

- Single-Walled Carbon Nanotubes via Spontaneous Hydrosilylation. *Small* **2009**, *5* (12), 1398-1402.
225. Menard-Moyon, C.; Izard, N.; Doris, E.; Mioskowski, C., Separation of Semiconducting from Metallic Carbon Nanotubes by Selective Functionalization with Azomethine Ylides. *J. Am. Chem. Soc.* **2006**, *128* (20), 6552-6553.
226. Strano, M. S.; Dyke, C. A.; Usrey, M. L.; Barone, P. W.; Allen, M. J.; Shan, H.; Kittrell, C.; Hauge, R. H.; Tour, J. M.; Smalley, R. E., Electronic Structure Control of Single-Walled Carbon Nanotube Functionalization. *Science* **2003**, *301* (5639), 1519-1522.
227. Dyke, C. A.; Stewart, M. P.; Tour, J. M., Separation of Single-Walled Carbon Nanotubes on Silica Gel. Materials Morphology and Raman Excitation Wavelength Affect Data Interpretation. *J. Am. Chem. Soc.* **2005**, *127* (12), 4497-4509.
228. Strano, M. S., Probing Chiral Selective Reactions Using a Revised Kataura Plot for the Interpretation of Single-Walled Carbon Nanotube Spectroscopy. *J. Am. Chem. Soc.* **2003**, *125* (51), 16148-16153.
229. Dyke, C. A.; Stewart, M. P.; Maya, F.; Tour, J. M., Diazonium-Based Functionalization of Carbon Nanotubes: XPS and GC-MS Analysis and Mechanistic Implications. *Synlett* **2004**, *1*, 155-160.
230. Cabana, J.; Lavoie, S. p.; Martel, R., Thermal Chemistry of Methylene- and Phenyl-Functionalized Carbon Nanotubes. *J. Am. Chem. Soc.* **2010**, *132* (4), 1389-1394.
231. Lim, J. K.; Yoo, B. K.; Yi, W.; Hong, S.; Paik, H.-j.; Chun, K.; Kim, S. K.; Joo, S.-W., Photodetachment of aryl moieties from covalently functionalized singlewalled carbon nanotubes by UV laser irradiation. *J. Mater. Chem.* **2006**, *16*, 2374 - 2379.
232. Balasubramanian, K.; Sordan, R.; Burghard, M.; Kern, K., A Selective Electrochemical Approach to Carbon Nanotube Field-Effect Transistors. *Nano Lett.* **2004**, *4* (5), 827-830.
233. An, L.; Fu, Q.; Lu, C.; Liu, J., A Simple Chemical Route To Selectively Eliminate Metallic Carbon Nanotubes in Nanotube Network Devices. *J. Am. Chem. Soc.* **2004**, *126* (34), 10520-10521.
234. Wu, C.; Guan, L., Increasing the semiconducting component in transparent conducting films of single-walled carbon nanotubes. *Carbon* **2011**, *49* (10), 3267-3273.
235. Wang, C.; Cao, Q.; Ozel, T.; Gaur, A.; Rogers, J. A.; Shim, M., Electronically Selective Chemical Functionalization of Carbon Nanotubes: Correlation between Raman Spectral and Electrical Responses. *J. Am. Chem. Soc.* **2005**, *127* (32), 11460-11468.
236. Baik, S.; Usrey, M.; Rotkina, L.; Strano, M., Using the Selective Functionalization of Metallic Single-Walled Carbon Nanotubes to Control Dielectrophoretic Mobility. *J. Phys. Chem. B* **2004**, *108* (40), 15560-15564.
237. Kim, W. J.; Usrey, M. L.; Strano, M. S., Selective Functionalization and Free Solution Electrophoresis of Single-Walled Carbon Nanotubes: Separate Enrichment of Metallic and Semiconducting SWNT. *Chem. Mater.* **2007**, *19* (7), 1571-1576.
238. Usrey, M. L.; Nair, N.; Agnew, D. E.; Pina, C. F.; Strano, M. S., Controlling the Electrophoretic Mobility of Single-Walled Carbon Nanotubes: A Comparison of Theory and Experiment. *Langmuir* **2007**, *23* (14), 7768-7776.

239. Fantini, C.; Usrey, M. L.; Strano, M. S., Investigation of Electronic and Vibrational Properties of Single-Walled Carbon Nanotubes Functionalized with Diazonium Salts. *J. Phys. Chem. C* **2007**, *111* (48), 17941-17946.
240. Usrey, M. L.; Lippmann, E. S.; Strano, M. S., Evidence for a Two-Step Mechanism in Electronically Selective Single-Walled Carbon Nanotube Reactions. *J. Am. Chem. Soc.* **2005**, *127* (46), 16129-16135.
241. Abdula, D.; Nguyen, K. T.; Shim, M., Raman Spectral Evolution in Individual Metallic Single-Walled Carbon Nanotubes upon Covalent Sidewall Functionalization. *J. Phys. Chem. C* **2007**.
242. Nair, N.; Usrey, M. L.; Kim, W. J.; Braatz, R. D.; Strano, M. S., Estimation of the (n,m) Concentration Distribution of Single-Walled Carbon Nanotubes from Photoabsorption Spectra. *Anal. Chem.* **2006**, *78* (22), 7689-7696.
243. Nair, N.; Kim, W. J.; Usrey, M. L.; Strano, M. S., A Structure-Reactivity Relationship for Single Walled Carbon Nanotubes Reacting with 4-Hydroxybenzene Diazonium Salt. *J. Am. Chem. Soc.* **2007**, *129* (13), 3946-3954.
244. Kim, W. J.; Nair, N.; Lee, C. Y.; Strano, M. S., Covalent Functionalization of Single-Walled Carbon Nanotubes Alters Their Densities Allowing Electronic and Other Types of Separation. *J. Phys. Chem. C* **2008**, *112* (19), 7326-7331.
245. Doyle, C. D.; Rocha, J.-D. R.; Weisman, R. B.; Tour, J. M., Structure-Dependent Reactivity of Semiconducting Single-Walled Carbon Nanotubes with Benzenediazonium Salts. *J. Am. Chem. Soc.* **2008**, *130* (21), 6795-6800.
246. Schmidt, G.; Gallon, S.; Esnouf, S.; Bourgoin, J.-P.; Pascale Chenevier, Mechanism of the Coupling of Diazonium to Single-Walled Carbon Nanotubes and Its Consequences. *Chem. Eur. J.* **2009**, *15* (9), 2101-2110.
247. Toyoda, S.; Yamaguchi, Y.; Hiwatashi, M.; Tomonari, Y.; Murakami, H.; Nakashima, N., Separation of Semiconducting Single-Walled Carbon Nanotubes by Using a Long-Alkyl-Chain Benzenediazonium Compound. *Chem. Asian J.* **2007**, *2* (1), 145-149.
248. Boul, P. J.; Nikolaev, P.; Sosa, E.; Arepalli, S., Potentially Scalable Conductive-Type Nanotube Enrichment Through Covalent Chemistry. *J. Phys. Chem. C* **2011**, *115* (28), 13592-13596.
249. Ghosh, S.; Rao, C., Separation of metallic and semiconducting single-walled carbon nanotubes through fluorine chemistry. *Nano Res.* **2009**, *2* (3), 183-191.
250. Neppiras, E. A., Acoustic cavitation. *Phys. Rep.* **1980**, *61* (3), 159-251.
251. Newman, C. M. H.; Bettinger, T., Gene therapy progress and prospects: Ultrasound for gene transfer. *Gene Ther.* **2007**, *14* (6), 465-475.
252. Santos, H. M.; Capelo, J. L., Trends in ultrasonic-based equipment for analytical sample treatment. *Talanta* **2007**, *73* (5), 795-802.
253. Kuijpers, M. W. A.; Iedema, P. D.; Kemmere, M. F.; Keurentjes, J. T. F., The mechanism of cavitation-induced polymer scission; experimental and computational verification. *Polymer* **2004**, *45* (19), 6461-6467.
254. Boyer, R.; Welsch, G.; Collings, E. W., *Materials Properties Handbook: Titanium Alloys*. ASM International: 1994.
255. Eda, G.; Fanchini, G.; Kanwal, A.; Chhowalla, M., Bundling dynamics of single walled carbon nanotubes in aqueous suspensions. *J. Appl. Phys.* **2008**, *103* (9), 093118-7.
256. Harvey, D., *Modern Analytical Chemistry*. McGraw-Hill: 2000.
257. Braun, C. L.; Smirnov, S. N., Why is water blue? *J. Chem. Educ.* **1993**, *70* (8), 612-614.

258. Bayly, J. G.; Kartha, V. B.; Stevens, W. H., The absorption spectra of liquid phase H₂O, HDO and D₂O from 0.7 μ m to 10 μ m. *Infrared Phys.* **1963**, *3* (4), 211-222.
259. Vedamuthu, M.; Singh, S.; Robinson, G. W., Properties of Liquid Water: Origin of the Density Anomalies. *J. Phys. Chem.* **1994**, *98* (9), 2222-2230.
260. Langford, V. S.; McKinley, A. J.; Quickenden, T. I., Temperature Dependence of the Visible-Near-Infrared Absorption Spectrum of Liquid Water. *J. Phys. Chem. A* **2001**, *105* (39), 8916-8921.
261. Rance, G. A.; Marsh, D. H.; Nicholas, R. J.; Khlobystov, A. N., UV-vis absorption spectroscopy of carbon nanotubes: Relationship between the π -electron plasmon and nanotube diameter. *Chem. Phys. Lett.* **2011**, *493* (1-3), 19-23.
262. Jacobsen, N. S.; Pantano, P., Determining the percentages of semi-conducting and metallic single-walled carbon nanotubes in bulk soot. *Carbon* **2011**, *49* (6), 1998-2006.
263. Murakami, Y.; Einarsson, E.; Edamura, T.; Maruyama, S., Polarization Dependence of the Optical Absorption of Single-Walled Carbon Nanotubes. *Phys. Rev. Lett.* **2005**, *94*, 087402.
264. Lingam, K.; Podila, R.; Loebick, C.; Chen, P.; Ke, P. C.; Powell, B.; Pfefferle, L.; Rao, A. M., Effect of bundling on the π -plasmon energy in sub-nanometer single wall carbon nanotubes. *Carbon* **2011**, *49* (12), 3803-3807.
265. Murakami, Y.; Maruyama, S., Effect of dielectric environment on the ultraviolet optical absorption of single-walled carbon nanotubes. *Phys. Rev. B* **2009**, *79* (15), 155445-5.
266. Takagi, Y.; Okada, S., Theoretical calculation for the ultraviolet optical properties of single-walled carbon nanotubes. *Phys. Rev. B* **2009**, *79* (23), 233406.
267. Kumar, P.; Bohidar, H. B., Aqueous dispersion stability of multi-carbon nanoparticles in anionic, cationic, neutral, bile salt and pulmonary surfactant solutions. *Colloid. Surface. A* **2010**, *361* (1-3), 13-24.
268. Choi, J. H.; Strano, M. S., Solvatochromism in single-walled carbon nanotubes. *Appl. Phys. Lett.* **2007**, *90* (22), 223114-3.
269. Lefebvre, J.; Finnie, P., Excited Excitonic States in Single-Walled Carbon Nanotubes. *Nano Lett.* **2008**, *8* (7), 1890-1895.
270. Wang, F.; Sfeir, M. Y.; Huang, L.; Huang, X. M. H.; Wu, Y.; Kim, J.; Hone, J.; O'Brien, S.; Brus, L. E.; Heinz, T. F., Interactions between Individual Carbon Nanotubes Studied by Rayleigh Scattering Spectroscopy. *Phys. Rev. Lett.* **2006**, *96* (16), 167401.
271. Itkis, M. E.; Perea, D. E.; Jung, R.; Niyogi, S.; Haddon, R. C., Comparison of Analytical Techniques for Purity Evaluation of Single-Walled Carbon Nanotubes. *J. Am. Chem. Soc.* **2005**, *127* (10), 3439-3448.
272. Tan, Y.; Resasco, D. E., Dispersion of Single-Walled Carbon Nanotubes of Narrow Diameter Distribution. *J. Phys. Chem. B* **2005**, *109* (30), 14454-14460.
273. Lian, Y.; Maeda, Y.; Wakahara, T.; Nakahodo, T.; Akasaka, T.; Kazaoui, S.; Minami, N.; Shimizu, T.; Tokumoto, H., Spectroscopic study on the centrifugal fractionation of soluble single-walled carbon nanotubes. *Carbon* **2005**, *43* (13), 2750-2759.
274. Wei, L.; Wang, B.; Wang, Q.; Li, L.-J.; Yang, Y.; Chen, Y., Effect of Centrifugation on the Purity of Single-Walled Carbon Nanotubes from MCM-41 Containing Cobalt. *J. Phys. Chem. C* **2008**, *112* (45), 17567-17575.
275. Itkis, M. E.; Perea, D. E.; Niyogi, S.; Rickard, S. M.; Hamon, M. A.; Hu, H.; Zhao, B.; Haddon, R. C., Purity Evaluation of As-Prepared Single-Walled Carbon

- Nanotube Soot by Use of Solution-Phase Near-IR Spectroscopy. *Nano Lett.* **2003**, *3* (3), 309-314.
276. Bahr, J. L.; Tour, J. M., Covalent chemistry of single-wall carbon nanotubes. *J. Mater. Chem.* **2002**, *12* (7), 1952-1958.
277. Bahr, J. L.; Tour, J. M., Highly Functionalized Carbon Nanotubes Using in Situ Generated Diazonium Compounds. *Chem. Mater.* **2001**, *13* (11), 3823-3824.
278. O'Connell, M. J.; Eibergen, E. E.; Doorn, S. K., Chiral selectivity in the charge-transfer bleaching of single-walled carbon-nanotube spectra. *Nat. Mater.* **2005**, *4* (5), 412-418.
279. Ferraro, J. R.; Nakamoto, K.; Brown, C. W., *Introductory Raman Spectroscopy* (second edition). Elsevier: 2003.
280. Smith, E.; Dent, G., *Modern Raman Spectroscopy – A Practical Approach*. John Wiley & Sons Ltd.: Chichester, 2005.
281. Irurzun, V. M.; Ruiz, M. P.; Resasco, D. E., Raman intensity measurements of single-walled carbon nanotube suspensions as a quantitative technique to assess purity. *Carbon* **2010**, *48* (10), 2873-2881.
282. Salzmann, C. G.; Chu, B. T. T.; Tobias, G.; Llewellyn, S. A.; Green, M. L. H., Quantitative assessment of carbon nanotube dispersions by Raman spectroscopy. *Carbon* **2007**, *45* (5), 907-912.
283. Carey, D. M.; Korenowski, G. M., Measurement of the Raman spectrum of liquid water. *J. Chem. Phys.* **1998**, *108*, 2669-2675.
284. Zelsmann, H. R., Temperature dependence of the optical constants for liquid H₂O and D₂O in the far IR region. *J. Mol. Struct.* **1995**, *350* (2), 95-114.
285. Wojdyr, M., Fityk: a general-purpose peak fitting program. *J. Appl. Crystallogr.* **2010**, *43* (5 Part 1), 1126-1128.
286. Maultzsch, J.; Telg, H.; Reich, S.; Thomsen, C., Radial breathing mode of single-walled carbon nanotubes: Optical transition energies and chiral-index assignment. *Phys. Rev. B* **2005**, *72* (20), 205438-16.
287. Jorio, A.; Fantini, C.; Pimenta, M. A.; Capaz, R. B.; Samsonidze, G. G.; Dresselhaus, G.; Dresselhaus, M. S.; Jiang, J.; Kobayashi, N.; Gruneis, A.; Saito, R., Resonance Raman spectroscopy (n,m)-dependent effects in small-diameter single-wall carbon nanotubes. *Phys. Rev. B* **2005**, *71* (7), 075401-11.
288. Thomsen, C.; Reich, S., Raman Scattering in Carbon Nanotubes. In *Light Scattering in Solids IX*, 2007; Vol. 108, pp 115-232.
289. Araujo, P. T.; Pesce, P. B. C.; Dresselhaus, M. S.; Sato, K.; Saito, R.; Jorio, A., Resonance Raman spectroscopy of the radial breathing modes in carbon nanotubes. *Physica E* **2010**, *42* (5), 1251-1261.
290. Cheng, Q.; Debnath, S.; Gregan, E.; Byrne, H., Vibrational mode assignments for bundled single-wall carbon nanotubes using Raman spectroscopy at different excitation energies. *Appl. Phys. A-Mater.* **2011**, *102* (2), 309-317.
291. Saito, R.; Hofmann, M.; Dresselhaus, G.; Jorio, A.; Dresselhaus, M. S., Raman spectroscopy of graphene and carbon nanotubes. *Adv. Phys.* **2011**, *60* (3), 413-550.
292. Piscanec, S.; Lazzeri, M.; Robertson, J.; Ferrari, A. C.; Mauri, F., Optical phonons in carbon nanotubes: Kohn anomalies, Peierls distortions, and dynamic effects. *Phys. Rev. B* **2007**, *75* (3), 035427.
293. Hároz, E. H.; Duque, J. G.; Rice, W. D.; Densmore, C. G.; Kono, J.; Doorn, S. K., Resonant Raman spectroscopy of armchair carbon nanotubes: Absence of broad G⁻ feature. *Phys. Rev. B* **2011**, *84* (12), 121403.

294. Blackburn, J. L.; Engtrakul, C.; McDonald, T. J.; Dillon, A. C.; Heben, M. J., Effects of Surfactant and Boron Doping on the BWF Feature in the Raman Spectrum of Single-Wall Carbon Nanotube Aqueous Dispersions. *J. Phys. Chem. B* **2006**, *110* (50), 25551-25558.
295. Paillet, M.; Poncharal, P.; Zahab, A.; Sauvajol, J. L.; Meyer, J. C.; Roth, S., Vanishing of the Breit-Wigner-Fano Component in Individual Single-Wall Carbon Nanotubes. *Phys. Rev. Lett.* **2005**, *94* (23), 237401.
296. Graupner, R., Raman spectroscopy of covalently functionalized single-wall carbon nanotubes. *J. Raman Spectrosc.* **2007**, *38* (6), 673-683.
297. Yao, N.; Wang, Z. L., *Handbook of Microscopy for Nanotechnology*. Kluwer Academic Publishers: New York, 2005.
298. Bhushan, B., *Springer Handbook of Nanotechnology*. Springer-Verlag: Berlin Heidelberg, 2004.
299. Giessibl, F. J., Advances in atomic force microscopy. *Rev. Mod. Phys.* **2003**, *75* (3), 949.
300. Rivière, J. C.; Myhra, S., *Handbook of Surface and Interface Analysis: Methods for Problem Solving, Second Edition*. CRC Press: Boca Raton, 2009.
301. Abramoff, M. D.; Magelhaes, P. J.; Ram, S. J., Image Processing with ImageJ. *Biophotonics International* **2004**, *11* (7), 36-42.
302. Poenitzsch, V. Z.; Musselman, I. H., Atomic Force Microscopy Measurements of Peptide-Wrapped Single-Walled Carbon Nanotube Diameters. *Microsc. Microanal.* **2006**, *12* (03), 221-227.
303. Emslie, A. G.; Bonner, F. T.; Peck, L. G., Flow of a Viscous Liquid on a Rotating Disk. *J. Appl. Phys.* **1958**, *29* (5), 858-862.
304. Nabok, A., *Organic and Inorganic Nanostructures*. Artech House: Boston, 2005.
305. Barman, S. N.; LeMieux, M. C.; Baek, J.; Rivera, R.; Bao, Z., Effects of Dispersion Conditions of Single-Walled Carbon Nanotubes on the Electrical Characteristics of Thin Film Network Transistors. *ACS Applied Materials & Interfaces* **2010**, *2* (9), 2672-2678.
306. Zhang, Q.; Vichchulada, P.; Lay, M. D., Length, Bundle, and Density Gradients in Spin Cast Single-Walled Carbon Nanotube Networks. *J. Phys. Chem. C* **2010**, *114* (39), 16292-16297.
307. Tenent, R. C.; Barnes, T. M.; Bergeson, J. D.; Ferguson, A. J.; To, B.; Gedvilas, L. M.; Heben, M. J.; Blackburn, J. L., Ultrasoother, Large-Area, High-Uniformity, Conductive Transparent Single-Walled-Carbon-Nanotube Films for Photovoltaics Produced by Ultrasonic Spraying. *Adv. Mater.* **2009**, *21* (31), 3210-3216.
308. Egerton, R. F., *Physical Principles of Electron Microscopy: An Introduction to TEM, SEM, and AEM*. Springer: New York, 2005.
309. Amelinckx, S.; van Dyck, D.; van Landuyt, J.; van Tendeloo, G., *Electron Microscopy Principles and Fundamentals*. Wiley-VCH: Weinheim, 1997.
310. Jeong, M. S.; Byeon, C. C.; Cha, O. H.; Jeong, H.; Han, J. H.; Choi, Y. C.; An, K. H.; Oh, K. H.; Kim, K. K.; Lee, Y. H., Purity Measurement Of Single-Walled Carbon Nanotubes By UV-Vis-NIR Spectroscopy and Thermogravimetric Analysis. *NANO: Brief Reports and Reviews* **2008**, *3* (2), 101-108.
311. Xu, Z.; Yang, X.; Yang, Z., A Molecular Simulation Probing of Structure and Interaction for Supramolecular Sodium Dodecyl Sulfate/Single-Wall Carbon Nanotube Assemblies. *Nano Lett.* **2010**, *10* (3), 985-991.
312. Matarredona, O.; Rhoads, H.; Li, Z.; Harwell, J. H.; Balzano, L.; Resasco, D. E., Dispersion of Single-Walled Carbon Nanotubes in Aqueous Solutions of the Anionic Surfactant NaDDBS. *J. Phys. Chem. B* **2003**, *107* (48), 13357-13367.

313. Richard, C.; Balavoine, F.; Schultz, P.; Ebbesen, T. W.; Mioskowski, C., Supramolecular Self-Assembly of Lipid Derivatives on Carbon Nanotubes. *Science* **2003**, *300* (5620), 775-778.
314. Wang, Q.; Han, Y.; Wang, Y.; Qin, Y.; Guo, Z.-X., Effect of Surfactant Structure on the Stability of Carbon Nanotubes in Aqueous Solution. *J. Phys. Chem. B* **2008**, *112* (24), 7227-7233.
315. Yurekli, K.; Mitchell, C. A.; Krishnamoorti, R., Small-Angle Neutron Scattering from Surfactant-Assisted Aqueous Dispersions of Carbon Nanotubes. *J. Am. Chem. Soc.* **2004**, *126* (32), 9902-9903.
316. Angelikopoulos, P.; Bock, H., Directed Self-Assembly of Surfactants in Carbon Nanotube Materials. *J. Phys. Chem. B* **2008**, *112* (44), 13793-13801.
317. Calvaresi, M.; Dallavalle, M.; Zerbetto, F., Wrapping Nanotubes with Micelles, Hemimicelles, and Cylindrical Micelles. *Small* **2009**, *5* (19), 2191-2198.
318. Angelikopoulos, P.; Gromov, A.; Leen, A.; Nerushev, O.; Bock, H.; Campbell, E. E. B., Dispersing Individual Single-Wall Carbon Nanotubes in Aqueous Surfactant Solutions below the cmc. *J. Phys. Chem. C* **2009**, *114* (1), 2-9.
319. Utsumi, S.; Kanamaru, M.; Honda, H.; Kanoh, H.; Tanaka, H.; Ohkubo, T.; Sakai, H.; Abe, M.; Kaneko, K., RBM band shift-evidenced dispersion mechanism of single-wall carbon nanotube bundles with NaDDBS. *J. Colloid Interface Sci.* **2007**, *308* (1), 276-284.
320. O'Connell, M. J.; Boul, P.; Ericson, L. M.; Huffman, C.; Wang, Y.; Haroz, E.; Kuper, C.; Tour, J.; Ausman, K. D.; Smalley, R. E., Reversible water-solubilization of single-walled carbon nanotubes by polymer wrapping. *Chem. Phys. Lett.* **2001**, *342* (3-4), 265-271.
321. Nativ-Roth, E.; Shvartzman-Cohen, R.; Bounioux, C. I.; Florent, M.; Zhang, D.; Szleifer, I.; Yerushalmi-Rozen, R., Physical Adsorption of Block Copolymers to SWNT and MWNT: A Nonwrapping Mechanism. *Macromolecules* **2007**, *40* (10), 3676-3685.
322. McDonald, T. J.; Engtrakul, C.; Jones, M.; Rumbles, G.; Heben, M. J., Kinetics of PL Quenching during Single-Walled Carbon Nanotube Rebundling and Diameter-Dependent Surfactant Interactions. *J. Phys. Chem. B* **2006**, *110* (50), 25339-25346.
323. Cardenas, J. F.; Glerup, M., The influence of surfactants on the distribution of the radial breathing modes of single walled carbon nanotubes. *Nanotechnology* **2006**, *17* (20), 5212-5215.
324. Huang, H.; Kajiura, H.; Maruyama, R.; Kadono, K.; Noda, K., Relative Optical Absorption of Metallic and Semiconducting Single-Walled Carbon Nanotubes. *J. Phys. Chem. B* **2006**, *110* (10), 4686-4690.
325. Okazaki, T.; Saito, T.; Matsuura, K.; Ohshima, S.; Yumura, M.; Iijima, S., Photoluminescence Mapping of "As-Grown" Single-Walled Carbon Nanotubes: A Comparison with Micelle-Encapsulated Nanotube Solutions. *Nano Lett.* **2005**, *5* (12), 2618-2623.
326. Vigolo, B.; Penicaud, A.; Coulon, C.; Sauder, C.; Pailler, R.; Journet, C.; Bernier, P.; Poulin, P., Macroscopic Fibers and Ribbons of Oriented Carbon Nanotubes. *Science* **2000**, *290* (5495), 1331-1334.
327. Wang, H.; Zhou, W.; Ho, D. L.; Winey, K. I.; Fischer, J. E.; Glinka, C. J.; Hobbie, E. K., Dispersing Single-Walled Carbon Nanotubes with Surfactants: A Small Angle Neutron Scattering Study. *Nano Lett.* **2004**, *4* (9), 1789-1793.
328. Hilding, J.; Grulke, E.; George Zhang, Z.; Lockwood, F., Dispersion of Carbon Nanotubes in Liquids. *Journal of Dispersion Science & Technology* **2003**, *24*, 1.

329. Fagan, J. A.; Landi, B. J.; Mandelbaum, I.; Simpson, J. R.; Bajpai, V.; Bauer, B. J.; Migler, K.; Walker, A. R. H.; Raffaele, R.; Hobbie, E. K., Comparative Measures of Single-Wall Carbon Nanotube Dispersion. *J. Phys. Chem. B* **2006**, *110* (47).
330. O'Connell, M. J.; Sivaram, S.; Doorn, S. K., Near-infrared resonance Raman excitation profile studies of single-walled carbon nanotube intertube interactions: A direct comparison of bundled and individually dispersed HiPco nanotubes. *Phys. Rev. B* **2004**, *69* (23), 235415-15.
331. Hertel, T.; Hagen, A.; Talalaev, V.; Arnold, K.; Hennrich, F.; Kappes, M.; Rosenthal, S.; McBride, J.; Ulbricht, H.; Flahaut, E., Spectroscopy of Single- and Double-Wall Carbon Nanotubes in Different Environments. *Nano Lett.* **2005**, *5* (3), 511-514.
332. Walsh, A. G.; Vamivakas, A. N.; Yin, Y.; Cronin, S. B.; ÅcnlÅ¼, M. S.; Goldberg, B. B.; Swan, A. K., Screening of Excitons in Single, Suspended Carbon Nanotubes. *Nano Lett.* **2007**, *7* (6), 1485-1488.
333. Fantini, C.; Cassimiro, J.; Peressinotto, V. S. T.; Plentz, F.; Souza Filho, A. G.; Furtado, C. A.; Santos, A. P., Investigation of the light emission efficiency of single-wall carbon nanotubes wrapped with different surfactants. *Chem. Phys. Lett.* **2009**, *473* (1-3), 96-101.
334. Duan, W. H.; Wang, Q.; Collins, F., Dispersion of carbon nanotubes with SDS surfactants: a study from a binding energy perspective. *Chem. Sci.* **2011**, *2* (7), 1407-1413.
335. Nativ-Roth, E.; Nap, R. J.; Szleifer, I.; Yerushalmi-Rozen, R., Order–disorder transition induced by surfactant micelles in single-walled carbon nanotubes dispersions. *Soft Matter* **2010**, *6* (21), 5289-5292.
336. Monteiro-Riviere, N. A.; Inman, A. O.; Wang, Y. Y.; Nemanich, R. J., Surfactant effects on carbon nanotube interactions with human keratinocytes. *J. Nanomedicine Nanotechnol.* **2005**, *1* (4), 293-299.
337. Goak, J. C.; Lee, S. H.; Han, J. H.; Jang, S. H.; Kim, K. B.; Seo, Y.; Seo, Y.-S.; Lee, N., Spectroscopic studies and electrical properties of transparent conductive films fabricated by using surfactant-stabilized single-walled carbon nanotube suspensions. *Carbon* **2011**, *49* (13), 4301-4313.
338. Park, J.; Seong, M.-J., Dispersion Efficiency of Carbon Nanotubes in Aqueous Solutions of Deoxycholate Sodium Salts. *J. Korean Phys. Soc.* **2010**, *56* (4), 1391-1394.
339. Ericson, L. M.; Pehrsson, P. E., Aggregation Effects on the Raman Spectroscopy of Dielectrophoretically Deposited Single-Walled Carbon Nanotubes. *J. Phys. Chem. B* **2005**, *109* (43), 20276-20280.
340. Shen, K.; Curran, S.; Xu, H.; Rogelj, S.; Jiang, Y.; Dewald, J.; Pietrass, T., Single-Walled Carbon Nanotube Purification, Pelletization, and Surfactant-Assisted Dispersion: A Combined TEM and Resonant Micro-Raman Spectroscopy Study. *J. Phys. Chem. B* **2005**, *109* (10), 4455-4463.
341. Schilling, T.; Jungblut, S.; Miller, M. A., Depletion-Induced Percolation in Networks of Nanorods. *Phys. Rev. Lett.* **2007**, *98* (10), 108303.
342. Khripin, C. Y.; Arnold-Medabalimi, N.; Zheng, M., Molecular-Crowding-Induced Clustering of DNA-Wrapped Carbon Nanotubes for Facile Length Fractionation. *ACS Nano* **2011**, *5* (10), 8258–8266.
343. Angelikopoulos, P.; Bock, H., The Nanoscale Cinderella Problem: Design of Surfactant Coatings for Carbon Nanotubes. *J. Phys. Chem. Lett.* **2011**, *2* (3), 139-144.

344. Chou, S. G.; Son, H.; Kong, J.; Jorio, A.; Saito, R.; Zheng, M.; Dresselhaus, G.; Dresselhaus, M. S., Length characterization of DNA-wrapped carbon nanotubes using Raman spectroscopy. *Appl. Phys. Lett.* **2007**, *90* (13), 131109.
345. Bergin, S. D.; Nicolosi, V.; Cathcart, H.; Lotya, M.; Rickard, D.; Sun, Z.; Blau, W. J.; Coleman, J. N., Large Populations of Individual Nanotubes in Surfactant-Based Dispersions without the Need for Ultracentrifugation. *J. Phys. Chem. C* **2008**, *112* (4), 972-977.
346. Jeong, S. H.; Kim, K. K.; Jeong, S. J.; An, K. H.; Lee, S. H.; Lee, Y. H., Optical absorption spectroscopy for determining carbon nanotube concentration in solution. *Synthetic Met.* **2007**, *157* (13-15), 570-574.
347. Naumov, A. V.; Ghosh, S.; Tsyboulski, D. A.; Bachilo, S. M.; Weisman, R. B., Analyzing Absorption Backgrounds in Single-Walled Carbon Nanotube Spectra. *ACS Nano* **2011**, *5* (3), 1639-1648.
348. Saito, T.; Ohmori, S.; Shukla, B.; Yumura, M.; Iijima, S., A Novel Method for Characterizing the Diameter of Single-Wall Carbon Nanotubes by Optical Absorption Spectra. *Appl. Phys. Express* **2009**, *2*, 095006.
349. Li, Z.; Zheng, L.; Yan, W.; Pan, Z.; Wei, S., Spectroscopic Characteristics of Differently Produced Single-Walled Carbon Nanotubes. *ChemPhysChem* **2009**, *10*, 2296-2304.
350. Simpson, J. R.; Fagan, J. A.; Becker, M. L.; Hobbie, E. K.; Hight Walker, A. R., The effect of dispersant on defects in length-separated single-wall carbon nanotubes measured by Raman spectroscopy. *Carbon* **2009**, *47* (14), 3238-3241.
351. Krause, B.; Mende, M.; Pötschke, P.; Petzold, G., Dispersability and particle size distribution of CNTs in an aqueous surfactant dispersion as a function of ultrasonic treatment time. *Carbon* **2010**, *48* (10), 2746-2754.
352. Cardenas, J. F.; Gromov, A., The effect of bundling on the G' Raman band of single-walled carbon nanotubes. *Nanotechnology* **2009**, (46), 465703.
353. Wang, J.; Jin, Z.; Cheng, J.; Li, Y., Assembling Structure of Single-Walled Carbon Nanotube Thin Bundles. *J. Phys. Chem. C* **2009**, *113* (19), 8132-8135.
354. Hertel, T.; Walkup, R. E.; Avouris, P., Deformation of carbon nanotubes by surface van der Waals forces. *Phys. Rev. B* **1998**, *58* (20), 13870.
355. Shim, J.; Vichchulada, P.; Zhang, Q.; Lay, M. D., Spectroscopic and Scanning Probe Studies of a Nondestructive Purification Method for SWNT Suspensions. *J. Phys. Chem. C* **2010**, *114* (1), 652-657.
356. Nishide, D.; Miyata, Y.; Yanagi, K.; Tanaka, T.; Kataura, H., Effective Separation of Carbon Nanotubes and Metal Particles from Pristine Raw Soot by Ultracentrifugation. *Jpn. J. Appl. Phys.* **2009**, *48*, 015004.
357. Feng, Q.-P.; Xie, X.-M.; Liu, Y.-T.; Gao, Y.-F.; Wang, X.-H.; Ye, X.-Y., Length sorting of multi-walled carbon nanotubes by high-speed centrifugation. *Carbon* **2007**, *45*, 2307-2320.
358. Fagan, J. A.; Becker, M. L.; Chun, J.; Nie, P.; Bauer, B. J.; Simpson, J. R.; Hight-Walker, A.; Hobbie, E. K., Centrifugal Length Separation of Carbon Nanotubes. *Langmuir* **2008**, *24* (24), 13880-13889.
359. Decker, J. E.; Walker, A. R. H.; Bosnick, K.; Clifford, C. A.; Dai, L.; Fagan, J.; Hooker, S.; Jakubek, Z. J.; Kingston, C.; Makar, J.; Mansfield, E.; Postek, M. T.; Simard, B.; Sturgeon, R.; Wise, S.; Vladar, A. E.; Yang, L.; Zeisler, R., Sample preparation protocols for realization of reproducible characterization of single-wall carbon nanotubes. *Metrologia* **2009**, *46* (6), 682-692.

360. Grossiord, N.; Regev, O.; Loos, J.; Meuldijk, J.; Koning, C. E., Time-Dependent Study of the Exfoliation Process of Carbon Nanotubes in Aqueous Dispersions by Using UV-Visible Spectroscopy. *Anal. Chem.* **2005**, *77* (16), 5135-5139.
361. Huang, Y. Y.; Knowles, T. P. J.; Terentjev, E. M., Strength of Nanotubes, Filaments, and Nanowires From Sonication-Induced Scission. *Adv. Mater.* **2009**, *21* (38-39), 3945-3948.
362. Chew, H. B.; Moon, M.-W.; Lee, K. R.; Kim, K.-S., Compressive dynamic scission of carbon nanotubes under sonication: fracture by atomic ejection. *Proc. R. Soc. A* **2011**, *467* (2129), 1270-1289.
363. Fagan, J. A.; Simpson, J. R.; Bauer, B. J.; DePaoliLacerda, S. H.; Becker, M. L.; Chun, J.; Migler, K. B.; HightWalker, A. R.; Hobbie, E. K., Length-Dependent Optical Effects in Single-Wall Carbon Nanotubes. *J. Am. Chem. Soc.* **2007**, *129* (34), 10607-10612.
364. Puech, N.; Blanc, C.; Grelet, E.; Zamora-Ledezma, C.; Maugey, M.; Zakri, C. c.; Anglaret, E.; Poulin, P., Highly Ordered Carbon Nanotube Nematic Liquid Crystals. *J. Phys. Chem. C* **2011**, *115* (8), 3272-3278.
365. Sostaric, J. Z.; Riesz, P., Sonochemistry of Surfactants in Aqueous Solutions: An EPR Spin-Trapping Study. *J. Am. Chem. Soc.* **2001**, *123* (44), 11010-11019.
366. Capelo, J. L.; Mota, A. M., Ultrasonication for Analytical Chemistry. *Curr. Anal. Chem.* **2005**, *1* (2), 193-201.
367. Liu, T.; Luo, S.; Xiao, Z.; Zhang, C.; Wang, B., Preparative Ultracentrifuge Method for Characterization of Carbon Nanotube Dispersions. *J. Phys. Chem. C* **2008**, *112* (49), 19193-19202.
368. Harrah, D. M.; Swan, A. K., The Role of Length and Defects on Optical Quantum Efficiency and Exciton Decay Dynamics in Single-Walled Carbon Nanotubes. *ACS Nano* **2011**, *5* (1), 647-655.
369. Singla, R.; Grieser, F.; Ashokkumar, M., Kinetics and Mechanism for the Sonochemical Degradation of a Nonionic Surfactant. *J. Phys. Chem. A* **2009**, *113* (12), 2865-2872.
370. Yim, B.; Okuno, H.; Nagata, Y.; Nishimura, R.; Maeda, Y., Sonolysis of surfactants in aqueous solutions: an accumulation of solute in the interfacial region of the cavitation bubbles. *Ultrason. Sonochem.* **2002**, *9* (4), 209-213.
371. Ashokkumar, M.; Niblett, T.; Tantiogco, L.; Grieser, F., Sonochemical Degradation of Sodium Dodecylbenzene Sulfonate in Aqueous Solutions. *Aust. J. Chem.* **2003**, *56* (10), 1045 - 1049
372. Manousaki, E.; Psillakis, E.; Kalogerakis, N.; Mantzavinos, D., Degradation of sodium dodecylbenzene sulfonate in water by ultrasonic irradiation. *Water Res.* **2004**, *38*, 3751-3759.
373. Abu-Hassan, M. A.; Kim, J. K.; Metcalfe, I. S.; Mantzavinos, D., Kinetics of low frequency sonodegradation of linear alkylbenzene sulfonate solutions. *Chemosphere* **2006**, *62* (5), 749-755.
374. Sato, H.; Sano, M., Characteristics of ultrasonic dispersion of carbon nanotubes aided by antifoam. *Colloid. Surface. A* **2008**, *322* (1-3), 103-107.
375. Brotchie, A.; Grieser, F.; Ashokkumar, M., Effect of Power and Frequency on Bubble-Size Distributions in Acoustic Cavitation. *Phys. Rev. Lett.* **2009**, *102* (8), 084302.
376. Galli, C., Radical Reactions of Arenediazonium Ions: An Easy Entry into the Chemistry of the Aryl Radical. *Chem. Rev.* **1988**, *88* (5), 765-792.

377. Szele, I.; Zollinger, H., Dediazonation of Arenediazonium Ions in Homogeneous Solution. Part XII. Solvent effects in competitive heterolytic and homolytic dediazoniations. *Helv. Chim. Acta* **1978**, *61*, 1721-1729.
378. Quintero, B.; Cabeza, M. C.; Martínez, M. I.; Gutiérrez, P.; Martínez, P. J., Dediazonation of *p*-hydroxy and *p*-nitrobenzenediazonium ions in an aqueous medium: Interference by the chelating agent diethylenetriaminepentaacetic acid. *Can. J. Chem.* **2003**, *81*, 832-839.
379. Bravo-Diaz, C.; Romero-Nieto, E. M.; Gonzalez-Romero, E., Micellar-Promoted Homolytic Dediazonation of *p*-Nitrobenzenediazonium Tetrafluoroborate. *Langmuir* **2000**, *16* (1), 42-48.
380. Canning, P. S. J.; Maskill, H.; McCrudden, K.; Sexton, B., A Product Analytical Study of the Thermal and Photolytic Decomposition of Some Arenediazonium Salts in Solution. *Bull. Chem. Soc. Jpn.* **2002**, *75* (4), 789-800.
381. Pazo-Llorente, R. n.; Rodriguez-Menacho, M. C.; González-Romero, E.; Bravo, D.; amp; x; az, C., Micellar Effects on Dediazonation and on Azo Coupling Reactions. *J. Colloid Interf. Sci.* **2002**, *248* (1), 169-175.
382. Marcoux, P. R.; Hapiot, P.; Batail, P.; Pinson, J., Electrochemical functionalization of nanotube films: growth of aryl chains on single-walled carbon nanotubes. *New J. Chem.* **2004**, *28* (2), 302-307.
383. Abiman, P.; Wildgoose, G. G.; Compton, R. G., Investigating the Mechanism for the Covalent Chemical Modification of Multiwalled Carbon Nanotubes Using Aryl Diazonium Salts. *Int. J. Electrochem. Sci.* **2008**, *3*, 104 - 117.
384. Lehr, J.; Williamson, B. E.; Downard, A. J., Spontaneous Grafting of Nitrophenyl Groups to Planar Glassy Carbon Substrates: Evidence for Two Mechanisms. *J. Phys. Chem. C* **2011**, *115* (14), 6629-6634.
385. Merino, E., Synthesis of azobenzenes: the coloured pieces of molecular materials. *Chem. Soc. Rev.* **2011**, *40* (7), 3835-3853.
386. Zollinger, H., Nitrogen as Leaving Group: Dediazoniations of Aromatic Diazonium Ions. *Angew. Chem. Int. Edit.* **1978**, *17*, 141-150.
387. Constantopoulos, K. T. The synthesis and characterization of photoresponsive polyhedral oligomeric silsesquioxanes. Flinders University, Adelaide, 2007.
388. Hirayama, K., *Handbook of Ultraviolet and Visible Absorption Spectra of Organic Compounds*. Plenum Press Data Division: New York, 1967.
389. Norwitz, G.; Nataro, N.; Keliher, P. N., Study of the steam distillation of phenolic compounds using ultraviolet spectrometry. *Analytical Chemistry* **1986**, *58* (3), 639-641.
390. Ando, R. m. A.; Borin, A. n. C.; Santos, P. S., Saturation of the Electron-Withdrawing Capability of the NO₂ Group in Nitroaromatic Anions: Spectroscopic and Quantum-Chemical Evidence. *J. Phys. Chem. A* **2007**, *111* (30), 7194-7199.
391. Williamson, B.; Rodebush, W. H., Ultraviolet Absorption Spectra of Organic Molecules. II. The Effect of Substituent Groups upon the Absorption of Biphenyl. *Journal of the American Chemical Society* **1941**, *63* (11), 3018-3025.
392. Lewis, E. S.; Suhr, H., The Reactions of the *p*-Nitrobenzenediazonium and Diazotate Ions with Acid and Base. *J. Am. Chem. Soc.* **1958**, *80* (6), 1367-1371.
393. Forbes, W. F., Light Absorption Studies: Part XI Electronic Absorption Spectra of Nitrobenzenes. *Can. J. Chem.* **1958**, *36* (10), 1350-1361.
394. Airinei, A.; Rusu, E.; Dorohoi, D., Solvent Influence on the Electronic Absorption Spectra of some Azoaromatic Compounds. *Spectrosc. Lett.* **2001**, *34* (1), 65-74.

395. Cook, A. H.; Jones, D. G.; Polya, J. B., 280. cis-Azo-compounds. Part III. Absorption spectra. *J. Chem. Soc.* **1939**, 1315-1320.
396. Milanesi, S.; Fagnoni, M.; Albin, A., (Sensitized) Photolysis of Diazonium Salts as a Mild General Method for the Generation of Aryl Cations. Chemoselectivity of the Singlet and Triplet 4-Substituted Phenyl Cations. *J. Org. Chem.* **2004**, *70* (2), 603-610.
397. Geng, H.-Z.; Lee, D. S.; Kim, K. K.; Han, G. H.; Park, H. K.; Lee, Y. H., Absorption spectroscopy of surfactant-dispersed carbon nanotube film: Modulation of electronic structures. *Chem. Phys. Lett.* **2008**, *455* (4-6), 275-278.
398. McDaniel, D. H.; Brown, H. C., An Extended Table of Hammett Substituent Constants Based on the Ionization of Substituted Benzoic Acids. *J. Org. Chem.* **1958**, *23* (3), 420-427.
399. Pazo-Llorente, R.; Bravo-Díaz, C.; González-Romero, E., Solvolysis of Some Arenediazonium Salts in Binary EtOH/H₂O Mixtures under Acidic Conditions. *Eur. J. Org. Chem.* **2003**, *2003* (17), 3421-3428.
400. Granite, M.; Radulescu, A.; Pyckhout-Hintzen, W.; Cohen, Y., Interactions between Block Copolymers and Single-Walled Carbon Nanotubes in Aqueous Solutions: A Small-Angle Neutron Scattering Study. *Langmuir* **2011**, *27* (2), 751-759.
401. Wang, H.; Xu, J., Theoretical evidence for a two-step mechanism in the functionalization single-walled carbon nanotube by aryl diazonium salts: Comparing effect of different substituent group. *Chem. Phys. Lett.* **2009**, *477* (1-3), 176-178.
402. Lim, H.; Lee, J. S.; Shin, H.-J.; Shin, H. S.; Choi, H. C., Spatially Resolved Spontaneous Reactivity of Diazonium Salt on Edge and Basal Plane of Graphene without Surfactant and Its Doping Effect. *Langmuir* **2010**, *26* (14), 12278-12284.
403. Hung, W.-C.; Elias, G.; Wai, C. M., Interaction of Aromatic Derivatives with Single-Walled Carbon Nanotubes. *ChemPhysChem* **2010**, *11*, 3439-3446.
404. Cardenas, J. F., Protonation and sonication effects on aggregation sensitive Raman features of single wall carbon nanotubes. *Carbon* **2008**, *46* (10), 1327-1330.
405. Kawamoto, H.; Uchida, T.; Kojima, K.; Tachibana, M., The feature of the Breit-Wigner-Fano Raman line in DNA-wrapped single-wall carbon nanotubes. *J. Appl. Phys.* **2006**, *99*, 094309.
406. Shoda, M.; Bandow, S.; Maruyama, Y.; Iijima, S., Probing Interaction between ssDNA and Carbon Nanotubes by Raman Scattering and Electron Microscopy. *J. Phys. Chem. C* **2009**, *113* (15), 6033-6036.
407. Strano, M. S.; Huffman, C. B.; Moore, V. C.; O'Connell, M. J.; Haroz, E. H.; Hubbard, J.; Miller, M.; Rialon, K.; Kittrell, C.; Ramesh, S.; Hauge, R. H.; Smalley, R. E., Reversible, Band-Gap-Selective Protonation of Single-Walled Carbon Nanotubes in Solution. *J. Phys. Chem. B* **2003**, *107* (29), 6979-6985.
408. Xu, Y.; Pehrsson, P. E.; Chen, L.; Zhang, R.; Zhao, W., Double-Stranded DNA Single-Walled Carbon Nanotube Hybrids for Optical Hydrogen Peroxide and Glucose Sensing. *J. Phys. Chem. C* **2007**, *111* (24), 8638-8643.
409. Cordero, N. A.; Alonso, J. A., Interaction of Surfactants Containing a Sulfuric Group with a (5,5) Carbon Nanotube. *J. Phys. Chem. C* **2010**, *114* (41), 17249-17256.
410. Engtrakul, C.; Davis, M. F.; Gennett, T.; Dillon, A. C.; Jones, K. M.; Heben, M. J., Protonation of Carbon Single-Walled Nanotubes Studied Using ¹³C and ¹H-

- 13C Cross Polarization Nuclear Magnetic Resonance and Raman Spectroscopies. *J. Am. Chem. Soc.* **2005**, *127* (49), 17548-17555.
411. Tummala, N. R.; Striolo, A., SDS Surfactants on Carbon Nanotubes: Aggregate Morphology. *ACS Nano* **2009**, *3* (3), 595-602.
412. Blackburn, J. L.; McDonald, T. J.; Metzger, W. K.; Engtrakul, C.; Rumbles, G.; Heben, M. J., Protonation Effects on the Branching Ratio in Photoexcited Single-Walled Carbon Nanotube Dispersions. *Nano Lett.* **2008**, *8* (4), 1047-1054.
413. Karachevtsev, V. A.; Glamazda, A. Y.; Plokhotnichenko, A. M.; Leontiev, V. S.; Linnik, A. S., Comparative study on protection properties of anionic surfactants (SDS, SDBS) and DNA covering of single-walled carbon nanotubes against pH influence: luminescence and absorption spectroscopy study. *Materialwissenschaft und Werkstofftechnik* **2011**, *42*, 41-46.
414. Li, M.; Chen, Q., Interactions between fullerene(C60) and poly(ethylene oxide) in their complexes as revealed by high-resolution solid-state 13C NMR spectroscopy. *Polymer* **2003**, *44* (9), 2793-2798.
415. Liu, T.; Xiao, Z.; Wang, B., The exfoliation of SWCNT bundles examined by simultaneous Raman scattering and photoluminescence spectroscopy. *Carbon* **2009**, *47* (15), 3529-3537.
416. Almgren, M.; Brown, W.; Hvidt, S., Self-aggregation and phase behavior of poly(ethylene oxide)-poly(propylene oxide)-poly(ethylene oxide) block copolymers in aqueous solution. *Colloid Polym. Sci.* **1995**, *273* (1), 2-15.
417. Schmidt, G.; Filoramo, A.; Derycke, V.; Bourgoin, J.-P.; Chenevier, P., Labile Diazo Chemistry for Efficient Silencing of Metallic Carbon Nanotubes. *Chem. Eur. J.* **2011**, *17* (5), 1415-1418.
418. Heller, D. A.; Barone, P. W.; Swanson, J. P.; Mayrhofer, R. M.; Strano, M. S., Using Raman Spectroscopy to Elucidate the Aggregation State of Single-Walled Carbon Nanotubes. *J. Phys. Chem. B* **2004**, *108* (22), 6905-6909.
419. Fantini, C.; Jorio, A.; Souza, M.; Strano, M. S.; Dresselhaus, M. S.; Pimenta, M. A., Optical Transition Energies for Carbon Nanotubes from Resonant Raman Spectroscopy: Environment and Temperature Effects. *Phys. Rev. Lett.* **2004**, *93* (14), 147406.
420. Fantini, C.; Jorio, A.; Santos, A. P.; Peressinotto, V. S. T.; Pimenta, M. A., Characterization of DNA-wrapped carbon nanotubes by resonance Raman and optical absorption spectroscopies. *Chem. Phys. Lett.* **2007**, *439* (1-3), 138-142.
421. Strano, M. S.; Doorn, S. K.; Haroz, E. H.; Kittrell, C.; Hauge, R. H.; Smalley, R. E., Assignment of (n,m) Raman and Optical Features of Metallic Single-Walled Carbon Nanotubes. *Nano Lett.* **2003**, *3* (8), 1091-1096.